

**University of Alberta**

*NMR studies of Troponin C-Troponin I complexes*

by

**Pascal Mercier**



A thesis submitted to the Faculty of Graduate Studies and Research  
in partial fulfillment of the requirements for the degree of  
Doctor of Philosophy

Department of Biochemistry

Edmonton, Alberta

Spring 2003

National Library  
of Canada

Bibliothèque nationale  
du Canada

Acquisitions and  
Bibliographic Services

Acquisisitons et  
services bibliographiques

395 Wellington Street  
Ottawa ON K1A 0N4  
Canada

395, rue Wellington  
Ottawa ON K1A 0N4  
Canada

*Your file* *Votre référence*

*ISBN: 0-612-82141-2*

*Our file* *Notre référence*

*ISBN: 0-612-82141-2*

The author has granted a non-exclusive licence allowing the National Library of Canada to reproduce, loan, distribute or sell copies of this thesis in microform, paper or electronic formats.

L'auteur a accordé une licence non exclusive permettant à la Bibliothèque nationale du Canada de reproduire, prêter, distribuer ou vendre des copies de cette thèse sous la forme de microfiche/film, de reproduction sur papier ou sur format électronique.

The author retains ownership of the copyright in this thesis. Neither the thesis nor substantial extracts from it may be printed or otherwise reproduced without the author's permission.

L'auteur conserve la propriété du droit d'auteur qui protège cette thèse. Ni la thèse ni des extraits substantiels de celle-ci ne doivent être imprimés ou autrement reproduits sans son autorisation.

# Canada

**University of Alberta**

**Library Release Form**

**Name of Author:** Pascal Mercier

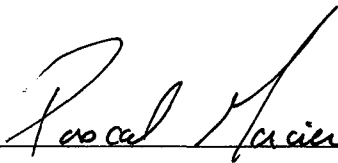
**Title of Thesis:** NMR Studies of Troponin C-Troponin I Complexes.

**Degree:** Doctor of Philosophy

**Year this Degree Granted:** 2003

Permission is hereby granted to the University of Alberta Library to reproduce single copies of this thesis and to lend or sell such copies for private, scholarly or scientific research purposes only.

The author reserves all other publication and other rights in association with the copyright in the thesis, and except as herein before provided, neither the thesis nor any substantial portion thereof may be printed or otherwise reproduced in any material form whatever without the author's prior written permission.



\_\_\_\_\_

**Dated:** April 1, 2003

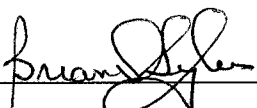
**Permanent address:**

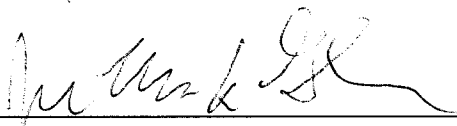
811 13e avenue est  
La Pocatière, QC  
Canada, G0R 1Z0

University of Alberta

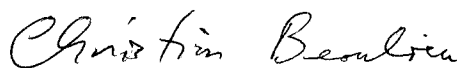
Faculty of Graduate Studies and Research

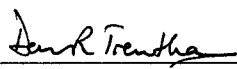
The undersigned certify that they have read, and recommend to the Faculty of Graduate Studies and Research for acceptance, a thesis entitled *NMR Studies of Troponin C-Troponin I Complexes* submitted by Pascal Mercier in partial fulfillment of the requirements for the degree of Doctor of Philosophy.

  
\_\_\_\_\_  
Dr. Brian D. Sykes (Supervisor)

  
\_\_\_\_\_  
Dr. Mark J.N. Glover

  
\_\_\_\_\_  
Dr. Paul G. Scott

  
\_\_\_\_\_  
Dr. Christian Beaulieu

  
\_\_\_\_\_  
Dr. David R. Trentham (External)

Dated: 6 March 2003

*À mes parents*

*La vie c'est court, mais c'est long des p'tits bouts*

*André Fortin, Les Colocs*

## ABSTRACT

An incredible amount of research has been done over the past 30 years on troponin C (TnC), a calcium-binding central to muscle contraction regulation, after its first discovery in 1968 by Ebashi [Ebashi, S. and Endo, M., *Prog Biophys Mol Biol*, **18**, 123-183, 1968]. As small as the protein is, it is part of a complex system involving several proteins whose network of interactions is under the influence of the intracellular calcium levels. Biochemical and biophysical studies have revealed an enormous amount of information about the structure and properties of TnC, but mostly as an isolated species. In the past five years, in a concerted effort to take the research to a higher level and shed some light on the interactions TnC makes with the other proteins of the muscle system, the scientific literature has witnessed the emergence of a large number of publications involving binary and tertiary complexes of TnC with other proteins of the regulatory unit, mainly the inhibitory Troponin I (TnI). Diverse regions of TnI have been shown to interact with TnC, and several mechanisms for calcium regulation have been proposed with different temporal interactions between TnC and TnI.

This thesis contributes to expanding the curriculum vitae of TnC, or at least discovering more of it, by presenting binding, structural and kinetics studies of three different TnC•TnI complexes using modern high-resolution, multinuclear and multidimensional nuclear magnetic resonance (NMR) spectroscopy. Chapter 2 presents a detailed study of the interaction between the C-terminal domain of skeletal TnC with the first 40 amino acid portion of the N-terminus (Rp40) and with the inhibitory peptide of

TnI (TnI<sub>96-115</sub>), in order to elucidate the nature of the proposed competition of these two peptides for the C-domain. The results showed the displacement of TnI<sub>96-115</sub> upon Rp40 binding and suggested constant occupancy of Rp40 on the CTnC due to its tight binding. The structure, dynamics and thermodynamics of the NTnC•Rp40 complex were investigated in greater detail in Chapter 3.

Electron microscopy studies have successfully probed the geometric and spatial organization of actin and tropomyosin on the thin filament, as well as the interactions with the myosin crossbridges. However, despite some recent advances in the direct observation of the sites of localization of troponin, the lack of high-resolution structure of the troponin complex and the averaging of the density in image reconstruction methods prevent complete fitting of the density maps and therefore, the relative orientation of the troponin proteins by electron microscopy has not to this day been determined. The work presented in Appendix 1 partially resolves this fundamental structural aspect of the troponin complex in muscles by reporting the orientation of TnC relative to actin in reconstituted muscle fibers, both in the relaxed and contracted states, as determined from fluorescence measurements. The structural consequences of the introduction of a fluorescent probe on TnC were examined by NMR for one of the required TnC mutants, along with the binding of the second TnI inhibitory region (TnI<sub>115-131</sub>), a fragment of TnI we call the 'switch peptide'. The NMR structure presented in Chapter 4 allowed for the better interpretation and validation of the fluorescence results reported in Chapter 5. The study outlined in Chapter 4 constitutes the first NMR structural investigation of the

switch peptide on the N-terminal domain of skeletal TnC. The determined structure also enable us to position the switch peptide in muscle fibers.

The magnesium level in resting cells is higher than that of calcium by several orders of magnitude. Previous studies have suggested  $Mg^{2+}/Ca^{2+}$  exchange within the  $Ca^{2+}$ -binding sites of TnC. Although the  $Ca^{2+}$ -induced structural changes in TnC are well characterized, there is no such information available for potential conformation changes induced by  $Mg^{2+}$  binding. We have investigated using NMR the effects of  $Mg^{2+}$  binding to the C-domain of TnC (CTnC) and proceeded to the elucidation of 3-dimensional structures of CTnC in the  $Mg^{2+}$ -saturated state using an approach based on automatic assignments of NOE peaks. Our results, presented in Chapter 6, show important changes in dynamic behavior and binding properties of  $CTnC \cdot Mg^{2+}$  relative to that of  $CTnC \cdot 2Ca^{2+}$ .

## ACKNOWLEDGMENTS

I first wish to express my most sincere gratitude to my supervisor, Professor Brian D. Sykes, for his constant support, guidance, encouragement and precious tips in more difficult times. The freedom I was given in my research coupled with your respect for my decisions have made my stay in your laboratory an exciting and unforgettable experience. It was simply the chance of a lifetime to do research with one of the most world-known NMR pioneers. You have taught me far more than science. Thanks for putting up with eastern French ways on an every day basis.

Many thanks to my friend and co-worker Dr. Leo Spyropoulos, for his tremendous help on the spectrometers, for giving me free access to his lab equipment, and for teaching me all the ins and outs of NMR processing, structure generation and relaxation. Leo, your passion for science and NMR has been and will always be a constant source of inspiration. Thanks for all the passionate debates and for the daily breaks at Tim's.

To Dr. Monica Li for trying to teach me the art of sample preparation and manipulation. Let's just hope that there is indeed hope for the lost causes Monica. Thanks to David Corson for his multiple protein expressions, your work is really appreciated and indispensable. Thanks to Gerry McQuaid for maintaining our spectrometers in Olympic shape and being such a friendly and helpful person. Thanks to

Robert Boyko for making our lives easier with handy computer software and for teaching by example diplomacy at baseball games. Go Magnets go!

I would also like to thank past and current lab members: Dr. Tharin Blumenschein, Margaret Daley, Angela Thiessen, Olga Baryshnikova, Leigh Willard, Linda Saltibus, Xu Wang, Darrin Lindhout, Grant Gay, Dr. Stéphane Gagné, Dr. John Bagu, Dr. Pierre Lavigne, Dr. Vincent Raussen and Dr. David Keiser for your various contribution to this work and for creating such a nice and friendly working atmosphere. Thanks to Sue Smith for handling all the paper work that I hate with a passion.

To the people at Nanuc, Dr. Ryan McKay, Erik Saude, Bruce Lix, Derryck Web and Emily Servais for letting me be a physical part of the organization and for being great co-workers. Special thanks to Ioannis Bastiolas for all his help in compiling and installing all the software I needed.

Thanks to Dr. Roisean Ferguson, Dr. David Trentham, Dr. John Corrie and Dr. Malcolm Irving from England for expanding the meaning of my research with the thrilling collaboration on the fluorescent-labeled troponin C mutants.

Toute ma gratitude à mes parents et ma famille pour leur support inconditionnel et leur aide sous toutes les formes depuis les 30 dernières années. Merci également à Irina pour ses encouragements, son niveau inespéré de compréhension et sa présence dans ma vie.

I am thankful to the Natural Sciences and Engineering Research Council of Canada, the Medical Research Council of Canada and the University of Alberta (Walter H. scholarship) for providing me with financial support.

## TABLE OF CONTENTS

	<i>Page</i>
<b>CHAPTER I Troponin C, Troponin I and the Muscle System</b>	1
CHAPTER OVERVIEW	1
STRUCTURAL ORGANIZATION OF STRIATED MUSCLES	2
1. The thick filament	6
2. The thin filament	7
3. Model of muscle contraction	13
4. Interactions between TnC and TnI	18
REFERENCES	24
<b>CHAPTER II Role of the Structural Domain of Troponin C Muscle Regulation: NMR Studies of Ca<sup>2+</sup> Binding and Subsequent Interactions with Regions 1-40 and 96-115 of Troponin</b>	27
INTRODUCTION	27
EXPERIMENTAL PROCEDURES	32
Construction of CTnC Mutant and protein isolation	32
Ca <sup>2+</sup> titration of [ <sup>15</sup> N]-CTnC	32
Rp40 titration of [ <sup>15</sup> N]-CTnC•2Ca <sup>2+</sup>	33
TnI <sub>96-115</sub> titration of [ <sup>15</sup> N]-CTnC•2Ca <sup>2+</sup>	33
Rp40 titration of [ <sup>15</sup> N]-CTnC•2Ca <sup>2+</sup> •TnI <sub>96-115</sub>	33
TnI <sub>96-115</sub> titration of [ <sup>15</sup> N]-CTnC•2Ca <sup>2+</sup> •Rp40	34
NMR spectroscopy	34
RESULTS	35
Titration of [ <sup>15</sup> N]-CTnC with Ca <sup>2+</sup>	35
Titration of CTnC•2Ca <sup>2+</sup> with Rp40	40
Titration of CTnC•2Ca <sup>2+</sup> with TnI <sub>96-115</sub>	43

Competitive binding A: Titration of CTnC•2Ca <sup>2+</sup> •TnI <sub>96-115</sub> with Rp40	44
Competitive binding B: Titration of CTnC•2Ca <sup>2+</sup> •Rp40 with TnI <sub>96-115</sub>	44
DISCUSSION	45
REFERENCES	53
<b>CHAPTER III Structure, Dynamics, and Thermodynamics of the Structural Domain of Troponin C in Complex with the Regulatory Peptide 1-40 of Rp40</b>	<b>56</b>
INTRODUCTION	56
EXPERIMENTAL PROCEDURES	59
Construction of plasmid vector encoding CTnC and protein isolation	59
NMR sample preparation	59
NMR experiments for structure determination	60
Distance and torsion angle restraints	60
Backbone amide <sup>15</sup> N relaxation measurements	63
Analysis of backbone amide <sup>15</sup> N relaxation measurements	65
Structure-based thermodynamic calculations for Rp40 binding to CTnC•2Ca <sup>2+</sup>	68
RESULTS	71
Structure of CTnC•2Ca <sup>2+</sup> •Rp40 determined by NMR spectroscopy	71
Backbone amide <sup>15</sup> N relaxation data	76
Determination of overall rotational correlation time	81
Determination of backbone amide <sup>15</sup> N S <sup>2</sup>	84
Backbone conformational entropy changes upon peptide binding determined from changes in S <sup>2</sup>	88
Structured-based thermodynamic calculations for Rp40 binding to CTnC•2Ca <sup>2+</sup>	89
DISCUSSION	92

REFERENCES	99
<b>CHAPTER IV The NMR Structure of a Bifunctional Rhodamine</b>	<b>102</b>
<b>Labeled N-domain of Troponin C Complexed with the</b>	
<b>Regulatory ‘Switch’ Peptide from Troponin I:</b>	
<b>Implications for in situ Fluorescence Studies in Muscle</b>	
<b>Fibers</b>	
INTRODUCTION	102
EXPERIMENTAL PROCEDURES	107
Synthesis of [ <sup>13</sup> C <sub>2</sub> ] Bisiodoacetamidorhodamine	107
Mutagenesis of sNTnC	108
Preparation of sNTnC	108
[ <sup>13</sup> C]Bifunctional rhodamine labeling of mutant sNTnC	109
NMR sample preparation	111
NMR experiments for structure determination	112
Structure determination, distance and torsion angle restraints	114
Determination of the orientation of BR label relative to the C helix	118
Backbone amide <sup>15</sup> N relaxation measurements	118
RESULTS AND DISCUSSION	120
Effect of ionic strength on dimerization	120
Spectral influence of atropisomerism in the bifunctional rhodamine	127
Structure of sNTnC•2Ca <sup>2+</sup> •TnI <sub>115-131</sub> •BR <sub>56-63</sub> determined by NMR	130
spectroscopy	
Consequences of the structure for polarized fluorescence studies	145
CONCLUSION	148
REFERENCES	150
<b>CHAPTER V In situ Orientations of Protein Domains: Troponin C in</b>	<b>153</b>
<b>Skeletal Muscle Fibers</b>	
GENERAL NOTE	153
SUMMARY	153

INTRODUCTION	154
RESULTS	158
BR probes do not affect TnC function	158
Changes in orientation of TnC helices upon Ca <sup>2+</sup> activation	159
Orientation of TnC domains	163
Structure of the N-lobe of BR-TnC complex to Ca <sup>2+</sup> and the TnI switch peptide	164
Determination of <i>in situ</i> domain orientations from polarized fluorescence studies	165
<i>In situ</i> orientation of the N-lobe of TnC at low [Ca <sup>2+</sup> ]	169
<i>In situ</i> orientation of the N-lobe of TnC when Ca <sup>2+</sup> is bound to the regulatory sites	171
DISCUSSION	172
EXPERIMENTAL PROCEDURES	177
Mutagenesis of TnC	177
Preparation of TnC	177
Bifunctional rhodamine labeling of mutant TnCs	178
Solutions	180
Incorporation of TnC into single muscle fibers	180
Fluorescence polarization, dipole order parameters and orientations	182
BR dipole orientations for in vitro structures of TnC	182
Maximum entropy analysis	183
Accession numbers	184
REFERENCES	184

**CHAPTER VI NMR Investigation of the C-domain of Troponin C in the Magnesium State**

GENERAL NOTE	190
INTRODUCTION	190
EXPERIMENTAL PROCEDURES	195
Expression and purification of sCTnC	195

Mg <sup>2+</sup> titration of [ <sup>15</sup> N]sCTnC	195
NMR sample preparation for chemical shift assignment and structure determination	196
NMR experiments for structure determination	197
Distance and torsion angle restraints	197
Backbone amide <sup>15</sup> N relaxation measurements	200
<b>RESULTS</b>	202
Titration of [ <sup>15</sup> N]sCTnC with Mg <sup>2+</sup>	202
Effect of temperature on sCTnC•Mg <sup>2+</sup>	207
Backbone amide <sup>15</sup> N relaxation measurements on sCTnC•Mg <sup>2+</sup>	209
Effect of the addition of Rp40 on sCTnC•Mg <sup>2+</sup>	213
Effect of higher magnesium concentration on sCTnC•Mg <sup>2+</sup>	216
Mg <sup>2+</sup> -induced structural changes on sCTnC	218
Structure of sCTnC•Mg <sup>2+</sup> determined by NMR spectroscopy	223
Influence of the starting model structure for automatic assignment and structures of sNTnC•Mg <sup>2+</sup>	233
<b>CONCLUSIONS</b>	236
<b>REFERENCES</b>	238
<b>CHAPTER VII Conclusion</b>	
Model of TnC•TnI interactions in muscle regulation	242
Three-dimensional models of interaction between TnC and TnI	245
<b>REFERENCES</b>	252
<b>Appendix I      Creation of topology and parameter files for rhodamine</b>	253
BR topology file in mtf format (CNS)	256
BR parameter file (CNS)	267
CNS script for BR linkage to sCTnC	274
<b>REFERENCES</b>	277

<b>Appendix II</b>	<b>Automatic NOE assignments with NMRView</b>	278
	How to use the script	278
	Source code	280
<b>Appendix III</b>	<b>Chemical shift assignment of sCTnC in complex with magnesium</b>	288

## LIST OF TABLES

<b>Table</b>		<i>Page</i>
III-1	NMR experiments conducted for the purpose of chemical shift assignment and obtaining NOE-based distance restraints for sCTnC•2Ca <sup>2+</sup> •Rp40.	61
III-2	Structural statistics for CTnC•2Ca <sup>2+</sup> in the CTnC•2Ca <sup>2+</sup> •Rp40 complex	73
III-3	Interhelical angles for CTnC•2Ca <sup>2+</sup> (skeletal and cardiac isoforms) free and bound to N-terminal TnI peptides.	75
III-4	Experimental backbone amide <sup>15</sup> N relaxation parameters and overall rotational correlation times at 500 and 600 MHz for [ <sup>15</sup> N]-CTnC in the Ca <sup>2+</sup> -saturated state and bound to Rp40.	78
III-5	Rotational diffusion anisotropy for CTnC•2Ca <sup>2+</sup> •Rp40.	83
III-6A	Change in accessible surface area for polar and non-polar residues upon Rp40 binding to CTnC•2Ca <sup>2+</sup> used for structure-based thermodynamic calculations.	90
III-6B	Structure-based thermodynamic analysis for binding of Rp40 to CTnC•2Ca <sup>2+</sup> .	90
IV-1	NMR experiments conducted for chemical shift assignment and NOE-based distance restraints for sNTnC•2Ca <sup>2+</sup> •TnI <sub>115-131</sub> •BR <sub>56-63</sub> .	113
IV-2	Structural statistics for sNTnC in the NTnC•2Ca <sup>2+</sup> •TnI <sub>115-131</sub> •BR <sub>56-63</sub> complex.	132
IV-3	Interhelical angles for sNTnC and cNTnC free and bound to TnI peptides.	144
V-1	Order parameters for the BR-TnCs in various physiological states.	160
V-2	BR dipole orientations for <i>in vitro</i> structures of TnC.	164
VI-1	NMR experiments conducted for the purpose of chemical shift assignment for sCTnC•Mg <sup>2+</sup> and obtaining NOE-based distance restraints at 30 °C.	198

VI-2	Dissociation constant and maximum shift extracted from changes in peak intensity of selected residues during sCTnC titration with Mg <sup>2+</sup> .	206
VI-3	Structural statistics for sCTnC•Mg <sup>2+</sup> .	229
VI-4	Interhelical angles for sNTnC and cNTnC free and bound to TnI peptides.	232
AIII-1	Chemical shift assignment of sCTnC in the sCTnC•Mg <sup>2+</sup> complex.	288

## LIST OF FIGURES

<b>Figure</b>		<i>Page</i>
I-1	Organization of skeletal muscle tissues.	3
I-2	Electron micrograph of parts of three myofibrils in longitudinal section.	4
I-3	Molecular model of the I-band, A-band, and M-line regions of the sarcomere.	5
I-4	The myosin molecule and its arrangement in the thick filament.	6
I-5	Molecular arrangement of the thin filament and structure of its components.	8
I-6	Schematic illustration of a possible thin filament regulation scheme.	14
I-7	Surface views and location of troponin and tropomyosin on 3D reconstructions of thin filaments.	17
I-8	Schematic summary of the interactions of with TnC and actin-Tm and a model depicting their role in the Ca <sup>2+</sup> -dependent regulation of muscle contraction (Triplet model).	19
I-9	Scheme of interactions of thin filament proteins (Filatov model).	20
I-10	Ribbon diagram of the TnC•TnI <sub>1-47</sub> •TnI <sub>96-115</sub> in the Maeda model.	22
I-11	Ribbon model of TnI in complex with TnC (Trehwella model).	23
II-1	Titration of CTnC with Ca <sup>2+</sup> . 500 MHz 2D- <sup>1</sup> H, <sup>15</sup> N}-HSQC NMR spectrum of CTnC.	36
II-2	Binding curves from changes in the 2D- <sup>1</sup> H, <sup>15</sup> N}-HSQC NMR spectrum of CTnC during titration with Ca <sup>2+</sup> , with Rp40, with TnI <sub>96-115</sub> and of CTnC•2Ca <sup>2+</sup> •TnI <sub>96-115</sub> during titration with Rp40.	38
II-3	2D- <sup>1</sup> H, <sup>15</sup> N}-HSQC NMR spectrum acquired during the titration of CTnC•2Ca <sup>2+</sup> with Rp40 and TnI <sub>96-115</sub> .	39
II-4	CTnC•2Ca <sup>2+</sup> backbone amide chemical shift changes upon Rp40 and TnI <sub>96-115</sub> binding.	42

II-5	500 MHz $^1\text{H}$ NMR spectra of $\text{CTnC}\cdot 2\text{Ca}^{2+}\cdot \text{Rp40}\cdot \text{TnI}_{96-115}$ at different $\text{Rp40}:\text{TnI}_{96-115}$ ratios and $\text{TnI}_{96-115}$ free in solution.	46
II-6	Molecular surface of CTnC in complex with Rp40 and $\text{TnI}_{96-115}$	50
III-1	Ensemble of 30 solution structures of $\text{CTnC}\cdot 2\text{Ca}^{2+}$ in the $\text{CTnC}\cdot 2\text{Ca}^{2+}\cdot \text{Rp40}$ complex and ribbon representation of the minimized average solution structure.	72
III-2	Distribution of NOEs as a function of residue number and backbone RMSD for the ensemble of 30 solution structures with respect to the average coordinates.	74
III-3	Backbone amide $^{15}\text{N}$ NMR relaxation times for $\text{CTnC}\cdot 2\text{Ca}^{2+}$ at 1.33 mM and for $\text{CTnC}\cdot 2\text{Ca}^{2+}\cdot \text{Rp40}$ at 0.33 mM.	77
III-4	Backbone amide $^{15}\text{N}$ NMR relaxation time ratios for $\text{CTnC}\cdot 2\text{Ca}^{2+}\cdot \text{Rp40}$ at 0.33 mM and at magnetic field strengths of 500 and 600 MHz.	80
III-5	Global rotational correlation time ( $\tau_m$ ) for $\text{CTnC}\cdot 2\text{Ca}^{2+}\cdot \text{Rp40}$ as a function of concentration.	82
III-6	Marginal density, $P(S^2   R_i)$ , as a function of $S^2$ and surface density plot of the marginal density of $S^2$ integrated over $R_{\text{ex}}$ and $\tau_c$ for residue $\text{F}^{112}$ .	85
III-7	Backbone amide $^{15}\text{N}$ $S^2$ on a per residue basis for $\text{CTnC}\cdot 2\text{Ca}^{2+}$ at 1.33 mM and $\text{CTnC}\cdot 2\text{Ca}^{2+}\cdot \text{Rp40}$ at 0.33 mM, changes in $S^2$ values for $\text{CTnC}\cdot 2\text{Ca}^{2+}$ observed upon Rp40 binding and contribution to conformational entropy on a per residue basis.	87
III-8	Strip plots taken at side-chain $^{13}\text{C}$ chemical shifts for residue $\text{I}^{104}$ from the $^{13}\text{C}$ part of the simultaneous 3D $^{13}\text{C}, ^{15}\text{N}$ -NOESY-HSQC spectrum.	96
IV-1	Selection of intermolecular NOE contacts between $\text{TnI}_{115-131}$ and sNTnC from the 3D $^{13}\text{C}/^{15}\text{N}$ -filtered/edited experiment.	117
IV-2	Overall amide envelope $R_1$ and $R_2$ relaxation rates for sNTnC in the $\text{sNTnC}\cdot 2\text{Ca}^{2+}\cdot \text{TnI}_{115-131}\cdot \text{BR}_{56-63}$ complex as a function of KCl concentration at a $^1\text{H}$ Larmor frequency of 500 MHz.	121

IV-3	Backbone amide $^{15}\text{N}$ NMR relaxation times and NOEs for $\text{sNTnC}\cdot 2\text{Ca}^{2+}\cdot \text{TnI}_{115-131}\cdot \text{BR}_{56-63}$ at 320 mM KCl at a magnetic field strength corresponding to a $^1\text{H}$ Larmor frequency of 500 and 600 MHz.	125
IV-4	Backbone amide $^{15}\text{N}$ NMR relaxation time and NOE ratios for $\text{sNTnC}\cdot 2\text{Ca}^{2+}\cdot \text{TnI}_{115-131}\cdot \text{BR}_{56-63}$ at 320 mM KCl and at magnetic field strengths corresponding to $^1\text{H}$ Larmor frequencies of 500 and 600 MHz.	126
IV-5	Structure of the bifunctional rhodamine after reaction with cysteine residues of the mutant TnC.	128
IV-6	Selected region of a 800 MHz $^{15}\text{N}$ -HSQC spectrum of sNTnC in the $\text{sNTnC}\cdot 2\text{Ca}^{2+}\cdot \text{TnI}_{115-131}\cdot \text{BR}_{56-63}$ complex.	129
IV-7	Backbone superimposition of the 20 lowest-energy solution structures of the $\text{sNTnC}\cdot 2\text{Ca}^{2+}\cdot \text{TnI}_{115-131}\cdot \text{BR}_{56-63}$ complex and ribbon representation of the minimized average solution structure.	134
IV-8	Distribution of NOEs as a function of residue number and backbone RMSD for the ensemble of 20 solution structures with respect to the average coordinates.	135
IV-9	Difference in N, HN, $\text{C}_\alpha$ and $\text{C}_\beta$ chemical shifts induced by BR attached to the C-helix at residues 56 and 63.	137
IV-10A	Molecular surface of the $\text{sNTnC}\cdot 2\text{Ca}^{2+}\cdot \text{TnI}_{115-131}\cdot \text{BR}_{56-63}$ complex.	139
IV-10B	Back view of the molecular surface shown in Figure IV-10A.	140
IV-11	Ribbon representation of the backbone superimposition of $\text{sNTnC}\cdot 2\text{Ca}^{2+}\cdot \text{TnI}_{115-131}\cdot \text{BR}_{56-63}$ with $\text{cNTnC}\cdot \text{Ca}^{2+}\cdot \text{cTnI}_{147-163}$ and $\text{cNTnC}\cdot \text{Ca}^{2+}\cdot \text{cTnI}_{147-163}\cdot \text{bepridil}$ .	143
V-1	Arrangement of tropomyosin and the troponin components TnT, TnI and TnC on the actin filament, ribbon representation TnC showing the four pairs of cysteine residues that were crosslinked in a series of mutant TnCs by the BR probe, ribbon representation of the N-lobe of TnC where the N-lobe is in the apo- and $\text{Ca}^{2+}$ -bound state and molecular structure of Bis-iodoacetamidrhodamine ( $\text{BR-I}_2$ ).	156

V-2	Fitted Gaussian orientation distribution parameters for each of the BR-labeled TnCs at various physiological states .	162
V-3	Ribbon representation of the lowest energy NMR structure of sNTnC•2Ca <sup>2+</sup> •TnI <sub>115-131</sub> •BR <sub>56-63</sub> .	162
V-4	Maximum entropy distributions for the N-lobe of TnC in various physiological states.	168
V-5	<i>In situ</i> orientation of the N-lobe of TnC on the actin filament.	170
VI-1	500 MHz 2D- <sup>1</sup> H, <sup>15</sup> N}-HSQC NMR spectrum of 2.7 mM apo sCTnC and sCTnC•Mg <sup>2+</sup> (20.2 mM Mg <sup>2+</sup> ) at 30 °C.	203
VI-2	Binding curves obtained from the averaged normalized peak intensity changes of different residues in the 2D- <sup>1</sup> H, <sup>15</sup> N}-HSQC NMR spectrum of sCTnC during titration with Mg <sup>2+</sup> .	205
VI-3	Series of 500 MHz 2D- <sup>1</sup> H, <sup>15</sup> N}-HSQC NMR spectra of sCTnC•Mg <sup>2+</sup> recorded at different temperatures.	208
VI-4	Comparison of the 500 MHz 2D- <sup>1</sup> H, <sup>15</sup> N}-HSQC NMR spectrum of sCTnC•Mg <sup>2+</sup> at 5 °C and 45 °C.	211
VI-5	<sup>15</sup> N backbone relaxation times for sCTnC•Mg <sup>2+</sup> at a magnetic field strength corresponding to a <sup>1</sup> H Larmor frequency of 500 MHz.	212
VI-6	500 MHz 2D <sup>1</sup> H, <sup>15</sup> N}-HSQC NMR spectrum of sNTnC•Mg <sup>2+</sup> •Rp40 (20.2 mM Mg <sup>2+</sup> ) at 30 °C.	215
VI-7	Comparison of the 600 MHz 2D- <sup>1</sup> H, <sup>15</sup> N}-HSQC NMR spectrum of sCTnC•Mg <sup>2+</sup> at 5 °C and 30 °C.	217
VI-8	Backbone amide chemical shift difference between the Mg <sup>2+</sup> - and Ca <sup>2+</sup> -saturated state of sCTnC.	220
VI-9	Mg <sup>2+</sup> -induced C <sub>α</sub> and C <sub>β</sub> (B) chemical shifts differences in sCTnC•Mg <sup>2+</sup> compared to that of TnC•4Ca <sup>2+</sup> .	222
VI-10	Backbone superimposition of the 16 lowest-energy solution structures of calbrain, the 50 lowest-energy solution structures of sNTnC•Mg <sup>2+</sup> , and ribbon diagrams of sCTnC•Mg <sup>2+</sup> and sCTnC in the sCTnC•2Ca <sup>2+</sup> •Rp40 complex.	224
VI-11	Ramachandran plots of sCTnC•Mg <sup>2+</sup> on a per residue basis.	225

VI-12	Distribution of NOEs as a function of residue number and backbone and side chain RMSD for the ensemble of 50 solution structures of sCTnC•Mg <sup>2+</sup> .	231
VII-1	A model for the structures of TnC and TnI in the ternary TnC•TnI•TnT complex, in the presence and absence of Ca <sup>2+</sup> .	243
VII-2	Backbone trace superimposition of the 15 lowest energy structures of sTnC•cTnI <sub>128-147</sub> •sTnI <sub>115-131</sub> •4Ca <sup>2+</sup> .	249
VII-3	Ribbon diagram of a chimera structure of sTnC•cTnI <sub>128-147</sub> •sTnI <sub>115-131</sub> •4Ca <sup>2+</sup> .	251
A1-1	Chemical structure of BR.	255

## ABBREVIATIONS

BR <sub>56-63</sub>	bifunctional rhodamine with both methyl groups <sup>13</sup> C labeled and attached to mutated residues C56 and C63 of sNTnC
cNTnC	N-domain of cardiac TnC
cCTnC	C-domain of cardiac TnC
CTnC	C-domain (residues 88-162) of skeletal TnC
DIPSI	decoupling in the presence of scalar interactions
DMF	dimethylformamide.
DSS	2,2-dimethyl-2-silapentane-5-sulfonic acid.
DTT	threo-1,4-dimercapto-2, 3-butanediol
HMQC	heteronuclear multi-quantum coherence.
HSQC	heteronuclear single-quantum coherence
NMR	nuclear magnetic resonance
NOE	nuclear Overhauser effect
NTnC	N-domain of (residues 1-90) of skeletal TnC
$R_1$	longitudinal relaxation rate ( $=1/T_1$ )
$R_2$	transverse relaxation rate ( $=1/T_2$ )
RMSD	root-mean-square standard deviation
Rp40	N-terminal synthetic peptide (residues 1-40) of rabbit TnI
$S^2$	order parameter
sCTnC	C-domain of skeletal TnC
sNTnC	N-domain (residues 1-90) of skeletal TnC
$T_1$	longitudinal relaxation time
$T_2$	transverse relaxation time
TnC	troponin C
TnI	troponin I
TnI <sub>96-115</sub>	inhibitory synthetic peptide (96-115) of chicken skeletal TnI
TnI <sub>115-131</sub>	synthetic 'switch' peptide (residues 115-131) of chicken skeletal TnI

TnI <sub>p</sub>	inhibitory peptide comprising residues 96-115 of skeletal troponin I
TnT	troponin T
TOCSY	total correlation spectroscopy
$\tau_c$	correlation time for fast internal motion
$\tau_m$	global rotational correlation time

## CHAPTER I

### *Troponin C, Troponin I and the Muscle System*

#### **CHAPTER OVERVIEW**

This thesis focuses on structural studies of binary complexes of the calcium regulatory protein Troponin C (TnC) from skeletal muscle and three regions of its target inhibitory protein Troponin I (TnI) using high resolution, multinuclear and multidimensional nuclear magnetic resonance spectroscopy (NMR). This complex is central to the calcium regulation of muscle contraction, and these structures are important to the elucidation of the mechanism of the regulatory process. This chapter concentrates on general structural aspects of the muscle machinery, with specific emphasis on the importance of the interactions between TnC and TnI, and on the rationale that motivated the research presented in this thesis. It is not intended to repeat the large quantity of information on muscle contraction available from detailed reviews published in the literature [(1-9) and references therein]. Since the studies presented in subsequent chapters were performed exclusively on the skeletal isoform of TnC and TnI, the distinctive characteristics of the cardiac system will not be discussed in detail. The reader may consult the sources mentioned above for more detail. Similarly, this chapter will not review any of the NMR aspects associated with data collection, pulse sequences, peak and chemical shift assignments, and structure generation. While the NMR methodology is constantly evolving, the general procedures employed have also been the

subject of recent reviews and I will discuss contributions I have made elsewhere in this thesis.

## **STRUCTURAL ORGANIZATION OF STRIATED MUSCLES**

Muscle contractile activity is controlled by a sophisticated, efficient and finely tuned protein machinery. The cardiac and skeletal systems perform vital functions, and many human dysfunctions have been associated with genetic mutations of muscle proteins. Detailed knowledge of these proteins is a prerequisite for the understanding of the different mechanisms of activation and regulation of muscle contraction, and thereby of disorders. It is also a necessity for the elaboration of cures through drug engineering. The following section presents an overall picture of the architecture of muscle fibers and introduces the nature and the function of the main protein components.

Muscle tissues consist of networks of filamentous fibers called myofibrils disposed in a parallel arrangement (see Figure I-1). As illustrated in Figure I-2, myofibrils have a striated appearance as seen visually under electron microscopy due to the alternation of a light, isotropic band called I-band, and a dark, anisotropic band called the A-band. Both bands show darker regions at their center due to the presence of Z disks (I-band) and M disks (A-band), which serve as anchoring units for the two main types of filaments, namely the thin and the thick filaments, respectively. The region separating two Z disks is known as the sarcomere and constitutes the basic contractile unit of myofibrils. A cartoon model of the different protein components of the sarcomere is depicted in Figure I-3. Muscles undergo changes from a relaxed to contracted state

following Ca binding to TnC, which is translated into a macroscopic movement of the thin filament passed the thick filament.

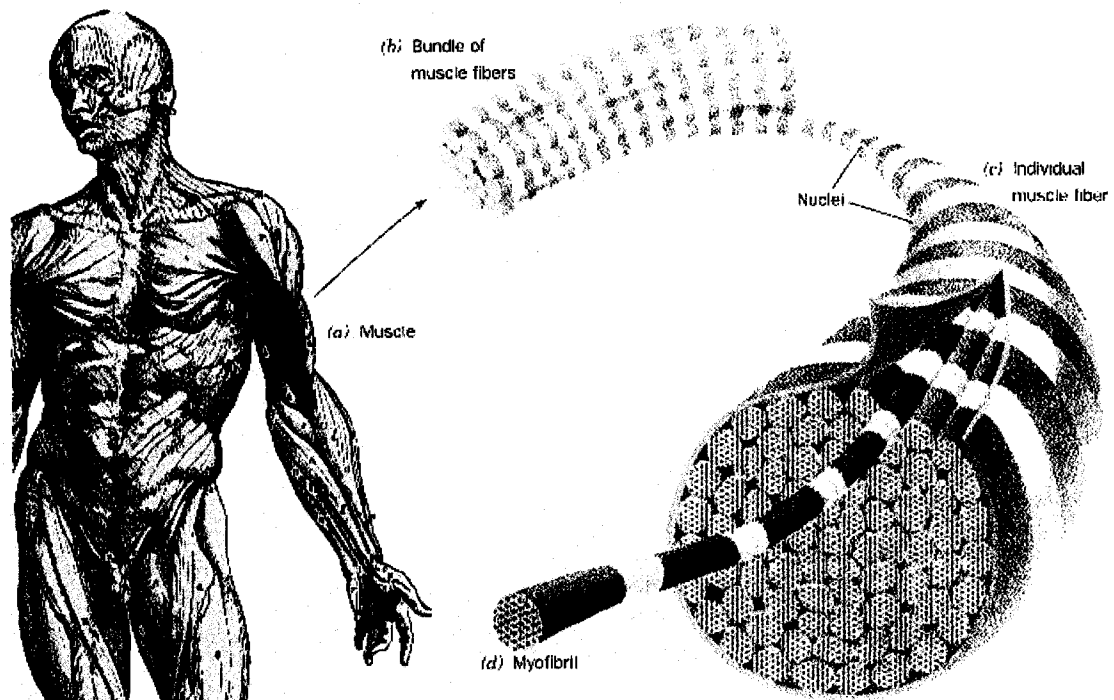


Figure I-1. Organization of skeletal muscle tissues: (a) Muscle, (b) muscle fiber bundles, (c) multinucleated cells forming a muscle fiber, and (d) myofibrils. Figure and legend adapted from (10).

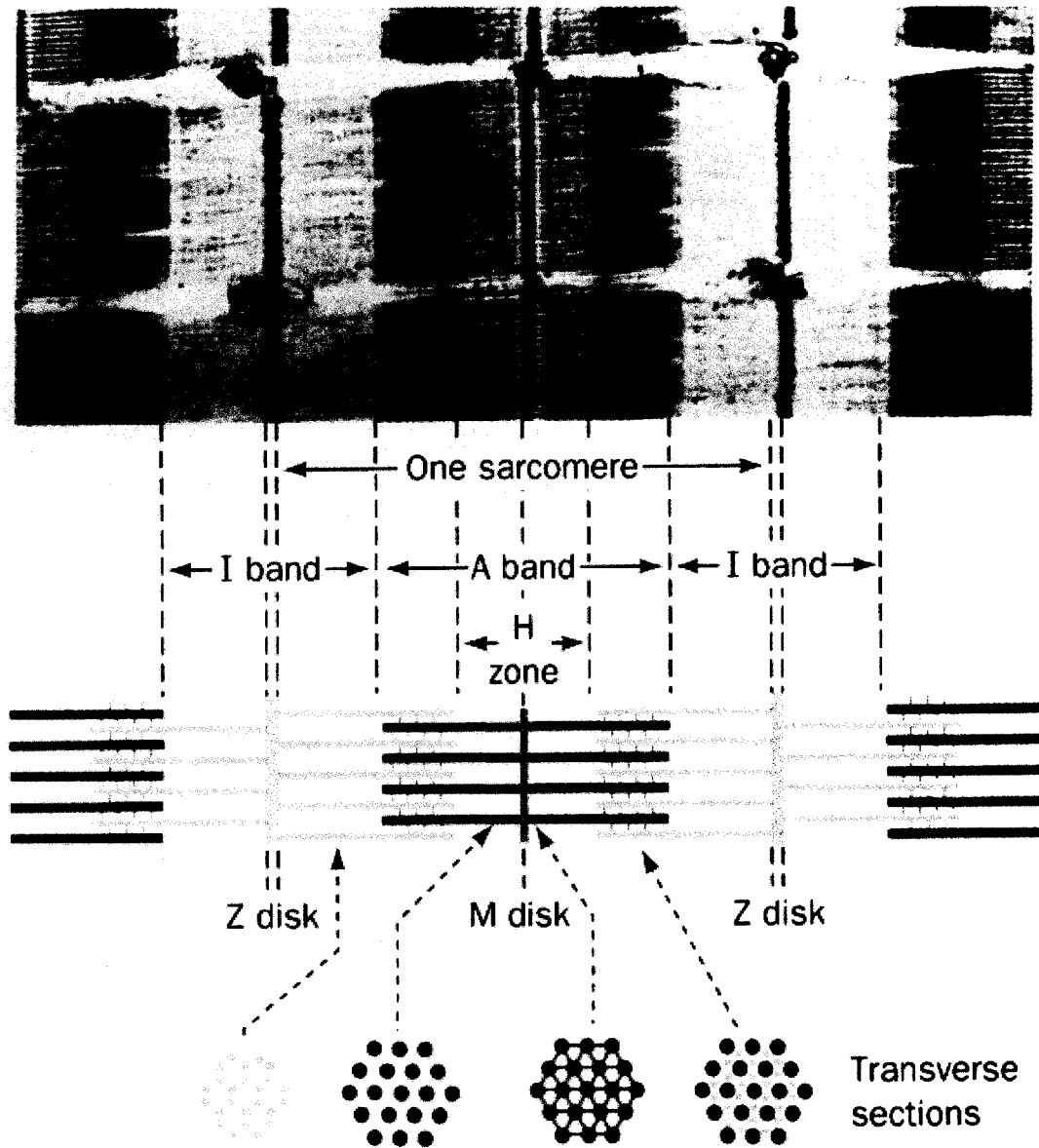


Figure I-2. An electron micrograph of parts of three myofibrils in longitudinal section. The myofibrils are separated by horizontal gaps. A myofibril's major features, as indicated in the accompanying interpretive drawings, are the light I band, which contains only hexagonally arranged thin filaments; the A band, whose dark H zone contains only hexagonally packed thick filaments, and whose even darker outer segments contain overlapping thick and thin filaments; the Z disk, to which the thin filaments are anchored; and the M disk, which arises from a bulge at the center of each thick filament. The myofibril's functional unit, the sarcomere, is the region between two successive Z disks. Figure and legend adapted from (10).

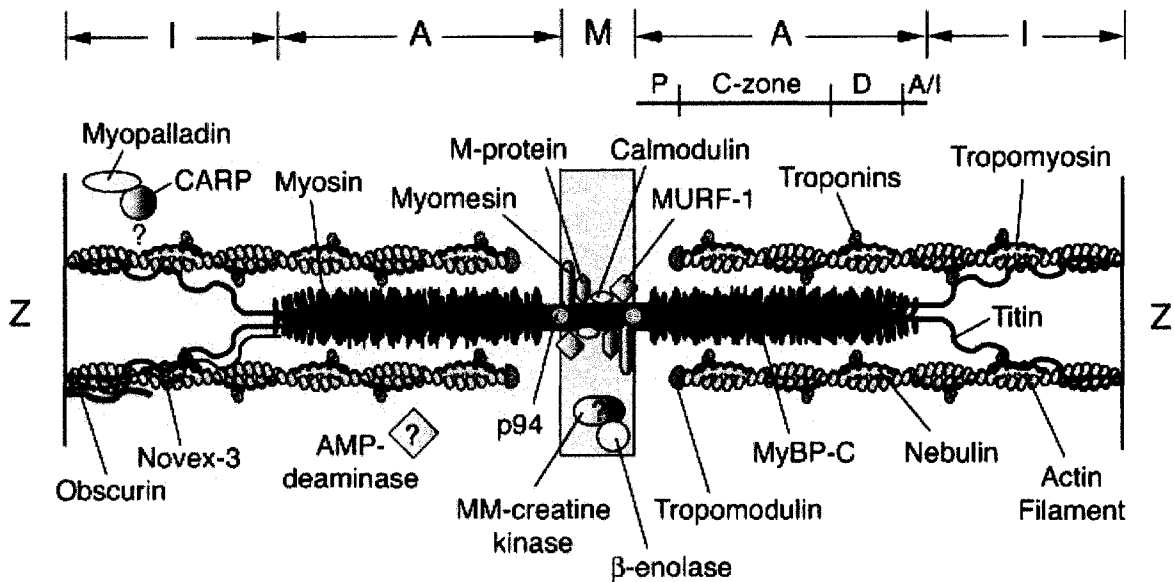


Figure I-3. Molecular model of the I-band, A-band, and M-line regions of the sarcomere. Polar thin filaments, containing actin, tropomyosin, troponins C, I, and T, and single molecules of skeletal muscle nebulin, span the I-band and interdigitate with the myosin (thick) filaments in the A-band, where they are capped at their pointed ends by tropomodulin. The myosin heads extend from the core of the thick filaments in the C-zone of the A-band, and are anchored and aligned in the middle of the sarcomere, the M-line. Single molecules of the giant protein titin extend an entire half sarcomere and are proposed to function as a template for sarcomere assembly. Titin's I-band region contains elastic elements that contribute to the passive force of myofibrils. Components whose binding sites are unknown are shown with question marks. Figure and legend adapted from (2).

*The thick filament*

The thick filament, contributing to the A-band at the center of the sarcomere, is almost entirely made of hundreds of copies of myosin (see Figure I-4). Myosin is composed of two heavy chains with molecular weight of ~200 kDa each and four light chains, two each of the so-called essential and regulatory light chains of molecular mass ~20 kDa. Thick filaments consist of myosin aggregates wherein myosin molecules associate via their C-terminal regions to form a long bipolar helical tail stabilized by coil-coil interactions. The “head” domain of myosin, also referred to as the S-1 fragment, is made of the N-terminal region of each heavy chain and two light chains. The globular heads of myosin extend out of the core of the thick filament and are responsible for the ATPase reaction that provides energy for the power stroke upon interaction with the thin filament. Thus, myosin constitutes the molecular motor for contractility, whereas the thin filament assumes responsibility for tight control and regulation.

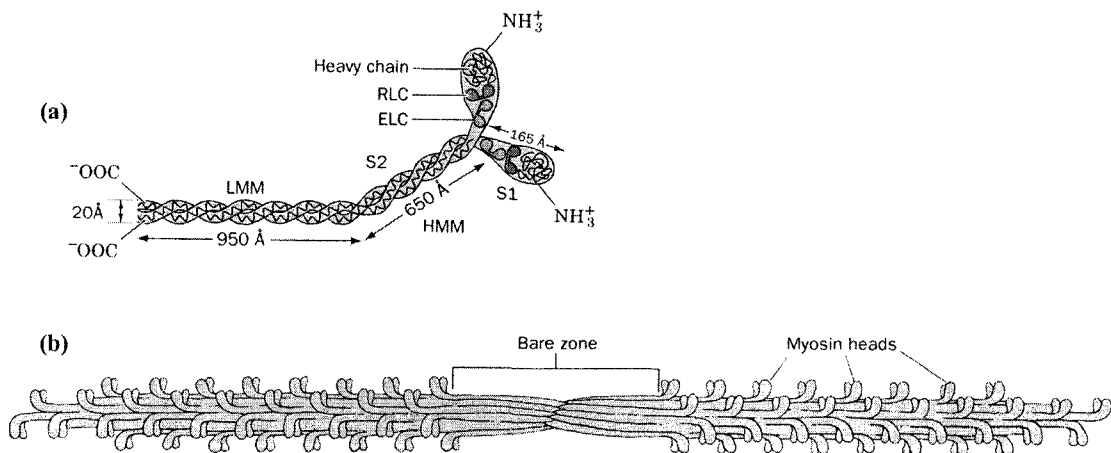


Figure I-4. (a) The myosin molecule; its rod-shaped tail is formed by the two extended  $\alpha$ -helices. (b) A thick filament typically contains several hundred myosin molecules organized in a repeating staggered. Figure and legend adapted from (10).

---

*The thin filament*

---

The composition of the thin filament is more complex than that of the thick filament, with 3 major components, troponin, tropomyosin and actin. Actin polymerizes spontaneously under physiological conditions (from G-actin to F-actin) to form the backbone of the thin filament, to which troponin and tropomyosin bind (see Figure I-5). The thin filament can be viewed as a single short-pitch left-handed helix strand of actin monomers with 13 monomers in 6 turns, each of a pitch of about 59 Å and an axial separation of 27.6 Å between successive monomers. The structure appears as two slowly twisting strands of actin monomer, with a cross over repeat of the strands between 360 and 380 Å.

A portion of the giant modular protein titin (M.W. ~3.6 MDa), the largest protein identified to date (11), also interacts with the actin filament. Titin is thought to play a structural role by acting as a molecular spring controlling the stiffness of myofibrils (12), and as a stabilizer by maintaining sarcomeric integrity. It has been suggested from the discovery of a Ser/Thr kinase domain at the C-terminal end that titin may also be involved in signaling pathways. The actin filament is capped by two different proteins, tropomodulin (~40 kDa) at the M disk, and CapZ (heterodimer of MW ~88 kDa) at the Z disk.

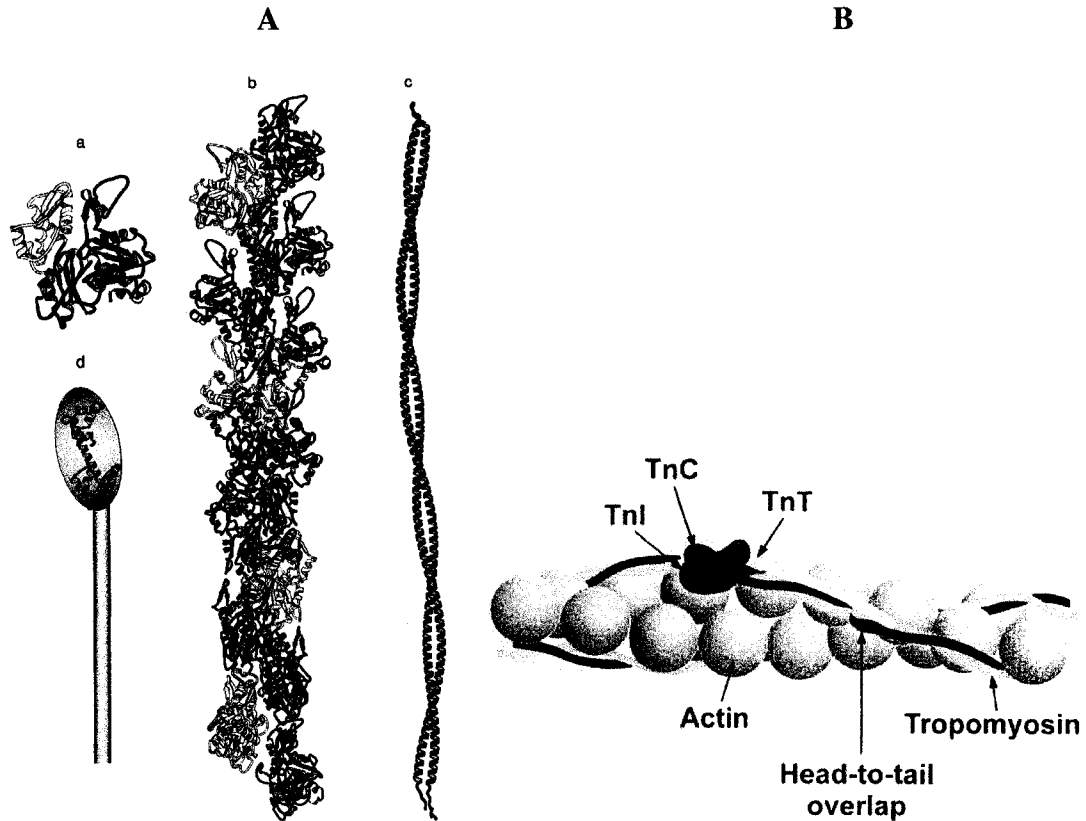


Figure I-5. Panel A) *a*) Ribbon diagram of the actin monomer structure as determined by Kabsch et al. (13) with subdomains: 1 (red), 2 (green), 3 (blue), and 4 (yellow). *b*) Ribbon diagram of the actin monomer in panel *a* placed into a 13/6 helix by Holmes et al. (14). Ribbon diagram of the twochain, coiled-coil  $\alpha$ -helical structure of tropomyosin. *d*) Schematic illustration of the troponin complex, drawn to the same scale as panels *a*–*c*, shows troponin-C (red) as a ribbon diagram (15) and troponin-T as the green rod and part of the blue oval, which also contains troponin-I. Panel B) A model of the molecular arrangement of troponin (Tn), tropomyosin (Tm), and actin in the skeletal muscle thin filament. The various troponin subunits [TnC (red), TnT (yellow), and TnI (green)] as they lie along the two-stranded tropomyosin shown as an  $\alpha$ - (brown) and  $\alpha$ -heterodimer (orange) that in turn lies along an actin (gray) strand, spanning 7 G-actin monomers. Figure and legend adapted from (1) and (4).

Tropomyosin (M.W. ~37 kDa) is a ~ 42 nm long  $\alpha$ -helical coil-coil, which lies along the grooves formed by the long-period strands of actin such that, in striated muscles, each tropomyosin molecule interacts with seven actin monomers (see (8) for an extensive review). Tropomyosin acts as a regulatory switch by blocking the myosin binding sites on actin and thereby inhibiting muscle contraction in the absence of calcium. Furthermore, tropomyosin stabilizes the thin filaments by inhibiting their fragmentation, slowing down polymerization and depolymerization at the end points and increasing their rigidity.

Regulation of muscle contraction occurs at the level of troponin, a three-component complex involving troponin C, troponin I, and troponin T, which is associated with tropomyosin in a 1:1 stoichiometry. The troponin complex, despite its relative small size, is the ultimate controller of muscle activity. In spite of intense research, there is still no high-resolution structure of the troponin complex available to date, nor for any binary complexes made of the combination of any of these three proteins in their full length. A preliminary X-ray structure was however presented (16).

Troponin C (M.W. ~20 kDa) is the troponin unit for which the highest amount of structural information is available. The structure, solved for the first time in 1985 by Herzberg and James using X-ray crystallography (15, 17, 18), revealed a dumbbell-shaped molecule with two globular domains (designated N and C, for the N and C-terminal domains, respectively) connected by a flexible central linker (17, 19-22). Each domain of TnC contains two paired helix-loop-helix EF hand motifs typical of calcium

binding proteins. The N-domain contains 5 helices (labeled N, A-D), whereas the C-domain includes only 4 (labeled E-H). Calcium binding sites III and IV in the C-domain are believed to be always occupied by either  $\text{Ca}^{2+}$  ( $K_a = 2.1 \cdot 10^7 \text{ M}^{-1}$ ) or  $\text{Mg}^{2+}$  ( $K_a = 2 \cdot 10^3 \text{ M}^{-1}$ ) under physiological conditions, whereas sites I and II in the N-domain are  $\text{Ca}^{2+}$  specific sites with weaker affinity ( $K_a = 3.2 \cdot 10^5 \text{ M}^{-1}$ ) (23, 24). In skeletal TnC, site I has lower  $\text{Ca}^{2+}$  affinity than site II due to the presence of 3 consecutive Gly residues, which increases backbone flexibility and lowers binding of  $\text{Ca}^{2+}$ . It has been postulated that the presence of a Gly or Ser residue at position 3 of the  $\text{Ca}^{2+}$  binding loops in the N-domain, instead of the Asp residue located at the homologous position in the two binding loops of the C-domain, was not as effective in coordinating  $\text{Ca}^{2+}$  and was in part responsible for the lowest affinity of the N-domain for  $\text{Ca}^{2+}$ . The cardiac isoform of the N-domain of TnC has the characteristic of having a defunct  $\text{Ca}^{2+}$  binding site due to a non-conservative insertion, and therefore only binds a single  $\text{Ca}^{2+}$  ion.

Both domains of skeletal TnC undergo important conformational changes following  $\text{Ca}^{2+}$  binding (21, 25). The structure of each domain undergoes a transition from an unstructured (C-domain), or “closed” (N-domain), to an “opened” state, where the B/C helix pair in the N-domain and the F/G helices of the C-domain move away from the NAD and EH units, respectively, similar to that of the movement of a draw bridge. Upon opening, a large hydrophobic surface becomes exposed, which constitutes an important binding site for different portions of TnI (26-30). Conversely, the structure of the cardiac N-domain remains closed upon  $\text{Ca}^{2+}$  binding (31), and subsequent binding of

TnI is necessary to promote the opening of the structure (32). The nature of the interaction between TnC and TnI will be discussed in more detail below.

Troponin I has long been identified as the key player in the inhibitory action of troponin (33) (see (5) for a comprehensive review). TnI was recognized for the first time as a distinct identity in earlier work on fragmentation of the troponin complex into “troponin A” and “troponin B”, where A referred to “the calcium sensitizing” and B to the inhibitory parts of troponin (34, 35), respectively. In 1972, Greaser et al. standardized the nomenclature by proposing the troponin C/troponin I/troponin T appellations (36). The region of TnI including residues 96-115 is able on its own to inhibit the actomyosin ATPase and is consequently designated the inhibitory region of TnI. Van Eyk et al. identified the region of TnI comprising residues 104-115 (numbers corresponding to the skeletal isoform) as the minimal sequence required for inhibition of skinned cardiac and skeletal fibers depleted of endogenous troponin I (37). TnI<sub>96-115</sub> produces only 50% of the inhibition compared to that of intact TnI, and other regions of TnI have been shown to be implicated in contractile inhibition, in particular the segment containing residues 115-131 (38), known as “the second TnI binding region” or “switch peptide”. In addition, it has also been demonstrated that the presence of tropomyosin enhances the inhibitory effect of TnI (5). Direct interactions between the two proteins were indeed reported (39, 40), but the exact binding sites of TnI on tropomyosin are still elusive.

The cardiac isoform of TnI contains a ~33 amino acid N-terminal peptide containing two phosphorylation sites (S23, S24) (41), which provide a second level of control for the interactions with TnC. Indeed, it is known that phosphorylation at these two sites by cAMP kinase results in changes of troponin I structure and lowering of  $\text{Ca}^{2+}$  affinity for NTnC (42, 43). Similarly, T142 phosphorylation in the cardiac inhibitory peptide decreased the binding affinity of this peptide by ~14 fold (44).

TnT (M.W. ~30 kDa) is believed to anchor the troponin complex on actin, and its specific functions are still somewhat obscure (see (9) for review). The N-terminus of TnT (T1 fragment, residues 1-158) is known to interact in  $\text{Ca}^{2+}$ -independent fashion with tropomyosin (39, 45-47) in the region around the junction point between the C-terminus of one and the N-terminal of another tropomyosin dimer. The C-terminal (T2 fragment, residues 159-259) region contains two supplementary tropomyosin  $\text{Ca}^{2+}$ -dependent binding sites (39), which provides an additional  $\text{Ca}^{2+}$ -dependent regulation of muscle contraction. Using five different and consecutive ~ 40 residue peptide constructs covering the whole TnT-T2 amino acid sequence, Blumenschein et al. identified by gel electrophoresis two regions of TnT-T2 interacting to with TnC (48). Residues 160-193 of TnT-T2 were found to bind to the CTnC in presence of  $\text{Ca}^{2+}$ , even in the additional presence of Rp40. On the other hand, TnI<sub>56-115</sub> and TnI<sub>96-139</sub>, which contains the primary inhibitory region of TnI, hinder its binding.

A recent study by Lehman et al. exposed a novel feature of the troponin T tail region (residues 1-153), as it inhibited both MgATPase activity and myosin S1-ADP

binding to the thin filament in the absence of TnI and TnC (49). These results highlight the role of TnT in positioning tropomyosin in the B-state and strongly support an earlier hypothesis that TnT, in addition to TnI, was responsible for inhibition of muscular contraction. Further research will be needed to investigate whether the TnT tail is in its native form without the presence of the two troponin components.

### *Model of muscle contraction*

---

Force development in muscle is initiated by the release of calcium from the sarcoplasmic reticulum inside the cell and the subsequent attachment of myosin heads to the actin filaments, which causes the myosin heads to “walk” on actin and forces the thin filament to move past the thick filament. Several models for the activation and inhibition of muscular contraction have been suggested in the last 30 years since the first discovery of the localization of  $\text{Ca}^{2+}$  to the thin filament by Ebashi and Endo (50). The latest and now most accepted form of the “steric blocking” model is shown in Figure I-6 (4).

Electron microscopy studies on muscle fibers have help visualized up to three distinct biochemical states of the thin filament (51), whose associated structural changes are presented in Figure I-6 (4). In the B state, also known as the “off” or “blocked” state, there is no calcium bound to the N-domain of TnC, and myosin attachment can form only via non-stereospecific weak binding to actin, and there is low actomyosin ATPase activity. In this state, troponin I is bound to actin, and tropomyosin is held in a blocking position. The second state (C state), referred to as the “active” or “closed” state, corresponds to a  $\text{Ca}^{2+}$ -activated state where stereospecific weak binding by myosin can

occur, but the ATPase activity is still low. Troponin I is released from actin, allowing some motion of tropomyosin. Finally, in the fully “on”, “open” or “rigor”, also known as the M state, tropomyosin is further pushed across the thin filament, allowing for high force generation through specific myosin binding to actin and enhanced ATPase activity. The kinetics of the cooperative switching between the states has been established (52, 53). The “cooperative unit” formed of seven actin monomers under the control of a single tropomyosin molecule together with a troponin molecule is thought to be rather too small to explain all the data, and it has been proposed that there is communication and cooperativity between successive heptades of actin units (54, 55). In addition to the movement transition of tropomyosin, the  $\text{Ca}^{2+}$  affinity of troponin increases during the “switching-on” of the regulatory unit.

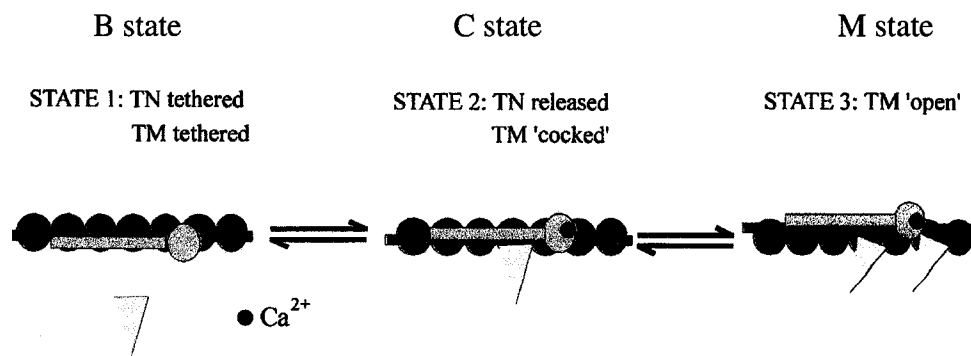


Figure I-6. Schematic illustration of a possible thin filament regulation scheme. The tropomyosin has three distinct positions on the actin filament. A major effect of  $\text{Ca}^{2+}$  binding is to move troponin, possibly with some small tropomyosin movement as well, thus freeing tropomyosin to move (it is ‘cocked’), although it takes head binding to move tropomyosin substantially to the open position. Red circles, actin monomers; green rods, tropomyosin; blue shapes, troponin; yellow shapes, myosin heads (S1). Figure and legend adapted from (4).

Electron microscopy and three-dimensional reconstitution of the thin filament based on the known atomic structure of actin (14) and the myosin head (56) have been used to directly visualize steric blocking and unblocking of myosin-binding sites on actin by tropomyosin (57, 58). In the absence of calcium, tropomyosin lies over the outer domain of actin, inhibiting strong myosin binding. In the presence of  $\text{Ca}^{2+}$ , tropomyosin undergoes a  $25^\circ$  azimuthal movement from the inner to the outer domain of actin, exposing some of the previously blocked myosin-binding sites. Subsequent saturation of the thin filament with myosin heads shifts tropomyosin by an additional  $10^\circ$ , thereby exposing the entire myosin-binding sites (see Figure I-7A).

In one of their latest studies using a mutant tropomyosin that binds every four actin monomers, Lehman et al. successfully reconstituted both troponin and tropomyosin in the low and high  $\text{Ca}^{2+}$ -concentration states (59). Figure I-7B shows the location of troponin and tropomyosin on 3D reconstructions of thin filaments. The broad contact seen between troponin and actin (Figure I-7B-f) is no longer seen in the presence of calcium (Figure I-7B-g). Because all actin monomers are treated as identical during three-dimensional reconstitutions of electron densities, the shape of troponin is uncertain. In the case where different part of troponin associate with more than one actin monomer, their effect would be averaged and merged as if they were derived from one monomer only.

Electron microscopy studies have provided strong evidence for the validity of the blocking mechanism by which TnI-actin interactions constrain tropomyosin in the actin

outer domain in the absence of  $\text{Ca}^{2+}$ , such that tropomyosin sterically interferes with myosin-actin binding. In light of the presence of interactions between troponin and tropomyosin, the possible implication of troponin in the transitional movement of tropomyosin still needs to be investigated. Moreover, possible induced conformational changes in the structure of actin following myosin S1 head binding might also contribute to tropomyosin translocation and cannot be neglected (60).

A high-resolution structure of the troponin complex would contribute significantly to filling the gaps separating us from a more complete and accurate understanding of muscle contraction and its associated kinetic mechanism. It would also greatly advance the fitting of electron density maps and allow for direct observation and identification of specific regions of troponin making contacts with tropomyosin and actin. The absence of high-resolution structure of troponin is one of the major factors currently preventing the determination of the relative orientation of the troponin proteins on the thin filament.

Recently, a novel technique based on polarized fluorescence measurements from bifunctional rhodamine probes covalently attached to Cys-mutated target proteins was introduced for mapping protein-domain orientations in the cellular environment. This method allows for establishing a direct correlation between data collected from *in vitro* studies on isolated systems with *in vivo* investigations of proteins in their natural environment. It has in particular proven to be successful in probing the orientation of the myosin light chain domain in different stages of muscle contraction (61, 62). Using the

same principles, Ferguson et al. have determined the orientation of fluorescent mutants of TnC in reconstituted muscle fibers (Chapter 5). The NMR structure of one of the fluorescent labeled mutants (Chapter 4) contributed largely to the validation and analysis of the fluorescence results.

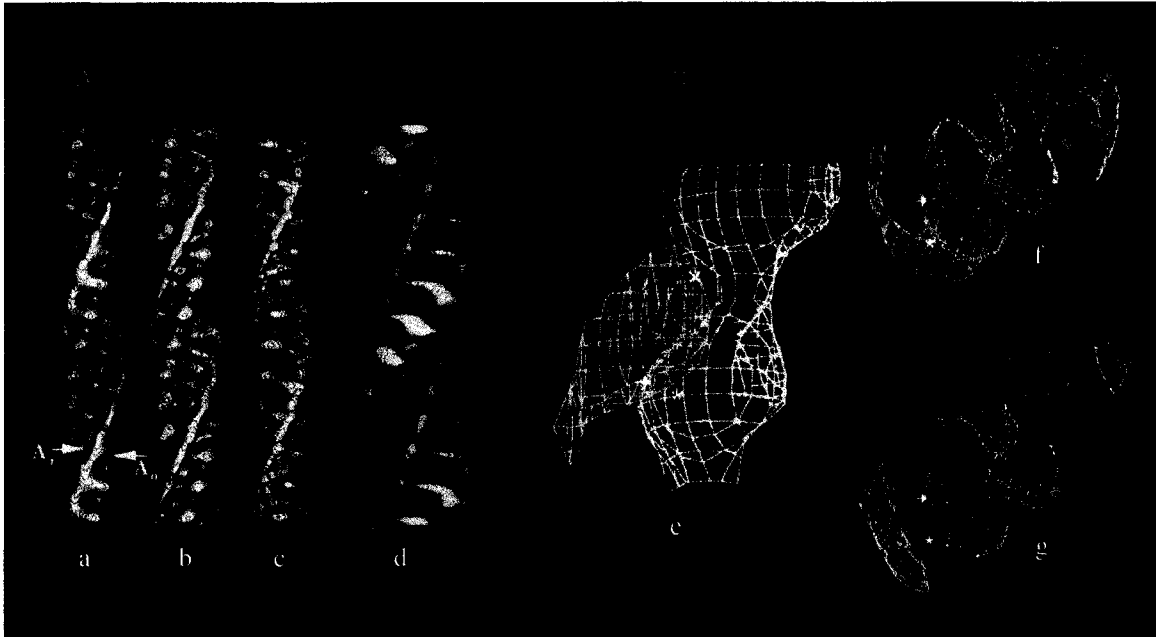


Figure I-7. **PANEL A)** Surface views of reconstructions of: a, frog skeletal muscle thin filaments in EGTA; b, Limulus thin filaments in  $\text{Ca}^{2+}$ ; c,d, Limulus thin filaments partially and fully decorated with myosin S-1 (two mol: seven mol S-1: seven mol actin, respectively). The tropomyosin strand is associated with the outer domain of actin (Ao) in the “off-state” (a), but moves across the actin surface closer to the inner domain (Ai) on addition of  $\text{Ca}^{2+}$  (b), and becomes centered on the latter following S-1 decoration (c, d). **PANEL B)** Location of troponin and tropomyosin on 3D reconstructions of thin filaments. (e) Filament surface at low  $[\text{Ca}^{2+}]$  viewed longitudinally with the pointed end of the filament facing up; troponin (cyan) and tropomyosin (red) shown superimposed on two actin monomers (yellow). Troponin lies on the peripheral edge of the strong myosin-binding site and covers potential sites of weak myosin-binding. The connectivity between troponin and tropomyosin and changing interactions between troponin and actin in the presence and absence of  $\text{Ca}^{2+}$  is compared in (f) and (g) with identical  $\sim 30 \text{ \AA}$  thick transverse slabs. In the absence of  $\text{Ca}^{2+}$  (f), troponin appears to connect tropomyosin and a broad region of the extreme periphery of actin. In the presence of  $\text{Ca}^{2+}$  (g), troponin appears to make contact with tropomyosin, but not with actin. Figure and legend adapter from (58) and (59).

---

*Interactions between TnC and TnI*

---

TnC is the target protein for  $\text{Ca}^{2+}$  released from the sarcoplasmic reticulum and therefore the ultimate molecular switch and commander of the cascade of protein-protein interactions ultimately leading to muscle contraction. Tightly coupled with this process is TnI, which fulfills a central responsibility in the regulation of muscle contraction. The interactions between TnI and TnC are fundamental to the activation and regulation of muscle contraction. Several years of research have been devoted to mapping the interactions sites between the two proteins. Unfortunately, the low solubility of TnI has, in part, prevented any structure of the TnC•TnI complex from being determined. A common alternative to direct structure determination of TnC•TnI consists of separate examination of partial binary complexes made of selected fractions of TnI. From the standpoint of using high-resolution multinuclear and multidimensional NMR for structure determination of the TnC•TnI system, this simplified approach has the advantage of improving NMR spectra by lowering the molecular weight and simplifying the spectra by the elimination of unnecessary regions of TnI not known to interact with TnC. However, the use of shorter TnI peptides increases the possibility of non-specific binding to TnC and deviations from the native structure of TnI. In a final analysis, the information collected from various partial complexes of TnC•TnI needs to be globalized. Ultimately, experimental results from different sources can be combined in the form of comprehensive models of TnC-TnI interaction, but discrepancies or uncertainties in the input data could prevent a unanimous rationalization of all the data.

In the past five years our NMR laboratory has been particularly active in mapping out the stoichiometry, the kinetics, the affinity and the sites of interaction of TnI on TnC, for both the cardiac and skeletal isoforms, as well as in determining the structure of several of the complexes (27-30, 32, 63-67). This research has not only exposed fundamental differences between the two systems, but also helped refine the TnC-TnI model. One of the TnC•TnI interaction models that prevailed in 1997 (38), before the publication of the work presented in Chapter 2, is depicted in Figure I-8. A slightly different and more complete model involving TnT and Tm is shown in Figure I-9.

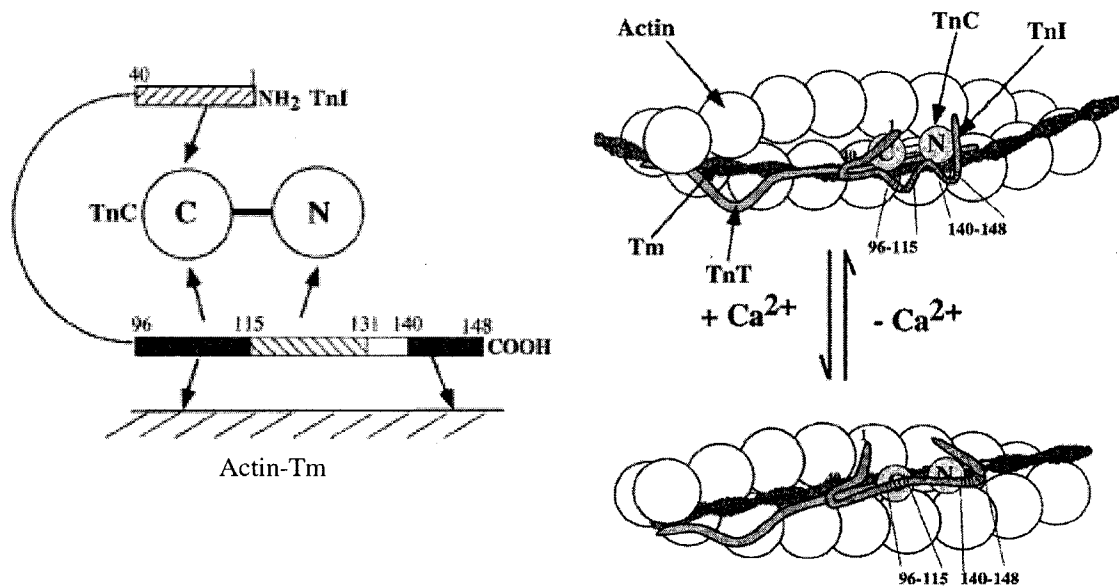


Figure I-8. Schematic summary of the interactions of TnI residues 1 to 40 and 96 to 148 with TnC and actin-Tm, and a model depicting their role in the Ca<sup>2+</sup>-dependent regulation of muscle contraction. Left: Arrows indicate the various regions of TnI involved in binding TnC and the actin-Tm. Regions of TnI proposed to interact with the N and C domains of TnC are hatched. Regions of TnI that bind the actin-Tm thin filament and are responsible for the full inhibitory activity are shaded. Right: a schematic model depicting the possible organization and changes occurring in the troponin complex in the absence and presence of Ca<sup>2+</sup>. Circular spheres represent actin monomers. Figure and legend adapted from (38).

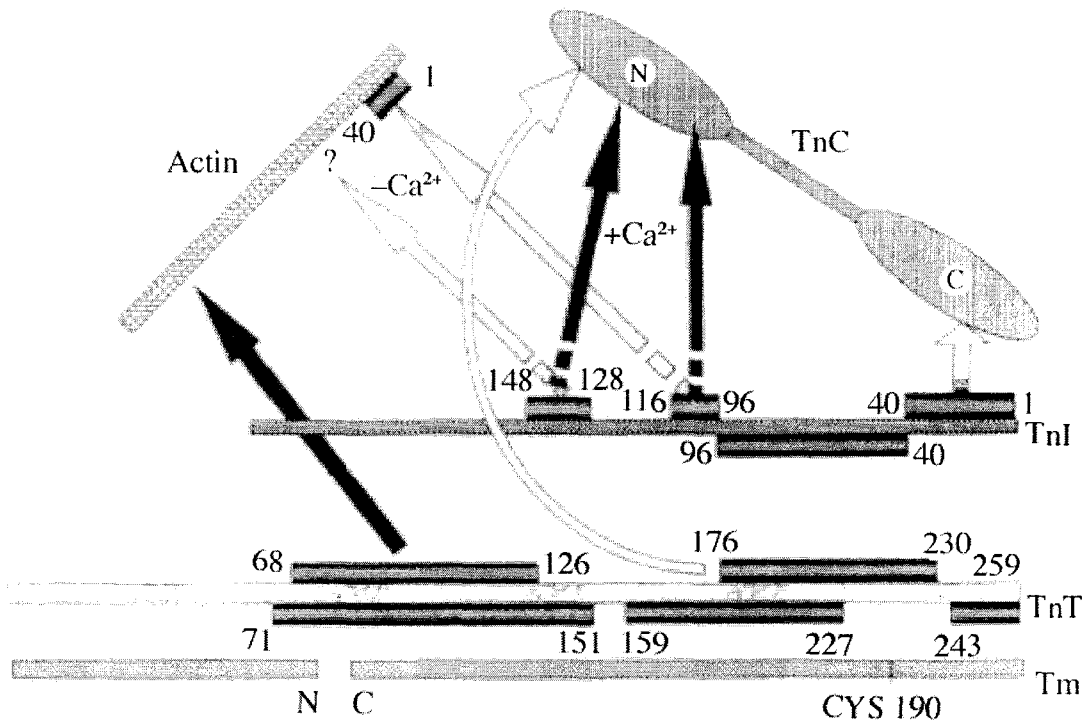


Figure I-9. Scheme of interactions of thin filament proteins. Each protein is shown as a segment. Residue numbers shown in rectangles that face each other or are connected by arrows indicate the sites of interaction between partners. The positions of the N- and C termini of the proteins are indicated. Arrows labeled  $+Ca^{2+}$  and  $-Ca^{2+}$  indicate the interactions that are enhanced in the presence or in the absence of  $Ca^{2+}$ , respectively. Tm, tropomyosin; TnT, troponin T; TnI, troponin I; TnC, troponin C. Figure and legend adapted from (3).

In these models, the N terminal region of TnI (1-40; Rp40) is anchored strongly onto the C domain of TnC in the relaxed state (in the absence of  $Ca^{2+}$ ), stabilizing the ternary complex with TnT. Meanwhile, the inhibitory region (residue 96-115) and the C-terminal region (140-148) of TnI interact with the actin-Tm filament inhibiting the ATPase activity. In the contracting state (in presence of  $Ca^{2+}$ ), it was suggested that binding of  $Ca^{2+}$  to the regulatory sites in the N-terminal domain of TnC would cause the

opening of the structure, exposing a hydrophobic pocket to which the central residues 116-131 of TnI would then bind. This binding event would trigger a movement of the inhibitory region (96-115) from the actin-Tm filament to the C domain of TnC, resulting in displacement of the N terminal region (1-40) from the C domain of TnC and a possible conformational change of residues 40-96. The proposed displacement of Rp40 by TnI<sub>96-115</sub> on CTnC is somewhat contradictory to previous results reported by the same research group (68), where this process had not been observed.

In the reported X-ray structure of TnC•2Ca<sup>2+</sup>•TnI<sub>1-47</sub> (69), the central helix is unwound at its center (residues Ala90-Ser94), creating a kink allowing for closer proximity of the two TnC domains and resulting in a more compact globular shape for the protein. Based on sequence homology between Rp40 and TnI<sub>115-131</sub> and a previous NMR structure of TnI<sub>96-115</sub> (70), the region of TnI covering residues 96-131 was modeled on TnC•2Ca<sup>2+</sup>•TnI<sub>1-47</sub> (see Figure I-10).

The compactness of TnC in the Maeda model (69) was incompatible with previous neutron scattering studies of TnC•TnI and TnC•TnI•TnT, which had shown that TnC adopted an extended form (71-73). Later, a CD study favored instead an extended conformation for the peptide when bound to TnC and shed some doubts about the validity of the helical nature of the TnI<sub>96-115</sub> (74). Based on X-ray, NMR and small-angle scattering structural information, as well as chemical-cross linking and fluorescence energy transfer studies, Trewhella et al. soon after proposed a model of interaction between TnI and TnC (see Figure I-11) where the inhibitory region was aligned with the

central helix near the C-domain of TnC and represented as a  $\beta$ -hairpin (75). These models will be discussed in Chapter 6 in light of the structural results presented in Chapter 2, 3 and 4.

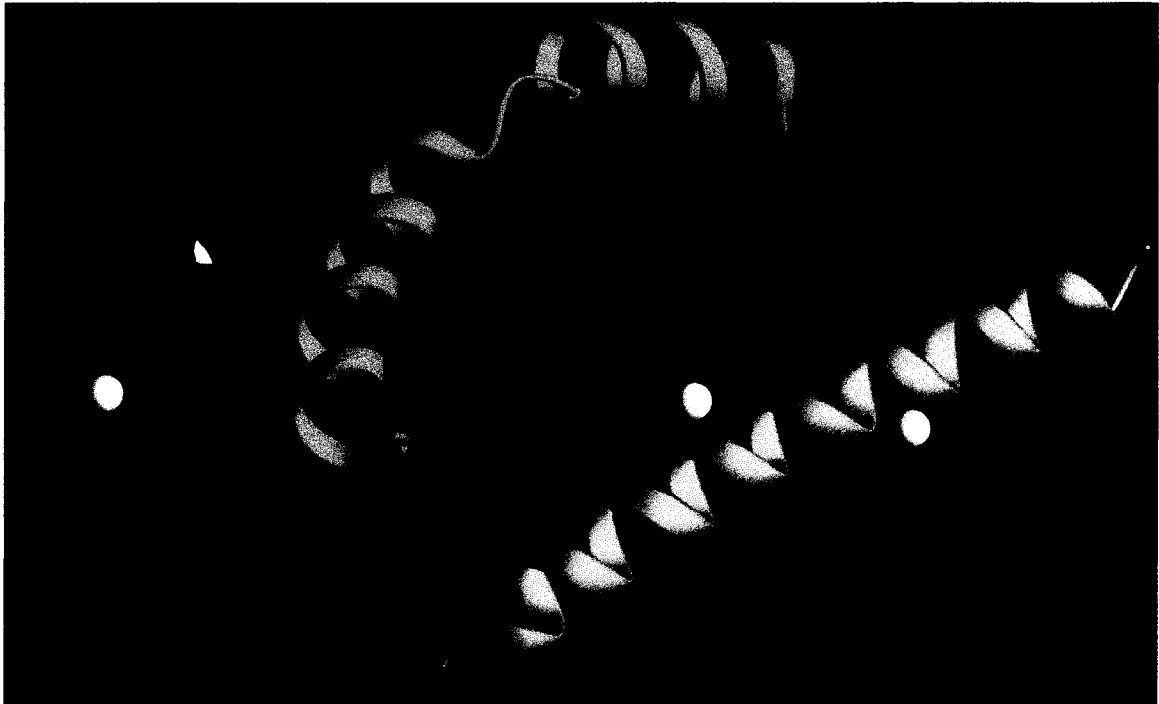


Figure I-10. Ribbon diagram of the TnC•TnI<sub>1-47</sub>•TnI<sub>96-115</sub> model (69). The two “open” N- and C-lobes of TnC are blue; the four calcium ions are shown as white balls and the TnI<sub>1-47</sub> and TnI<sub>96-115</sub>  $\alpha$ -helices are shown in yellow and cyan, respectively.

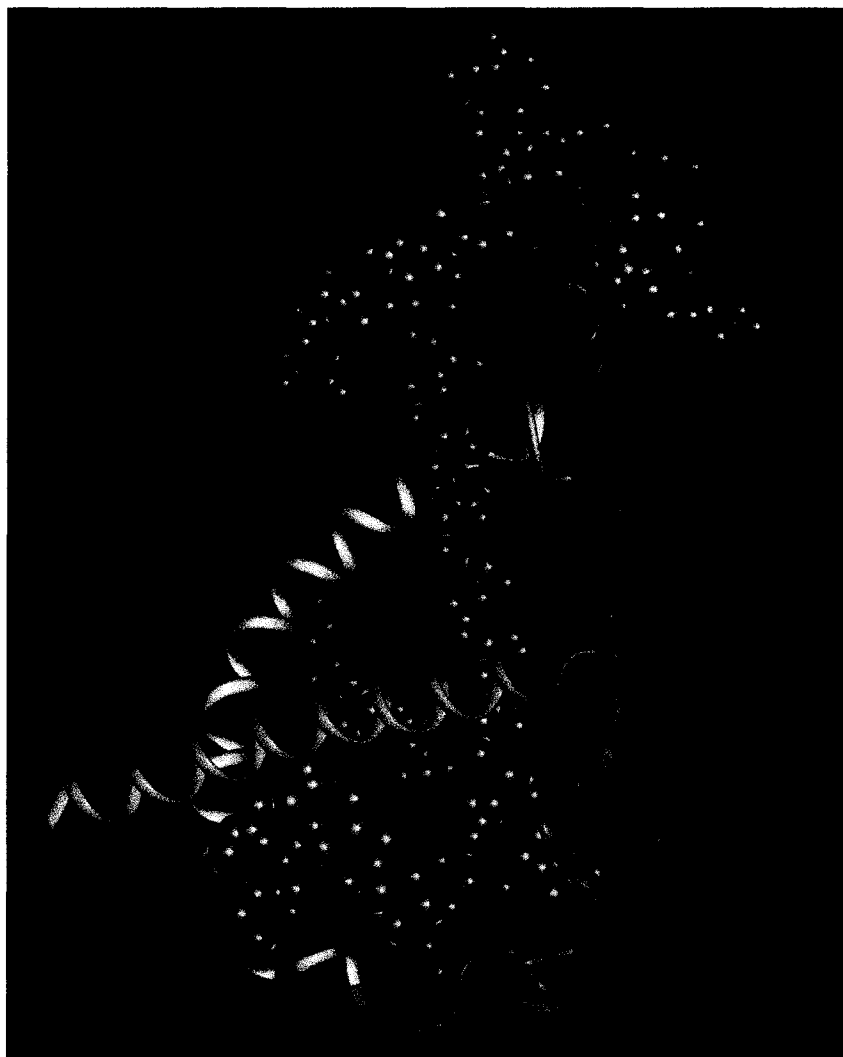


Figure I-11. Ribbon model of TnI in complex with TnC from Tung et al (75). TnC (gray) is shown as Van der Waals spheres with the N-domain at the top. TnI is shown in five segments: Segment I (cyan), TnI<sub>3-33</sub>; Segment II (green strands), TnI<sub>34-53</sub>; Segment III (yellow), TnI<sub>54-94</sub>; Segment IV inhibitory region (red), TnI<sub>95-114</sub>; Segment V (pink), TnI<sub>115-134</sub>. In the model, the segments III and V together coil around TnC in a left-handed sense.

**REFERENCES**

1. Gordon, A. M., Homsher, E., and Regnier, M. (2000) *Physiol. Rev.* 80, 853-924.
2. Clark, K. A., McElhinny, A. S., Beckerle, M. C., and Gregorio, C. C. (2002) *Annu Rev Cell Dev Biol* 18, 637-706.
3. Filatov, V. L., Katrukha, A. G., Bulargina, T. V., and Gusev, N. B. (1999) *Biochemistry (Mosc)* 64, 969-985.
4. Squire, J. M., and Morris, E. P. (1998) *FASEB J.* 12, 761-771.
5. Perry, S. V. (1999) *Mol. Cell. Biochem.* 190, 9-32.
6. Farah, C. S., and Reinach, F. C. (1995) *FASEB J.* 9, 755-767.
7. Tobacman, L. S. (1996) *Annu. Rev. Physiol.* 58, 447-481.
8. Perry, S. V. (2001) *J Muscle Res Cell Motil* 22, 5-49.
9. Perry, S. V. (1998) *J Muscle Res Cell Motil* 19, 575-602.
10. Voet, D., and Voet, J. G. (1995) in *Biochemistry* pp 500-502, 1234-1252, John Wiley & Sons, Inc., Toronto.
11. Bang, M. L., Centner, T., Fornoff, F., Geach, A. J., Gotthardt, M., McNabb, M., Witt, C. C., Labeit, D., Gregorio, C. C., Granzier, H., and Labeit, S. (2001) *Circ Res* 89, 1065-1072.
12. Granzier, H., and Labeit, S. (2002) *J Physiol* 541, 335-342.
13. Kabsch, W., Mannherz, H. G., Suck, D., Pai, E. F., and Holmes, K. C. (1990) *Nature* 347, 37-44.
14. Holmes, K. C., Popp, D., Gebhard, W., and Kabsch, W. (1990) *Nature* 347, 44-49.
15. Herzberg, O., and James, M. N. G. (1985) *Nature* 313, 653-659.
16. Takeda, S., Yamashida, A., Maeda, K., and Maeda, Y. (2002) *Biophys. J.* 82, 832.
17. Herzberg, O., and James, M. N. G. (1988) *J. Mol. Biol.* 203, 761-779.
18. Sundaralingam, M., Bergstrom, R., Strasburg, G., Rao, S. T., Roychowdhury, P., Greaser, M., and Wang, B. C. (1985) *Science* 227, 945-948.
19. Satyshur, K. A., Rao, S. T., Pyzalska, D., Drendal, W., Greaser, M., and Sundaralingam, M. (1988) *J. Biol. Chem.* 263, 1628-1647.
20. Slupsky, C. M., and Sykes, B. D. (1995) *Biochemistry* 34, 15953-15964.
21. Gagné, S. M., Tsuda, S., Li, M. X., Smillie, L. B., and Sykes, B. D. (1995) *Nat. Struct. Biol.* 2, 784-789.
22. Houdusse, A., Love, M. L., Dominguez, R., Grabarek, Z., and Cohen, C. (1997) *Structure* 5, 1695-1711.
23. Szczesna, D., Guzman, G., Miller, T., Zhao, J., Farokhi, K., Ellemberger, H., and Potter, J. D. (1996) *J. Biol. Chem.* 271, 8381-8386.
24. Vogel, H. J., Drakenberg, T., and Forsen, S. (1983) *NMR of NEWLY ACCESSIBLE NUCLEI* 1, 157.
25. Gagné, S. M., Li, M. X., and Sykes, B. D. (1997) *Biochemistry* 36, 4386-4392.
26. Gagné, S. M., Li, M. X., McKay, R. T., and Sykes, B. D. (1998) *Biochem. Cell. Biol.* 76, 301-312.
27. Mercier, P., Li, M. X., and Sykes, B. D. (2000) *Biochemistry* 39, 2902-2911.
28. Mercier, P., Spyrapoulos, L., and Sykes, B. D. (2001) *Biochemistry* 40, 10063-10077.

29. McKay, R. T. (1999) in *Department of Biochemistry*, Univ. of Alberta, Edmonton.
30. McKay, R. T., Tripet, B. P., Hodges, R. S., and Sykes, B. D. (1997) *J. Biol. Chem.* 272, 28494-28500.
31. Sia, S. K., Li, M. X., Spyrapoulos, L., Gagné, S. M., Liu, W., Putkey, J. A., and Sykes, B. D. (1997) *J. Biol. Chem.* 272, 18216-18221.
32. Li, M. X., Spyrapoulos, L., and Sykes, B. D. (1999) *Biochemistry* 38, 8289-8298.
33. Syska, H., Wilkinson, J. M., Grand, R. J., and Perry, S. V. (1976) *Biochem. J.* 153, 375-387.
34. Hartshorne, D. J., and Mueller, H. (1968) *Biochem Biophys Res Commun* 31, 647-653.
35. Schaub, M. C., and Perry, S. V. (1969) *Biochem. J.* 115, 993-1004.
36. Greaser, M. L., Yamaguchi, M., Brekke, C., Potter, J. D., and Gergely, J. (1972) *Cold Spring harbour Sym Quant Biol* 37, 235-244.
37. Van Eyk, J. E., and Hodges, R. S. (1988) *J. Biol. Chem.* 263, 1726-1732.
38. Tripet, B. P., Van Eyk, J. E., and Hodges, R. S. (1997) *J. Mol. Biol.* 271, 728-750.
39. Pearlstone, J. R., and Smillie, L. B. (1983) *J. Biol. Chem.* 258, 2534-2542.
40. Mak, A. S., Golosinska, K., and Smillie, L. B. (1983) *J. Biol. Chem.* 258, 14330-14334.
41. Sulakhe, P. V., and Vo, X. T. (1995) *Mol Cell Biochem* 149-150, 103-126.
42. Chandra, M., Dong, W. J., Pan, B. S., Cheung, H. C., and Solaro, R. J. (1997) *Biochemistry* 36, 13305-13311.
43. Jaquet, K., Lohmann, K., Czisch, M., Holak, T., Gulati, J., and Jaquet, R. (1998) *J Muscle Res Cell Motil* 19, 647-659.
44. Lindhout, D. A., Li, M. X., Schieve, D., and Sykes, B. D. (2002) *Biochemistry* 41, 7267-7274.
45. Potter, J. D., Sheng, Z., Pan, B. S., and Zhao, J. (1995) *J. Biol. Chem.* 270, 2557-2562.
46. Fisher, D., Wang, G., and Tobacman, L. S. (1995) *J. Biol. Chem.* 270, 25455-25460.
47. Mak, A. S., and Smillie, L. B. (1981) *J. Mol. Biol.* 149, 541-550.
48. Blumenschein, T. M., Tripet, B. P., Hodges, R. S., and Sykes, B. D. (2001) *J. Biol. Chem.* 276, 36606-36612.
49. Tobacman, L. S., Nihli, M., Butters, C., Heller, M., Hatch, V., Craig, R., Lehman, W., and Homsher, E. (2002) *J. Biol. Chem.* 277, 27636-27642.
50. Ebashi, S., and Endo, M. (1968) *Prog Biophys Mol Biol* 18, 123-183.
51. McKillop, D. F., and Geeves, M. A. (1993) *Biophys. J.* 65, 693-701.
52. Maytum, R., Lehrer, S. S., and Geeves, M. A. (1999) *Biochemistry* 38, 1102-1110.
53. Lehrer, S. S., and Geeves, M. A. (1998) *J. Mol. Biol.* 277, 1081-1089.
54. Geeves, M. A., and Lehrer, S. S. (1994) *Biophys. J.* 67, 273-282.
55. Butters, C. A., Willadsen, K. A., and Tobacman, L. S. (1993) *J. Biol. Chem.* 268, 15565-15570.

56. Rayment, I., Rypniewski, W. R., Schmidt-Base, K., Smith, R., Tomchick, D. R., Benning, M. M., Winkelmann, D. A., Wesenberg, G., and Holden, H. M. (1993) *Science* 261, 50-58.
57. Lehman, W., Vibert, P., Uman, P., and Craig, R. (1995) *J. Mol. Biol.* 251, 191-196.
58. Vibert, P., Craig, R., and Lehman, W. (1997) *J. Mol. Biol.* 266, 8-14.
59. Lehman, W., Rosol, M., Tobacman, L. S., and Craig, R. (2001) *J. Mol. Biol.* 307, 739-744.
60. Cassell, M., and Tobacman, L. S. (1996) *J. Biol. Chem.* 271, 12867-12872.
61. Corrie, J. E. T., Brandmeier, B. D., Ferguson, R. E., Trentham, D. R., Kendrick-Jones, J., Hopkins, S. C., van der Heide, U. A., Goldman, Y. E., Sabido-David, C., Dale, R. E., Criddle, S., and Irving, M. (1999) *Nature* 400, 425-430.
62. Hopkins, S. C., Sabido-David, C., van der Heide, U. A., Ferguson, R. E., Brandmeier, B. D., Dale, R. E., Kendrick-Jones, J., Corrie, J. E. T., Trentham, D. R., Irving, M., and Goldman, Y. E. (2002) *J. Mol. Biol.* 318, 1275-1291.
63. McKay, R. T., Pearlstone, J. R., Corson, D. C., Gagné, S. M., Smillie, L. B., and Sykes, B. D. (1998) *Biochemistry* 37, 12419-12430.
64. McKay, R. T., Tripet, B. P., Pearlstone, J. R., Smillie, L. B., and Sykes, B. D. (1999) *Biochemistry* 38, 5478-5489.
65. McKay, R. T., Saltibus, L. F., Li, M. X., and Sykes, B. D. (2000) *Biochemistry* 39, 12731-12738.
66. Li, M. X., Saude, E. J., Wang, X., Pearlstone, J. R., Smillie, L. B., and Sykes, B. D. (2002) *Eur. Biophys. J.* 31, 245-256.
67. Wang, X., Li, M. X., and Sykes, B. D. (2002) *J. Biol. Chem.* 277, 31124-31133.
68. Ngai, S. M., Sonnichsen, F. D., and Hodges, R. S. (1994) *J. Biol. Chem.* 269, 2165-2172.
69. Vassilyev, D. G., Takeda, S., Wakatsuki, S., Maeda, K., and Maeda, Y. (1998) *Proc. Natl. Acad. Sci. U.S.A.* 95, 4847-4852.
70. Campbell, A. P., and Sykes, B. D. (1991) *J. Mol. Biol.* 222, 405-421.
71. Olah, G. A., and Trehwella, J. (1994) *Biochemistry* 33, 12800-12806.
72. Olah, G. A., Rokop, S. E., Wang, C. L., Blechner, S. L., and Trehwella, J. (1994) *Biochemistry* 33, 8233-8239.
73. Stone, D. B., Timmins, P. A., Schneider, D. K., Krylova, I., Ramos, C. H. I., Reinach, F. C., and Mendelson, R. A. (1998) *J. Mol. Biol.* 281, 689-704.
74. Hernández, G., Blumenthal, D. K., Kennedy, M. A., Unkefer, C. J., and Trehwella, J. (1999) *Biochemistry* 38, 6911-6917.
75. Tung, C. S., Wall, M. E., Gallagher, S. C., and Trehwella, J. (2000) *Protein Sci.* 9, 1312-1326.

## CHAPTER II

### *Role of the Structural Domain of Troponin C Muscle Regulation: NMR Studies of Ca<sup>2+</sup> Binding and Subsequent Interactions with Regions 1-40 and 96-115 of Troponin I<sup>†</sup>*

#### **INTRODUCTION**

Muscle contraction is regulated by Ca<sup>2+</sup> binding to the troponin complex, which triggers a cascade of altered protein-protein interactions ultimately leading to force development. The troponin complex is comprised of three components, troponin C (TnC), TnI, TnT. TnC responds to the Ca<sup>2+</sup> signal, TnI inhibits interactions between thick and thin filaments in the absence of Ca<sup>2+</sup>, and TnT anchors troponin to actin and transmits the Ca<sup>2+</sup> signal along the thin filament, thereby enhancing the actomyosin ATPase activity (for reviews, see (1-6)).

TnC is a dumbbell-shaped molecule with two globular domains connected by a central linker (7-11). Each domain contains two metal binding sites, designated sites I and II in the N domain and sites III and IV in the C domain, with each site consisting of two helix-loop-helix EF hand motifs typical of calcium binding proteins (12). Sites III/IV are Ca<sup>2+</sup>/Mg<sup>2+</sup> sites, which are believed to be always occupied by either Ca<sup>2+</sup> or Mg<sup>2+</sup> in muscle cells, whereas sites I/II are Ca<sup>2+</sup> specific sites (see reviews listed above and (13-15)). While Ca<sup>2+</sup> or Mg<sup>2+</sup> bound C-domain anchors troponin to the thin filament, association and dissociation of Ca<sup>2+</sup> from sites I/II (in the N-domain) triggers switching between muscle contraction and relaxation, respectively. The N-domain of TnC is composed of five  $\alpha$ -helices, a short  $\beta$ -sheet and is structured in the apo state. Ca<sup>2+</sup> binding to sites I/II is

---

<sup>†</sup> The results presented in this chapter apply to the skeletal isoform of TnC (sTnC abbreviation is not used). Any reference to the cardiac isoform of TnC is explicitly stated. The results presented in this chapter are taken integrally from: Mercier, P, Li, M. X. and Sykes, B. D. *Biochemistry*, 39, 2902-2911, 2000. Some of the conclusions have been enhanced in the context of latter results and are presented in Chapter VII.

accompanied by a rearrangement of secondary structural elements such that helices B and C move as a unit relative to N, A, and D helices. As a result, a hydrophobic patch on the surface of the molecule is exposed, which has been shown to interact with TnI (for a review, see (16) and references therein). On the other hand, CTnC is largely unstructured and Ca<sup>2+</sup> binding to sites III and IV leads to a structured globular domain with an exposed hydrophobic pocket (16). The replacement of Ca<sup>2+</sup> by other metal ions, such as Mn<sup>2+</sup>, Cd<sup>2+</sup>, and Tb<sup>2+</sup>, in sites III/IV has minimal effect on the globular fold of the domain, as revealed by the X-ray structures of Mn<sup>2+</sup>, Cd<sup>2+</sup>, and Tb<sup>2+</sup> metal complexes of troponin C (17).

Since NTnC accomplishes a regulatory role while CTnC plays predominantly a structural role, the Ca<sup>2+</sup> binding mechanisms for the two domains are distinct from each other. Previously, we performed a Ca<sup>2+</sup> titration of NTnC using 2D-<sup>1</sup>H, <sup>15</sup>N} HMQC NMR spectroscopy (18). The results demonstrated that Ca<sup>2+</sup> binding to the regulatory domain occurs in a stepwise manner with the Ca<sup>2+</sup> affinity of one site being approximately 10-fold greater than the other. We were able to assign the order of the stepwise binding as site II then site I by following Ca<sup>2+</sup> binding to an E41A mutant of NTnC (19). The same approach has been used to investigate Ca<sup>2+</sup> binding to cardiac TnC (19), calmodulin (CaM) (20, 21), and calbindin D<sub>9k</sub>(22), as well as the interaction between TnC and TnI peptides (23, 24). This method is especially powerful since it can reveal information that pertains to individual atoms throughout the protein sequence.

While much is known about how Ca<sup>2+</sup> induces structural changes in NTnC and initiates a cascade of protein-protein interactions leading to muscle contraction, less is known about TnI inhibition of actomyosin-ATPase. Neutron scattering studies have shed some light on the general aspects of the TnI•TnC interaction (25, 26). However, there are no high-resolution structures of the complex due in part to the low solubility of TnI. Several groups have used different synthetic fragments of TnI complexed with TnC (23-39)

in order to identify the sites of interaction between TnI and TnC. Together, these studies provide information about the structure of the TnC•TnI complex and broaden knowledge regarding the inhibition of muscle contraction by TnI.

Considerable attention has been focussed on the inhibitory region (residues 96-115) of TnI since it was first identified by Syska *et al.* (40). Studies by Talbot and Hodges (41) using synthetic peptides revealed that residues 104-115 represent the minimal sequence required for inhibition. Further studies with TnI<sub>104-115</sub> by Van Eyk and Hodges (42) suggested that the major switch between contraction and relaxation involves a movement of the inhibitory region of TnI from TnC to actin-tropomyosin, respectively. Farah and coworkers showed that TnC and TnI interact in an antiparallel fashion (43). Recent work by Tripet *et al.* further refined the binding organization of TnI to TnC, specifically with the N-terminal 1-40 and the inhibitory region 96-115 of TnI binding to the C-domain, the 40-96 region of TnI interacting with TnT and/or tropomyosin (30), the 115-131 region of TnI interacting with the N-domain of TnC, and the C-terminal region of TnI interacting with actin. Thus, the interactions between CTnC and the N-domain of TnI are critical for maintaining TnC in the ternary troponin complex (for a review, see (4)).

The location of binding sites for the inhibitory region of TnI on TnC has long been in dispute. Early chemical cross-linking studies (44-50) suggested that both the N- and C-domains of TnC are in close proximity to the inhibitory region of TnI and support the conclusion that TnC in the presence of TnI adopts a more compact conformation in solution than in its crystal structure. However, small-angle X-ray scattering data indicate no such conformational change in TnC upon addition of TnI<sub>96-115</sub> (51) and available neutron scattering studies in presence of intact TnI (25, 26) or with the whole troponin complex (52) are consistent with an extended structure for TnC.

Structural studies of the inhibitory region include the NMR structure of TnI<sub>104-115</sub> in the TnC•4Ca<sup>2+</sup>•TnI<sub>104-115</sub> complex (31) and a recent NMR and CD investigation of TnI<sub>96-115</sub> in the TnC•4Ca<sup>2+</sup>•TnI<sub>96-115</sub> complex (39). By monitoring chemical shift perturbation, Campbell and Sykes (31) have suggested that TnI<sub>104-115</sub> interacts with the hydrophobic cleft in CTnC. Slupsky *et al.* (34) have reported similar findings for TnI<sub>104-115</sub> binding sites on a synthetic peptide heterodimer representing sites III/IV of the CTnC. Based on these results and photochemical cross-linking studies between TnC and TnI<sub>104-115</sub>, Ngai *et al.* (27) constructed a model of CTnC•TnI<sub>104-115</sub> that indicates the TnI<sub>104-115</sub> structure determined by Campbell and Sykes (31) fits within the hydrophobic patch of CTnC.

A recent X-ray structure of skeletal TnC in complex with TnI<sub>1-47</sub> showed that TnI<sub>3-33</sub> forms a long  $\alpha$ -helix that binds within the hydrophobic groove of CTnC as well (53). The corresponding region of cardiac TnI<sub>33-80</sub> has also been shown to bind within the hydrophobic patch of the C-domain of cardiac TnC (37). Functional studies of this region by Ngai and Hodges (54) have shown that Rp40 can effectively compete with TnI or TnI inhibitory peptide (residues 96-115) for TnC, suggesting that the N-terminus of TnI may play both a structural and functional role.

Based on the crystal structure of TnC•2Ca<sup>2+</sup>•TnI<sub>1-47</sub>, Maeda *et al.* (53) have proposed a model of interaction of TnC and TnI in which the central linker of TnC is unwound at its center. As a result, TnC would possess a more compact structure, allowing direct interactions between the N and the C domains. According to this model, the inhibitory region interacts with both the N- and C-domains of TnC even when the hydrophobic patch in CTnC is occupied by TnI<sub>1-47</sub> (53). On the other hand, Tripet *et al.* (30) have proposed that Rp40 and TnI<sub>96-115</sub> may bind to similar sites within CTnC but are regulated by other Ca<sup>2+</sup>-dependent changes in the interaction between TnC and TnI. It was identified that the binding of TnI<sub>116-131</sub> to NTnC plays a key role in modulating the affinity

between Rp40 and TnI<sub>96-115</sub> for CTnC. Their results showed that in the absence of TnI<sub>116-131</sub>, Rp40 dominates in affinity for TnC over TnI<sub>96-115</sub>, whereas the affinity is reversed in the presence of TnI<sub>116-131</sub>. Therefore, in order to release inhibition, the binding of TnI<sub>116-131</sub> to TnC is critical. In addition, Farah *et al.* (43) have suggested that residues 116-156 of TnI are responsible for the expression of maximum inhibition, in addition to the inhibitory region. Moreover, a recent paper by Ramos (55) suggested that the entire C-terminal region of TnI is necessary for the regulatory activity of TnI.

In spite of structural and functional studies, there are no quantitative affinities and exact stoichiometries reported for Rp40 and TnI<sub>96-115</sub> binding to TnC. In this paper, we have performed detailed titrations of Ca<sup>2+</sup>, Rp40 and TnI<sub>96-115</sub> binding to CTnC as monitored by 2D-<sup>1</sup>H, <sup>15</sup>N}-HSQC NMR spectroscopy. The titrations allow for the determination of binding constants, the stoichiometry and the evaluation of competitive binding of Rp40 and TnI<sub>96-115</sub> to CTnC. The binding sites of Rp40 and TnI<sub>96-115</sub> on CTnC are mapped following chemical shift changes upon peptide binding, and together with Ca<sup>2+</sup> binding properties, this work provides insight into the role of the structural domain in muscle contraction.

## EXPERIMENTAL PROCEDURES

### *Construction of CTnC Mutant and Protein Isolation.*

The engineering of CTnC (88-162) into the expression vector pET3a was as described for NTnC (1-90) (56) except for the use of two different oligonucleotides that are complementary to the sequence and restriction enzyme sites. The expression and purification of [ $^{15}\text{N}$ ]-CTnC in minimal media follows the procedure as described for [ $^{15}\text{N}$ ]-NTnC (18, 56). During expression in *E. coli*, the N-terminal methionine, corresponding to the initiation codon, is not cleaved off.

### *Ca<sup>2+</sup> Titration of [ $^{15}\text{N}$ ]-CTnC.*

Decalcification of [ $^{15}\text{N}$ ]-CTnC and NMR sample preparation was as described for [ $^{15}\text{N}$ ]-NTnC (18). Since CTnC has higher affinity for  $\text{Ca}^{2+}$  than NTnC, the 25mM  $(\text{NH}_4)\text{HCO}_3$  buffer pH for the decalcification step was raised to 8.5. The solution conditions were 100 mM KCl, 10 mM imidazole and 15 mM DTT in 90%  $\text{H}_2\text{O}/10\%$   $\text{D}_2\text{O}$  at pH 6.7 (uncorrected for  $^2\text{H}$  isotope effects). The protein concentration was determined to be 0.9 mM by amino acid analysis in triplicate. All solutions used in this study were treated with Chelex 100 before use to remove metal contaminants. A stock solution of 50 mM  $\text{CaCl}_2$  in 90%  $\text{H}_2\text{O}/10\%$   $\text{D}_2\text{O}$  was prepared from standardized 100 mM  $\text{CaCl}_2$  in water. With a 10  $\mu\text{L}$  Hamilton syringe, aliquots of 5  $\mu\text{L}$  of stock  $\text{CaCl}_2$  solution were added to the NMR tube (the volume of the NMR sample was 500  $\mu\text{L}$ ) for each titration point and mixed thoroughly. The total volume increase was 45  $\mu\text{L}$  and the change in protein concentration due to dilution was taken into account for data analysis. Changes in pH due to additions of stock  $\text{CaCl}_2$  solution were negligible. Both 1D  $^1\text{H}$  and 2D- $\{^1\text{H}, ^{15}\text{N}\}$ -HSQC NMR spectra were acquired at every titration point.

---

*Rp40 Titration of [<sup>15</sup>N]-CTnC•2Ca<sup>2+</sup>.*

---

Rp40 peptide, acetyl- GDEEKRNRAITARRQHLKSVMLQIAATELEKEEGRR-EAEK-amide was synthesized and purified as described in Ngai & Hodges (54). Since Rp40 peptide is not soluble in aqueous solution at concentrations needed for stock solutions, solid peptide was added to a 0.51 mM NMR sample of CTnC•2Ca<sup>2+</sup>. Titration points of 0.1, 0.25, 0.35, 0.5, 0.7, 0.75, 0.85, 0.9, 1, 1.05, and 1.2 molar equivalents of Rp40 were observed, consecutively. The initial concentration of CTnC•2Ca<sup>2+</sup> and Rp40:CTnC ratios were determined by amino acid analyses in duplicate. Both 1D <sup>1</sup>H and 2D-<sup>1</sup>H, <sup>15</sup>N}-HSQC NMR spectra were acquired at every titration point. The pH was adjusted to 6.7 after each Rp40 addition.

---

*TnI<sub>96-115</sub> Titration of [<sup>15</sup>N]-CTnC•2Ca<sup>2+</sup>.*

---

The synthetic peptide TnI<sub>96-115</sub>, acetyl-QKLFDLRGKFKRPPLRRVR-amide, was prepared and analyzed as by Tripet *et al.* (30). Two stock solutions of TnI<sub>96-115</sub> of 20 and 50 mM were prepared in double distilled water, respectively. Molar equivalents of 0.7, 0.15, 0.2, 0.3, 0.35, 0.40, 0.5, 0.55, 0.62, 0.7, 0.75, 0.8, 1.3, 2.0 and 2.7 of TnI<sub>96-115</sub> were added to the NMR sample consecutively using 1.5 μL aliquots of the 20 mM solution for the first 12 points, one 4.8 μL aliquot of the 50 mM solution for the thirteenth point, and 6 μL aliquots of the 50 mM solution for the last two points. The initial concentration of [<sup>15</sup>N]-CTnC was determined to be 0.80 mM by amino acid analysis in duplicate. Both 1D <sup>1</sup>H and 2D-<sup>1</sup>H, <sup>15</sup>N}-HSQC NMR spectra were acquired at every titration point.

---

*Rp40 Titration of [<sup>15</sup>N]-CTnC•2Ca<sup>2+</sup>•TnI<sub>96-115</sub>.*

---

Solid Rp40 peptide was added to an NMR sample containing [<sup>15</sup>N]-CTnC•2Ca<sup>2+</sup>•TnI<sub>96-115</sub> following the same procedure for the titration of CTnC•2Ca<sup>2+</sup> with Rp40. Molar equivalents

of 0.2, 0.3, 0.4, 0.56, 0.7, 0.83, 0.98 and 1.2 molar equivalents of Rp40, as determined by amino acid analysis in duplicate, were added to the NMR sample, consecutively. The initial CTnC and TnI<sub>96-115</sub> concentrations were determined to be 0.7 mM and 1.9 mM by amino acid analysis in duplicate (initial complex: 1 CTnC: 2.7 TnI<sub>96-115</sub>), respectively. Both 1D <sup>1</sup>H and 2D-<sup>1</sup>H, <sup>15</sup>N}-HSQC NMR spectra were acquired at every titration point.

---

*TnI<sub>96-115</sub> Titration of [<sup>15</sup>N]-CTnC•2Ca<sup>2+</sup>•Rp40.*

---

A TnI<sub>96-115</sub> stock solution of 20 mM was prepared in double distilled water. For the first eight titration points, 2 μL aliquots were added to a NMR tube containing [<sup>15</sup>N]-CTnC•2Ca<sup>2+</sup>•Rp40. The ninth addition was performed by adding a 12 μL aliquot, and the last two additions were performed by adding solid peptide directly to the NMR sample. The initial concentration of [<sup>15</sup>N]-CTnC and Rp40 were determined to be 0.51 mM and 0.61 mM, respectively, by amino acid analysis in duplicate. Amino acid analysis gave 0.15, 0.3, 0.45, 0.6, 0.75, 0.9, 1.05, 1.2, 2.1, 5.3 and 10.4 molar equivalents of TnI<sub>96-115</sub> to [<sup>15</sup>N]-CTnC•2Ca<sup>2+</sup>•Rp40, respectively. Both 1D <sup>1</sup>H and 2D-<sup>1</sup>H, <sup>15</sup>N}-HSQC NMR spectra were acquired at every titration point.

---

*NMR Spectroscopy.*

---

All 1D <sup>1</sup>H and 2D-<sup>1</sup>H, <sup>15</sup>N}-HSQC NMR spectra were recorded on a Varian Unity INOVA 500 MHz spectrometer. The 1D <sup>1</sup>H NMR spectra were acquired using a spectral width of 6200 Hz, a <sup>1</sup>H pulse width of 10 μs (90°), and an acquisition time of 2.5 s. The 2D-<sup>1</sup>H, <sup>15</sup>N}-HSQC NMR spectra were acquired using the sensitivity-enhanced gradient pulse scheme developed by Lewis E. Kay and co-workers (57, 58). The <sup>1</sup>H and <sup>15</sup>N sweep widths were 6200 and 1500 Hz, respectively. A minimum of 8 transients were acquired for each titration point. Processing of the data sets was accomplished using the VNMR software package (VNMR 5.3B, Varian, Palo Alto, CA) and the program NMRPipe (59).

**RESULTS***Titration of [<sup>15</sup>N]-CTnC with Ca<sup>2+</sup>.*

Ca<sup>2+</sup> binding to [<sup>15</sup>N]-CTnC was followed by 2D-<sup>1</sup>H, <sup>15</sup>N}-HSQC NMR spectroscopy. The 2D-<sup>1</sup>H, <sup>15</sup>N}-HSQC NMR spectra of [<sup>15</sup>N]-CTnC at the beginning of the titration (CTnC•apo) and the end of the titration (CTnC•2Ca<sup>2+</sup>) are shown in Figure II-1A and II-1B, respectively. In the apo state, most of the amide resonances are located at the center of the plotted region with little dispersion in <sup>1</sup>H chemical shifts (Figure II-1A). The peaks fall within regions of <sup>1</sup>H chemical shift characterized as “random coil” by Wüthrich (60). The <sup>15</sup>N chemical shifts also correspond to random coil values (61). These observations suggest that CTnC•apo does not adopt a defined structure in solution. The first Ca<sup>2+</sup> addition (0.56:1 molar ratio) to CTnC results in dramatic changes in the 2D-<sup>1</sup>H, <sup>15</sup>N}-HSQC NMR spectra with the appearance of a new set of signals corresponding to CTnC•2Ca<sup>2+</sup>. As the  $[Ca^{2+}]_{total}:[CTnC]_{total}$  ratio is increased, these resonances increase in intensity with no line broadening throughout the entire titration until the spectrum shown in Figure II-1B is obtained. Concomitantly, the resonances corresponding to CTnC•apo become less intense and completely disappear when the  $[Ca^{2+}]_{total}:[CTnC]_{total}$  ratio reaches two.

The increased chemical shift dispersion indicates that CTnC is undergoing a Ca<sup>2+</sup>-induced structural folding. The spectral changes are consistent with slow exchange kinetics on the NMR time scale and further additions of Ca<sup>2+</sup> generate no increase in signal intensity. These results indicate that the stoichiometry of Ca<sup>2+</sup> binding to CTnC is 2:1, corresponding to binding of Ca<sup>2+</sup> to sites III and IV. The 2D-<sup>1</sup>H, <sup>15</sup>N}-HSQC NMR spectrum of CTnC•2Ca<sup>2+</sup> (Figure II-1B) was completely assigned with the exception of the

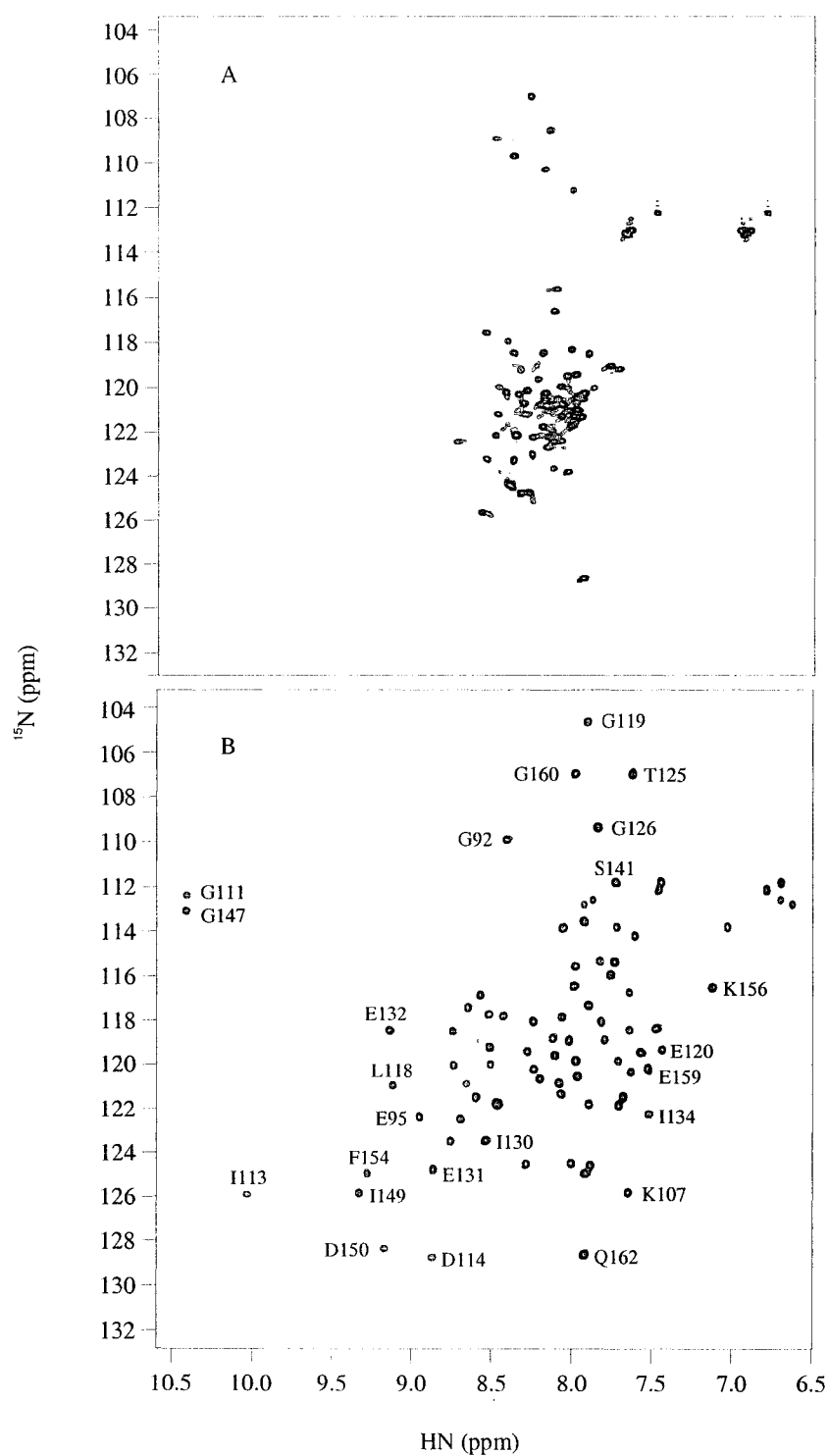
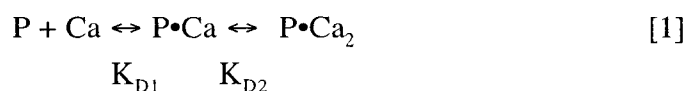


Figure II-1. Titration of CTnC with  $\text{Ca}^{2+}$ . 500 MHz 2D- $\{^1\text{H}, ^{15}\text{N}\}$ -HSQC NMR spectrum of CTnC. (A) in the apo state and (B) in the  $\text{Ca}^{2+}$ -saturated state ( $\text{CTnC}\cdot 2\text{Ca}^{2+}$ ). Assignments for some residues are indicated.

first two N-terminal residues, which were not observed, likely due to rapid exchange with water.  $\text{Ca}^{2+}$  binding to CTnC was quantified by plotting the normalized intensity changes of each residue during the  $\text{Ca}^{2+}$  titration as a function of the  $[\text{Ca}^{2+}]_{\text{total}}/[\text{CTnC}]_{\text{total}}$  ratio (Figure II-2A). The curve in Figure II-2A clearly shows that two equivalents of  $\text{Ca}^{2+}$  are needed to saturate CTnC. The spectroscopic changes between 0 to 2 equivalents of  $\text{Ca}^{2+}$  are linear, implying that either sites III and IV in CTnC have intrinsically identical  $\text{Ca}^{2+}$  binding sites or bind  $\text{Ca}^{2+}$  with strong positive cooperativity (18). Curve fitting using the equation



corresponding to the  $\text{Ca}^{2+}$ -binding equilibrium for a two-site protein yields macroscopic or stoichiometric dissociation constants of  $K_{D1} \leq 0.1 \mu\text{M}$  and  $K_{D2} \leq 0.42 \mu\text{M}$ . As pointed out by Ferguson-Miller and Koppenol, (62),  $K_{D2} = 4K_{D1}$  indicates that the intrinsic microscopic binding constants for the two sites are the same, and  $K_{D2} > 4K_{D1}$  indicates positive cooperativity between the two sites. Since  $\text{Ca}^{2+}$ -induced changes on CTnC are uniform throughout the sequence, and any residue gives an identical curve as that shown in Figure II-2A, it is extremely unlikely that the two  $\text{Ca}^{2+}$  binding sites are independent. The binding affinity for  $\text{Ca}^{2+}$  ( $K_D \leq 0.1 \mu\text{M}$ ) agrees with previously published constants (1-3).

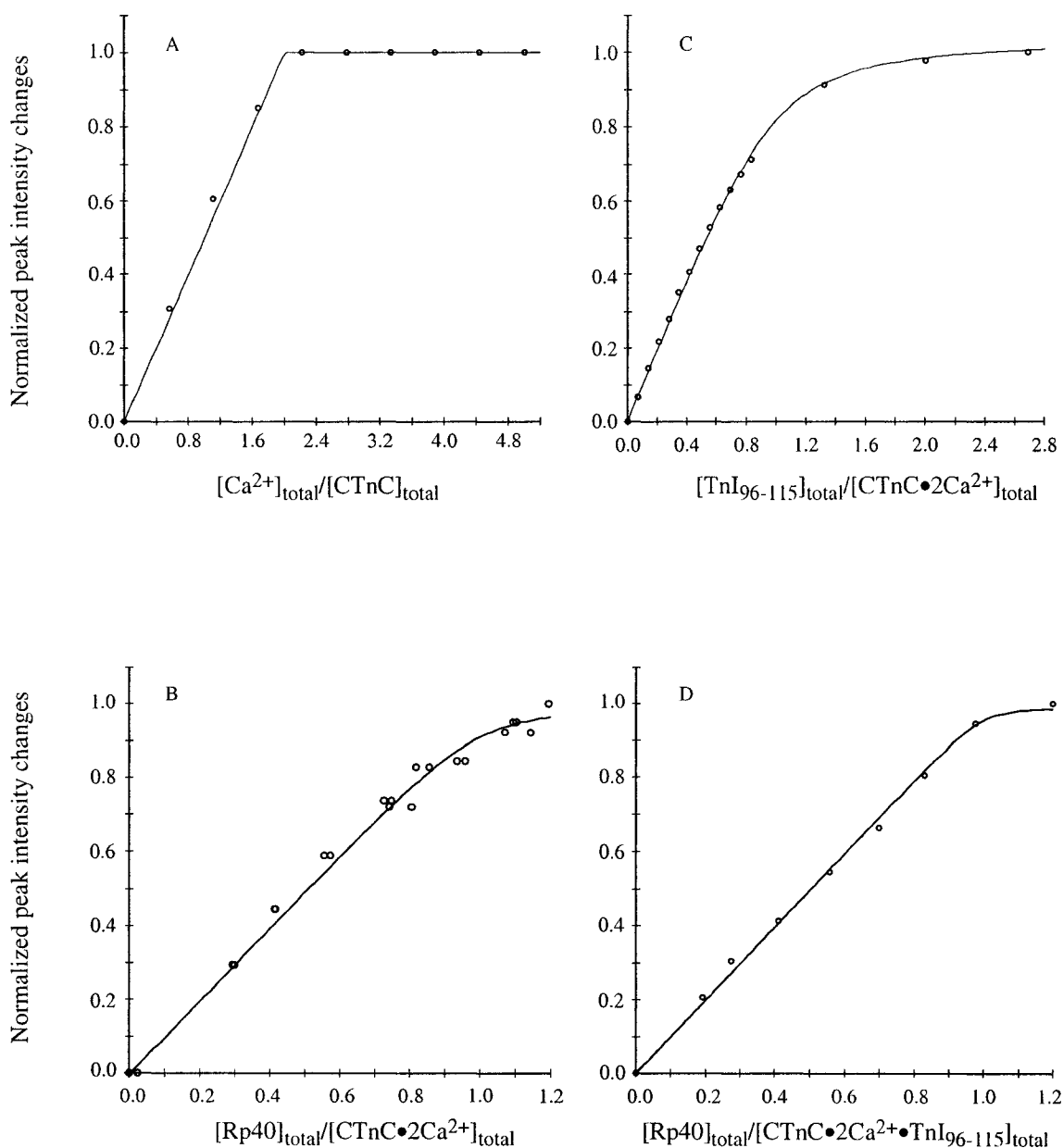


Figure II-2. Binding curves obtained from the averaged normalized peak intensity changes in the 2D- $\{^1\text{H}, ^{15}\text{N}\}$ -HSQC NMR spectrum of (A) CTnC during titration with  $\text{Ca}^{2+}$  ( $K_D \leq 0.1 \mu\text{M}$ ), (B)  $\text{CTnC}\cdot 2\text{Ca}^{2+}$  during titration with Rp40 ( $K_D = 2 \pm 1 \mu\text{M}$ ), (C)  $\text{CTnC}\cdot 2\text{Ca}^{2+}$  during titration with  $\text{TnI}_{96-115}$  ( $K_D = 47 \pm 7 \mu\text{M}$ ), and (D)  $\text{CTnC}\cdot 2\text{Ca}^{2+}\cdot \text{TnI}_{96-115}$  during titration with Rp40 ( $K_D = 3 \pm 1 \mu\text{M}$ ). In (B), because of slight variance in the  $[\text{Rp40}]_{\text{total}}/[\text{CTnC}\cdot 2\text{Ca}^{2+}]_{\text{total}}$  ratios calculated from amino acid analysis in duplicate, the ratios were not averaged to increase the accuracy of the fit. Errors in normalized peak intensity changes (A, B, D) and normalized chemical shift changes (C) were estimated from standard deviations when averaging values observed for different residues (see text). The largest calculated standard deviations are 0.04 (A), 0.03 (B), 0.03 (C) and 0.04 (D).

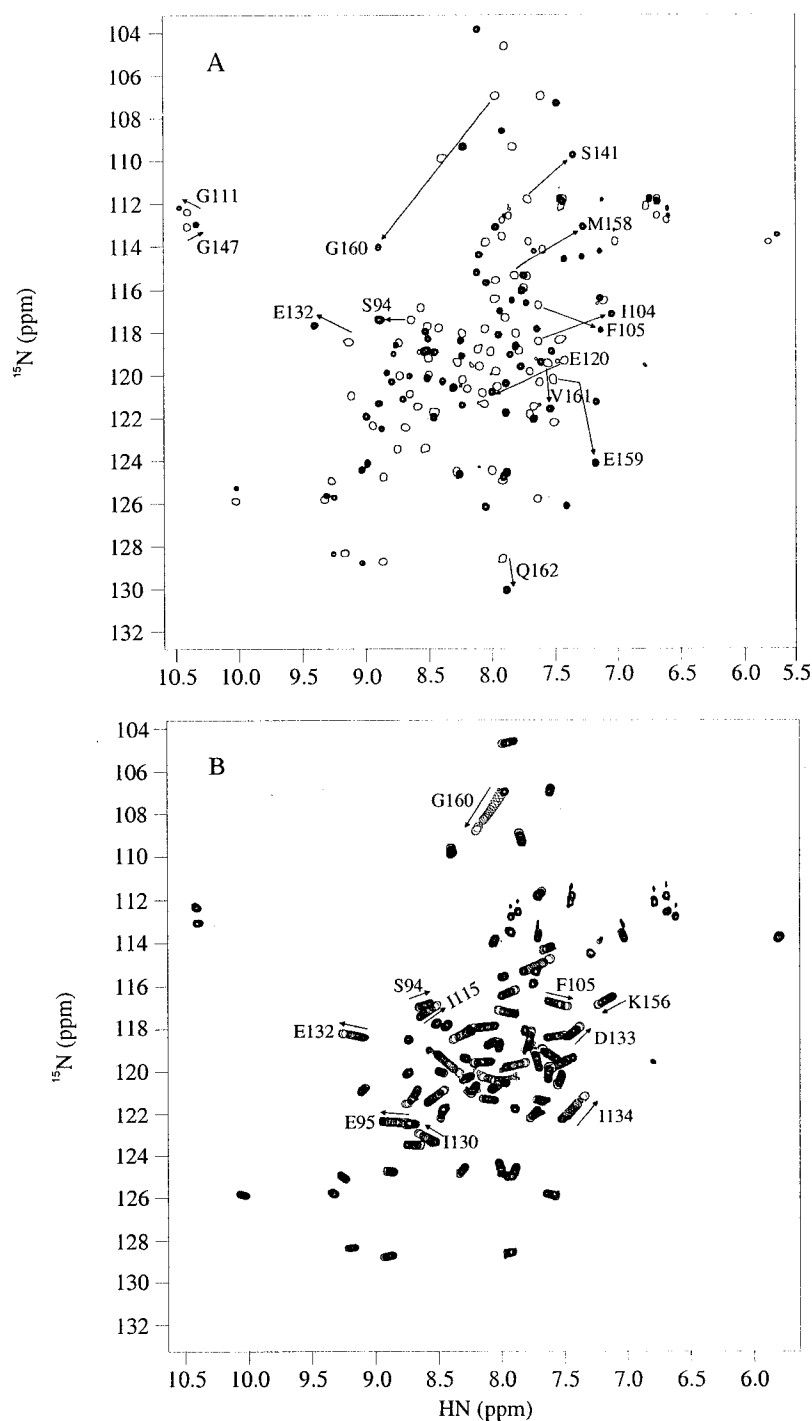


Figure II-3. 500 MHz 2D- $\{^1\text{H}, ^{15}\text{N}\}$ -HSQC NMR spectrum acquired during the titration of  $\text{CTnC}\cdot 2\text{Ca}^{2+}$  with (A) Rp40 and (B)  $\text{TnI}_{96-115}$ . In (A), the 2D- $\{^1\text{H}, ^{15}\text{N}\}$ -HSQC NMR spectrum of  $\text{CTnC}\cdot 2\text{Ca}^{2+}$  is shown in single contours, whereas peaks associated with complex formation with Rp40:CTnC at a 1:1 ratio are shown in multiple contours. In (B), the 2D- $\{^1\text{H}, ^{15}\text{N}\}$ -HSQC NMR spectrum of  $\text{CTnC}\cdot 2\text{Ca}^{2+}$  is shown in multiple contours, whereas peak changes upon each  $\text{TnI}_{96-115}$  addition are shown in single contours. In both panels, the direction of the chemical shift changes for some residues undergoing large perturbations are indicated by an arrow.

*Titration of CTnC•2Ca<sup>2+</sup> with Rp40.*

Figure II-3 shows a superimposition of the 2D-<sup>1</sup>H, <sup>15</sup>N}-HSQC NMR spectra of CTnC•2Ca<sup>2+</sup> and CTnC•2Ca<sup>2+</sup>•Rp40. Similarly to Ca<sup>2+</sup> binding to CTnC, Rp40 binding to CTnC•2Ca<sup>2+</sup> occurs with slow exchange kinetics on the NMR time scale. Thus, as the titration progresses, the resonance peaks corresponding to CTnC•2Ca<sup>2+</sup> become less intense while those corresponding to CTnC•2Ca<sup>2+</sup>•Rp40 grow. Line broadening is not observed. When the [Rp40]<sub>total</sub>/[CTnC•2Ca<sup>2+</sup>]<sub>total</sub> ratio reaches 1, all cross-peaks corresponding to CTnC•2Ca<sup>2+</sup> completely disappear while those corresponding to CTnC•2Ca<sup>2+</sup>•Rp40 attain maximum intensity. The normalized intensity changes of seven residues (C101, D106, S141, E159, G160, V161 and Q162) gave identical values at each titration point. The curve shown in Figure 2B shows the normalized intensity changes of the seven peaks with the [Rp40]<sub>total</sub>/[CTnC•2Ca<sup>2+</sup>]<sub>total</sub> ratio calculated from two amino acid analyses. Curve fitting to the following equation



yields a  $K_D$  of  $2 \pm 1 \mu\text{M}$ , indicating that Rp40 and CTnC•2Ca<sup>2+</sup> form a tight complex. This result quantitatively explains the enhanced interaction between the N-terminus of TnI and CTnC as observed in many biological and biophysical experiments (for a review, see Farah and Reinach (4)). For instance, it was found that the complex between TnC and Rp40 is stable even in the presence of 6M urea (54).

The CTnC residues perturbed by Rp40 binding were identified by plotting the total change in backbone amide <sup>1</sup>HN and <sup>15</sup>N chemical shift for each resonance (see Figure II-4A). The total change in chemical shift was calculated with the following equation adopted from McKay et al. (23)

$$\Delta \delta_{\text{total}} = \sqrt{(\Delta \delta^{15}\text{N})^2 + (\Delta \delta^1\text{H})^2} \quad [3]$$

where  $\Delta \delta^{15}\text{N}$  and  $\Delta \delta^1\text{H}$  are the chemical shift changes in Hz. Although Rp40 induces chemical shift changes for backbone amide  $^1\text{HN}$  and  $^{15}\text{N}$  of  $\text{CTnC} \cdot 2\text{Ca}^{2+}$  throughout the sequence, the  $\alpha$ -helical regions (E, F, G, and H helices) are perturbed to a greater extent than other residues, especially at the end of the H-helix.

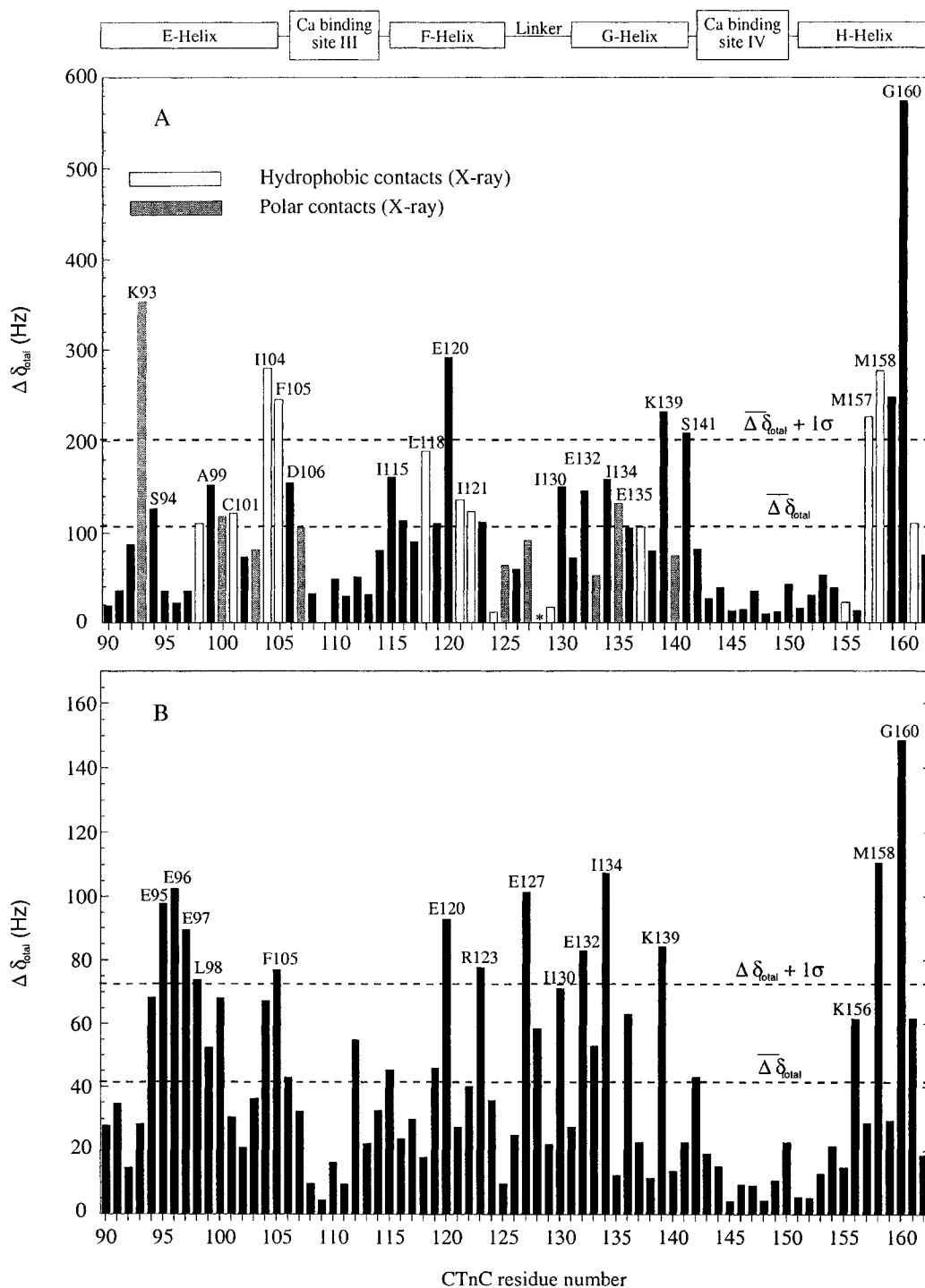


Figure II-4. CTnC•2Ca<sup>2+</sup> backbone amide chemical shift changes upon (A) Rp40 and (B) Tnl<sub>96-115</sub> binding. The total chemical shift change ( $\Delta\delta_{\text{total}}$ ) for each residue was obtained using equation 3. The two dashed lines indicate the mean chemical shift change and the mean chemical shift plus one standard deviation. (\*) In (A), the backbone amide resonance of H128 could not be identified in the 2D-<sup>1</sup>H, <sup>15</sup>N}-HSQC NMR spectrum of CTnC•2Ca<sup>2+</sup>•Rp40. Residues identified by Vassylyev *et al.* (53) making hydrophobic (grey bars) and polar contacts (white bars) to CTnC are specifically colored.

*Titration of CTnC•2Ca<sup>2+</sup> with TnI<sub>96-115</sub>.*

Figure II-3B depicts the TnI<sub>96-115</sub>-induced backbone amide <sup>1</sup>HN, <sup>15</sup>N chemical shift changes for CTnC•2Ca<sup>2+</sup>. Unlike Ca<sup>2+</sup> binding to CTnC and Rp40 binding to CTnC•2Ca<sup>2+</sup>, TnI<sub>96-115</sub> binding to CTnC•2Ca<sup>2+</sup> occurs with fast exchange kinetics on the NMR time scale. Thus, progressive shifting of the resonances is observed and the chemical shifts at every titration point correspond to the weighed average of the peptide-free and -bound species. Some residues that undergo relatively large chemical shift changes and do not overlap with other resonances are identified in Figure II-3B. When the chemical shift changes of E95, F105, E132, I134, K156 and G160 are normalized and plotted against the  $[\text{TnI}_{96-115}]_{\text{total}}/[\text{CTnC}\cdot 2\text{Ca}^{2+}]_{\text{total}}$  ratio, similar curves are obtained. Figure II-2C shows the averaged normalized chemical shift changes of the six chosen residues. Curve fitting to the following equation



yields a dissociation constant  $K_D = 47 \pm 7 \mu\text{M}$ , which is 24 times larger than that observed for Rp40. Several studies have examined the binding affinities of TnI<sub>96-115</sub> and TnI<sub>104-115</sub> with intact or isolated CTnC (see (28, 32, 63, 64) and references therein). The reported binding affinities are in good agreement with the value reported here ( $47 \pm 7 \mu\text{M}$ ). The total chemical shift changes calculated using equation 3 are plotted against the CTnC sequence (Figure II-4B). Compared to Rp40-induced chemical shift changes in CTnC•2Ca<sup>2+</sup> (Figure II-4A), similar patterns for TnI<sub>96-115</sub>-induced changes are observed. The changes occur along the entire sequence, but are relatively larger in the  $\alpha$ -helical regions (E, F, G, and H helices). These results indicate that TnI<sub>96-115</sub> may compete with Rp40 for a similar location on CTnC.

---

*Competitive binding: A. Titration of CTnC•2Ca<sup>2+</sup>•TnI<sub>96-115</sub> with Rp40.*

---

Following the titration of CTnC•2Ca<sup>2+</sup> with TnI<sub>96-115</sub>, Rp40 was titrated into the CTnC•TnI<sub>96-115</sub>•2Ca<sup>2+</sup> complex. The 2D-<sup>1</sup>H, <sup>15</sup>N}-HSQC NMR spectrum of CTnC•2Ca<sup>2+</sup>•TnI<sub>96-115</sub> exhibited changes with the first addition of Rp40. New peaks exhibiting the same chemical shifts as CTnC•2Ca<sup>2+</sup>•Rp40 emerged and gained in intensity as the ratio of Rp40:CTnC•2Ca<sup>2+</sup>•TnI<sub>96-115</sub> increased, whereas the peaks corresponding to CTnC•2Ca<sup>2+</sup>•TnI<sub>96-115</sub> diminished in intensity. Rp40 was added until no further changes in the spectrum were observed. The final 2D-<sup>1</sup>H, <sup>15</sup>N}-HSQC NMR spectrum of CTnC•2Ca<sup>2+</sup>•TnI<sub>96-115</sub>•Rp40 (data not shown) is identical to that of CTnC•2Ca<sup>2+</sup>•Rp40 (Figure II-3A). Following the same data treatment procedures as in the titration of CTnC•2Ca<sup>2+</sup> with Rp40, a K<sub>D</sub> of 3 ± 1 μM is obtained (Figure II-2D), which is identical to the affinity of Rp40 binding to CTnC•2Ca<sup>2+</sup> (Figure II-2B). These results suggest Rp40 can displace TnI<sub>96-115</sub> completely for CTnC•2Ca<sup>2+</sup> and its affinity for CTnC•2Ca<sup>2+</sup> is unaffected by the presence of TnI<sub>96-115</sub> within experimental error. Additional evidence for the displacement of TnI<sub>96-115</sub> was provided from 1D <sup>1</sup>H NMR spectra recorded during the titration. Figure II-5 shows shifting of TnI<sub>96-115</sub> resonances from aromatic sidechains toward the free peptide chemical shifts in solution as the addition of Rp40 displaces TnI<sub>96-115</sub> from the complex.

---

*Competitive binding: B. Titration of CTnC•2Ca<sup>2+</sup>•Rp40 with TnI<sub>96-115</sub>.*

---

Following the titration of CTnC•2Ca<sup>2+</sup> with Rp40, TnI<sub>96-115</sub> was added to the complex. No changes in the 2D-<sup>1</sup>H, <sup>15</sup>N}-HSQC NMR spectrum of CTnC•2Ca<sup>2+</sup>•Rp40 were observed, even at a TnI<sub>96-115</sub>:Rp40 ratio of 10:1. It is obvious that TnI<sub>96-115</sub> cannot bind to the complex of CTnC•2Ca<sup>2+</sup>•Rp40 in any fashion. Thus it cannot displace Rp40 from CTnC•2Ca<sup>2+</sup>.

**DISCUSSION**

When TnC is anchored to the thin filament by its C-terminal domain, the rapid association of  $\text{Ca}^{2+}$  with the N-terminal  $\text{Ca}^{2+}$ -specific regulatory sites of TnC initiates muscle contraction. In the past few years, we have been successful in determining the solution structures of skeletal and cardiac TnC in various states (9, 10, 24, 35, 65-67). These structures, together with  $\text{Ca}^{2+}$ - and peptide-binding studies (18, 19, 23, 36), have allowed us to dissect the mechanism and energetics of  $\text{Ca}^{2+}$  induced structural changes in the regulatory domain of TnC and subsequent interactions with TnI. In this report, we have focused on the structural domain of TnC and studied in detail  $\text{Ca}^{2+}$  and TnI peptide binding to CTnC by using 2D- $\{^1\text{H}, ^{15}\text{N}\}$ -HSQC NMR spectroscopy.

Previously, fluorescence and far UV CD spectroscopy (68) have been used to examine  $\text{Ca}^{2+}$  binding to CTnC (residues 88-162). Pearlstone and Smillie (28, 69) have applied the same spectroscopic techniques to the measurement of binding affinities of TnI<sub>96-116</sub>, TnI<sub>104-116</sub>, and TnI<sub>96-148</sub> to CTnC. Changes in fluorescence or CD spectra reflect global conformational changes accompanying  $\text{Ca}^{2+}$  or peptide binding to CTnC, but do not reveal details at the atomic level that can be used to elucidate the detailed binding mechanism. Shaw and Sykes (70-73) demonstrated the power of  $^1\text{H}$  NMR spectroscopy in determining the stoichiometry and binding of  $\text{Ca}^{2+}$  to synthetic peptide homo- and heterodimeric TnC domains. 2D- $\{^1\text{H}, ^{15}\text{N}\}$ -HSQC NMR spectroscopy is an even more powerful diagnostic tool as chemical shift overlap encountered in  $^1\text{H}$  NMR spectra can be overcome (18, 23, 24, 35, 36).

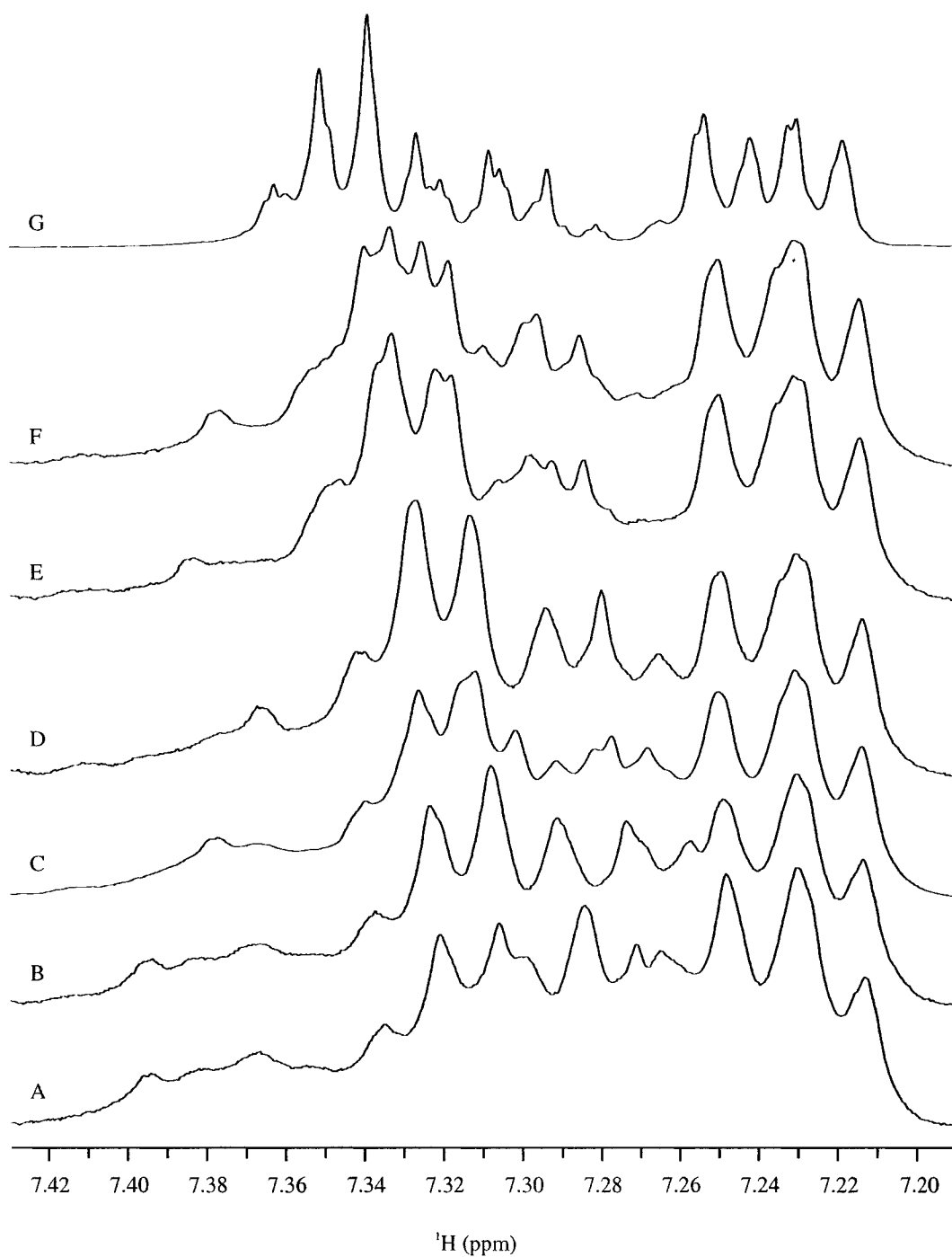


Figure II-5. 500 MHz <sup>1</sup>H NMR spectra of CTnC•2Ca<sup>2+</sup>•Rp40•TnI<sub>96-115</sub> at (A) 0, (B) 0.08, (C) 0.17, (E) 0.27, (E) 0.39 and (F) 0.61 Rp40:TnI<sub>96-115</sub> ratios and TnI<sub>96-115</sub> free in solution (G).

The amide NH chemical shifts shown in the 2D- $\{^1\text{H}, ^{15}\text{N}\}$ -HSQC NMR spectrum of CTnC•apo (Figure II-1A) reflect the characteristics of a “random coil” peptide whereas the dispersion of amide signals seen for CTnC•2Ca<sup>2+</sup> (Figure II-1B) are more typical of a structured protein. Chemical shift changes observed upon Ca<sup>2+</sup>-binding to CTnC allow monitoring of Ca<sup>2+</sup> induced “folding” of this domain. For example, the appearance of Gly<sup>111</sup> and Gly<sup>147</sup> at ~10.5 ppm (Figure II-1B) indicates that the two glycine amide protons are involved in important EF-hand hydrogen bonding interactions, as observed in X-ray structures of TnC (see review by Strynadka (74)). Although the 2D- $\{^1\text{H}, ^{15}\text{N}\}$ -HSQC NMR spectrum of CTnC•apo is indicative of a predominant “random coil” conformation, previous far UV CD studies of CTnC•apo suggested a small fraction of preformed  $\alpha$ -helical content (68). This suggests that CTnC•apo may not be completely “random coil” but contains some partial structures.

Fredricksen and Swenson (75) examined the relationship between stability and function for isolated N- and C- domains of TnC. It was demonstrated that while Ca<sup>2+</sup> affinity and cooperativity are higher for the C-domain, it is unstructured in the apo state, whereas the N-domain has lower Ca<sup>2+</sup> affinity but a stable, folded apo state. This agrees with our results for NTnC (18) and CTnC (this study). The high positive cooperativity and high affinity for Ca<sup>2+</sup> of paired sites III/IV of CTnC preclude a regulatory role in muscle regulation. On the other hand, the step-wise binding of Ca<sup>2+</sup> to site II followed by binding to site I to NTnC allows this domain to play a regulatory role, with Ca<sup>2+</sup> affinities in an appropriate physiological concentration range, and rapid enough Ca<sup>2+</sup> dissociation to be kinetically competent (see discussions in references (19) and (65)).

The interaction of CTnC•2Ca<sup>2+</sup> with TnI is important to its structural function. Both Rp40 and TnI<sub>96-115</sub> are implicated in binding to CTnC•2Ca<sup>2+</sup> (see Tripet et al. (30) and references therein). There is controversy surrounding the binding of these two regions of

TnI to TnC, particularly since the observation that the N-terminal residues of TnI interact with CTnC (43), and that Rp40 can effectively compete with TnI or TnI<sub>104-115</sub> for binding to TnC (54). Two models have been proposed for the interaction of the N-terminal region of TnI with CTnC. The first one suggests that Rp40 and TnI<sub>96-115</sub> share overlapping binding sites on CTnC, which are alternately occupied by either one or the other depending on Ca<sup>2+</sup>-dependent interactions between NTnC and TnI (30, 36, 39). On the other hand, the second model has TnI<sub>1-47</sub> specifically involved in binding to the hydrophobic patch within CTnC, regardless of Ca<sup>2+</sup>-dependent interactions between NTnC and TnI (53). The competitive binding of Rp40 and TnI<sub>96-115</sub> presented here show that both regions of TnI bind to similar sites within the C-domain of TnC but that Rp40 can displace TnI<sub>96-115</sub> completely. Thus, either the inhibitory region is not bound to the structural domain of TnC in intact muscle, or other Ca<sup>2+</sup>-dependent interactions between TnI and TnC, possibly also involving TnT and actin, are necessary to help displace Rp40.

The Rp40- and TnI<sub>96-115</sub>-induced chemical shift changes for the backbone amides of CTnC•2Ca<sup>2+</sup> can be used to identify the location of the binding sites for the respective peptides. Chemical shift mapping has proven to be a convenient way to locate target binding sites on proteins. A recent paper by Biekofsky *et al.* (21) has discussed in detail the potential of using <sup>15</sup>N chemical shifts as probes for monitoring individual Ca<sup>2+</sup> coordination site in EF hand proteins. Previously, we successfully applied chemical shift mapping to identify binding sites of TnI<sub>115-131</sub> and TnI<sub>96-148</sub> on NTnC (23, 35) and cardiac TnI<sub>147-163</sub> on cardiac NTnC (24).

Molecular surfaces of CTnC mapping out total chemical shift changes upon binding of TnI<sub>96-115</sub> and Rp40 are shown in Figure II-6. To reflect the difference in extent of total chemical shift changes for both peptides, the surfaces were colored on a color gradient scale from white to red (see color bar in Figure II-6). The X-ray structure determined for

TnC•2Ca<sup>2+</sup>•TnI<sub>1-47</sub> (53) and the Ngai model of CTnC•TnI<sub>96-115</sub> (27), which includes the C-domain of the X-ray structure determined for whole TnC•4Ca<sup>2+</sup> by James *et al.* (7), were used to compare the perturbation sites caused by the binding of Rp40 and TnI<sub>96-115</sub>, respectively.

In Figure II-6B, the TnC residues whose backbone amide chemical shifts are perturbed match similar regions where Rp40-CTnC contacts were observed in the X-ray structure of TnC•2Ca<sup>2+</sup>•TnI<sub>1-47</sub> (53). Corresponding residues for the C-domain of cardiac TnC were also identified in the interaction with cardiac TnI<sub>33-80</sub> (37). Residues that undergo large backbone amide chemical shift changes are mostly hydrophobic and mainly located in the hydrophobic patch of CTnC•2Ca<sup>2+</sup>, indicating that Rp40 binds to this particular region. This is consistent with the X-ray structure (53), in which Met<sup>21</sup> of Rp40 makes contacts deep in the hydrophobic patch of TnC and was suggested to be a key residue in anchoring Rp40. Two other regions identified in red, located in the C- and N-termini of TnC, are also found to be strongly influenced by Rp40 binding (Figure II-6B). <sup>15</sup>N T<sub>2</sub> NMR relaxation studies of the CTnC•2Ca<sup>2+</sup>•Rp40 complex have revealed that Rp40 restricts the flexibility of residues located in these hinge and terminal regions compared to CTnC•2Ca<sup>2+</sup> (see chapter III).

In the case of TnI<sub>96-115</sub>, no high-resolution structure of this peptide bound to the C-domain of CTnC is available, so we have used the model of Ngai *et al* (27) showing the complex between CTnC and the shorter TnI<sub>104-115</sub> peptide. A comparison between Figure II-4A and II-4B, and Figure II-6B and II-6C, shows that the TnI<sub>96-115</sub> inhibitory peptide perturbs the local environment of some of the same CTnC residues involved in binding Rp40, reinforcing the hypothesis of similar binding sites. The fact that Rp40 displaces TnI<sub>96-115</sub> also implies at least partially overlapping sites.

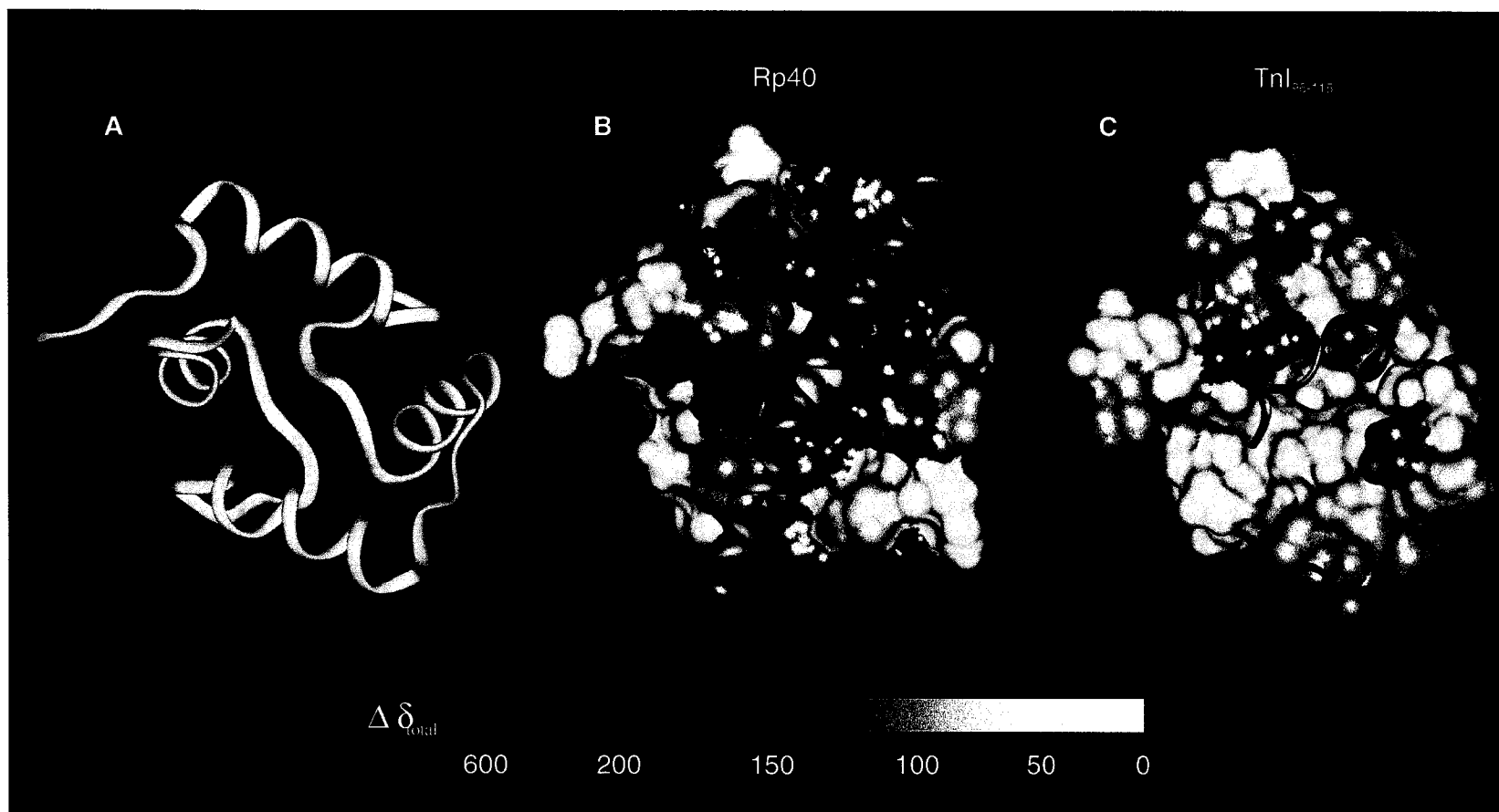


Figure II-6. Molecular surface of CTnC in complex with (B) Rp40 and (C) TnI<sub>96-115</sub>. The orientation of the protein backbone is shown as a ribbon diagram in (A). To show the difference in the extent of the total chemical shift changes ( $\Delta\delta_{\text{total}}$ ) between Rp40 and TnI<sub>96-115</sub> binding (Figure II-4), the surfaces were colored using a color gradient (from white to red – see color bar). Residues undergoing total chemical shift changes larger than 200 Hz (which corresponds to  $\approx \overline{\Delta\delta_{\text{total}}} + 1\sigma$  with Rp40) were colored pure red. Smaller total chemical shift changes were colored on a linear scale. The X-ray structure of CTnC•TnI<sub>1-47</sub> (53) and model of CTnC•TnI<sub>96-115</sub> (27) were used in (A) and (B), respectively.

The CTnC•2Ca<sup>2+</sup> amide chemical shift changes induced by TnI<sub>96-115</sub> are similarly distributed as in the case of Rp40, with perturbations of residues located in helical regions (helices E, F, G and H). Residues undergoing the largest chemical shift changes include Ser<sup>94</sup>, Phe<sup>105</sup>, Glu<sup>120</sup>, Lys<sup>139</sup>, Met<sup>158</sup> and Gly<sup>160</sup>, in both cases. However, as judged by the magnitude of chemical shift changes (see Figure II-4), the perturbations induced by TnI<sub>96-115</sub> are much weaker. A close examination of the chemical shift data suggests key differences between Rp40 and TnI<sub>96-115</sub> binding. The CTnC chemical shift changes (Figure II-4B) imply that six charged residues (Glu<sup>95</sup>, Glu<sup>96</sup>, Glu<sup>97</sup>, Glu<sup>120</sup>, Glu<sup>127</sup>, Glu<sup>132</sup>, Arg<sup>123</sup> and Lys<sup>139</sup>) likely participate in the binding of TnI<sub>96-115</sub>. Thus, the nature of the interaction with TnC is more electrostatic for TnI<sub>96-115</sub>, as opposed to more hydrophobic for Rp40, which is also consistent with the relatively high percentage of charged residues in TnI<sub>96-115</sub>.

Previous NMR structural studies based on transferred NOE experiments by Campbell *et al.* reported that TnI<sub>104-115</sub> adopts an amphiphilic helix-like structure, distorted at the center around the two Pro residues (33). However, recent NMR and CD results indicate that TnI<sub>96-115</sub> remains in an extended form upon binding to TnC, with a possible bend at Gly<sup>104</sup> (39). The eight residue difference between TnI<sub>104-115</sub> and TnI<sub>96-115</sub> might explain the differences in secondary structure observed for these two peptides. The shorter TnI peptide may bind slightly differently, whereas the extensive TnI<sub>96-115</sub> contacts identified in this report suggest a more extended structure for the longer peptide.

A recent structure of cNTnC•cTnI<sub>147-163</sub>•2Ca<sup>2+</sup> shows that cTnI<sub>147-163</sub> is helical from residues 151 to 156. At the end N-terminal of the helix, the peptide makes a turn which allows Ile<sup>148</sup> to make hydrophobic contacts with cardiac NTnC, placing Arg<sup>147</sup> in a position where an interaction with the acidic residues of the C-helix is possible. Based on chemical shift mapping results, we believe TnI<sub>96-115</sub> may also adopt a similar turn to avoid contact with the H-helix and interact with the G-helix. Only minor rearrangement of the location of

TnI<sub>96-115</sub> relative to TnI<sub>104-115</sub> would be necessary to satisfy the contact region located between the E and H helices on TnC (Figure II-6C). Thus, even though TnI<sub>96-115</sub> and Rp40 share common epitopes on TnC, the two peptides may have different structures and orientations in the bound form. Together with previous structural data, our results suggest that Rp40 makes several contacts within the hydrophobic patch, while TnI<sub>96-115</sub> may bind across the top of the hydrophobic patch. Thus, both electrostatic and hydrophobic interactions may be involved in TnI<sub>96-115</sub> binding to CTnC, while hydrophobic interactions dominate in the case of Rp40.

In this paper, 2D  $\{^1\text{H}, ^{15}\text{N}\}$  HSQC NMR spectroscopy was used to demonstrate that two equivalents of  $\text{Ca}^{2+}$  are required for folding CTnC. Unlike the step-wise binding mechanism observed for NTnC, CTnC binds  $\text{Ca}^{2+}$  with high positive cooperativity and high affinity. Rp40 and TnI<sub>96-115</sub> were shown to bind to CTnC•2Ca<sup>2+</sup> with dissociation constants of  $2 \pm 1 \mu\text{M}$  and  $47 \pm 7 \mu\text{M}$ , respectively. Residues of CTnC that are perturbed by the binding of Rp40 or TnI<sub>96-115</sub> were identified using chemical shift mapping. The chemical shift changes suggest that Rp40 binds to the hydrophobic pocket of CTnC•2Ca<sup>2+</sup>, while TnI<sub>96-115</sub> binds across the top of the hydrophobic pocket. The measured  $K_D$ 's quantitatively explain the displacement of TnI<sub>96-115</sub> from CTnC•2Ca<sup>2+</sup> by Rp40. In the Tripet *et al.* (30) model, the binding of the inhibitory region of TnI to the C-terminal domain of TnC is important in the release of the actomyosin ATPase inhibition. Our results imply that for this to be possible,  $\text{Ca}^{2+}$  dependent interactions between TnC and other regions of TnI, or other components of the thin filament, must be involved. The results of peptide studies with short peptides such as TnI<sub>96-115</sub> must always be interpreted with caution. There may be other interaction sites that are missing or the binding of TnI<sub>96-115</sub> to the target protein is in a non-physiologically relevant site.

## REFERENCES

1. Leavis, P. C., and Gergely, J. (1984) *CRC Crit. Rev. in Biochem.* 16, 235-305.
2. Zot, A. S., and Potter, J. D. (1987) *Annu. Rev. Biophys. and Biophys. Chem.* 16, 535-559.
3. Grabarek, Z., Tao, T., and Gergely, J. (1992) *J Muscle Res Cell Motil* 13, 383-393.
4. Farah, C. S., and Reinach, F. C. (1995) *FASEB J.* 9, 755-767.
5. Tobacman, L. S. (1996) *Annu. Rev. Physiol.* 58, 447-481.
6. Squire, J. M., and Morris, E. P. (1998) *FASEB J.* 12, 761-771.
7. Herzberg, O., and James, M. N. G. (1988) *J. Mol. Biol.* 203, 761-779.
8. Satyshur, K. A., Rao, S. T., Pyzalska, D., Drendal, W., Greaser, M., and Sundaralingam, M. (1988) *J. Biol. Chem.* 263, 1628-1647.
9. Slupsky, C. M., and Sykes, B. D. (1995) *Biochemistry* 34, 15953-15964.
10. Gagné, S. M., Tsuda, S., Li, M. X., Smillie, L. B., and Sykes, B. D. (1995) *Nat. Struct. Biol.* 2, 784-789.
11. Houdusse, A., Love, M. L., Dominguez, R., Grabarek, Z., and Cohen, C. (1997) *Structure* 5, 1695-1711.
12. Leavis, P. C., Rosenfeld, S. S., and Gergely, J. (1978) *J. Biol. Chem.* 253, 5452-5459.
13. Potter, J. D., and Gergely, J. (1975) *J Biol Chem* 250, 4628-4633.
14. Szczesna, D., Guzman, G., Miller, T., Zhao, J., Farokhi, K., ElleMBERGER, H., and Potter, J. D. (1996) *J. Biol. Chem.* 271, 8381-8386.
5. Gergely, J. (1998) *Adv. Exp. Med. Biol.* 453, 169-176.
16. Gagné, S. M., Li, M. X., McKay, R. T., and Sykes, B. D. (1998) *Biochem. Cell Biol.* 76, 301-312.
17. Rao, S. T., Satyshur, K. A., Greaser, M. L., and Sundaralingam, M. (1996) *Acta Crystall. Section D* 52, 916-922.
18. Li, M. X., Gagné, S. M., Tsuda, S., Kay, C. M., Smillie, L. B., and Sykes, B. D. (1995) *Biochemistry* 34, 8330-8340.
19. Li, M. X., Gagné, S. M., Spyrapoulos, L., Kloks, C. P. A. M., Audette, G., Chandra, M., Solaro, R. J., Smillie, L. B., and Sykes, B. D. (1997) *Biochemistry* 36, 12519-12525.
20. Evenas, J., Thulin, E., Malmendal, A., Forsén, S., and Carlstrom, G. (1997) *Biochemistry* 36, 3448-3457.
21. Biekofsky, R. R., Martin, S. R., Browne, J. P., Bayley, P. M., and Feeney, J. (1998) *Biochemistry* 37, 7617-7629.
22. Wimberly, B., Thulin, E., and Chazin, W. J. (1995) *Protein Sci.* 4, 1045-1055.
23. McKay, R. T., Tripet, B. P., Hodges, R. S., and Sykes, B. D. (1997) *J. Biol. Chem.* 272, 28494-28500.
24. Li, M. X., Spyrapoulos, L., and Sykes, B. D. (1999) *Biochemistry* 38, 8289-8298.
25. Olah, G. A., Rokop, S. E., Wang, C.-L. A., Blechner, S. L., and Trewhella, J. (1994) *Biochemistry* 33, 8233-8239.
26. Olah, G. A., and Trewhella, J. (1994) *Biochemistry* 33, 12800-12806.
27. Ngai, S.-M., Sönnichsen, F. D., and Hodges, R. S. (1994) *J. Biol. Chem.* 269, 2165-2172.
28. Pearlstone, J. R., and Smillie, L. B. (1995) *Biochemistry* 34, 6932-6940.
29. Pearlstone, J. R., and Smillie, L. B. (1997) *Biophys. J.* 72, A331.
30. Tripet, B. P., Van Eyk, J. E., and Hodges, R. S. (1997) *J. Mol. Biol.* 271, 728-750.
31. Campbell, A. P., and Sykes, B. D. (1991) *J. Mol. Biol.* 222, 405-421.
32. Campbell, A. P., Cachia, P. J., and Sykes, B. D. (1991) *Biochem. Cell Biol.* 69, 674-681.

33. Campbell, A. P., Van Eyk, J. E., Hodges, R. S., and Sykes, B. D. (1992) *Biochim Biophys. Acta* 1160, 35-54.
34. Slupsky, C. M., Shaw, G. S., Campbell, A. P., and Sykes, B. D. (1992) *Protein Sci.* 1, 1595-1603.
35. McKay, R. T., Pearlstone, J. R., Corson, D. C., Gagné, S. M., Smillie, L. B., and Sykes, B. D. (1998) *Biochemistry* 37, 12419-12430.
36. McKay, R. T., Tripet, B. P., Pearlstone, J. R., Smillie, L. B., and Sykes, B. D. (1999) *Biochemistry* 38, 5478-5489.
37. Gasmi-Seabrook, G., Howarth, J. W., Finley, N., Abusamhadneh, E., Gaponenko, V., Brito, R. M., Solaro, R. J., and Rosevear, P. R. (1999) *Biochemistry* 38, 8313-8322.
38. Gaponenko, V., Abusamhadneh, E., Abbott, M. B., Finley, N., Gasmi-Seabrook, G., Solaro, R. J., Rance, M., and Rosevear, P. R. (1999) *J. Biol. Chem.* 274, 16681-16684.
39. Hernández, G., Blumenthal, D. K., Kennedy, M. A., Unkefer, C. J., and Trewhella, J. (1999) *Biochemistry* 38, 6911-6917.
40. Syska, H., Wilkinson, J. M., Grand, R. J. A., and Perry, S. V. (1976) *Biochem. J.* 153, 375-387.
41. Talbot, J. A., and Hodges, R. S. (1981) *J. Biol. Chem.* 256, 2798-22802.
42. Van Eyk, J. E., and Hodges, R. S. (1988) *J. Biol. Chem.* 263, 1726-1732.
43. Farah, C. S., Miyamoto, C. A., Ramos, C. H. I., da Silva, A. C. R., Quaggio, R. B., Fujimori, K., Smillie, L. B., and Reinach, F. C. (1994) *J. Biol. Chem.* 269, 5230-5240.
44. Kobayashi, T., Tao, T., Grabarek, Z., Gergely, J., and Collins, J. H. (1991) *J. Biol. Chem.* 266, 13746-13751.
45. Kobayashi, T., Tao, T., Gergely, J., and Collins, J. H. (1994) *J. Biol. Chem.* 269, 5725-5729.
46. Kobayashi, T., Grabarek, Z., Gergely, J., and Collins, J. H. (1995) *Biochemistry* 34, 10946-10952.
47. Kobayashi, T., Leavis, P. C., and Collins, J. H. (1996) *Biochim. Biophys. Acta* 1294, 25-30.
48. Kobayashi, T., Zhao, X., Wade, R., and Collins, J. H. (1999) *Biochim. Biophys. Acta* 1430, 214-221.
49. Leszyk, J., Collins, J. H., Leavis, P. C., and Tao, T. (1988) *Biochemistry* 27, 6983-6987.
50. Leszyk, J., Grabarek, Z., Gergely, J., and Collins, J. H. (1990) *Biochemistry* 29, 299-304.
51. Blechner, S. L., Olah, G. A., Strynadka, N. C., Hodges, R. S., and Trewhella, J. (1992) *Biochemistry* 31, 11326-11334.
52. Stone, D. B., Timmins, P. A., Schneider, D. K., Krylova, I., Ramos, C. H. I., Reinach, F. C., and Mendelson, R. A. (1998) *J. Mol. Biol.* 281, 689-704.
53. Vassilyev, D. G., Takeda, S., Wakatsuki, S., Maeda, K., and Maeda, Y. (1998) *Proc. Natl. Acad. Sci. U.S.A.* 95, 4847-4852.
54. Ngai, S.-M., and Hodges, R. S. (1992) *J. Biol. Chem.* 267, 15715-15720.
55. Ramos, C. H. I. (1999) *J. Biol. Chem.* 274, 18189-18195.
56. Gagné, S. M., Tsuda, S., Li, M. X., Chandra, M., Smillie, L. B., and Sykes, B. D. (1994) *Protein Sci.* 3, 1961-1974.
57. Kay, L. E., Keifer, P., and Saarinen, T. (1992) *J. Am. Chem. Soc.* 114, 10663-10665.
58. Zhang, O., Kay, L. E., Olivier, J. P., and Forman-Kay, J. D. (1994) *J. Biomol. NMR* 4, 845-858.
59. Delaglio, F., Grzesiek, S., Vuister, G. W., Zhu, G., Pfeifer, J., and Bax, A. (1995) *J. Biomol. NMR* 6, 277-293.

60. Wüthrich, K. (1986) *NMR of proteins and nucleic acids.*, John Wiley & Sons, New York.
61. Wishart, D. S., Sykes, B. D., and Richards, F. M. (1991) *J. Mol. Biol.* 222, 311-333.
62. Ferguson-Miller, S. and Koppenol, W. H. (1981) *TIBS* 6, IV-VII.
63. Cachia, P. J., Van Eyk, J., Ingraham, R. H., McCubbin, W. D., Kay, C. M., and Hodges, R. S. (1986) *Biochemistry* 25, 3553-3562.
64. Swenson, C. A., and Fredricksen, R. S. (1992) *Biochemistry* 31, 3420-3429.
65. Gagné, S. M., Li, M. X., and Sykes, B. D. (1997) *Biochemistry* 36, 4386-4392.
66. Sia, S. K., Li, M. X., Spyropoulos, L., Gagné, S. M., Liu, W., Putkey, J. A., and Sykes, B. D. (1997) *J. Biol. Chem.* 272, 18216-18221.
67. Spyropoulos, L., Li, M. X., Sia, S. K., Gagné, S. M., Chandra, M., Solaro, R. J., and Sykes, B. D. (1997) *Biochemistry* 36, 12138-12146.
68. Li, M. X., Chandra, M., Pearlstone, J. R., Racher, K. I., Trigo-Gonzalez, G., Borgford, T., Kay, C. M., and Smillie, L. B. (1994) *Biochemistry* 33, 917-925.
69. Pearlstone, J. R., Sykes, B. D., and Smillie, L. B. (1997) *Biochemistry* 36, 7601-7606.
70. Shaw, G. S., Hodges, R. S., and Sykes, B. D. (1990) *Science* 249, 280-283.
71. Shaw, G. S., Golden, L. F., Hodges, R. S., and Sykes, B. D. (1991) *J. Am. Chem. Soc.* 113, 5557-5562.
72. Shaw, G. S., Hodges, R. S., and Sykes, B. D. (1991) *Biochemistry* 30, 8339-8347.
73. Shaw, G. S., Hodges, R. S., and Sykes, B. D. (1992) *Biopolymers* 32, 391-397.
74. Strynadka, N. C., and James, M. N.G. (1989) *Annu. Rev. Biochem.* 58, 951-998.
75. Fredricksen, S. R., and Swenson, C. A. (1996) *Biochemistry* 35, 14012-14026.

## CHAPTER III

### *Structure, Dynamics, and Thermodynamics of the Structural Domain of Troponin C in Complex with the Regulatory Peptide 1-40 of Troponin I*<sup>†</sup>

#### INTRODUCTION

Sliding of the thin filament past the thick filament constitutes the mechanical basis of muscle contraction. The thin filament is comprised of three major components, actin, tropomyosin, and the troponin complex, whereas the thick filament consists mainly of myosin. Regulation of muscle contraction occurs at the level of troponin, where binding of  $\text{Ca}^{2+}$  triggers a cascade of altered protein-protein interactions, leading to force development. Troponin is a three-component complex involving troponin C (TnC), TnI, and TnT. TnC responds to the  $\text{Ca}^{2+}$  signal, TnI is thought to inhibit interactions between thick and thin filaments in the absence of  $\text{Ca}^{2+}$ , and TnT is believed to anchor troponin to actin and transmit the  $\text{Ca}^{2+}$  signal along the thin filament, thereby enhancing the actomyosin ATPase activity from which energy is derived (for reviews, see (1-6)).

X-ray and NMR structural studies of TnC reveal a dumbbell-shaped molecule with two globular domains (designated N and C, for the N and C-terminal domains, respectively) connected by a central linker (7-11). Each domain contains two helix-loop-helix EF hand motifs typical of calcium binding proteins (12). Sites III and IV in the C-domain are believed to be fully occupied by either  $\text{Ca}^{2+}$  or  $\text{Mg}^{2+}$  under physiological conditions, whereas sites I and II in the N-domain are  $\text{Ca}^{2+}$  specific sites with weaker affinity (see reviews listed above and (13)). Following  $\text{Ca}^{2+}$  binding to TnC in either of the globular

---

<sup>†</sup> The results presented in this chapter apply to the skeletal isoform of TnC (sTnC abbreviation is not used). Any reference to the cardiac isoform of TnC is explicitly stated. The results presented in this chapter are taken integrally from: Mercier, P, Spyropoulos, L. and Sykes, B. D. *Biochemistry*, 40, 10063-10077, 2001.

domains, a hydrophobic 'pocket' becomes exposed, which constitutes an important binding site for different portions of TnI (for a review, see (14) and references therein).

The interaction between the  $\text{Ca}^{2+}$ -binding and inhibitory proteins of the troponin complex is central to the regulation of muscle contraction. While much is known about how  $\text{Ca}^{2+}$  induces structural changes in the regulatory domain of TnC and initiates a cascade of protein-protein interactions leading to muscle contraction, much less is known about TnC interactions with TnI and TnT. Neutron scattering studies have shed some light on the general aspects of the TnI•TnC interaction (15, 16) in the binary complex and in the presence of TnT (17), but despite several years of investigation, there are still no high-resolution structures of the complex, due in part to the low solubility of TnI. A common approach to investigate the sites of interactions between TnC and TnI involves the use of relatively short synthetic fragments of TnI complexed with TnC (18-34).

The first forty residues of TnI (Rp40) represent a region of particular interest. This segment of TnI was first identified by Syska *et al.* (35) to bind to TnC and further work by Ngai *et al.* (36) established that Rp40 could effectively compete with the inhibitory peptide TnI<sub>104-115</sub> and block its inhibitory properties with respect to contraction. Later, Tripet *et al.* (21) showed that the ability of Rp40 to compete with TnI<sub>104-115</sub> is modulated by other TnC-TnI interactions, mainly by the interaction of TnI<sub>116-131</sub> with the N-domain of TnC (NTnC). These results were corroborated in our previous study with Rp40 (22), where we demonstrated, using solution NMR spectroscopic techniques, that Rp40 and TnI<sub>96-115</sub> share common binding sites on CTnC, but that the interaction of Rp40 is much stronger (Rp40  $K_d = 2 \pm 1 \mu\text{M}$ , TnI<sub>96-115</sub>  $K_d = 47 \pm 7 \mu\text{M}$ ) and that Rp40 could displace TnI<sub>96-115</sub> in the absence of NTnC and any other portion of TnI. The exact nature of the structural and/or functional role of Rp40 is still not yet fully understood. The crystal structure of TnC in complex with TnI<sub>1-47</sub> determined by Vassilyev *et al.* (34) revealed that TnI<sub>3-33</sub> forms a long

$\alpha$ -helix that binds within the hydrophobic pocket of CTnC. The corresponding region of cardiac TnI<sub>33-80</sub> has also been shown to bind within the hydrophobic patch of the C-domain of cardiac TnC (30, 31).

NMR spectroscopy is of great utility for probing not only the atomic structures of proteins, but has also proven to be a powerful tool for the study of dynamic and thermodynamic properties of proteins through backbone amide  $^{15}\text{N}$  and  $^{13}\text{C}/^2\text{H}$  side-chain relaxation measurements (37-40). The model-independent approach to relaxation data analysis introduced by Lipari and Szabo allows for extraction of a global macromolecular rotational correlation time ( $\tau_m$ ), as well as an internal correlation time ( $\tau_e$ ) and an order parameter ( $S^2$ ) that is related to the amplitude of internal motion for each residue (41, 42).  $S^2$  can be interpreted as the orientational probability distribution of a given bond vector (N-H, C-H), thermodynamic parameters such as entropy and heat capacity can be estimated in a semi-quantitative fashion from changes in  $S^2$  obtained upon ligand binding, or temperature changes (43). These approaches have been useful in furthering our understanding of the role of time-dependent conformational fluctuations involved in the binding of metal ions and peptides, for example, and can provide insight into understanding the contribution of dynamics to the overall stability of a protein.

In this paper, we have determined the solution structure of the  $\text{Ca}^{2+}$ -saturated state of CTnC in complex with Rp40 peptide using NMR spectroscopy, and performed a series of NMR relaxation experiments in order to investigate changes in backbone dynamics induced by binding of Rp40. The changes in backbone dynamics were used to estimate the contribution of backbone conformational entropy to the thermodynamics of peptide binding. The solution structure of  $\text{CTnC}\cdot 2\text{Ca}^{2+}$  in the  $\text{CTnC}\cdot 2\text{Ca}^{2+}\cdot\text{Rp40}$  complex was found to be similar to the structure of CTnC in the crystal structure of  $\text{TnC}\cdot 2\text{Ca}^{2+}\cdot\text{TnI}_{1-47}$  (34).

## EXPERIMENTAL PROCEDURES

### *Construction of plasmid vector encoding CTnC and protein isolation.*

The engineering of CTnC (88-162) into the expression vector pET3a was as described for NTnC (1-90) (44) except for the use of two different oligonucleotides that are complimentary to the sequence and restriction enzyme sites. The expression and purification of [ $^{15}\text{N}$ ]-CTnC and [ $^{13}\text{C}/^{15}\text{N}$ ]-CTnC in minimal media follows the procedure described for [ $^{15}\text{N}$ ]- NTnC (44, 45). During expression in *E. coli*, the N-terminal methionine, corresponding to the initiation codon, is not cleaved off. Decalcification of both [ $^{15}\text{N}$ ]-CTnC and [ $^{13}\text{C}/^{15}\text{N}$ ]-CTnC was as described for [ $^{15}\text{N}$ ]-NTnC (45). Since CTnC has higher affinity for  $\text{Ca}^{2+}$  than NTnC, the pH of the 25mM  $(\text{NH}_4)\text{HCO}_3$  buffer was raised to 8.5 for the decalcification step to increase the efficiency of EDTA. Unlabeled Rp40 peptide, acetyl-GDEEKRNRAITARRQHLKSVMLQIAATELEKEEGRREA EK-amide, was synthesized and purified as described in Ngai & Hodges (36).

### *NMR sample preparation.*

[ $^{15}\text{N}$ ]-CTnC and [ $^{13}\text{C}$ ,  $^{15}\text{N}$ ] CTnC were dissolved in 600  $\mu\text{L}$  NMR buffer (treated with Chelex 100 to remove metal contaminants) containing 100 mM KCl, 10 mM imidazole and 15 mM DTT in 90%  $\text{H}_2\text{O}/10\%$   $\text{D}_2\text{O}$ . Since Rp40 has very low solubility in aqueous solution, it was slowly added in solid form directly to the sample, until a precipitate was observed. To facilitate peptide solubilization, the pH of the solution prior to Rp40 addition was raised to 8.5. After complete dissolution of Rp40, the pH of the final sample was adjusted to 6.8 if necessary (uncorrected for  $^2\text{H}$  isotope effects). The solution was then filtered, and 480  $\mu\text{L}$  were transferred into an NMR tube, to which 10  $\mu\text{L}$  of 1M DSS and 10  $\mu\text{L}$  of 1.3%  $\text{NaN}_3$  were added. The protein and peptide concentrations were determined to

be 1.33 and 1.91 mM, respectively, by amino acid analysis in duplicate, corresponding to a peptide/protein ratio of 1.44.

*NMR experiments for structure determination.*

---

Chemical shift assignment of CTnC•2Ca<sup>2+</sup> not bound to Rp40 was based on the chemical shift assignment of TnC•4Ca<sup>2+</sup> previously reported by Slupsky *et al.* (9). For CTnC•Ca<sup>2+</sup> in the CTnC•Ca<sup>2+</sup>•Rp40 complex, the assignment of <sup>1</sup>H, <sup>13</sup>C, and <sup>15</sup>N resonances, and the subsequent structural determination, were carried out using NMR experiments listed in Table III-1. The aromatic protons of Phe residues are unassigned. The 2D <sup>15</sup>N/<sup>13</sup>C-filtered DIPSI and NOESY experiments did not allow for the assignment of Rp40 resonances, due to line broadening as a result of chemical exchange, and poor chemical shift dispersion for the peptide resonances. All NMR spectra were acquired at 30 °C on Varian INOVA 500, Unity 600 or INOVA 800 MHz spectrometers (see Table III-1) equipped with 5 mm triple resonance probes and z-axis pulsed field gradients for the 500 and 600 MHz instruments and triple-axis gradients for the 800 MHz spectrometer. All experimental FIDs were processed using the program NMRpipe (46) and analyzed using either PIPP (46) or NMRView programs (47). Generally, linear prediction up to half the number of experimental points was used in indirect dimensions. Data were then zero-filled to twice the number of acquired plus predicted points, and typically multiplied by a sine-bell apodization function shifted by 60° to 90° before Fourier transformation.

*Distance and torsion angle restraints.*

---

Proton-proton distance restraints were derived from measured peak intensities in the 3D <sup>15</sup>N NOESY-HSQC and simultaneous 3D <sup>15</sup>N/<sup>13</sup>C-NOESY-HSQC experiments and calibrated as previously described (48) with the error on the peak intensities set to 40%, and the lower bound on all proton-proton restraints set to 1.7 Å. The <sup>1</sup>H resonances of Rp40

Table III-1. NMR experiments conducted for the purpose of chemical shift assignment and obtaining NOE-based distance restraints for sCTnC•2Ca<sup>2+</sup>•Rp40.

Exp. Name	Nuclei <sup>a</sup>	<sup>1</sup> H	nt <sup>b</sup>	x-pts <sup>c</sup>	y-pts	z-pts	x-sw	y-sw	z-sw	Mix <sup>d</sup>	Ref.
<sup>15</sup> N-HSQC	<sup>1</sup> H, <sup>15</sup> N	600	16	960	256	-	7500	1800	-	-	(83, 84)
DISPL-HSQC	<sup>1</sup> H, <sup>1</sup> H, <sup>15</sup> N	600	12	1024	256	64	8000	6550	1690	-	(85)
HCCH-TOCSY	<sup>1</sup> H, <sup>1</sup> H, <sup>13</sup> C	500	16	768	256	64	6000	3200	3000	-	(86)
CBCA(CO)NNH	<sup>1</sup> H, <sup>13</sup> C, <sup>15</sup> N	500	32	768	100	64	6000	7794	1650	-	(83)
HNCACB	<sup>1</sup> H, <sup>13</sup> C, <sup>15</sup> N	500	32	1024	108	72	600	7794	1500	-	(83)
<sup>15</sup> N-noesy-HSQC	<sup>1</sup> H, <sup>1</sup> H, <sup>15</sup> N	600	12	1024	256	64	8000	6579	1700	125	(85)
<sup>15</sup> N-noesy-HSQC	<sup>1</sup> H, <sup>1</sup> H, <sup>15</sup> N	600	12	1024	256	64	8000	6579	1700	50	(85)
<sup>13</sup> C, <sup>15</sup> N-noesy <sup>e</sup>	<sup>1</sup> H, <sup>1</sup> H, <sup>13</sup> C/ <sup>15</sup> N	800	16	1088	280	72	10000	9000	4243	75	(87)
HNHA	<sup>1</sup> H, <sup>1</sup> H, <sup>15</sup> N	600	8	1024	152	96	8000	4807	1650	-	(50)
HNHB	<sup>1</sup> H, <sup>13</sup> C, <sup>13</sup> C(O)	500	16	902	256	72	6200	4900	1500	-	(88)
<sup>15</sup> N/ <sup>13</sup> C filtered	<sup>1</sup> H, <sup>1</sup> H	500	128	4096	1024	-	6200	6200	-	-	(89)
DIPSI <sup>f</sup>											
<sup>15</sup> N/ <sup>13</sup> C filtered	<sup>1</sup> H, <sup>1</sup> H	500	128	4096	1024	-	6200	6200	-	-	(89)
NOESY <sup>f</sup>											

<sup>a</sup> the nucleus acquired in each dimension (*e.g.* <sup>1</sup>H, <sup>15</sup>N indicates proton x, nitrogen y).

<sup>b</sup> the number of transients acquired for each FID.

<sup>c</sup> 'x,y,z'-pts and 'sw' is the number of complex points and sweep width in each respective dimension (x is the directly detected dimension).

<sup>d</sup> mixing times are given in milliseconds.

<sup>e</sup> <sup>13</sup>C, <sup>15</sup>N-NOESY-HSQC is a simultaneously <sup>13</sup>C, <sup>15</sup>N-edited NOESY-HSQC.

<sup>f</sup> The sequence was heavily modified in-house (L. Spyropoulos).

could not be assigned, thus only symmetry-related cross-peaks were selected from the simultaneous  $^{15}\text{N}/^{13}\text{C}$  3D NOESY-HSQC, minimizing the probability of misinterpretation of a protein-peptide NOE as a protein-protein NOE. Approximately eighty ambiguous contacts, thought to be proton-proton NOE contacts between CTnC•2Ca<sup>2+</sup> and Rp40 were excluded from structure calculations. Intramolecular CTnC•2Ca<sup>2+</sup> NOEs within the CTnC•2Ca<sup>2+</sup>•Rp40 complex with distance violations greater than 0.3 Å were closely examined before further rounds of structure refinement. Based on homologous calcium binding sites, 11 Ca<sup>2+</sup>-distance restraints of 2.0-2.8 Å site III and IV were incorporated (49). Unfortunately, CTnC•2Ca<sup>2+</sup>•Rp40 NOE distance restraints were not incorporated, due to ambiguity in assignment of peptide resonances.

Backbone  $\phi$  dihedral angle restraints were obtained from  $^3J_{\text{HNH}\alpha}$  coupling constants derived from the 3D HNHA spectrum (50). For the HNHA experiment, a correction factor of 1.055 was used (48). The peak intensities were assumed to have errors equal to the noise level, and the minimum restraint range was set to  $\pm 20^\circ$ . The backbone  $\psi$  dihedral angle was determined from the  $d_{\text{N}\alpha}/d_{\alpha\text{N}}$  ratio as previously described. For  $d_{\text{N}\alpha}/d_{\alpha\text{N}}$  ratios  $> 1.2$ ,  $\psi$  was restricted to  $-30 \pm 110^\circ$ . For  $d_{\text{N}\alpha}/d_{\alpha\text{N}}$  ratios  $< 0.71$ ,  $\psi$  was limited to  $-120 \pm 100^\circ$ . Methylene hydrogens for 14 residues were stereospecifically assigned by comparing intraresidue  $^1\text{H}_{\text{N}} - ^1\text{H}_{\beta 1}$  and  $^1\text{H}_{\text{N}} - ^1\text{H}_{\beta 2}$  cross-peak intensities in a short-mixing time 3D  $^{15}\text{N}$ -edited DIPSI-HSQC (50 ms) (51), carefully inspecting intraresidue  $^1\text{H}_{\text{N}} - ^1\text{H}_{\beta 1}$  and  $^1\text{H}_{\text{N}} - ^1\text{H}_{\beta 2}$  NOE cross-peak intensities from the 3D  $^{15}\text{N}$ -edited NOESY-HSQC (50 ms) and 3D simultaneous  $^{15}\text{N}/^{13}\text{C}$ -edited NOESY-HSQC (75 ms), comparing intraresidue  $^1\text{H}_{\alpha} - ^1\text{H}_{\beta 1}$  and  $^1\text{H}_{\alpha} - ^1\text{H}_{\beta 2}$  NOE cross-peak intensities from the 3D simultaneous  $^{15}\text{N}/^{13}\text{C}$ -edited NOESY-HSQC (75 ms), and carefully inspecting intraresidue  $^1\text{H}_{\text{N}} - ^1\text{H}_{\beta 1}$  and  $^1\text{H}_{\text{N}} - ^1\text{H}_{\beta 2}$  cross-peak intensities from a 3D  $^{15}\text{N}$ -edited HNHB spectrum. Restraints for the  $\chi_1$  angle of 60, 180, or  $-60^\circ$  ( $\pm 60^\circ$ ) were imposed if the results from the three experiments were

consistent with a single side chain rotamer. In later stages of the structure refinement, direct refinement against  $^{13}\text{C}_\alpha$  and  $^{13}\text{C}_\beta$  chemical shifts for residues located in regions of well-defined secondary structure was employed to further restrain both  $\phi$  and  $\psi$  backbone dihedral angles (52).

Structures were generated with Xplor 3.1 (53) using a simulated annealing protocol with 10000 high-temperature steps and 7000 cooling steps. The type and number of distance and dihedral restraints are summarized in Table III-2. Starting from an extended conformation, an initial set of 100 structures was generated using only NOE-derived distance restraints to probe incorrect NOEs. Following removal of any NOEs yielding distance violations larger than 0.2 Å from the starting set of restraints, the Vadar (D.S. Wishart, L. Willard, and B.D. Sykes, unpublished) and Procheck (54) programs were used to identify the well-defined secondary structure elements from the 30 lowest total energy structures taken from the initial 100 structures, and  $\phi$  angle restraints were applied for subsequent rounds of refinement. The structure was further refined by successively including  $\psi$  and  $\chi_1$  angle restraints,  $\text{Ca}^{2+}$  distance restraints in sites III and IV, and directly refining against  $^{13}\text{C}_\alpha$  and  $^{13}\text{C}_\beta$  chemical shifts. The structural statistics presented in Table III-2 are for the 30 structures of lowest total energy obtained from a set of 30 low energy structures taken from an ensemble of 100 structures generated from an elongated conformation, after refinement of the structure was complete.

#### *Backbone amide $^{15}\text{N}$ relaxation measurements.*

---

All relaxation data were acquired at 30 °C on Varian INOVA 500 MHz and Unity 600 MHz spectrometers. Sensitivity-enhanced pulse sequences developed by Farrow *et al.* (37) were used to measure  $^{15}\text{N}$ - $T_1$ ,  $^{15}\text{N}$ - $T_2$ , and  $\{^1\text{H}\}$ - $^{15}\text{N}$  NOE.

Prior to the addition of Rp40, backbone amide  $^{15}\text{N}$  backbone relaxation data for  $[^{15}\text{N}]\text{-CTnC}\cdot 2\text{Ca}^{2+}$  were collected at 500 MHz. The same NMR sample ( $[^{15}\text{N}]\text{-CTnC}\cdot 2\text{Ca}^{2+}\cdot \text{Rp40}$ ) was used for structure determination and backbone relaxation measurements. Due to partial dimerization of the  $\text{CTnC}\cdot 2\text{Ca}^{2+}\cdot \text{Rp40}$  complex in solution (see Results) backbone amide  $^{15}\text{N}$  NMR relaxation data were collected at three different concentrations of the protein-peptide complex at 600 MHz (1.33, 0.65, and 0.33 mM by consecutively diluting the same sample by a factor of 2) and at the initial (1.33 mM) and final protein concentration (0.33 mM) at 500 MHz. The protein and Rp40 concentrations were determined in duplicate by amino acid analysis after each dilution.

All  $^{15}\text{N}\text{-}T_1$ ,  $^{15}\text{N}\text{-}T_2$ , and  $\{^1\text{H}\}\text{-}^{15}\text{N}$  NOE experiments were collected with  $794 (t_1) \times 96 (t_2)$  complex points at 500 MHz and  $970 (t_1) \times 96 (t_2)$  complex points at 600 MHz. The  $T_1$  relaxation delays were 11.1, 55.5, 122.1, 199.8, 277.5, 388.5, 499.5, 666, 888 and 1100 ms on both instruments. The delay between repetitions of the pulse sequence was set to 1.2 s for the  $T_1$  experiment. The  $T_2$  relaxation delays were set to  $16.61 \times n$  and  $16.544 \times n$  ms (where  $n = 1, 2, \dots, 10$ ) on the 500 and 600 MHz spectrometers, respectively. For the  $T_2$  experiment, the delay between repetitions of the pulse sequence was 3 s at 500 and 600 MHz.  $\{^1\text{H}\}\text{-}^{15}\text{N}$  NOEs were measured in the absence (incorporating a relaxation delay of 5 s between repetitions of the pulse sequence) and presence of proton saturation (incorporating 3 s of  $^1\text{H}$  saturation, and a delay between repetitions of the pulse sequence of 2 s). All relaxation data were processed using the NMRpipe program (46) and analyzed using PIPP (55) or NMRView (47). The data were processed as described above, with the exception that linear prediction was not used.

*Analysis of backbone amide  $^{15}\text{N}$  relaxation measurements.*

Magnetic dipole-dipole interactions between the  $^{15}\text{N}$  nucleus and the amide  $^1\text{H}$ , and the chemical shift anisotropy of the  $^{15}\text{N}$  nucleus are the predominant relaxation mechanisms contributing to the macroscopic relaxation times  $T_1$ , and  $T_2$ , and cross-relaxation giving rise to the  $\{^1\text{H}\}$ - $^{15}\text{N}$  NOE, for a given backbone amide  $^{15}\text{N}$ . The  $^{15}\text{N}$ - $T_1$ ,  $-T_2$ , and  $\{^1\text{H}\}$ - $^{15}\text{N}$  NOE relaxation parameters are theoretically well established (37, 56) and are expressed as a linear combination of a spectral density function at the resonance frequencies of  $^{15}\text{N}$  and  $^1\text{H}_\text{N}$  nuclei:

$$\frac{1}{T_1} = d^2 [J(\omega_H - \omega_N) + 3J(\omega_N) + 6J(\omega_H + \omega_N)] + c^2 [J(\omega_N)] \quad [1]$$

$$\begin{aligned} \frac{1}{T_2} = & \frac{d^2}{2} [4J(0) + J(\omega_H - \omega_N) + 3J(\omega_N) + 6J(\omega_H + \omega_N) + 6J(\omega_H)] \\ & + \frac{c^2}{6} [4J(0) + 3J(\omega_N)] + R_{ex} \end{aligned} \quad [2]$$

$$\text{NOE} = 1 + \frac{\gamma_H}{\gamma_N} d^2 [6J(\omega_H + \omega_N) - J(\omega_H - \omega_N)] T_1 \quad [3]$$

where  $d^2 = \frac{0.1\gamma_H^2\gamma_N^2\hbar^2}{4\pi^2 r_{\text{NH}}^6}$  and  $c^2 = \left(\frac{2}{15}\right)\gamma_N^2 H_0^2 (\sigma_1 - \sigma_\perp)^2$ ,  $\gamma_H$  is the proton magnetogyric ratio ( $2.68 \times 10^8 \text{ rad s}^{-1} \text{ T}^{-1}$ ),  $\gamma_N$  is the magnetogyric ratio of  $^{15}\text{N}$  ( $-2.71 \times 10^7 \text{ rad s}^{-1} \text{ T}^{-1}$ ),  $r_{\text{NH}}$  is the proton-nitrogen internuclear distance (1.02 Å),  $\sigma_1$  and  $\sigma_\perp$  are the principal components of the  $^{15}\text{N}$  chemical shift anisotropy (CSA) tensor ( $(\sigma_1 - \sigma_\perp)^2 = -160 \text{ ppm}$ ),  $\hbar$  is Planck's constant divided by  $2\pi$  ( $1.05 \times 10^{-34} \text{ J s}$ ),  $H_0$  is the strength of the magnetic field,  $\omega_N$  is the Larmor frequency of  $^{15}\text{N}$  and  $\omega_H$  is the Larmor frequency of  $^1\text{H}_\text{N}$ , and  $R_{ex}$  ( $\text{s}^{-1}$ ) accounts for

the contribution of potentially genuine microsecond to millisecond time-scale internal motions, in a phenomenological fashion. The second-rank chemical shift anisotropy tensor for the  $^{15}\text{N}$  nucleus was assumed to be axially symmetric, and parallel to the amide  $^{15}\text{N}$ - $^1\text{H}_\text{N}$  bond vector.

Backbone amide  $^{15}\text{N}$  NMR relaxation data were interpreted using the Lipari-Szabo model-free approach (41, 42), where the spectral density function  $J(\omega)$  is expressed as

$$J(\omega) = \frac{2}{5} \left[ \frac{S^2 \tau_m}{(1 + \omega^2 \tau_m^2)} + \frac{(1 - S^2) \tau}{(1 + \omega^2 \tau^2)} \right] \quad [4]$$

where  $\tau^{-1} = \tau_m^{-1} + \tau_e^{-1}$ ,  $S^2$ , the order parameter, accounts for the degree of spatial restriction for a backbone amide  $^{15}\text{N}$ - $^1\text{H}_\text{N}$  bond vector and ranges from 0 to 1, with 0 indicating completely unrestricted internal motion and 1 indicating completely restricted internal motion,  $\tau_m$  is the global molecular rotational correlation time,  $\tau_e$  is the correlation time for fast internal motions ( $\tau_e \ll \tau_m$ ). When internal motions occur on two different time-scales, equation 4 can be extended in a heuristic fashion:

$$J(\omega) = \frac{2}{5} \left[ \frac{S^2 \tau_m}{(1 + \omega^2 \tau_m^2)} + \frac{(S_f^2 - S^2) \tau_s'}{(1 + \omega^2 \tau_s'^2)} \right] \quad [5]$$

where  $S^2 = S_f^2 S_s^2$  and  $\tau_s' = \tau_s \tau_m / (\tau_s + \tau_m)$ .  $S_f^2$  describes the order parameter for fast picosecond internal motions,  $S_s^2$  is the order parameter for nanosecond time-scale internal motions faster than  $\tau_m$  but slower than  $\tau_e$ ,  $\tau_s$  is a correlation time for nanosecond time-scale internal motions (57, 58). The correlation time for picosecond internal motions is assumed not to contribute to relaxation.

The experimental backbone amide relaxation parameters for each residue were fit using five different models for the spectral density function ( $S^2$ - $\tau_m$ ,  $S^2$ - $\tau_m$ - $\tau_e$ ,  $S^2$ - $\tau_m$ - $R_{ex}$ ,  $S^2$ - $\tau_m$ - $\tau_e$ - $R_{ex}$  and a two time-scale model (57, 58)). For each residue, parameters for each model of the spectral density function were adjusted to minimize the objective function given by:

$$\chi^2 = \frac{(T_{1,c} - T_{1,e})^2}{\sigma_{T_1}^2} + \frac{(T_{2,c} - T_{2,e})^2}{\sigma_{T_2}^2} + \frac{(\text{NOE}_c - \text{NOE}_e)^2}{\sigma_{\text{NOE}}^2} \quad [6]$$

where the subscripts ‘c’ and ‘e’ indicate calculated and experimental values, respectively, and  $\sigma$  is the error of the individual relaxation parameters.

In order to improve the reliability of the fits for backbone amide NMR relaxation data of CTnC•2Ca<sup>2+</sup>•Rp40, the 500 and 600 MHz datasets were combined into a single set and fit using Bayesian statistical methods developed by Andrec *et al.* (59). One advantage of Bayesian statistical methods is that no particular model selection is made relative to the data. Furthermore, the analysis is not subject to convergence problems, which may arise when fitting using classical approaches. The data were fit to the  $S^2$ ,  $\tau_e$ ,  $R_{ex}$  model (with a  $\tau_m$  of 7.36 ns), which represents the most parameterized form of the single time-scale model. Given that  $R_{ex}$  is expected to increase with the square of the magnetic field for genuine chemical exchange,  $R_{ex}$  was restrained such that  $R_{ex}^{600} = (6/5)^2 R_{ex}^{500}$ .

The marginal density of  $S^2$  for the  $i^{\text{th}}$  residue,  $P(S^2 | R_i)$ , was calculated with the program Mathematica using the function NIntegrate. The limits of the integral for the calculation of  $P(S^2 | R_i)$  were set from 0 to 100 ms for  $\tau_e$  and from 0 to 5 s for  $R_{ex}$ . The prior probability,  $P(S^2, \tau_e, R_{ex}, \tau_m)$ , was taken to be equal to 1 in the region defined by  $0 \leq S^2 \leq 1$ ,  $\tau_e \geq 0$ ,  $R_{ex} \geq 0$ , and 0 outside this region. For each residue, the value of  $S^2$  was

incremented in steps of 0.05, and the marginal density of  $S^2, P(S^2 | R_i)$ , was calculated for a minimum of 21  $S^2$  values, 10 points around a central point, whose value had *a priori* been estimated from a classical fit using the  $S^2$ - $\tau_e$  model. For each residue,  $S^2$  and associated uncertainty was calculated by plotting  $P(S^2 | R_i)$  as a function of  $S^2$  and fitting the curve to a Gaussian distribution.

#### Structure-based thermodynamic calculations for Rp40 binding to CTnC•2Ca<sup>2+</sup>.

The STC program (available at <http://www.pence.ca/mc/comp/proj/stc/stc.html>) (60) was used to calculate the thermodynamics of binding of Rp40 to CTnC•2Ca<sup>2+</sup>. The crystal structures of TnC•2Ca<sup>2+</sup>•TnI<sub>1-47</sub> (34) and TnC•4Ca<sup>2+</sup> (11), both solved using rabbit skeletal TnC, not chicken skeletal TnC as in the current study, were used as reference structures for the protein-ligand and the free protein structure, respectively. The coordinates of the C-domain in both structures were isolated by removal of the coordinates corresponding to residues 1-85 of the N-domain. Residues 86-91 of CTnC, form an  $\alpha$ -helix in the original structure of TnC•4Ca<sup>2+</sup> (11), but were given an extended conformation using the InsightII program (61) in order to better reflect the lack of secondary structure in this region when CTnC is isolated from the N-domain.

The crystal structure of TnC•2Ca<sup>2+</sup>•TnI<sub>1-47</sub> only includes residues 3-33 of TnI (34), thus structure-based thermodynamic calculations may not properly reflect the correct binding situation with Rp40 using the X-ray coordinates. Residues 1-2 and 34-47 of TnI<sub>1-47</sub> are believed to be disordered in the crystal. Also, there is no structural data for unbound Rp40. Thus, it was assumed that residues 1-2 and 34-40 are unstructured in the free state, and therefore do not contribute to entropy changes upon binding and we have used the structure of TnI<sub>3-33</sub> from the crystal structure as a model for the free peptide structure to perform the structure-based thermodynamic calculations for estimating the

binding affinity of Rp40 to CTnC•2Ca<sup>2+</sup>. This assumption might not be valid since secondary structure prediction using the program Peptool (62) indicates that Rp40 is 95% helical, spanning residues 2 to 39. Additionally, binding of Rp40 to CTnC•2Ca<sup>2+</sup> may lead to structuring of the C-terminal end of the peptide, assuming that the C-terminal end of the peptide is unstructured in the free state, and this would contribute significantly to the thermodynamics of binding.

Details for the structure-based thermodynamic calculations are similar to those reported by Lavigne *et al.* (60). The standard entropy of dissociation  $\Delta S_d^0$  for protein dissociation can be expressed as the sum of the changes in the following: solvation entropy ( $\Delta S_{sol}$ ), conformational entropy ( $\Delta S_{conf}$ ), and overall rotational/translational entropy ( $\Delta S_{rt}$ ):

$$\Delta S_d^0 = \Delta S_{sol}(T) + \Delta S_{conf} + \Delta S_{rt} \quad [7]$$

The entropic contribution of solvation ( $\Delta S_{sol}$ ) is temperature-dependant and can be calculated from changes in accessible surface area of non-polar ( $\Delta ASA_{np}$ ) and polar residues ( $\Delta ASA_{pol}$ ) (60, 63). The change in conformational entropy ( $\Delta S_{conf}$ ) can be decomposed according to:

$$\Delta S_{conf} = \Delta S_{bu \rightarrow ex} + \Delta S_{ex \rightarrow u} + \Delta S_{bb} \quad [8]$$

where  $\Delta S_{bu \rightarrow ex}$  is the gain in conformational entropy for a side-chain upon exposure, following disordering of tertiary or quaternary interactions,  $\Delta S_{ex \rightarrow u}$  is the change in conformational entropy of the side chain corresponding to secondary structure unfolding, and  $\Delta S_{bb}$  corresponds to the gain in conformational entropy for unfolding of the backbone. For structure-based thermodynamic calculations we enhanced the STC program to allow the

inclusion of the contribution from backbone conformational entropy ( $\Delta S_{bb}$ ) as calculated from backbone amide  $^{15}\text{N}$  NMR relaxation data for the CTnC•2Ca $^{2+}$ •Rp40 complex. Due to a lack of experimental backbone amide  $^{15}\text{N}$  relaxation data for the peptide,  $\Delta S_{bb}$  for Rp40 was not included. The STC program was further adapted to incorporate the conformational entropy contribution of the side-chains ( $\Delta S_{ex \rightarrow u}$ ) based on the change of accessible surface area of side-chains ( $\Delta \text{ASA}_{sc}$ ) when the secondary structure unfolds according to:

$$\Delta S_{ex \rightarrow u} = \Delta \text{ASA}_{sc} / \Delta \text{ASA}_{sc}^* \cdot \Delta S_{ex \rightarrow u}^* \quad [9]$$

where  $\Delta \text{ASA}_{sc}^*$  and  $\Delta S_{ex \rightarrow u}^*$  are standard values reported by Miller *et al.* (64) and D'Aquino *et al.* (63).

**RESULTS***Structure of CTnC•2Ca<sup>2+</sup>•Rp40 determined by NMR spectroscopy.*

The 30 lowest-energy structures of CTnC•2Ca<sup>2+</sup> in the CTnC•2Ca<sup>2+</sup>•Rp40 complex were generated with 873 NOE-derived distances restraints, 86 dihedral angle restraints, and 11 distance restraints to the Ca<sup>2+</sup> ions, are shown superimposed in Figure III-1A. The average structure is compared to the C-domain of TnC in the X-ray structure of TnC•2Ca<sup>2+</sup>•TnI<sub>1-47</sub> (34) in Figure III-1B. The structural statistics for the ensemble of solution structures are given in Table III-2. The distribution of NOEs (intraresidue, sequential, medium, and long-range) and the backbone atom RMSD values relative to the average structure for each residue are provided in Figure III-2. Backbone RMSD values were calculated from the 30 lowest-energy structures after superimposition of the backbone atoms of residues 95-158 of CTnC in the CTnC•2Ca<sup>2+</sup>•Rp40 complex onto the average structure. The mean backbone RMSD to the average structure for residues 95-157 of CTnC•2Ca<sup>2+</sup> in the CTnC•2Ca<sup>2+</sup>•Rp40 complex is  $0.77 \pm 0.17$  using all residues in that region,  $0.63 \pm 0.14$  with residues having backbone RMSD < 1.0 and  $0.80 \pm 0.17$  with residues having backbone RMSD > 1.0. The quality of the ensemble of solution structures was analyzed with the program Procheck (54). 85% of the residues in well-defined regions were found to be in most favored  $\phi$  and  $\psi$  regions of the Ramachandran map, with another 15% in additional allowed regions. There were no NOE violations greater than 0.2 Å. A total of 7 different distance violations in the range 0.1 – 0.2 Å were detected in 7 different structures of the family of 30 structures, and therefore no structure had more than 1 distance violation. Only one dihedral violation > 1° in one structure was detected within the final ensemble of structures. The structure of CTnC•2Ca<sup>2+</sup> in complex with Rp40 is very similar to the

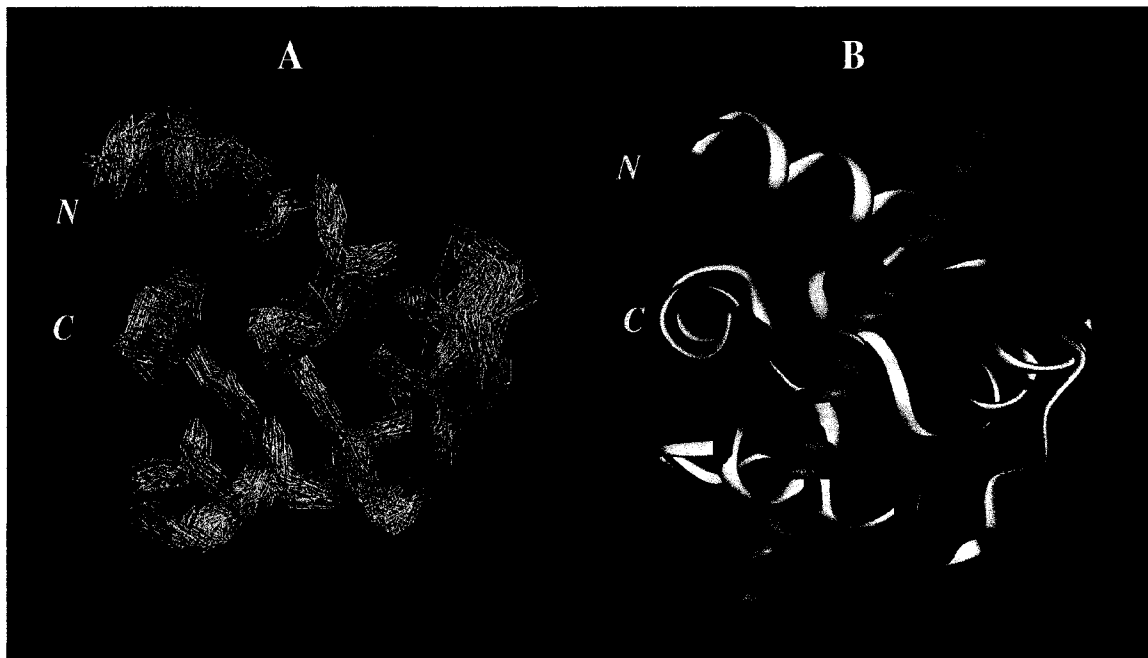


Figure III-1. A) Ensemble of 30 solution structures of CTnC•2Ca<sup>2+</sup> in the CTnC•2Ca<sup>2+</sup>•Rp40 complex superimposed onto the average structure of CTnC•2Ca<sup>2+</sup> (only residues 94-158 are shown). B) Ribbon representation of the minimized average solution structure of CTnC•2Ca<sup>2+</sup>•Rp40 (red) superimposed on the crystal structure of TnC•2Ca<sup>2+</sup>•TnI<sub>1-47</sub> (white). TnI<sub>1-47</sub> is shown in green (only residues 6-29 are shown). It was not possible to determine the structure of Rp40 within the CTnC•2Ca<sup>2+</sup>•Rp40 complex. The coordinates for the structure have been deposited in the RCSB Protein Data Bank (PDB accession code 1JC2).

C-domain of TnC•2Ca<sup>2+</sup> in complex with TnI<sub>1-47</sub> (34) as previously determined by X-ray crystallography (backbone RMSD of 1.0 upon superimposition of residues 95-158). A comparison of the angles between  $\alpha$ -helices within CTnC in the CTnC•2Ca<sup>2+</sup>•Rp40 complex and the CTnC•2Ca<sup>2+</sup>•TnI<sub>1-47</sub> complex in Table III-3 indicates that no significant change occurs in the degree of structural “openness”, or exposure of the hydrophobic patch of CTnC•2Ca<sup>2+</sup> upon binding of Rp40.

Table III-2. Structural statistics for CTnC•2Ca<sup>2+</sup> in the CTnC•2Ca<sup>2+</sup>•Rp40 complex.

NOE restraints	
Total	873
Intra-residue	447
Sequential ( i-j  = 1)	208
Medium range (2 ≤  i-j  ≤ 4)	140
Long range ( i-j  ≥ 5)	78
Dihedral Restraints	
$\phi$	33
$\psi$	32
$\chi_1$	21
Restraints violations	
Distance > 0.1 Å	7 (0.23/str.)
Dihedral > 1°	1 (0.03/str.)
RMSD to averaged structure (Å)	
Well defined regions <sup>a</sup> (N,C $\alpha$ ,C)	0.63 ± 0.14
All regions <sup>b</sup> (N,C $\alpha$ ,C)	0.77 ± 0.17
Heavy atoms	0.80 ± 0.17
E-helix (95-105)	0.36 ± 0.15
F-helix (116-124)	0.25 ± 0.15
G-helix (131-141)	0.26 ± 0.09
H-helix (151-158)	0.24 ± 0.06
$\beta$ -sheets (112-114, 148-150)	0.22 ± 0.08
Energies <sup>c</sup> (kcal mol <sup>-1</sup> )	
E <sub>total</sub>	348 ± 4
E <sub>NOE</sub>	1.4 ± 0.5
E <sub>Dihedral</sub>	0.03 ± 0.02
$\phi, \psi$ in core or allowed regions <sup>d</sup>	
Residues in most favored regions	84.6 %
Residues in additional allowed regions	14.9 %
Residues in generously allowed regions	0.3 %
Residues in disallowed regions	0.1 %

<sup>a</sup> Using residues 95-158 having backbone RMSD smaller than 1.00; <sup>b</sup> Using residues 95-158; <sup>c</sup> Using all residues in the 30 first lowest -energy structures; <sup>d</sup> Using residues 95-158 as determined by the program Procheck (54)

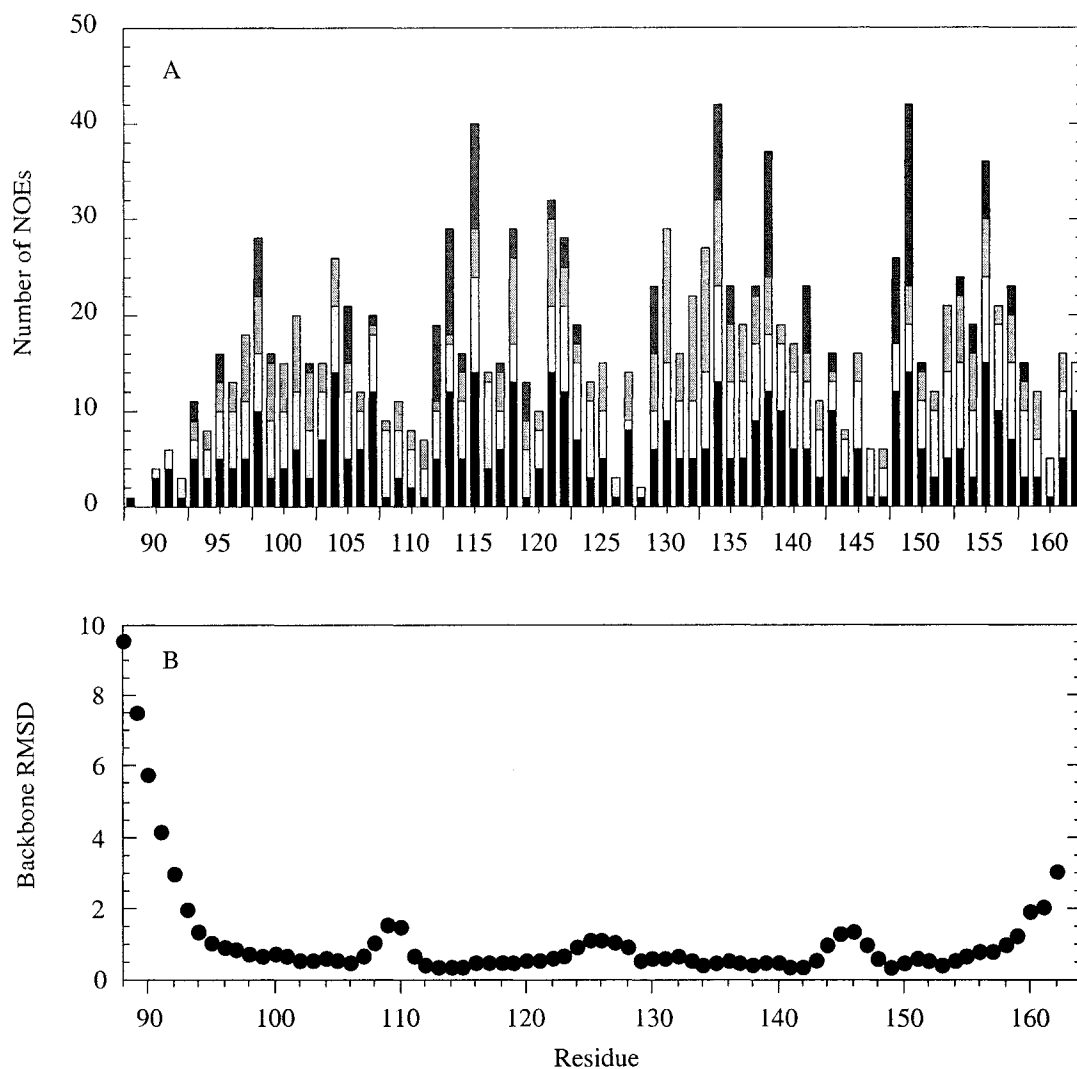


Figure III-2. A) Distribution of NOEs as a function of residue number. Intraresidue, sequential, medium, and long-range NOEs are identified by black, white, slight gray, and dark gray columns, respectively. B) Backbone RMSD for the ensemble of 30 solution structures with respect to the average coordinates.

Table III-3. Interhelical angles for CTnC•2Ca<sup>2+</sup> (skeletal and cardiac isoforms) free and bound to N-terminal TnI peptides.

Helix pair	bound			free		
	CTnC•2Ca <sup>2+</sup> •Rp40 <sup>a</sup>	cCTnC•2Ca <sup>2+</sup> •TnI <sub>33-80</sub> <sup>e</sup>	TnC•2Ca <sup>2+</sup> •TnI <sub>1-47</sub> <sup>b</sup>	TnC•4Ca <sup>2+</sup> <sup>d</sup>	cCTnC•2Ca <sup>2+</sup> <sup>f</sup>	TnC•2Ca <sup>2+</sup> <sup>c</sup>
E/F	93 ± 7	82 ± 4	100	89 ± 6	114 ± 4	108
E/G	132 ± 7	157 ± 7	134	137 ± 6	122 ± 5	124
E/H	112 ± 6	112 ± 3	116	110 ± 5	114 ± 5	122
F/G	127 ± 5	120 ± 5	122	133 ± 6	117 ± 3	126
F/H	41 ± 6	59 ± 4	47	36 ± 6	42 ± 4	33
G/H	115 ± 3	87 ± 5	107	107 ± 7	122 ± 4	111

<sup>a</sup> Using residues 95-105, 115-124, 131-141 and 151-158 for helices E, F, G and H, respectively. (pdb entry 1JC2)

<sup>b</sup> Using residues 91-103, 112-120, 128-138 and 148-155 for helices E, F, G and H, respectively. (pdb entry 1A2X) (34)

<sup>c</sup> Using residues 89-105, 115-125, 131-142 and 151-159 for helices E, F, G and H, respectively. (pdb entry 5TNC) (7)

<sup>d</sup> Using residues 96-105, 115-124, 131-141 and 151-157 for helices E, F, G and H, respectively. (pdb entry 1TNW) (9)

<sup>e</sup> Using residues 95-103, 114-123, 130-138 and 150-156 for helices E, F, G and H, respectively. (pdb entry 1GGS) (30, 31)

<sup>f</sup> Using residues 95-102, 114-123, 132-139 and 151-157 for helices E, F, G and H, respectively. (pdb entry 3CTN) (90)

*Backbone amide  $^{15}\text{N}$  relaxation data.*

Backbone amide  $^{15}\text{N}$  NMR relaxation data for CTnC•2Ca $^{2+}$  at 500 MHz were analyzed for 73 of 75 residues. The backbone resonances of M $^{88}$  and M $^{89}$  were not observed due to rapid exchange with water. Partial resonance overlap for residues S $^{94}$  and I $^{115}$ , E $^{96}$  and K $^{139}$ , V $^{129}$  and K $^{143}$ , in the  $^1\text{H}$ - $^{15}\text{N}$  HSQC NMR spectra restricted the relaxation data analysis for the [ $^{15}\text{N}$ ]-CTnC•2Ca $^{2+}$ •Rp40 complex to 67 residues at 500 MHz and 600 MHz. The  $^{15}\text{N}$ - $^1\text{H}_\text{N}$  backbone amide resonance of H $^{128}$  could not be assigned in the  $^1\text{H}$ - $^{15}\text{N}$  HSQC NMR spectra.

The experimental backbone amide  $^{15}\text{N}$  relaxation values for [ $^{15}\text{N}$ ]-CTnC•2Ca $^{2+}$  and [ $^{15}\text{N}$ ]-CTnC•Ca $^{2+}$ •Rp40 are shown in Figure III-3. The  $T_1$ ,  $T_2$  and NOE values of [ $^{15}\text{N}$ ]-CTnC•2Ca $^{2+}$  show similar patterns in comparison to the cardiac isoform [ $^{15}\text{N}$ ]-cNTnC•Ca $^{2+}$ , where large deviations from average values are observed at both the N and C-termini (the first and last residues of the E and H helix, respectively), as well as in the FG linker and the calcium binding sites III and IV, to a smaller extent. These regions correspond structurally to the A and D helices (E and H helices in the C-domain), the BC linker (FG linker in the C-domain) and Ca $^{2+}$  binding sites I and II (analogous to sites III and IV in the C-domain), which were shown to be the most flexible parts of [ $^{15}\text{N}$ ]-cNTnC•Ca $^{2+}$  (38). The average measured backbone relaxation parameters are listed in Table III-4. Residues whose internal motions affect their measured  $T_1$  values were excluded from the calculation of the averages, as determined using NOE criteria. For example, residues with NOE values smaller than 0.6 at 500 MHz and smaller than 0.65 at 600 MHz were rejected. For CTnC•2Ca $^{2+}$  in the absence of Rp40, this included residues 89-96, 98, 115, 124-130, 133, 138, and 159-162, which are located at the N- and C-termini, the FG linker, and the Ca $^{2+}$  binding sites. For CTnC•2Ca $^{2+}$ •Rp40, residues 89-93, 122, 123, 160 and 162 were excluded.

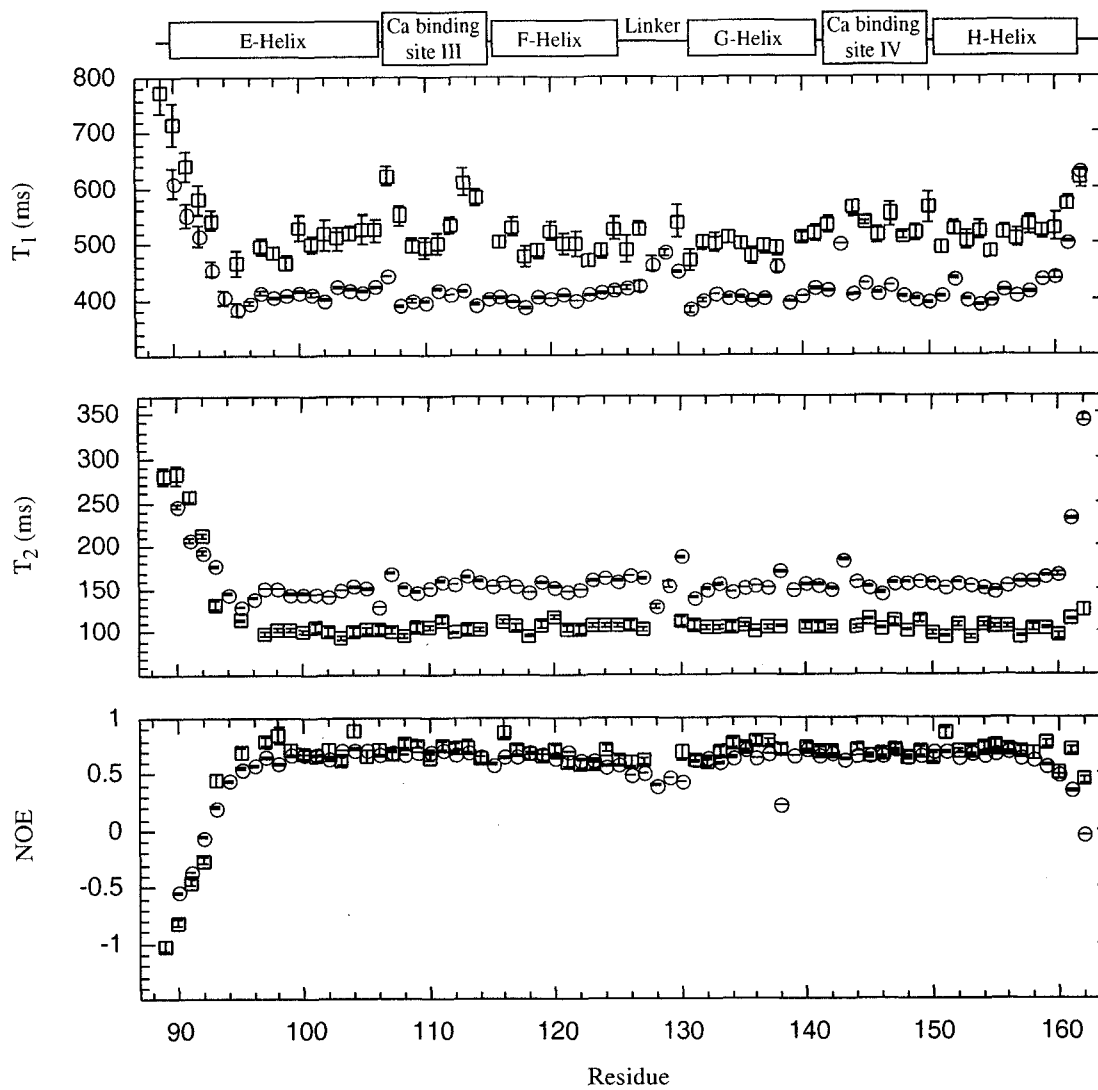


Figure III-3. Backbone amide <sup>15</sup>N NMR relaxation times for CTnC•2Ca<sup>2+</sup> (circles) at 1.33 mM and CTnC•2Ca<sup>2+</sup>•Rp40 (squares) at 0.33 mM and at a magnetic field strength corresponding to a <sup>1</sup>H Larmor frequency of 500 MHz.

Table III-4. Experimental backbone amide  $^{15}\text{N}$  relaxation parameters and overall rotational correlation times ( $\tau_m$ ) at 500 and 600 MHz for  $[^{15}\text{N}]\text{-CTnC}$  in the  $\text{Ca}^{2+}$ -saturated state and bound to Rp40<sup>a</sup>.

	$[^{15}\text{N}]\text{-CTnC}\cdot 2\text{Ca}^{2+}$	$[^{15}\text{N}]\text{-CTnC}\cdot 2\text{Ca}^{2+}\cdot \text{Rp40}$		
	(1.33 mM)	(1.33 mM)	(0.65 mM)	(0.33 mM)
$T_1^{500}$ (ms)	410 ± 18 (0.4 %)	571 ± 31 (0.9 %)	-	518 ± 32 (3.2 %)
$T_2^{500}$ (ms)	154 ± 8 (0.5 %)	96 ± 4 (1 %)	-	105 ± 5 (2.7 %)
$\text{NOE}^{500}$	0.67 ± 0.03 (0.7 %)	0.71 ± 0.03 (3 %)	-	0.71 ± 0.06 (8.4 %)
$T_1^{600}$ (ms)	-	694 ± 42 (0.81 %)	649 ± 40 (1.7 %)	639 ± 38 (1.9%)
$T_2^{600}$ (ms)	-	90 ± 5 (0.88 %)	101 ± 5 (1.1 %)	103 ± 5 (1.9 %)
$\text{NOE}^{600}$	-	0.75 ± 0.03 (2 %)	0.76 ± 0.04 (4 %)	0.75 ± 0.05 (6.0 %)
$T_1^{600}/T_1^{500}$	-	1.22 ± 0.03	-	1.24 ± 0.05
$T_2^{600}/T_2^{500}$	-	0.94 ± 0.03	-	0.98 ± 0.05
$T_1^{500}/T_2^{500}$	-	6.0 ± 0.5	-	4.9 ± 0.4
$T_1^{600}/T_2^{600}$	-	7.7 ± 0.7	-	6.3 ± 0.6
$\text{NOE}^{600}/\text{NOE}^{500}$	-	1.06 ± 0.05	-	1.06 ± 0.1
$\tau_m^{500}$ (ns)	4.78 ± 0.11	8.52 ± 0.24	-	7.56 ± 0.22
$\tau_m^{600}$ (ns)	-	8.25 ± 0.26	7.42 ± 0.30	7.32 ± 0.15

<sup>a</sup> The numbers in parentheses correspond to the average errors on individual  $T_1$ ,  $T_2$  and NOE values from which the average was calculated.

Figure III-3 indicates that binding of Rp40 perturbs the dynamics of CTnC by reducing backbone flexibility in the  $\text{Ca}^{2+}$  binding sites and more strikingly, at the C-terminal end of the H-helix, as judged by changes in the overall pattern of the  $T_1$ ,  $T_2$ , and NOE values plotted as a function of residue number. For  $[\text{}^{15}\text{N}]\text{-cNTnC}\cdot\text{Ca}^{2+}\cdot\text{Rp40}$  at 0.33 mM, a second dataset was collected at 600 MHz to evaluate the quality of the data. Figure III-4 illustrates different relaxation parameter ratios per residue for backbone amide  $^{15}\text{N}$  relaxation data collected at 500 and 600 MHz. The statistics for residues whose relaxation is not significantly affected by internal motions ( $\text{NOE}^{500} > 0.6$  and  $\text{NOE}^{600} > 0.65$ ) are listed in Table III-4. As expected, the average  $T_1^{600}/T_1^{500}$  ratio ( $1.24 \pm 0.05$ ) is  $> 1$ , but the pattern of the  $T_1$  data is constant throughout the sequence. Figure III-4b indicates that  $T_2^{500}$  and  $T_2^{600}$  are equivalent for the majority of residues. The average  $T_2^{600}/T_2^{500}$  ( $0.98 \pm 0.05$ ) is slightly less than 1, consistent with theoretical predictions that indicate that the contribution from dipole-dipole relaxation ( $T_{2,\text{DD}}$ ) should be almost identical at both fields, whereas chemical shift anisotropy will contribute more to  $T_2$  relaxation ( $T_{2,\text{CSA}}$ ) with increasing magnetic field strength. The  $T_1/T_2$  ratios from which  $\tau_m$  was calculated are plotted in Figure III-4c. The average  $\text{NOE}^{600}/\text{NOE}^{500}$  ratio ( $1.06 \pm 0.1$ ) is larger than 1, which is also consistent with theoretical predictions. Taking into account that the average  $S^2$  for structured regions in proteins is usually around 0.85 at  $\sim 30$  °C, and assuming isotropic overall rotational tumbling for a protein of 7.32 kDa and  $\tau_e$  ranging from 0 to 100 ps, the  $S^2$ - $\tau_m$ - $\tau_e$  model predicts that  $\text{NOE}^{600}/\text{NOE}^{500}$  ranges from 0.98 to 1.03, which is in agreement with the average experimental value.

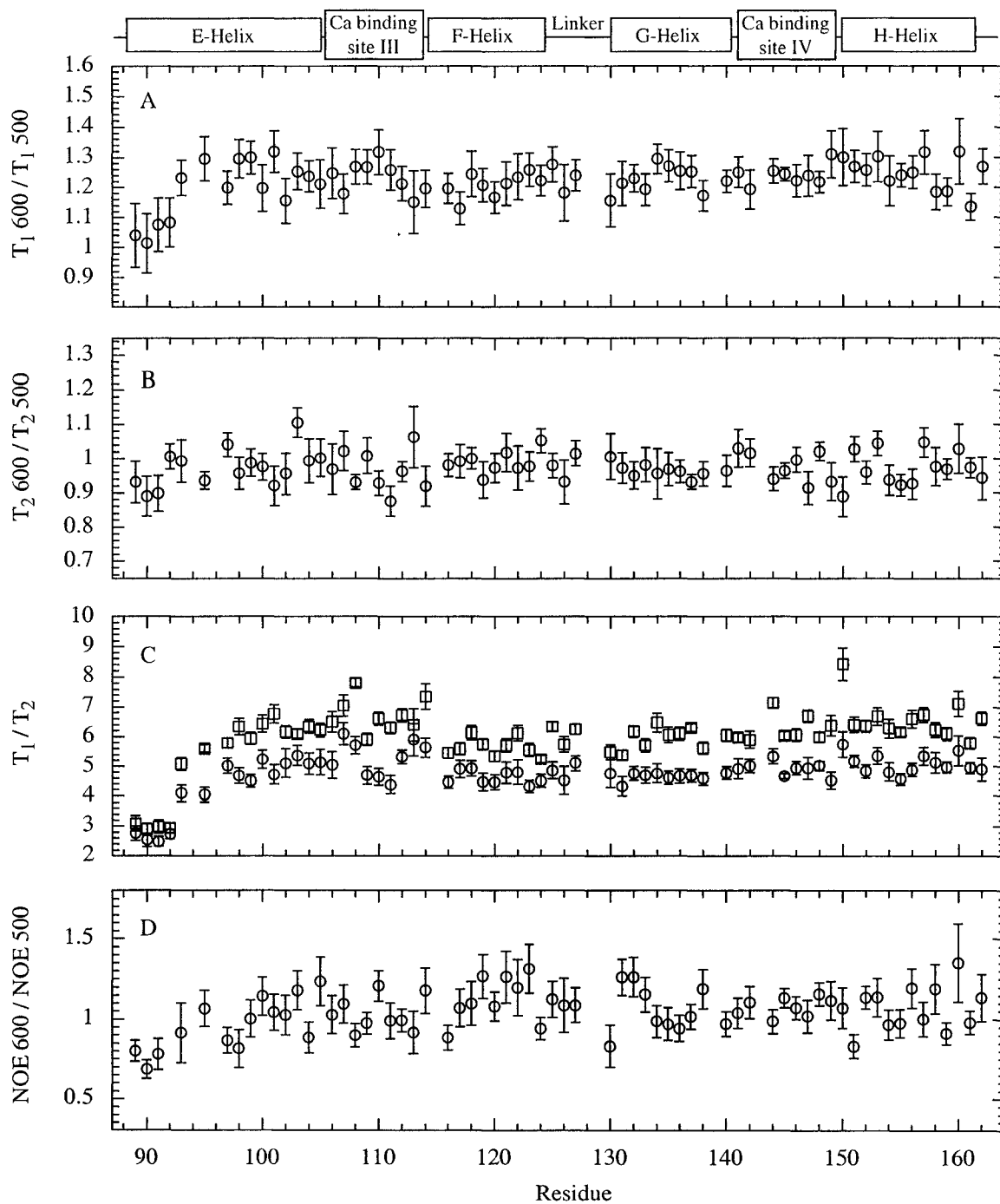


Figure III-4. Backbone amide  $^{15}\text{N}$  NMR relaxation time ratios for  $\text{CTnC}\cdot 2\text{Ca}^{2+}\cdot \text{Rp40}$  (circles) at 0.33 mM and at magnetic field strengths corresponding to  $^1\text{H}$  Larmor frequencies of 500 and 600 MHz. In C) the  $T_1/T_2$  ratios are identified by squares at 600 MHz and by circles at 500 MHz.

*Determination of overall rotational correlation time.*

Backbone amide  $^{15}\text{N}$  NMR relaxation data were interpreted using the Lipari-Szabo model-free approach (41, 42). From the normalized values of the principal axes of the inertia tensor, 1.6:1.07:1.0 for  $\text{CTnC}\cdot 2\text{Ca}^{2+}$  (7) (calculated from the crystal structure of  $\text{TnC}\cdot 4\text{Ca}^{2+}$ ) and 1.32:1.07:1.0 for  $\text{CTnC}\cdot 2\text{Ca}^{2+}\cdot \text{Rp40}$  (34) (using coordinates from the crystal structure of  $\text{TnC}\cdot 2\text{Ca}^{2+}\cdot \text{TnI}_{1-47}$ ), the overall rotational tumbling was initially assumed to be isotropic. The overall macromolecular correlation time ( $\tau_m$ ) was determined using two different methods. In the first approach,  $\tau_m$  was determined using an in-house-Mathematica script (P. Mercier) from the  $T_1/T_2$  ratio of residues falling within one standard deviation of the mean, after removal of residues whose NOE value was under a given threshold ( $\text{NOE}^{500} > 0.6$ ,  $\text{NOE}^{600} > 0.65$ ). This ensures the elimination of residues whose relaxation is affected by fast internal motions in the picosecond time-scale. The overall correlation time was determined by optimizing a  $\chi^2$  function given by:

$$\chi^2 = \sum_{i=1}^N \left( \frac{(T_1/T_2)_e - (T_1/T_2)_c}{\sigma_{T_1/T_2}} \right)^2 \quad [10]$$

over the N remaining residues. The 'e' and 'c' subscript indicate experimental values and predicted values, respectively.

In the second approach, individual residues were fit to the  $S^2$ - $\tau_m$ - $\tau_e$  model, including fitting the experimental NOE values, and where  $\tau_m$  was adjusted separately for each residue. A global  $\tau_m$  was obtained from the average  $\tau_m$  determined for each residue. Both methods gave identical results, summarized in Table III-4.

The global correlation  $\tau_m$  obtained for CTnC•2Ca<sup>2+</sup> in the absence of Rp40 ( $\tau_m = 4.8 \pm 0.1$  ns) is in good agreement with the expected value ( $\tau_m \sim 4.5$  ns) for isotropic tumbling on the basis of molecular weight ( $\tau_m(\text{ns}) \sim \text{M.W.}(\text{kDa})/2$ ). However, since the calculated  $\tau_m$  ( $8.52 \pm 0.24$  at 500 MHz and  $8.25 \pm 0.26$  at 600 MHz) for CTnC•2Ca<sup>2+</sup>•Rp40 at 1.33 mM was larger than the expected value (6.8 ns) assuming isotropic tumbling, and based on the molecular weight, the sample was diluted two-fold twice, and a full set of <sup>15</sup>N-*T*<sub>1</sub>, -*T*<sub>2</sub>, and {<sup>1</sup>H}-<sup>15</sup>N NOE data were acquired for each dilution. Figure III-5 shows the value of  $\tau_m$  as a function of concentration for the CTnC•2Ca<sup>2+</sup>•Rp40 complex.  $\tau_m$  was fit to a monomer-dimer equilibrium, giving a dimerization constant,  $K_{\text{dimer}} \sim 8.3$  mM. Thus, the percent dimer is estimated to be 20% at 1.33 mM, 12% at 0.65 mM, and 7% at 0.33 mM. The monomer-dimer equilibrium occurs in the fast exchange limit on the NMR time-scale, thus, at 0.33 mM, the peak intensities in the <sup>15</sup>N-*T*<sub>1</sub>, <sup>15</sup>N-*T*<sub>2</sub> <sup>1</sup>H-<sup>15</sup>N HSQC NMR spectra are heavily weighted towards the monomeric species, and were fit to a single exponential, two-parameter decay. The global  $\tau_m$  extracted from the experimental backbone amide <sup>15</sup>N relaxation data thus reflects the weighted average corresponding to the proportions of monomer and dimer, and is weighted mostly towards the monomeric  $\tau_m$ .

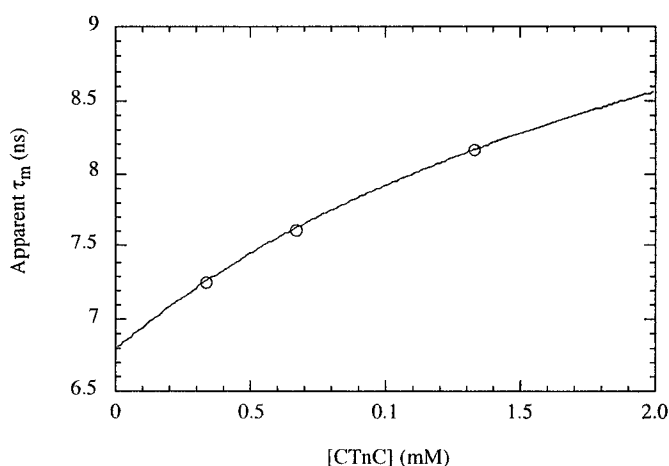


Figure III-5. Global rotational correlation time ( $\tau_m$ ) for CTnC•2Ca<sup>2+</sup>•Rp40 as a function of concentration. The curve was fit to a monomer-dimer equilibrium yielding a dimerization constant of 8.3 mM.

Using criteria established by Tjandra *et al.* (65), the rotational diffusion anisotropy of CTnC•2Ca<sup>2+</sup>•Rp40 was examined using residues not affected by fast picosecond and slower millisecond time-scale motions. An average  $T_1/T_2$  ratio was first calculated with residues having NOEs > 0.6 at 500 MHz and NOE > 0.65 at 600 MHz. Residues having a  $T_1/T_2$  ratio outside the range defined by the mean  $\pm$  1 standard deviation, or located in random-coil secondary structure elements and the  $\beta$ -sheets region, were excluded. The analysis was carried out using an in-house written program (39) with 25 and 31 residues at 500 MHz and 600 MHz, respectively. The degree of anisotropy was calculated with respect to isotropic, axially symmetric, and fully asymmetric rotational tumbling models using atomic coordinates derived from the 30 solution structures of CTnC•2Ca<sup>2+</sup>•Rp40 determined herein and the crystal structure of TnC•2Ca<sup>2+</sup>•TnI<sub>1-47</sub> (34). The statistics of the analysis are reported in Table III-5. Based on the observation that the degree of anisotropy was found to be small ( $D_{\parallel}/D_{\perp} \sim 1.1$ ) and that the improvement in  $\chi^2$  was not meaningful according to a statistical F-test, the model-free analysis was carried out under the assumption of isotropic rotational tumbling.

Table III-5. Rotational diffusion anisotropy for CTnC•2Ca<sup>2+</sup>•Rp40.

	(500 MHz) <sup>a</sup>	(500 MHz) <sup>b</sup>	(600 MHz) <sup>a</sup>	(600 MHz) <sup>b</sup>
$D_{\parallel}/D_{\perp}$	1.10 $\pm$ 0.03	1.14	1.10 $\pm$ 0.01	1.16
E <sup>c</sup>	20 $\pm$ 1	94.3	94 $\pm$ 2	12.8
E <sub>v</sub> <sup>c</sup>	0.94 $\pm$ 0.06	3.8	3.49 $\pm$ 0.08	0.68
F <sub>x</sub> <sup>c</sup>	2.7 $\pm$ 0.6	3.1	2.5 $\pm$ 0.3	6.8

<sup>a</sup> Using atom coordinates from the assemble of NMR structures

<sup>b</sup> Using atom coordinates from the X-ray structure of TnC•2Ca<sup>2+</sup>•TnI<sub>1-47</sub> (34).

<sup>c</sup> E, E<sub>v</sub> and F<sub>x</sub> are as defined in Table 2 of ref (39).

---

*Determination of backbone amide  $^{15}\text{N}$   $S^2$ .*

---

For  $[^{15}\text{N}]\text{-CTnC}\cdot 2\text{Ca}^{2+}$  in the absence of Rp40, the experimental relaxation parameters ( $^{15}\text{N}-T_1$ ,  $^{15}\text{N}-T_2$  and  $\{^1\text{H}\}\text{-}^{15}\text{N}$  NOE) for each residue were fit to 5 motional models, using the Lipari-Szabo model-free analysis as implemented in the program Tensor 2 (see Experimental Procedures) (66). The changes in  $S^2$  between  $\text{CTnC}\cdot 2\text{Ca}^{2+}$  and  $\text{CTnC}\cdot 2\text{Ca}^{2+}\cdot \text{Rp40}$  are discussed in detail below.

Due to the presence of dimer, the backbone amide  $^{15}\text{N}$  NMR relaxation data for the  $\text{CTnC}\cdot 2\text{Ca}^{2+}\cdot \text{Rp40}$  complex at 0.33 mM were fit using different methods. The 500 and 600 MHz datasets were first fit separately using the program Tensor 2 (66), using the model-free approach as described above. To verify the validity of the results, the two datasets were then combined and fit simultaneously using the  $S^2\text{-}\tau_m\text{-}\tau_e\text{-}R_{\text{ex}}$  model using Bayesian analysis (59). The details of the procedure utilized herein differ slightly from the original paper (see Experimental Procedures). For residues having  $P(S^2 | R_i)$  close to 0 or significantly lower than values observed for other residues, the experimental data were evaluated using a two time-scale model. The use of a two time-scale model greatly increased the value  $P(S^2 | R_i)$  for residues 89, 90, 91, 93, 95, 97, 103, 116, 117, 119, 120, 121, 123, 124, 126, 131, 133, 138 and 161. The  $S^2$  values determined by independent analysis of the two datasets at 500 and 600 MHz using the standard model-free approach within the Tensor 2 program, and the  $S^2$  values determined using Bayesian analysis for the combined data, are in agreement with each other. The results of Bayesian statistical analysis for extraction of  $S^2$ ,  $\tau_e$ , and  $R_{\text{ex}}$  values for  $\text{F}^{112}$  are presented in Figure III-6.

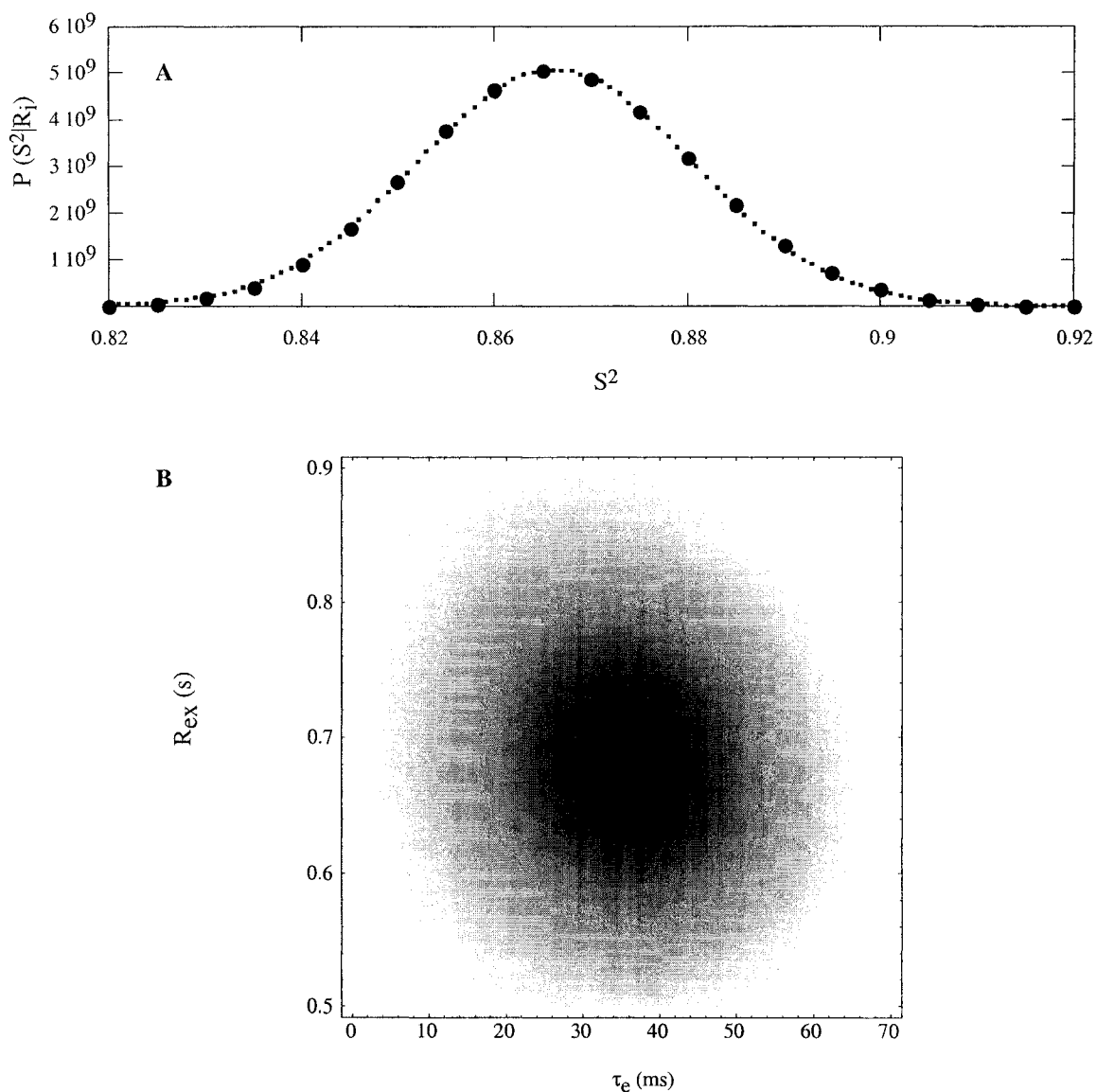


Figure III-6. A) Marginal density,  $P(S^2 | R_i)$ , as a function of  $S^2$  for residue  $F^{112}$  (filled circles: calculated values, dots: predicted value with a Gaussian distribution centered at  $S^2 = 0.866$  with  $\sigma = 0.014$ ). B) Surface density plot of the marginal density of  $S^2$  integrated over  $R_{ex}$  and  $\tau_e$  for residue  $F^{112}$  (plot was generated with  $S^2$  set to 0.866). The darker region represents  $(\tau_e, R_{ex})$  values that reproduce the experimental relaxation parameters with the highest probability.

Protein dimerization is known to result in values of  $S^2$  larger than the true values. Schurr *et al.* have shown, using simulated data, that the best-fit  $S^2$  values are closer to their actual values when  $\tau_m$  is allowed to float for each residue, rather than using a global correlation time for the entire protein (67). The fits were shown to be excellent for pure monomers or dimers, but the best-fit internal motion parameters were judged as being unreliable when the fraction of monomer was between 0.9 and 0.2. Given that the proportion of monomer is  $> 0.9$  for 0.33 mM CTnC•2Ca<sup>2+</sup>•Rp40, and the degree of rotational tumbling anisotropy is small compared to cases investigated by Schurr *et al.*, the 500 and 600 MHz relaxation datasets, as well as the data set that is a combination of the two, were fit to the  $S^2$ - $\tau_e$ - $\tau_m$  model using the protocol recommended by Schurr *et al.* (67), where  $\tau_m$  is independently evaluated for each residue. The  $S^2$  values were consistent with the ones determined by the standard protocol where a global  $\tau_m$  value is used, except for residues needing the two time-scale model or  $R_{ex}$  terms in order to properly fit the relaxation data. For this reason,  $S^2$  values obtained using a global  $\tau_m$  are reliable. The  $S^2$  values determined from the Bayesian analysis using the dataset formed by the union of the 500 and 600 MHz datasets were chosen as final values for CTnC•2Ca<sup>2+</sup>•Rp40. The combined data set is potentially more reliable because the fitted parameters are over-determined. The backbone amide  $S^2$  values obtained for CTnC•2Ca<sup>2+</sup> in the absence and in the presence of Rp40 are presented in Figure III-7A and III-7B, and the change in  $S^2$  for CTnC•2Ca<sup>2+</sup> on a per residue basis upon Rp40 binding is shown in Figure III-7C. The crystallographic B factors of the backbone nitrogen atoms of TnC in the TnC•2Ca<sup>2+</sup>•TnI<sub>1-47</sub> (34) complex are also shown in Figure III-7B, for qualitative comparison to  $S^2$  values. Intuitively, one might expect a correlation between backbone  $S^2$  and B factors, as conformational disorder in the crystal structure may be indicative of enhanced mobility in solution. However, the two parameters are not directly or linearly correlated (68).

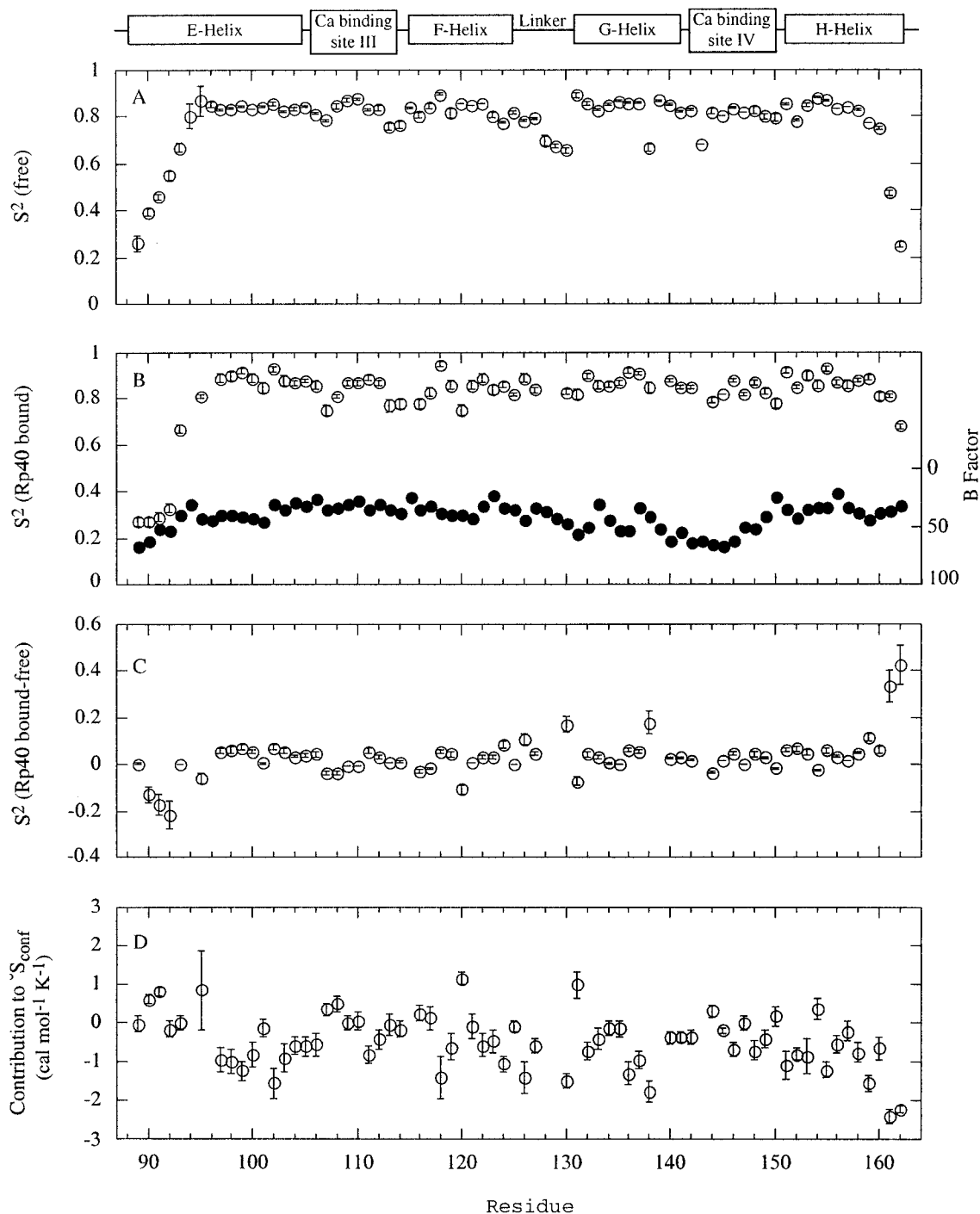


Figure III-7. Backbone amide  $^{15}\text{N}$   $S^2$  on a per residue basis for  $\text{CTnC}\cdot 2\text{Ca}^{2+}$  (squares) at 1.33 mM (A) and  $\text{CTnC}\cdot 2\text{Ca}^{2+}\cdot \text{Rp40}$  at 0.33 mM (B). Changes in  $S^2$  values for  $\text{CTnC}\cdot 2\text{Ca}^{2+}$  observed upon Rp40 binding (C). Contribution to conformational entropy on a per residue basis (D). The crystallographic B factors (filled circles) for the nitrogen atoms of TnC in the  $\text{TnC}\cdot 2\text{Ca}^{2+}\cdot \text{TnI}_{1-47}$  (34) complex are included in B) for qualitative comparison.

*Backbone conformational entropy changes upon peptide binding determined from changes in  $S^2$ .*

The free energy change ( $\Delta G$ ) associated with the binding of a ligand to a protein dictates the binding affinity. Changes in both enthalpy ( $\Delta H$ ), or structure, and entropy ( $\Delta S$ ), or dynamics, contribute to the energetics of the interaction.

Building on the work of Akke *et al.* (69), Yang and Kay (70) developed methodology to correlate changes in conformational entropy associated with bond vector fluctuations on the nanosecond-picosecond time scale with a two-state transition. From  $S^2$  values determined from backbone amide  $^{15}\text{N}$  NMR relaxation data of CTnC•2Ca $^{2+}$ , the contribution of conformational entropy can be calculated according to:

$$\frac{\Delta S_p(j)}{k} = \ln \left( \frac{3 - \sqrt{1 + 8S_b}}{3 - \sqrt{1 + 8S_a}} \right) \quad [11]$$

where  $k$  is Boltzmann's constant,  $\Delta S_p(j)$  is the entropy change associated with the  $j^{\text{th}}$  backbone  $^{15}\text{N}$ - $^1\text{H}_{\text{N}}$  vector,  $S_a$  and  $S_b$  are the square root of the Lipari-Szabo order parameter for state  $a$  (CTnC•2Ca $^{2+}$ ) and  $b$  (CTnC•2Ca $^{2+}$ •Rp40), respectively. The contribution to free energy from changes in backbone conformational entropy, on a per residue basis, was calculated from the changes in backbone amide  $^{15}\text{N}$   $S^2$  values and is shown in Figure III-7D. A value of  $9.6 \pm 0.7$  kcal mol $^{-1}$  ( $-\Delta S$ ) at 30 °C is obtained by summing the individual contribution for each residue. At present, it is not clear if the motion for each residue is independent, and given that NMR-derived  $S^2$  values are not sensitive to motions outside the picosecond-millisecond timescale, or translational motion, and that separability of these motions is assumed, the analysis of thermodynamics from NMR relaxation data can only be performed in a semi-quantitative manner. For this reason, the value of  $9.6 \pm 0.7$  kcal mol $^{-1}$  ( $-\Delta S$ ) for the change in backbone conformational entropy reported here is an

approximation, and should be viewed as an upper limit. Nevertheless, according to this result, the binding of Rp40 is entropically unfavorable, as the backbone of CTnC•2Ca<sup>2+</sup> ‘stiffens’ upon Rp40 binding. The observation that the backbone flexibility of CTnC•2Ca<sup>2+</sup> is reduced upon binding of Rp40 is in agreement with the common notion that binding should reduce flexibility, perhaps for the backbone of a protein, but particularly for the sidechains (71). Interestingly, cases have been reported in the literature where backbone amide <sup>15</sup>N S<sup>2</sup> values decrease upon ligand binding (72), which is counterintuitive (73), but may very well be a critically important factor in contributing favorably to ligand binding.

*Structure-based thermodynamic calculations for Rp40 binding to CTnC•2Ca<sup>2+</sup>.*

---

The entropic contribution to the thermodynamics of Rp40 binding to CTnC•2Ca<sup>2+</sup> was estimated from structure-based thermodynamic calculations using the program STC (60) (see Experimental Procedures). The results obtained from the structure-based thermodynamic calculations using STC (Table III-6), indicate that the binding of Rp40 to CTnC•2Ca<sup>2+</sup> is entropically favorable. This result highlights the importance of other entropic factors apart from changes in conformational entropy that play a role in determination of the binding affinity.

The total decrease in accessible surface area for non-polar residues ( $\Delta\text{ASA}_{\text{np}}$ ) upon complex formation is > 200% than the decrease of accessible surface area of polar residues ( $\Delta\text{ASA}_{\text{pol}}$ ), and therefore, solvation entropy is the dominant term in equation [12]. Upon Rp40 binding, the total hydrophobic surface area of the CTnC•2Ca<sup>2+</sup> decreases by 771 Å<sup>2</sup> from 3053 to 2282 Å<sup>2</sup>. Since the structure of CTnC•2Ca<sup>2+</sup> in the CTnC•2Ca<sup>2+</sup>•Rp40 complex is similar to the structure of unbound CTnC•2Ca<sup>2+</sup>, most of the diminution in accessible non-polar surface area is attributable to a reduction of the size of the hydrophobic patch of CTnC•2Ca<sup>2+</sup> that is formed by the core residues of CTnC•2Ca<sup>2+</sup>. The hydrophobic

Table III-6A. Change in accessible surface area for polar ( $\Delta\text{ASA}_{\text{pol}}$ ) and non-polar residues ( $\Delta\text{ASA}_{\text{np}}$ ) upon Rp40 binding to  $\text{CTnC}\cdot 2\text{Ca}^{2+}$  used for structure-based thermodynamic calculations.

Species	$\Delta\text{ASA}_{\text{pol}}$ ( $\text{\AA}^2$ )	$\Delta\text{ASA}_{\text{np}}$ ( $\text{\AA}^2$ )
Rp40	222	740
$\text{CTnC}\cdot 2\text{Ca}^{2+}$	513	771
Total	735	1511

\* positive values indicate a decrease in accessible surface area upon complex formation.

Table III-6B. Structure-based thermodynamic analysis for binding of Rp40 to  $\text{CTnC}\cdot 2\text{Ca}^{2+}$ .

$\Delta\text{Cp}_{\text{bind}}$ ( $\text{cal mol}^{-1} \text{K}^{-1}$ )	489
$\Delta\text{H}_{\text{bind}}$ ( $\text{kcal mol}^{-1}$ )	4.33
$\Delta\text{S}_{\text{bind}}$ ( $\text{cal mol}^{-1} \text{K}^{-1}$ )	42
$\Delta\text{S}_{\text{sol}}$ ( $\text{cal mol}^{-1} \text{K}^{-1}$ )	144
$\Delta\text{S}_{\text{rt}}$ ( $\text{cal mol}^{-1} \text{K}^{-1}$ )	-8
$\Delta\text{S}_{\text{conf}}$ ( $\text{cal mol}^{-1} \text{K}^{-1}$ )	-94
$\Delta\text{S}_{\text{bu}\rightarrow\text{ex}}$ ( $\text{cal mol}^{-1} \text{K}^{-1}$ )	-47
$\Delta\text{S}_{\text{ex}\rightarrow\text{u}}$ ( $\text{cal mol}^{-1} \text{K}^{-1}$ )	-15
$\Delta\text{S}_{\text{bb}}$ ( $\text{cal mol}^{-1} \text{K}^{-1}$ )	-32
$-\text{T}\Delta\text{S}_{\text{bind}}$ ( $\text{kcal mol}^{-1}$ )	-12.68
$\Delta\text{G}_{\text{bind}}$ ( $\text{kcal mol}^{-1}$ )	-8.35
$\text{K}_{\text{a}}$ ( $\text{MM}^{-1}$ )	1.05
$\text{K}_{\text{d}}$ ( $\mu\text{M}$ )	0.95

patch of CTnC•2Ca<sup>2+</sup> forms the binding interface for Rp40. The positive gain in entropy achieved by burying hydrophobic residues upon complex formation ( $\Delta S_{sol} = 144 \text{ cal mol}^{-1} \text{ K}^{-1}$ ) compensates, in large part, for the cost associated with a decrease in backbone flexibility ( $\Delta S_{bb} = -31.9 \pm 2.3 \text{ cal mol}^{-1} \text{ K}^{-1}$  for CTnC•2Ca<sup>2+</sup> upon Rp40 binding from backbone amide <sup>15</sup>N relaxation data) and the burial of side-chains ( $\Delta S_{bu \rightarrow ex} = -47 \text{ cal mol}^{-1} \text{ K}^{-1}$ ). The structure-based thermodynamic calculations were carried out with coordinates for TnI<sub>1-33</sub> in the free state taken from the crystal structure. This yields a dissociation constant of 0.95  $\mu\text{M}$ . This value is close to the value determined by following chemical shift changes of the backbone amide <sup>1</sup>H-<sup>15</sup>N resonances of CTnC•2Ca<sup>2+</sup> upon titration with Rp40 peptide ( $2 \pm 1 \mu\text{M}$ ) (22). If the last 7 residues of Rp40 do not indeed contribute significantly to the binding of Rp40, the agreement between the two results suggest that the structure of Rp40 does not change considerably upon binding.

Interestingly, structure-based thermodynamic calculations performed without considering the contribution of backbone and side-chain conformational entropy lead to a binding constant of  $2 \times 10^{-9} \mu\text{M}$ , which is unrealistically tight binding, thus emphasizing the importance of including the contribution of conformational entropy when performing structure-based thermodynamic calculations for high affinity protein-ligand complexes. In light of the extent of the decrease in flexibility for the backbone of CTnC•2Ca<sup>2+</sup> upon binding to Rp40, and the importance for calculation of thermodynamic parameters, it is likely that conformational entropy changes for the peptide backbone upon complex formation with CTnC•2Ca<sup>2+</sup> also play an important role. A decrease in TnI<sub>3-33</sub> backbone flexibility upon binding to CTnC•2Ca<sup>2+</sup> would contribute to an increase in the value of the dissociation constant (0.95  $\mu\text{M}$ ).

## DISCUSSION

The general role of TnC in regulating muscle contraction is now quite well understood (1-6). However, no high-resolution structures of TnC with TnI and/or TnT are available, and the specific interactions occurring between members of the troponin complex during different stages of muscle contraction still need to be elucidated. In the past few years, we have successfully determined the solution structures of TnC in various states, and in complex with different peptides of TnI, for both the skeletal and cardiac isoform (9, 10, 25, 28, 48, 49). These studies, coupled with backbone and side-chain NMR relaxation data (38, 39), have given us insight into the mechanism and energetics of  $\text{Ca}^{2+}$  and peptide binding to TnC. The collective efforts of different research groups have allowed for the construction of different models for the interactions between different components of the TnI•TnC•TnT ternary complex (21, 74, 75).

The  $\text{Ca}^{2+}$ -binding sites of the C-domain of TnC are believed to be always occupied by either  $\text{Mg}^{2+}$  or  $\text{Ca}^{2+}$  under physiological conditions. Due to the high affinity for  $\text{Ca}^{2+}$  for the ion binding sites of the C-domain of TnC, this domain is believed to assume a structural role within intact muscle. On the other hand, the N-terminal domain of TnC does not bind metal ions in the resting state of intact muscle. In addition, association of  $\text{Ca}^{2+}$  with the N-terminal  $\text{Ca}^{2+}$ -specific regulatory sites of TnC is thought to give rise to conformational changes within TnC that essentially constitutes the molecular switch that initiates muscle contraction. Classification of the roles for the C- and N-terminal domains as structural and regulatory, respectively, may not reflect the genuine physiological roles of the two domains of TnC within intact muscle. Functional studies by the Hodges group have indicated that CTnC may participate to some extent in the regulation of muscle contraction by interacting with different regions of TnI in the resting and contracted states (21). Following  $\text{Ca}^{2+}$  binding to NTnC, the inhibitory TnI peptide, TnI<sub>96-115</sub>, is believed to switch binding partners,

from actin to TnC, thus removing the steric block on actin, and allowing for myosin binding and completion of the power stroke.

A key component of the inhibitory mechanism of contraction is arguably the binding location and structure of TnI<sub>96-115</sub>. A study involving following <sup>1</sup>H chemical shift perturbations by NMR led to the proposal that TnI<sub>104-115</sub> forms a short helix, distorted around two central proline residues, and interacts with the hydrophobic patch on CTnC•2Ca<sup>2+</sup> (76). The CTnC•2Ca<sup>2+</sup>•TnI<sub>104-115</sub> complex was subsequently modeled with the short TnI peptide anchored in the hydrophobic pocket of TnC (18). A more recent study using both NMR and CD spectroscopic data by Trewella *et al.* indicates that TnI<sub>104-115</sub> adopts an extended conformation when bound to TnC (33).

Recently, it has been demonstrated that while TnI<sub>116-131</sub> is bound to NTnC, TnI<sub>95-115</sub> can displace the Rp40 peptide from TnC when it is bound to CTnC•2Ca<sup>2+</sup> in intact TnC (21). This result is somewhat contradictory to a previous study by the same research group, which shows that Rp40 can prevent intact TnI binding to intact TnC (36). It was proposed that TnI<sub>116-131</sub> modulates TnI<sub>96-115</sub> binding to TnC and that it might contribute to displacement of Rp40 from TnC. Based on this hypothesis, the authors proposed that the hydrophobic patch of CTnC alternately binds TnI<sub>96-115</sub> in the presence of Ca<sup>2+</sup>-saturated NTnC, and the N-terminal region of TnI (Rp40) under conditions of low Ca<sup>2+</sup> concentration. However, more recent studies question this model for the TnI-TnC interaction, as detailed in the following discussion. First, in a previous paper (22), we showed that in the absence of NTnC and TnI<sub>116-131</sub>, the binding affinity of Rp40 for TnC was ~ 24 times larger than that of TnI<sub>96-115</sub> ( $K_{d-Rp40} = 2 \pm 1 \mu\text{M}$ ,  $K_{d-TnI96-115} = 47 \pm 7 \mu\text{M}$ ). By following chemical shift changes with <sup>1</sup>H-<sup>15</sup>N HSQC NMR spectroscopy, we have also suggested that the peptides share common binding sites on TnC. However, the changes in backbone amide <sup>1</sup>H-<sup>15</sup>N chemical shifts induced by TnI<sub>96-115</sub> binding did not indicate that

the peptide is bound within the hydrophobic patch of TnC (18), but rather, binds across the top of one end of the hydrophobic patch. On the other hand, the location of Rp40 deduced from backbone amide  $^1\text{H}$ - $^{15}\text{N}$  chemical shift mapping matches perfectly the binding site of TnI<sub>1-47</sub> as determined by X-ray diffraction (34). Our results also clearly demonstrate that Rp40 prevents TnI<sub>96-115</sub> from binding to CTnC•2Ca<sup>2+</sup> and completely displaces TnI<sub>96-115</sub> from CTnC•2Ca<sup>2+</sup>.

Fluorescence resonance energy transfer and chemical photo-crosslinking studies with the intact binary complex TnI•TnC and the intact ternary complex (TnI•TnC•TnT) have led to important conclusions that support a structural role for the N-terminal region of TnI rather than a functional role (75, 77). The distance between residue 6 of TnI and residue 89 of TnC was shown to be Ca<sup>2+</sup> independent, which is not consistent with a regulatory mechanism involving movement of Rp40 in and out of the hydrophobic patch of CTnC•2Ca<sup>2+</sup>.

In this manuscript we present the solution structure of CTnC•2Ca<sup>2+</sup> bound to Rp40 and examine changes induced in backbone dynamics of CTnC•2Ca<sup>2+</sup> upon Rp40 binding. The superimposition of the 30 lowest total energy structures determined by NMR, presented in Figure III-1A, shows that the structure is well-defined from residues 94 to 160, with somewhat increased RMSD deviations from the average backbone atom positions for the two Ca<sup>2+</sup>-binding loops. As shown in Figure III-2A, the smaller number of distance restraints per residue for regions close to the Ca<sup>2+</sup>-binding loops are likely to be responsible for increased RMSD values in these regions, rather than increased backbone flexibility in comparison to the rest of the protein (see Figure III-7B). The linker region is relatively well-defined compared to regions of secondary structure for CTnC•2Ca<sup>2+</sup> bound to Rp40. As shown in Figure III-1B, the average structure calculated from a family of 30 structures (Figure III-1A), is similar to that for the crystal structure TnC•2Ca<sup>2+</sup>•TnI<sub>1-47</sub>. As reported in

Table III-3, both the structure of CTnC•2Ca<sup>2+</sup>•Rp40 determined herein and the structure of TnC•2Ca<sup>2+</sup>•TnI<sub>1-47</sub> determined by X-ray crystallography show a similar degree of openness, interpreted in terms of interhelical angles between helices within CTnC. The E/F helices are slightly more closed in comparison to the solution structure of TnC•4Ca<sup>2+</sup> determined by NMR (9), but show similar interhelical angles with respect to the structure of TnC•2Ca<sup>2+</sup> determined by X-ray crystallography (7). Whereas a slight opening of CTnC was observed in the cardiac isoform of the CTnC•2Ca<sup>2+</sup>•TnI<sub>33-80</sub> complex with respect to the CTnC•2Ca<sup>2+</sup> (30, 31), there is no significant change in the degree of structural openness for the skeletal isoform of CTnC•2Ca<sup>2+</sup> upon Rp40 binding reported herein.

The structure and sites of interaction of Rp40 bound to CTnC•2Ca<sup>2+</sup> could not be determined in the present study. Attempts to obtain <sup>1</sup>H chemical shift assignments for the bound peptide through the use of 2D <sup>13</sup>C/<sup>15</sup>N filtered experiments were unrewarding, primarily due to the fact that the peptide resonances were overlapping. However, the unassigned <sup>1</sup>H<sub>α</sub> chemical shifts (78, 79) are indicative of an α-helical structure for Rp40 in the complex, in agreement with X-ray structural studies (34). Moreover, the residues for which NOE peaks observed in the simultaneous 3D <sup>13</sup>C,<sup>15</sup>N-NOESY-HSQC experiment that did not have the expected symmetrical cross-peak and therefore expected to be NOEs between protein and peptide, also correspond to residues that are in close proximity to the peptide in the crystal structure of TnC•2Ca<sup>2+</sup>•TnI<sub>1-47</sub> (34). Figure III-8 shows strip plots for residue I<sup>104</sup> from TnC taken from the simultaneous 3D <sup>13</sup>C,<sup>15</sup>N-NOESY-HSQC experiment. I<sup>104</sup> is within 2 Å of 47 different peptide protons in the X-ray structure, and is therefore a key residue in terms of number of contacts with the target protein TnC (the analogous residue from rabbit TnC is I<sup>101</sup> in rabbit TnC used for the crystal structure determination (34)). For CTnC, I<sup>104</sup> is also the residue for which the largest number of <sup>1</sup>H-<sup>1</sup>H contacts to Rp40 could be observed by NMR in this study, followed by residues T<sup>125</sup> and V<sup>161</sup> from TnC. Residue T<sup>125</sup>, corresponding to S<sup>122</sup> in rabbit TnC, is not a key residue

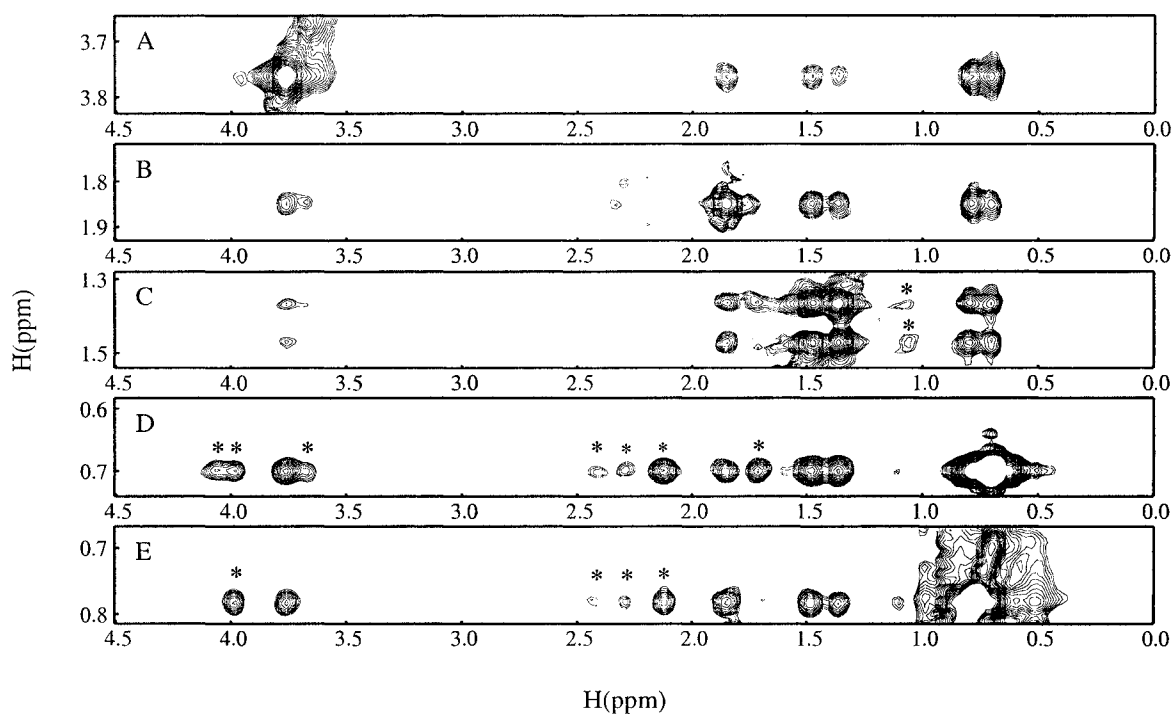


Figure III-8. Strip plots taken at side-chain  $^{13}\text{C}$  chemical shifts for residue  $\text{I}^{104}$  (A:  $^{13}\text{C}_{\alpha}$ , B:  $^{13}\text{C}_{\beta}$ , C:  $^{13}\text{C}_{\gamma}$ , D and E:  $^{13}\text{C}_{\delta 1, \delta 2}$ ) from the  $^{13}\text{C}$  part of the simultaneous 3D  $^{13}\text{C}, ^{15}\text{N}$ -NOESY-HSQC spectrum. Stars indicate cross-peaks lacking symmetry related cross-peaks, and therefore are likely to be NOE contacts between  $\text{CTnC}\cdot 2\text{Ca}^{2+}$  and Rp40.

involved in the binding of  $\text{TnI}_{1-47}$  to TnC, as judged by number of proton contacts observed between this residue and TnC in the crystal structure. The side-chain of  $\text{V}^{161}$  of TnC participates in several hydrophobic contacts, and this has implications for changes in the flexibility for the C-terminal H- helix.

Backbone amide  $^{15}\text{N}$  relaxation measurements indicate concentration dependent dimerization for the  $\text{CTnC}\cdot 2\text{Ca}^{2+}\cdot \text{Rp40}$  complex in solution. Unlike  $\text{NTnC}\cdot 2\text{Ca}^{2+}$  that tends to self-associate at mM concentrations (80),  $\text{CTnC}\cdot 2\text{Ca}^{2+}$  is not known to self-associate in solution. Interestingly, the structure of calmodulin in complex with the peptide

$\text{GAD}_p$  ( $\text{CAM}\cdot(\text{GAD}_p)_2$ ) has been recently reported ((81)). The complex was shown to dimerize *via*  $\text{GAD}_p$  and possessed a two-fold symmetry axis, with two  $\text{GAD}_p$  peptides units forming a cross. Analogous to the peptide-induced dimerization observed for calmodulin, we propose that Rp40 may be responsible for the observed dimerization of the  $\text{CTnC}\cdot 2\text{Ca}^{2+}\cdot\text{Rp40}$  complex, possibly *via* helix-helix interactions of Rp40 with itself. Whilst the structural determination of  $\text{CTnC}\cdot 2\text{Ca}^{2+}$  in the  $\text{CTnC}\cdot 2\text{Ca}^{2+}\cdot\text{Rp40}$  complex was performed at a concentration that would include 20% dimer, the  $^1\text{H}$ - $^1\text{H}$  NOE data do not indicate the presence of a dimeric form.

The binding of Rp40 to  $\text{CTnC}\cdot 2\text{Ca}^{2+}$  results in a decrease in flexibility for CTnC, particularly at the C-terminal end of the H-helix, where the largest changes in  $S^2$  (see Figure III-7C) and backbone amide  $^1\text{H}$ - $^{15}\text{N}$  chemical shifts (22) are observed. The tight binding of Rp40 to  $\text{CTnC}\cdot 2\text{Ca}^{2+}$  contributes to a reduction in conformational space that is sampled by the extreme C-terminal end of  $\text{CTnC}\cdot 2\text{Ca}^{2+}$ . The flexibility of the linker between the F and G helices is also reduced, and this was also observed in a study with the corresponding cardiac complex ( $\text{cCTnC}\cdot 2\text{Ca}^{2+}\cdot\text{TnI}_{33-80}$  (30, 31)). However, with the cardiac isoform, the flexibility at the C-terminal end of cCTnC was not affected by the binding of N-terminal TnI peptides ( $\text{TnI}_{33-80}$ ,  $\text{TnI}_{1-80}$ ), in the absence (30, 31) and the presence of the cardiac-specific TnI 33 residue N-terminal extension (82). This might be the result of a difference in the binding affinities of the cardiac TnI peptide compared to the skeletal TnI peptide to their corresponding CTnC isoforms, and could also indicate slight differences in CTnC residues between the two isoforms that make contact to their respective TnI peptides.

The contribution of pico to nanosecond time-scale backbone amide  $^{15}\text{N}$ - $^1\text{H}$  bond vector motions to conformational entropy, as derived from NMR relaxation data, indicates that binding of Rp40 to  $\text{CTnC}\cdot 2\text{Ca}^{2+}$  is an entropically unfavorable event. However, approximation of other entropic factors (such as solvation entropy) with structure-based

thermodynamic calculations using the program STC, indicates that the overall change in entropy upon binding is positive and overcomes the enthalpy term, which is positive and unfavorable. Thus, structure-based thermodynamic calculations indicate that the binding reaction is driven by a large positive increase in solvation entropy, as hydrophobic side-chains are buried upon complex formation. The large decrease in accessible hydrophobic surface area for non-polar residues appears to be a critical factor determining the thermodynamics governing binding of Rp40 to CTnC•2Ca<sup>2+</sup>, at least when estimating thermodynamic parameters from structure. The large increase in solvent entropy is responsible, in part, for overcoming the entropic penalty associated with a reduction in flexibility for the backbone of CTnC•2Ca<sup>2+</sup> (measured here using backbone amide <sup>15</sup>N NMR relaxation measurements), and potential decreases in flexibility for the protein and peptide side-chains upon formation of the CTnC•2Ca<sup>2+</sup>•Rp40 complex.

**REFERENCES**

1. Squire, J. M., and Morris, E. P. (1998) *Faseb J* 12, 761-71.
2. Filatov, V. L., Katrukha, A. G., Bulargina, T. V., and Gusev, N. B. (1999) *Biochemistry (Mosc)* 64, 969-85.
3. Finn, B. E., and Drakenberg, T. (1999) *Adv. Inorg. Chem.* 46, 441-494.
4. Gergely, J. (1998) *Adv. Exp. Med. Biol.* 453, 169-76.
5. Perry, S. V. (1999) *Mol. Cell. Biochem.* 190, 9-32.
6. Gordon, A. M., Homsher, E., and Regnier, M. (2000) *Physiol. Rev.* 80, 853-924.
7. Herzberg, O., and James, M. N. G. (1988) *J. Mol. Biol.* 203, 761-779.
8. Satyshur, K. A., Rao, S. T., Pyzalska, D., Drendal, W., Greaser, M., and Sundaralingam, M. (1988) *J. Biol. Chem.* 263, 1628-1647.
9. Slupsky, C. M., and Sykes, B. D. (1995) *Biochemistry* 34, 15953-15964.
10. Gagné, S. M., Tsuda, S., Li, M. X., Smillie, L. B., and Sykes, B. D. (1995) *Nat. Struct. Biol.* 2, 784-789.
11. Houdusse, A., Love, M. L., Dominguez, R., Grabarek, Z., and Cohen, C. (1997) *Structure* 5, 1695-711.
12. Kretsinger, R. H. (1976) *Annu Rev Biochem* 45, 239-66.
13. Szczesna, D., Guzman, G., Miller, T., Zhao, J., Farokhi, K., Ellemberger, H., and Potter, J. D. (1996) *J. Biol. Chem.* 271, 8381-8386.
14. Gagné, S. M., Li, M. X., McKay, R. T., and Sykes, B. D. (1998) *Biochem. Cell Biol.* 76, 301-12.
15. Olah, G. A., Rokop, S. E., Wang, C.-L. A., Blechner, S. L., and Trewhella, J. (1994) *Biochemistry* 33, 8233-8239.
16. Olah, G. A., and Trewhella, J. (1994) *Biochemistry* 33, 12800-12806.
17. Stone, D. B., Timmins, P. A., Schneider, D. K., Krylova, I., Ramos, C. H. I., Reinach, F. C., and Mendelson, R. A. (1998) *J. Mol. Biol.* 281, 689-704.
18. Ngai, S.-M., Sönnichsen, F. D., and Hodges, R. S. (1994) *J. Biol. Chem.* 269, 2165-2172.
19. Pearlstone, J. R., and Smillie, L. B. (1995) *Biochemistry* 34, 6932-6940.
20. Pearlstone, J. R., and Smillie, L. B. (1997) *Biophys. J.* 72, A331.
21. Tripet, B. P., Van Eyk, J. E., and Hodges, R. S. (1997) *J. Mol. Biol.* 271, 728-750.
22. Mercier, P., Li, M. X., and Sykes, B. D. (2000) *Biochemistry* 39, 2902-11.
23. McKay, R. T., Tripet, B. P., Pearlstone, J. R., Smillie, L. B., and Sykes, B. D. (1999) *Biochemistry* 38, 5478-89.
24. McKay, R. T., Tripet, B. P., Hodges, R. S., and Sykes, B. D. (1997) *J. Biol. Chem.* 272, 28494-28500.
25. McKay, R. T., Pearlstone, J. R., Corson, D. C., Gagné, S. M., Smillie, L. B., and Sykes, B. D. (1998) *Biochemistry* 37, 12419-30.
26. McKay, R. T. (1999) in *Department of Biochemistry*, Univ. of Alberta, Edmonton.
27. Li, M. X., Spyropoulos, L., and Sykes, B. D. (1998) *Biophys. J.* 74, A51.
28. Li, M. X., Spyropoulos, L., and Sykes, B. D. (1999) *Biochemistry* 38, 8289-98.
29. Finley, N., Abbott, M. B., Abusamhadneh, E., Gaponenko, V., Dong, W., Gasmi-Seabrook, G., Howarth, J. W., Rance, M., Solaro, R. J., Cheung, H. C., and Rosevear, P. R. (1999) *FEBS Lett* 453, 107-12.
30. Gasmi-Seabrook, G. M., Howarth, J. W., Finley, N., Abusamhadneh, E., Gaponenko, V., Brito, R. M., Solaro, R. J., and Rosevear, P. R. (1999) *Biochemistry* 38, 14432.
31. Gasmi-Seabrook, G., Howarth, J. W., Finley, N., Abusamhadneh, E., Gaponenko, V., Brito, R. M., Solaro, R. J., and Rosevear, P. R. (1999) *Biochemistry* 38, 8313-8322.

32. Abbott, M. B., Dvoretzky, A., Gaponenko, V., and Rosevear, P. R. (2000) *FEBS Lett* 469, 168-72.
33. Hernández, G., Blumenthal, D. K., Kennedy, M. A., Unkefer, C. J., and Trewhella, J. (1999) *Biochemistry* 38, 6911-6917.
34. Vassilyev, D. G., Takeda, S., Wakatsuki, S., Maeda, K., and Maeda, Y. (1998) *Proc. Natl. Acad. Sci. U.S.A.* 95, 4847-52.
35. Syska, H., Wilkinson, J. M., Grand, R. J. A., and Perry, S. V. (1976) *Biochem. J.* 153, 375-387.
36. Ngai, S.-M., and Hodges, R. S. (1992) *J. Biol. Chem.* 267, 15715-15720.
37. Farrow, N. A., Muhandiram, R., Singer, A. U., Pascal, S. M., Kay, C. M., Gish, G., Shoelson, S. E., Pawson, T., Forman-Kay, J. D., and Kay, L. E. (1994) *Biochemistry* 33, 5984-6003.
38. Spyrapoulos, L., Gagné, S. M., Li, M. X., and Sykes, B. D. (1998) *Biochemistry* 37, 18032-18044.
39. Gagné, S. M., Tsuda, S., Spyrapoulos, L., Kay, L. E., and Sykes, B. D. (1998) *J. Mol. Biol.* 278, 667-86.
40. Spyrapoulos, L., Gagné, S. M., Gronwald, W., Kay, L. E., and Sykes, B. D. (1998) in *Proceedings for The International School of Structural Biology and Magnetic Resonance, 3rd Course on Protein Dynamics, Function and Design* (Jardetzky, O., and LeFeure, F. J., Eds.) pp 1471-62, Plenum Press, New York, NY.
41. Lipari, G., and Szabo, A. (1982) *J. Am. Chem. Soc.* 104, 4546-4559.
42. Lipari, G., and Szabo, A. (1982) *J. Am. Chem. Soc.* 104, 4559-4570.
43. Yang, D., Mok, Y. K., Forman-Kay, J. D., Farrow, N. A., and Kay, L. E. (1997) *J. Mol. Biol.* 272, 790-804.
44. Gagné, S. M., Tsuda, S., Li, M. X., Chandra, M., Smillie, L. B., and Sykes, B. D. (1994) *Prot. Sci.* 3, 1961-1974.
45. Li, M. X., Gagné, S. M., Tsuda, S., Kay, C. M., Smillie, L. B., and Sykes, B. D. (1995) *Biochemistry* 34, 8330-8340.
46. Delaglio, F., Grzesiek, S., Vuister, G. W., Zhu, G., Pfeifer, J., and Bax, A. (1995) *J. Biomol. NMR* 6, 277-293.
47. Johnson, B. A., and Blevins, R. A. (1994) *J. Biomol. NMR* 4, 603-614.
48. Gagné, S. M., Li, M. X., and Sykes, B. D. (1997) *Biochemistry* 36, 4386-4392.
49. Spyrapoulos, L., Li, M. X., Sia, S. K., Gagné, S. M., Chandra, M., Solaro, R. J., and Sykes, B. D. (1997) *Biochemistry* 36, 12138-12146.
50. Kuboniwa, H., Grzesiek, S., Delaglio, F., and Bax, A. (1994) *J. Biomol. NMR* 4, 871-8.
51. Clore, G. M., Bax, A., and Gronenborn, A. M. (1991) *J. Biomol. NMR* 1, 13-22.
52. Kuszewski, J., Qin, J., Gronenborn, A. M., and Clore, G. M. (1995) *J. Magn. Reson. B* 106, 92-6.
53. Brünger, A. T. (1992) *X-PLOR Version 3.1 A system for X-ray Crystallography and NMR*, Yale University Press, New Haven.
54. Laskowski, R. A., MacArthur, M. W., Moss, D. S., and Thornton, J. M. (1993) *J. Appl. Crystallogr.* 26, 283-290.
55. Garrett, D. S., Powers, R., Gronenborn, A. M., and Clore, G. M. (1991) *J. Magn. Reson.* 95, 214-220.
56. Abragam, A. (1961) *Principles of Nuclear Magnetism*, Vol. 32, Oxford University Press, Toronto.
57. Clore, G. M., Szabo, A., Bax, A., Kay, L. E., Driscoll, P. C., and Gronenborn, A. M. (1990) *J. Am. Chem. Soc.* 112, 4989-4991.
58. Clore, G. M., Driscoll, P. C., Wingfield, P. T., and Gronenborn, A. M. (1990) *Biochemistry* 29, 7387-401.
59. Andrec, M., Montelione, G. T., and Levy, R. M. (1999) *J. Magn. Reson.* 139, 408-21.

60. Lavigne, P., Bagu, J. R., Boyko, R., Willard, L., Holmes, C. F., and Sykes, B. D. (2000) *Protein Sci.* 9, 252-64.
61. Molecular Simulations Inc. (1995), San Diego.
62. Wishart, D. S., Stothard, P., and Van Domselaar, G. H. (2000) *Methods Mol. Biol.* 132, 93-113.
63. D'Aquino, J. A., Gomez, J., Hilser, V. J., Lee, K. H., Amzel, L. M., and Freire, E. (1996) *Proteins* 25, 143-56.
64. Miller, S., Janin, J., Lesk, A. M., and Chothia, C. (1987) *J. Mol. Biol.* 196, 641-56.
65. Tjandra, N., Wingfield, P., Stahl, S., and Bax, A. (1995) *J. Am. Chem. Soc.* 117, 12562-12566.
66. Dosset, P., Hus, J. C., Blackledge, M., and Marion, D. (2000) *J. Biomol. NMR* 16, 23-8.
67. Schurr, J. M., Babcock, H. P., and Fujimoto, B. S. (1994) *J. Magn. Reson. B* 105, 211-24.
68. Powers, R., Clore, G. M., Garrett, D. S., and Gronenborn, A. M. (1993) *J. Magn. Reson. B* 101, 325-327.
69. Akke, M., Bruschiweiler, R., and Palmer, A. G. (1993) *J. Am. Chem. Soc.* 115, 9832-9833.
70. Yang, D., and Kay, L. E. (1996) *J. Mol. Biol.* 263, 369-382.
71. Lee, A. L., Kinnear, S. A., and Wand, A. J. (2000) *Nat. Struct. Biol.* 7, 72-7.
72. Zidek, L., Novotny, M. V., and Stone, M. J. (1999) *Nat. Struct. Biol.* 6, 1118-21.
73. Forman-Kay, J. D. (1999) *Nat. Struct. Biol.* 6, 1086-7.
74. Tung, C. S., Wall, M. E., Gallagher, S. C., and Trewthella, J. (2000) *Protein Sci.* 9, 1312-26.
75. Luo, Y., Wu, J. L., Li, B., Langsetmo, K., Gergely, J., and Tao, T. (2000) *J. Mol. Biol.* 296, 899-910.
76. Campbell, A. P., and Sykes, B. D. (1991) *J. Mol. Biol.* 222, 405-421.
77. Luo, Y., Leszyk, J., Li, B., Gergely, J., and Tao, T. (2000) *Biochemistry* 39, 15306-15.
78. Wishart, D. S., and Sykes, B. D. (1994) *Methods Enzymol.* 239, 363-392.
79. Wishart, D. S., Sykes, B. D., and Richards, F. M. (1991) *J. Mol. Biol.* 222, 311-333.
80. Spyrapoulos, L., Gagné, S. M., and Sykes, B. D. (2001) in *Proceedings for the International School of Structural Biology and Magnetic Resonance, 4th Course on Protein Dynamics, Function and Design* (Jardetzky, O., and Lefevre, J. F., Eds.) pp 37-44, Plenum Press, New York, NY, USA.
81. Yap, K. L., Yuan, T., Vogel, H. J., and Ikura, M. (2001) in *Keystone Symposia - Frontiers of NMR in Molecular Biology VII*.
82. Gaponenko, V., Abusamhadneh, E., Abbott, M. B., Finley, N., Gasmi-Seabrook, G., Solaro, R. J., Rance, M., and Rosevear, P. R. (1999) *J. Biol. Chem.* 274, 16681-4.
83. Muhandiram, D. R., and Kay, L. E. (1994) *J. Magn. Reson. B* 103, 203-216.
84. Kay, L. E., Keifer, P., and Saarinen, T. (1992) *J. Am. Chem. Soc.* 114, 10663-10665.
85. Zhang, O., Kay, L. E., Olivier, J. P., and Forman-Kay, J. D. (1994) *J. Biomol. NMR* 4, 845-858.
86. Kay, L. E., Xu, G. Y., Singer, A. U., Muhandiram, D. R., and Forman-Kay, J. D. (1993) *J. Magn. Reson. B* 101, 333-337.
87. Pascal, S. M., Muhandiram, D. R., Yamazaki, T., Forman-Kay, J. D., and Kay, L. E. (1994) *J. Magn. Reson. B* 103, 197-201.
88. Archer, S. J., Ikura, N. I., Torchia, D. A., and Bax, A. (1991) *J. Magn. Reson.* 95, 636-641.
89. Ogura, K., Terasawa, H., and Inagaki, F. (1996) *J. Magn. Reson. B* 112, 63-8.
90. Sia, S. K., Li, M. X., Spyrapoulos, L., Gagné, S. M., Liu, W., Putkey, J. A., and Sykes, B. D. (1997) *J. Biol. Chem.* 272, 18216-18221.

## CHAPTER IV

*The NMR Structure of a Bifunctional Rhodamine Labeled N-Domain of Troponin C  
Complexed with the Regulatory 'Switch' Peptide from Troponin I:  
Implications for in Situ Fluorescence Studies in Muscle Fibers*

### INTRODUCTION

Regulation of contraction in skeletal and cardiac muscle involves a series of protein conformational changes and protein-protein interactions that follow intracellular calcium release from the sarcoplasmic reticulum. Troponin C (TnC) is the protein of the troponin complex that binds the released calcium. The other two components, TnI and TnT, contribute to the regulation of muscle contraction by sterically blocking and weakening myosin head binding sites on actin in the absence of calcium and by stabilizing the binding of the whole troponin complex to actin [for reviews see (1-6)].

TnC is composed of two  $\text{Ca}^{2+}$ -binding domains (designated N and C for the N- and C-domains, respectively) joined by a linker (7-9). Each domain consists of two helix-loop-helix EF hand motifs (designated I and II in the N-domain, III and IV in the C-domain) typically found in  $\text{Ca}^{2+}$ -binding proteins. In the skeletal isoform of TnC (sTnC) each domain binds two calcium ions, whereas in the cardiac isoform (cTnC) the N-domain has a defunct site and only binds a single calcium. Crystal and solution structures of skeletal TnC in the apo and calcium-saturated states have revealed large modifications in interhelical angles upon calcium binding for both domains (10), which result in the exposure of hydrophobic surface clefts that are important sites of interaction with

different portions of TnI (11-15). The C-domain of TnC (CTnC) is normally thought to play a structural role as it is occupied by calcium or magnesium under all physiological conditions. In contrast, the N-domain of TnC (NTnC) plays a major regulatory role as occupancy of the  $\text{Ca}^{2+}$ -binding site(s) varies over the physiological range of  $\text{Ca}^{2+}$  concentration.

Interactions between TnC, TnI, and TnT are central to understanding the regulation of muscular contraction. As yet, there is no high-resolution structure of the TnC•TnI•TnT complex, although it has been studied by neutron diffraction methods (16-18), and a preliminary X-ray structure of TnC complexed with peptides of TnI and TnT has been presented (19). Several groups have relied on binary complexes of TnC with different fragments of TnI to identify the TnC binding sites and evaluate binding affinities. Three distinct regions of TnI have been particularly studied: the N-terminus (11, 14, 20, 21), the inhibitory region (20, 22-24), and the switch region (12, 25, 26). A peptide comprising the first 40 N-terminal residues of TnI (Rp40) binds strongly ( $K_d < 1 \mu\text{M}$ ) to the hydrophobic pocket of CTnC (20). Much consideration has been given to the inhibitory region of TnI (residues 96-115; TnI<sub>p</sub>) since it was first identified by Syska et al. (27), as it contains the shortest TnI portion required for inhibition of actomyosin ATPase activity. It was proposed that TnI<sub>p</sub> was bound to the hydrophobic pocket of CTnC, sharing similar binding sites and competing with Rp40 (25, 28). However, recent studies have shown that Rp40 dominates the interaction and likely remains bound to the C-domain in a  $\text{Ca}^{2+}$ -independent fashion (20, 29, 30). The structure of TnI<sub>p</sub> bound to the C-domain has been determined (D. A. Lindhout and B. D. Sykes, unpublished results).

The switch peptide, TnI<sub>115-131</sub>, was shown to enhance the binding affinity of TnI<sub>p</sub> to TnC in a Ca<sup>2+</sup>-dependent manner (25) and was proposed to bind to the hydrophobic pocket of NTnC, which was later corroborated using NMR chemical shift mapping (26). The switch peptide has been modeled as an  $\alpha$  helix bound to the hydrophobic pocket of NTnC, which positioned TnI<sub>p</sub> in the vicinity of the linker between the C- and the N-domains of TnC (14). The switch peptide has also been modeled as an  $\alpha$  helix anchored to the hydrophobic groove of NTnC, with TnI<sub>p</sub> as a  $\beta$ -hairpin (31).

NMR studies of cardiac TnC and TnI have given structural insight into the distinctive kinetics and thermodynamics of mechanisms responsible for activation of cardiac relative to skeletal muscle (32, 33). Unlike sNTnC, conformational opening of cNTnC does not occur upon calcium binding (34) but rather follows binding of the switch peptide (residues 147-163 for the cardiac isoform). Residues 151-156 of the cardiac switch peptide adopt a helical conformation in the NMR structure of cNTnC•Ca<sup>2+</sup>•TnI<sub>147-163</sub>, (12), while residues 147-149, although in contact with the protein, do not have well-defined secondary structure, and residues 157-163 appear disordered because of a lack of intramolecular NOEs for this region. Several hydrophobic interactions involving TnI residues I148, M153, M154, L157, and L158 stabilize the switch peptide in the hydrophobic pocket of cNTnC. The dissociation constant of the cardiac switch peptide ( $154 \pm 10 \mu\text{M}$ ) was 6 times weaker than that of the skeletal isoform ( $24 \pm 4 \mu\text{M}$ ), highlighting differences in the regulation of cardiac muscle.

NMR and X-ray crystallographic studies on isolated components or partial complexes of troponin have brought insights into its general structural organization, but may reveal only part of the role of troponin, as important interactions might be missing. Neutron scattering and electron microscopic studies have probed the structure of TnC as part of larger complexes, enhancing our understanding of muscle regulation at a higher level of molecular organization. For instance, electron microscopy studies on reconstituted thin filaments have brought direct evidence for the location of tropomyosin and troponin on actin (35-37), but the orientation of TnC relative to the actin fiber axis has yet to be determined.

Techniques based on fluorescence polarization have been developed to investigate the orientation and motions of proteins in their cellular environment (38, 39), and we have applied these methods to study how TnC is orientated in skeletal muscle and how domains of TnC respond to changes in the physiological state (40). In that study, a bifunctional rhodamine (BR) probe was covalently attached to several mutants of TnC, each containing a pair of cysteines that are seven residues apart on an  $\alpha$  helix and with their  $\beta$ -carbon atoms in solvent-exposed positions. The BR-labeled TnC mutants were each exchanged into permeabilized skinned muscle fibers, and analysis of their fluorescence polarization permitted determination of the angle of individual  $\alpha$ -helices of TnC with respect to a cellular reference frame, in that case the actin filament axis. When data from several probes are combined the information content is greater, leading to a more complete description of protein domain orientations within the cellular reference frame.

The present study contributes in two ways to the above approach. First, the *in situ* studies require atomic resolution structures determined *in vitro*, which can then be orientated within the cellular reference frame using the fluorescence polarization data. We here determined by NMR spectroscopy the structure of a mutant sNTnC labeled with bifunctional rhodamine in a complex with  $\text{Ca}^{2+}$  ions and the TnI switch peptide. In this work, BR was [ $^{13}\text{C}$ ]labeled in its two methyl groups for NMR distance and dynamic measurements. A benefit of this structure, the first that contains the switch peptide, is that it allowed Ferguson et al. (40) to orient the peptide as well as TnC in the cellular frame. It is also important to know whether introduction of the BR probe perturbs the protein structure. The incorporation of fluorescent probes on biomolecules is very common, but their effects on the tertiary structure of their hosts are rarely assessed. One way to study this is through cellular functional assays. In the case of TnC, the ability of the BR-labeled TnC mutants to mimic the muscle relaxation-activation response to  $\text{Ca}^{2+}$  was verified (40). The present more direct approach reveals the structure of sNTnC with the BR-probe attached. It also addresses the question of whether the attachment of the probe alters the protein globally or in the vicinity of the label, and whether the rhodamine label makes interactions with the protein, specifically with the hydrophobic region exposed upon calcium binding. We call the structure  $\text{sNTnC}\cdot 2\text{Ca}^{2+}\cdot \text{TnI}_{115-131}\cdot \text{BR}_{56-63}$ , since it contains the N-domain of skeletal TnC, two  $\text{Ca}^{2+}$  ions, the switch peptide of TnI, and the BR probe attached to cysteine residues 56 and 63 (mutated from E56 and E63).

**EXPERIMENTAL PROCEDURES***Synthesis of [<sup>13</sup>C<sub>2</sub>]Bisidoacetamidorhodamine.*

3-Methoxybenzenesulfonamide (*41*) (11.01 g, 41.88 mmol) was added in five portions to a suspension of NaH (1.675 g, 41.9 mmol) (60% dispersion in mineral oil) in dry DMF (53 mL) under nitrogen at 20 °C. The mixture was stirred for 0.5 h and cooled to 10 °C. [<sup>13</sup>C]Iodomethane (5.0 g, 35.2 mmol; Goss Scientific, Essex, U.K.) in dry DMF (13.7 mL) was added dropwise over 15 min. The solution was allowed to warm to room temperature and stirred for 2.5 h. Water was added carefully to destroy any unreacted NaH and the solution was evaporated under vacuum to remove most of the DMF. The syrupy residue was partitioned between ether and water and the ether extract was washed with 1 M NaOH, H<sub>2</sub>O (×3) and brine, dried over anhydrous Na<sub>2</sub>SO<sub>4</sub> and evaporated to give 3-methoxy-*N*-[<sup>13</sup>C]methylbenzenesulfonamide as a solid (9.33 g, 95.7% yield) that was suitable for use in the subsequent synthesis as previously described for the nonisotopic rhodamine (*41*). The <sup>1</sup>H NMR spectrum of the final [<sup>13</sup>C<sub>2</sub>]bisidoacetamidorhodamine was identical to that of the unlabeled compound, except that the *N*-methyl signal appeared as a doublet,  $J_{\text{C,H}}$  137.5 Hz, and the signal at  $\delta$  3.54 for the methylene groups adjacent to the nitrogens bearing the isotopic methyls was perturbed from the clean triplet of the nonisotopic compound on account of a small 3-bond coupling.

---

*Mutagenesis of sNTnC.*

---

The expression vector (Pet3a) for chicken skeletal NTnC was kindly provided by Dr. L. B. Smillie (University of Alberta, Canada). A double cysteine mutant of sNTnC (E56C, E63C) was obtained using the QuikChange site-directed mutagenesis kit (Stratagene Europe) and expressed in *Escherichia coli* BL21 DE3 cells. The entire gene was sequenced (Oswel, Southampton, UK).

The expression of sNTnC was carried out overnight in minimal medium at 35 °C. The medium consisted of M9 salts as described by Maniatis et al. (42) with  $(\text{NH}_4)_2\text{SO}_4$  replacing  $\text{NH}_4\text{Cl}$ . Each 1 L of medium at pH 7.5 contained 6 g of  $\text{Na}_2\text{HPO}_4$ , 3 g of  $\text{KH}_2\text{PO}_4$ , 0.5 g of  $\text{NaCl}$  and 2 g of  $^{15}\text{N}(\text{NH}_4)_2\text{SO}_4$  to which was added 2 mL of mineral mixture (1 M  $\text{MgSO}_4$ , 0.1 mM  $\text{FeCl}_3$ , and 12.5 mM  $\text{ZnSO}_4$ ), 1 mL of 100 mM  $\text{CaCl}_2$ , and 1 mL of vitamin mixture (0.1 mg/100 mL each of biotin, choline chloride, folic acid, niacinamide, D-pantothenic acid and pyridoxal chloride, 0.5 g of thiamine, and 0.01 g/100 mL riboflavin, all in  $\text{H}_2\text{O}$ ).  $^{13}\text{C}$ Glucose (3 g) dissolved in 20 mL of  $\text{H}_2\text{O}$  was added with ampicillin (100 mg/L).  $^{15}\text{N}(\text{NH}_4)_2\text{SO}_4$  (98.0 atom %) and  $[\text{U-}^{13}\text{C}]$ glucose (99.0 atom %) were purchased from Goss Scientific, Essex, U.K.

---

*Preparation of sNTnC.*

---

The mutant sNTnC was purified from 4 L of bacterial lysate on a 100 mL Q-Sepharose fast-flow (Amersham Biosciences) ion exchange column with a linear 0-400 mM KCl gradient in 6 M urea, 25 mM Tris/HCl, 1 mM  $\text{MgCl}_2$ , pH 7.5, in a total volume

of 1 L. sNTnC typically eluted at 250 mM KCl. Fractions were analyzed for purity by 12% acrylamide SDS-PAGE. Pure fractions were pooled, concentrated by ultrafiltration (YM3 membrane, Amicon), and dialyzed into 10 mM Tris/HCl, 100 mM NaCl, 1 mM MgCl<sub>2</sub>, pH 7.5 (2 × 5 L each for 2 h, then 1 × 5 L overnight, all at 4 °C). The dialysis bag was placed on a bed of solid sucrose and sNTnC (yield 50-60 mg) concentrated to a final concentration of 10-20 mg/mL. Mass spectrometry showed that labeled sNTnC typically had ~ 95% enrichment of <sup>13</sup>C and <sup>15</sup>N.

#### *[<sup>13</sup>C]Bifunctional Rhodamine Labeling of Mutant sNTnC.*

A total of 60 mg of sNTnC was gel filtered (2.5 mL of maximum sample volume per PD-10 column, Amersham Biosciences) into labeling buffer containing 25 mM Tris/HCl, 100 mM NaCl, 1 mM MgCl<sub>2</sub>, pH 7.4. The eluted sNTnC was diluted to 1 mg/mL (105 μM) and incubated with 105 μM tris(carboxyethyl)phosphine for 30 min on ice to reduce disulfides formed during storage. [<sup>13</sup>C<sub>2</sub>]Bisiodoacetamidorhodamine was added to a final concentration of 200 μM from an 18 mM stock solution in DMF, and the reaction mixture was incubated in the dark at 20 °C. The course of the reaction was monitored by analytical reverse phase HPLC (C18 Hichrom VYDAC column, #218TP54, guard column #218GCC54) with a linear gradient of 60% solvent A (H<sub>2</sub>O/0.1% TFA) and 40% solvent B (acetonitrile/0.1% TFA) to 40% solvent A and 60% solvent B over 20 min. Protein elution was monitored by absorbance at 215 nm and rhodamine fluorescence ( $\lambda_{\text{ex}}$  549 nm,  $\lambda_{\text{em}}$  > 580 nm). sNTnC in which both cysteines had reacted with one bisiodoacetamidorhodamine (the desired product) eluted at 51% solvent B, coincident with unreacted sNTnC (reduced form). sNTnC labeled with two rhodamines

and unreacted sNTnC (oxidized form) eluted at 50.5% and 53.5% solvent B, respectively, although the latter was not usually detected during labeling. These assignments were made retrospectively after mass spectrometric analysis of individual fractions. In preparative runs, the absorption-fluorescence ratio of the peak at 51% solvent B stabilized after 40 min and the reaction was quenched by addition of sodium 2-mercaptoethanesulfonate to a final concentration of 3.3 mM. 2.5 mL aliquots of the quenched reaction were filtered through PD-10 columns into FPLC buffer (10 mM K phosphate, 1 mM MgCl<sub>2</sub>, pH 7.5) to remove any rhodamine not complexed with sNTnC. The protein (typically at 0.4 mg/mL) was purified in 12 mg batches on a 16/10 Mono-Q ion exchange column (160 × 10 mm, Amersham Biosciences). The protein was eluted with a linear 0.25–0.35 M NaCl gradient at 4 mL/min at 4 °C. Fractions were assayed for purity by analytical HPLC (as described above). Fractions containing pure sNTnC•BR<sub>56-63</sub> were pooled and dialyzed against 10 mM KCl, 0.42 mM CaCl<sub>2</sub> (2 × 5 L each for 2 h, then 1 × 5 L overnight, all at 4 °C). The contents of the bag were then concentrated to 10 mL by ultrafiltration, and the protein was analyzed by electrospray mass spectrometry. The 10 mL solution of protein (typical yield 12 mg) was subsequently freeze-dried and stored at –20 °C. A small amount of protein was solubilized in H<sub>2</sub>O, and reanalyzed by mass spectrometry to check that the freeze-drying process had not caused methionine oxidation of the protein. Protein concentration was measured using an extinction coefficient for the rhodamine of 52,000 M<sup>-1</sup> cm<sup>-1</sup> at 528 nm (41). The stoichiometry and specificity of labeling cysteines with bisiodoacetamidorhodamine were confirmed by a combination of HPLC, tryptic digestion and electrospray mass spectrometry. sNTnC•BR<sub>56-63</sub> had the expected molecular weight (± 2 Da) (i.e. the calculated difference

in molecular weight between unlabeled [ $^{13}\text{C}/^{15}\text{N}$ ]sNTnC and that complexed with bifunctional rhodamine). The sNTnC•BR<sub>56-63</sub> conjugate was purified to >90% homogeneity. Cross-linking of protein cysteines with bisiodoacetamidorhodamine produces diastereoisomers because of the restricted rotation of the carboxy-substituted phenyl ring about the single bond joining it to the three coplanar rings that comprise the fluorophore (38). Diastereoisomers were only partially separated by preparative Mono-Q chromatography, so protein solutions for NMR spectroscopy contained a mixture of diastereoisomers.

#### *NMR Sample Preparation.*

---

A portion of the freeze-dried protein that contained ~6 mg of [ $^{13}\text{C}/^{15}\text{N}$ ]sNTnC•2Ca<sup>2+</sup>•BR<sub>56-63</sub> was dissolved in 500  $\mu\text{L}$  of NMR buffer (first treated with Chelex 100 to remove metal contaminants) containing 10 mM imidazole, 1.3% NaN<sub>3</sub> in 90% H<sub>2</sub>O/10% D<sub>2</sub>O. A total of 4.43 mg of the TnI<sub>115-131</sub> peptide [Ac-RMSADAMLKALLGSKHK-NH<sub>2</sub>, synthesized and purified as described previously (25)] was then added directly to the solution, after which the pH was adjusted to 6.8 using 1 M HCl. The sNTnC/ TnI<sub>115-131</sub> ratio was approximately 1:3.3 assuming from previous experience that 60% and 80% of weighed amounts were the mutant protein and peptide, respectively. This sample gave a poor signal/noise ratio in different 3D experiments. An additional 1.9 mg of TnI peptide was added to the solution to minimize dimerization of the complex via the hydrophobic pocket of sNTnC. Individual <sup>15</sup>N backbone  $T_2$  relaxation times on a per residue basis did not significantly increase, suggesting that the protein was already saturated with the peptide. The pH of the sample dropped to 6.5 and

was not readjusted. To investigate the effect of salt concentration, the sample was first diluted by a factor of 2 with a solution containing 80% H<sub>2</sub>O, 20% D<sub>2</sub>O, and 4 mM CaCl<sub>2</sub> and reconcentrated using Centricon tubes (MW cutoff = 3 kDa) to lower the KCl concentration to 50 mM. The remaining solution (460 μL) was transferred to an NMR tube, and 5 μL of 10 mM DSS was added. The pH remained at 6.5. A <sup>15</sup>N-HSQC spectrum was acquired (solution now at 50 mM KCl) and was identical to the spectrum acquired at 100 mM KCl, so no additional TnI peptide was added. Backbone <sup>15</sup>N T<sub>1</sub> and T<sub>2</sub> relaxation experiments were performed at different ionic strengths (in a series up to 320 mM KCl) by gradually adding 7.8 μL aliquots of a 3 M KCl solution to the sample (see Results and Discussion).

#### *NMR Experiments for Structure Determination.*

---

The assignment of <sup>1</sup>H, <sup>13</sup>C, and <sup>15</sup>N resonances for sNTnC and TnI<sub>115-131</sub> in the [<sup>13</sup>C/<sup>15</sup>N]sNTnC•2Ca<sup>2+</sup>•TnI<sub>115-131</sub>•BR<sub>56-63</sub> complex and subsequent structural determination were carried out using NMR experiments listed in Table IV-1. The aromatic protons of Phe residues of sNTnC were unassigned, and the β methylene protons as well as the methyl groups were not stereospecifically assigned. The 2D <sup>15</sup>N/<sup>13</sup>C-filtered DIPSI and NOESY experiments did not allow for the assignment of TnI resonances for residues 127 and 129-131, because of line broadening as a result of chemical exchange and poor chemical shift dispersion for the peptide resonances. All NMR spectra were acquired at 30 °C on Varian INOVA 500, Unity 600 or INOVA 800 MHz spectrometers (see Table IV-1) equipped with 5 mm triple resonance probes and z-axis pulsed field gradients for the 500 and 600 MHz instruments and triple-axis gradients for the 800 MHz

Table IV-1. NMR experiments conducted for chemical shift assignment and NOE-based distance restraints.

Experiment	Nuclei <sup>a</sup>	<sup>1</sup> H	nt <sup>b</sup>	x-pts <sup>c</sup>	y-pts	z-pts	x-sw	y-sw	z-sw	Mix <sup>d</sup>	Ref.
<sup>15</sup> N-HSQC	<sup>1</sup> H, <sup>15</sup> N	800	8	1344	256	-	12000	2320	-	-	(62, 63)
HCC-TOCSY	<sup>1</sup> H, <sup>1</sup> H, <sup>15</sup> N	500	32	816	188	64	6800	3200	1450	-	
HCCH-TOCSY	<sup>1</sup> H, <sup>1</sup> H, <sup>13</sup> C	500	16	870	264	72	6800	3200	3600	-	(64)
CBCA(CO)NNH	<sup>1</sup> H, <sup>13</sup> C, <sup>15</sup> N	600	64	1042	96	64	8150	9175	1680	-	(62)
HNCACB	<sup>1</sup> H, <sup>13</sup> C, <sup>15</sup> N	600	64	1044	80	78	8150	9180	1680	-	(62)
<sup>15</sup> N-NOESY-HSQC	<sup>1</sup> H, <sup>1</sup> H, <sup>15</sup> N	600	24	998	256	64	7880	6718	1680	50	(65)
3D <sup>13</sup> C/ <sup>15</sup> N-edited NOESY	<sup>1</sup> H, <sup>1</sup> H, <sup>13</sup> C/ <sup>15</sup> N	800	16	1408	284	70	12000	9118	6000	100	(66)
2D <sup>15</sup> N/ <sup>13</sup> C-filtered DIPSI <sup>e</sup>	<sup>1</sup> H( <sup>14</sup> N/ <sup>12</sup> C), <sup>1</sup> H( <sup>14</sup> N/ <sup>12</sup> C)	600	64	2250	1536	-	7500	5500	-	-	(67)
2D <sup>15</sup> N/ <sup>13</sup> C-filtered NOESY <sup>e</sup>	<sup>1</sup> H( <sup>14</sup> N/ <sup>12</sup> C), <sup>1</sup> H( <sup>14</sup> N/ <sup>12</sup> C)	600	64	2250	1536	-	7500	5500	-	50	(67)
3D <sup>13</sup> C/ <sup>15</sup> N-filtered/edited NOESY	<sup>1</sup> H( <sup>14</sup> N/ <sup>12</sup> C), <sup>1</sup> H, <sup>13</sup> C	600	32	800	240	60	8000	4900	3600	75	(68)
3D <sup>13</sup> Me- <sup>13</sup> Me specific NOESY <sup>e</sup>	<sup>1</sup> H, <sup>13</sup> C, <sup>13</sup> C	800	32	896	120	64	9000	2700	2700	100	

<sup>a</sup> The nucleus acquired in each dimension (*e.g.* <sup>1</sup>H, <sup>15</sup>N indicates proton x, nitrogen y).

<sup>b</sup> The number of transients acquired for each FID.

<sup>c</sup> The number of complex points (x,y,z-pts) and sweep width (sw) in each respective dimension (x is the directly detected dimension).

<sup>d</sup> Mixing times are given in milliseconds.

<sup>e</sup> The sequence was modified in-house (Dr. L. Spyropoulos).

spectrometer. All experimental FIDs were processed using the program NMRpipe (50) and analyzed with NMRView 5.0.4 (51). Generally, linear prediction up to half the number of experimental points was used in indirect dimensions. Data were then zero-filled to twice the number of acquired plus predicted points, and typically multiplied by a sine-bell apodization function shifted by 60° or 90° before Fourier transformation.

#### Structure Determination, Distance and Torsion Angle Restraints.

All structures were generated using the program CNS 1.1 (52) with a simulated annealing protocol using torsion angle dynamics for the initial high temperature and cooling steps, and Cartesian dynamics for a second cooling step, unless otherwise stated.

A) *sNTnC*. Proton-proton distance restraints were derived from measured peak intensities in the 3D  $^{15}\text{N}$  NOESY-HSQC and simultaneous 3D  $^{15}\text{N}/^{13}\text{C}$ -NOESY-HSQC experiments and calibrated as previously described (53) with the error on the peak intensities set to 40%. Only symmetry-related cross-peaks or peaks not present in the 3D  $^{13}\text{C}/^{15}\text{N}$ -filtered/edited experiment were selected from the simultaneous  $^{15}\text{N}/^{13}\text{C}$  3D NOESY-HSQC to minimize the probability of misinterpreting a protein-peptide NOE as a protein-protein NOE. In case of duplicate NOE restraints, calibrated distances from the 50 ms 3D  $^{15}\text{N}$ -NOESY-HSQC prevailed over those of the simultaneous 3D  $^{15}\text{N}/^{13}\text{C}$ -NOESY-HSQC experiment. A set of 100 structures of *sNTnC* was first generated starting from an elongated chain and gradually refined using only NOE distance restraints. NOEs with distance violations greater than 0.2 Å were closely

examined before further rounds of structure refinement. In the latest stages of refinement,  $H_{\alpha}$ ,  $C_{\alpha}$ , and  $C_{\beta}$  chemical shifts were used to derive  $\phi$  and  $\psi$  angle restraints with the program Talos (50) for residues located in well-defined regions, as determined with the programs Procheck (54) and Vadar (D. S. Wishart, L. Willard, and B. D. Sykes, unpublished). Talos-derived angles were compared to experimental values determined from the  $d_{N\alpha}/d_{\alpha N}$  ratio as previously described (55). For  $d_{N\alpha}/d_{\alpha N}$  ratios  $> 1.2$ ,  $\psi$  was restricted to  $-30 \pm 110^{\circ}$ . For  $d_{N\alpha}/d_{\alpha N}$  ratios  $< 0.71$ ,  $\psi$  was limited to  $-120 \pm 100^{\circ}$ . All  $\phi$  dihedral restraints were modified to cover a minimum range of  $\pm 30^{\circ}$ .

B) *TnI*<sub>115-131</sub>. The 2D  $^{15}\text{N}/^{13}\text{C}$  filtered DIPSI and NOESY experiments were used in conjunction to assign the peptide chemical shifts. None of the backbone and side chain resonances of residues 127 and 129-131 could be assigned. NOEs were classified as weak, medium, and strong, and accordingly calibrated with the 'bin method' using the built-in calibration script in NMRView. Preliminary structures were generated from an extended chain, without the second cooling step using Cartesian dynamics of the annealing protocol. Once the secondary structure was properly defined using NOE-derived distance restraints only, backbone  $\phi$  and  $\psi$  angle restraints derived from the Talos program (50) using HN and  $H_{\alpha}$  chemical shifts for residues 119-124 were further introduced for refinement.

C) *sNTnC*•*TnI*<sub>115-131</sub>. NOE contacts between the protein and the peptide were assigned from the 3D  $^{13}\text{C}/^{15}\text{N}$ -filtered/edited experiment, which allows only NOEs

arising from  $^{12}\text{C}$ -attached protons on TnI and ending on  $^{13}\text{C}$ -attached protons on sNTnC to be observed. Strip plots taken from the 3D  $^{13}\text{C}/^{15}\text{N}$ -filtered/edited experiment are shown in Figure IV-1. The 3D  $^{15}\text{N}/^{13}\text{C}$ -NOESY-HSQC spectrum was used in conjunction to confirm peak assignments. All NOEs were calibrated to  $4 \pm 2 \text{ \AA}$ . An initial set of 100 structures was first generated using pre-folded structures of sNTnC and TnI<sub>115-131</sub> as previously determined. In the first round of structure generation, all NOEs between sNTnC and TnI<sub>115-131</sub> were treated as ambiguous. Further rounds of refinement enabled specific assignments to be made for 52 of the 57 intermolecular NOEs between sNTnC and TnI<sub>115-131</sub>. To ensure independent folding of the complex from pre-folded structures of TnI and TnC, the final set of structures was generated starting from extended chains. On the basis of homologous calcium binding sites, the default built-in annealing protocol in the CNS program (52) was modified to allow the introduction of 11  $\text{Ca}^{2+}$ -distance restraints before the second cooling step.

D) *sNTnC*•*BR*<sub>56-63</sub>. No NOE contacts were detected between the  $^{13}\text{C}$ -labeled methyl groups of BR and sNTnC in the 3D  $^{13}\text{C}/^{15}\text{N}$ -edited NOESY, 3D  $^{13}\text{C}/^{15}\text{N}$ -filtered/edited, and 3D  $^{13}\text{Me}$ - $^{13}\text{Me}$  specific NOESY experiments. However, intra-BR NOEs between the methyl groups and the xanthene aromatic protons were observed in the 2D  $^{15}\text{N}/^{13}\text{C}$ -filtered NOESY experiment.

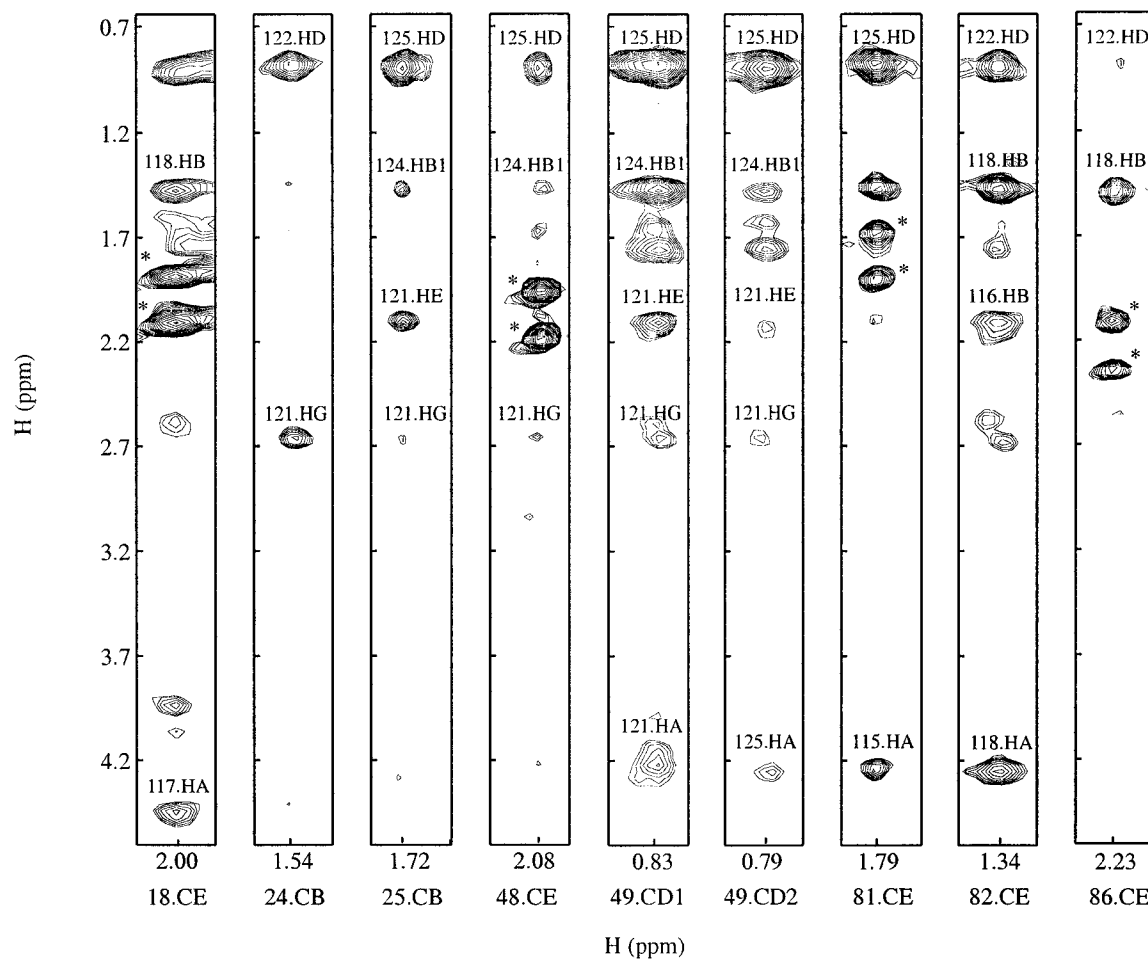


Figure IV-1. Selection of intermolecular NOE contacts between  $\text{TnI}_{115-131}$  and  $\text{sNTnC}$  from the  $3\text{D } ^{13}\text{C}/^{15}\text{N}$ -filtered/edited experiment. Peaks marked with asterisks are believed to be double-diagonal artifact peaks and were not assigned. The  $^{13}\text{C}$  planes from which the spectra were plotted are indicated at the bottom of each strip.

---

*Determination of the Orientation of BR Label Relative to the C Helix.*

---

Two families of 1000 structures of the complex including the BR label were generated, one for each of the isomeric configurations of the carboxylate group relative to the xanthene system. The CNS topology and energy parameter files (see Appendix 1) for the BR label were built from Gerard Kleywegt's XPLO2D server (version 3.0.2) (<http://alpha2.bmc.uu.se/hicup/xdict.html>) and carefully inspected and modified to allow for flexibility around single bonds in the BR. The orientation of the long axis of the xanthene to the C helix was determined for the 500 lowest energy structures out of the family of 1000 as follows. For each structure, a vector describing the orientation of the C helix was first calculated from the coordinates of the N, CO and C $_{\alpha}$  atoms of the residues located between the N-terminal (residue 56) and the C-terminal (residue 63) of the C helix, using an algorithm borrowed from an in-house program (S. M. Gagné). The two direction vectors describing the orientation of the plane of the xanthene system were then calculated using the coordinates of the carbon nuclei of the xanthene system. Finally the angle between the C helix and the xanthene plane was calculated.

---

*Backbone Amide <sup>15</sup>N Relaxation Measurements.*

---

All relaxation data were acquired at 30 °C on Varian INOVA 500 MHz and Unity 600 MHz spectrometers. Sensitivity-enhanced pulse sequences developed by Farrow et al. (56) were used to measure backbone <sup>15</sup>N- $T_1$ , <sup>15</sup>N- $T_2$ , and {<sup>1</sup>H}-<sup>15</sup>N NOE. Because of partial dimerization of the sNTnC•2Ca<sup>2+</sup>•TnI<sub>115-131</sub>•BR<sub>56-63</sub> complex in solution (see

Results and Discussion), the overall backbone  $T_1$  and  $T_2$  relaxation times were measured at 500 MHz from the decay of the amide envelope using only the one-dimensional trace of the first increment of the  $^{15}\text{N}$ - $T_1$ - and  $T_2$ -HSQC spectra at different ionic strengths. The amide envelope signal was integrated using the Varian Vnmr software. No  $^{13}\text{C}$  and  $^{15}\text{N}$  decoupling was applied during signal acquisition. The delays between acquisitions were 1.2 and 4 s for  $T_1$  and  $T_2$  measurements, respectively, and for both overall backbone  $T_1$  and  $T_2$  measurements, 384 transients were collected with 870 complex points.

Using two-dimensional spectroscopy, a set of backbone  $^{15}\text{N}$ - $T_1$ ,  $^{15}\text{N}$ - $T_2$ , and  $\{^1\text{H}\}$ - $^{15}\text{N}$  NOE experiments were collected at 320 mM KCl with 870 ( $t_1$ )  $\times$  128 ( $t_2$ ) complex points at 500 MHz and 986 ( $t_1$ )  $\times$  128 ( $t_2$ ) complex points at 600 MHz. The  $T_1$  relaxation delays were 11.1, 55.5, 122.1, 199.8, 277.5, 388.5, 499.5, 666, 888, and 1100 ms on both instruments. The delay between repetitions of the pulse sequence was set to 1.2 s for the  $T_1$  experiment. The  $T_2$  relaxation delays were set to  $16.61 \times n$  and  $16.544 \times n$  ms (where  $n = 1, \dots, 8$ ) on the 500 and 600 MHz spectrometers, respectively. For the  $T_2$  experiment, the delay between repetitions of the pulse sequence was set to 4 s to avoid overheating because of the higher salt concentration.  $\{^1\text{H}\}$ - $^{15}\text{N}$  NOEs were measured in the absence (incorporating a relaxation delay of 5 s between repetitions of the pulse sequence) and presence of proton saturation (incorporating 3 s of  $^1\text{H}$  saturation, and a delay of 2 s between repetitions of the pulse sequence). All relaxation data were processed using the NMRpipe program (50) and analyzed using NMRView (51).

## RESULTS AND DISCUSSION

One aim of the present work was to determine the structure of a protein domain in which a pair of surface residues had been replaced by cysteines and cross-linked with a bifunctional rhodamine (BR). This tests the approach for determining the *in situ* orientation of protein domains by polarized fluorescence measurements (38-40). The method depends on two main assumptions: first, that the 3D-structure and function of the target domain are not modified by the mutagenesis, BR labeling, and reconstitution of the functional complex. Second, that the fluorescence dipole of the probe is approximately parallel to the line joining the  $\beta$ -carbon atoms of the two cysteine residues. In this paper, we determine the structure of a  $\text{Ca}^{2+}$ -saturated bifunctional rhodamine labeled N-domain of skeletal TnC in a complex ( $\text{sNTnC} \cdot 2\text{Ca}^{2+} \cdot \text{TnI}_{115-131} \cdot \text{BR}_{56-63}$ ) with the 'switch' peptide from the inhibitory protein TnI. This complex was chosen to represent as closely as possible the regulatory state in activated skeletal muscle.

### *Effect of Ionic Strength on Dimerization.*

---

It was important at the outset of the work to investigate the oligomeric state of the  $\text{sNTnC} \cdot 2\text{Ca}^{2+} \cdot \text{TnI}_{115-131} \cdot \text{BR}_{56-63}$  complex, since the N-domain of TnC is known to undergo weak self-association in solution (57). To investigate this, the  $^{15}\text{N}$  backbone  $R_1$  and  $R_2$  NMR relaxation rates for the overall amide envelope of sNTnC in the complex were measured at different ionic strengths using the first increment of  $^{15}\text{N}$ - $T_1$  and  $-T_2$  HSQC spectra.  $R_1$  and  $R_2$  depend on the rotational correlation time, and thus ultimately upon the molecular weight of the complex in solution. As seen in Figure IV-2, an overall decrease

in  $R_2$  and increase in  $R_1$  values were observed with increasing KCl concentration, indicative of a reduction in the effective molecular weight of the complex.

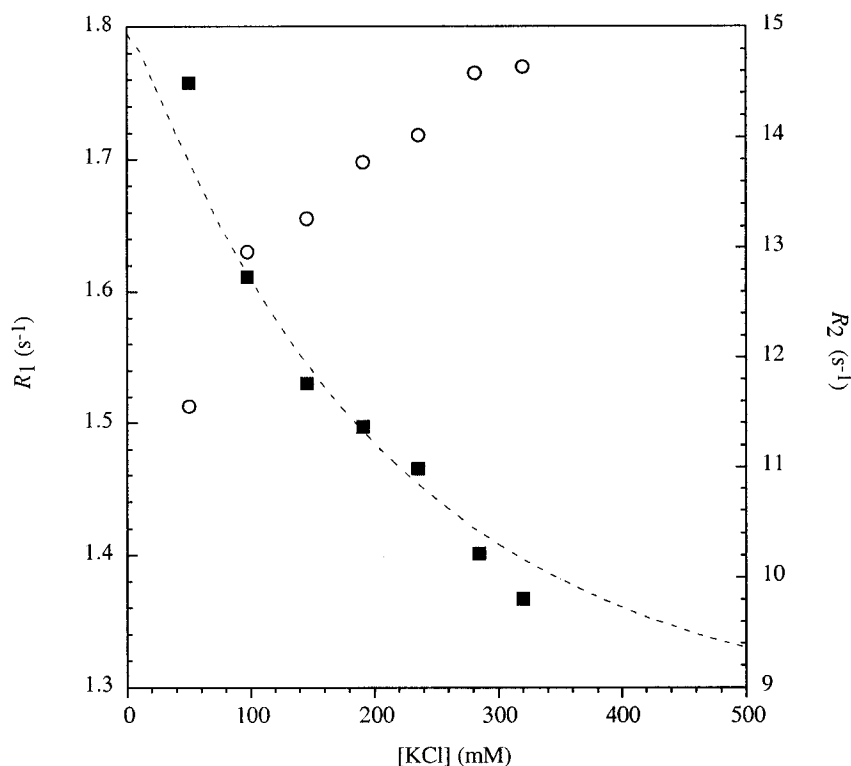


Figure IV-2. Overall amide envelope  $R_1$  (circles) and  $R_2$  (squares) relaxation rates for sNTnC in the sNTnC•2Ca<sup>2+</sup>•TnI<sub>115-131</sub>•BR<sub>56-63</sub> complex as a function of KCl concentration at a <sup>1</sup>H Larmor frequency of 500 MHz. The dashed line is a fit to a KCl dependent dimerization constant.

The expected values of  $R_1$  and  $R_2$  for a monomeric and dimeric complex were calculated using the Lipari-Szabo model-free approach (58, 59) under the expectation that the  $\tau_m$  (in ns) is equal to half the molecular weight (in kDa) (57) for an isotropically tumbling complex at 30 °C, and assuming an average backbone order parameter ( $S^2$ ) of 0.85. The calculated values for the <sup>15</sup>N  $R_1$  and  $R_2$  relaxation rates for sNTnC in the

sNTnC•2Ca<sup>2+</sup>•TnI<sub>115-131</sub>•BR<sub>56-63</sub> complex are 2.10 and 8.3 s<sup>-1</sup>, respectively, for the monomer, and 1.2 and 15.1 s<sup>-1</sup> for the dimer. On this basis, Figure IV-2 shows values approaching those expected for the dimer at low salt, and progressing toward those for the monomer at high salt. At the final KCl concentration of 320 mM, the observed backbone  $R_1$  (1.77 s<sup>-1</sup>) and  $R_2$  (9.80 s<sup>-1</sup>) values correspond to a rotational correlation time of 8.3 ns and molecular weight of ~ 16.6 kDa, which is consistent with the presence of some dimeric species in solution.

Since  $R_2$  is proportional to  $\tau_m$ , the proportion of dimer was estimated by fitting the amide envelope  $R_2$  curve to a monomer-dimer equilibrium, assuming an overall backbone  $S^2$  of 0.85 and a correlation time for fast internal motion ( $\tau_e$ ) of 50 ns at a field strength corresponding to a proton frequency of 500 MHz. The global correlation time  $\tau_m$  giving rise to the observed backbone  $R_2$  values was taken to vary with the fraction of monomer in solution according to

$$\begin{aligned}\tau_m &= f_M \tau_{m \text{ monomer}} + (1 - f_M) \tau_{m \text{ dimer}} \\ &= f_M \frac{MW_{\text{monomer}}}{2} + (1 - f_M) MW_{\text{monomer}}\end{aligned}$$

where  $f_M$  is the fraction of monomer in solution and  $MW_{\text{monomer}}$  the molecular weight of the monomer (13.2 kDa). The fraction of monomer was calculated using

$$f_M = \frac{-K_d + \sqrt{K_d^2 + 8M_o}}{4M_o}$$

with an initial monomer concentration ( $M_o$ ) estimated at 0.6 mM. The dimerization equilibrium constant,  $K_d$ , was estimated to be dependent on the millimolar concentration of KCl according to:

$$K_d = K_{d(0)} \left( 1 + a[\text{KCl}] + b[\text{KCl}]^2 \right)$$

Best fit values of  $K_{d(0)}$ ,  $a$  and  $b$  were 5  $\mu\text{M}$ , 0 and 0.005, respectively. At the final concentration of 320 mM, the fraction of monomer is estimated to be  $\approx 0.75$  (i.e. 6:1 monomer:dimer molar ratio). The same value was extracted by fitting the  $R_1$  curve with the same approach.

Complete sets of  $^{15}\text{N}$  backbone relaxation data were acquired at a KCl concentration of 320 mM at 500 and 600 MHz using 2D  $^{15}\text{N}$ -HSQC spectroscopy. The values of  $T_1$ ,  $T_2$  and NOE are plotted on a per residue basis in Figure IV-3 at the two field strengths. The patterns observed for the  $T_1$ ,  $T_2$  and NOE values of sNTnC are typical for the C- and N-domain of TnC in the calcium-saturated state (60), with more flexibility at the ends of the terminal helices. The various relaxation parameter ratios for backbone amide  $^{15}\text{N}$  data collected at 500 and 600 MHz are illustrated per residue in Figure IV-4. After removal of residues whose  $T_1$  values are affected by internal motions, as determined from a lower limit NOE value ( $\text{NOE}^{500} > 0.6$ ,  $\text{NOE}^{600} > 0.65$ ), the average ratios (mean  $\pm$  SD) are  $1.27 \pm 0.05$  for  $T_1^{600}/T_1^{500}$ ,  $0.97 \pm 0.05$  for  $T_2^{600}/T_2^{500}$  and  $1.09 \pm 0.13$  for  $\text{NOE}^{600}/\text{NOE}^{500}$ . The global macromolecular correlation time ( $\tau_m$ ) was

determined from the  $T_1/T_2$  ratio of residues falling within one standard deviation of the mean using an in-house Mathematica script (P. Mercier), after removal of residues whose NOE value was under a given threshold ( $\text{NOE}^{500} > 0.6$ ,  $\text{NOE}^{600} > 0.65$ ) to ensure the elimination of residues whose relaxation is affected by picosecond time-scale internal motions. The dipole-dipole contribution from  $^{13}\text{C}$  relaxation due to the  $^{13}\text{C}$  labeling of sNTnC was included in the calculations. The values found for  $\tau_m$  (8.39 ns at 500 MHz and 8.22 ns at 600 MHz) are consistent with those determined from the overall  $T_2$  decay of the amide envelope. Attempts to extract meaningful values for backbone order parameter values using conventional analysis procedures were unsuccessful. Schurr et al. (61) have shown using simulated data that best-fit internal motion parameters are unreliable in the presence of protein dimerization when the fraction of monomer is between 0.2 and 0.9. In this study, the extracted backbone order parameters for sNTnC were artificially high ( $S^2 \geq 0.92$  on average).

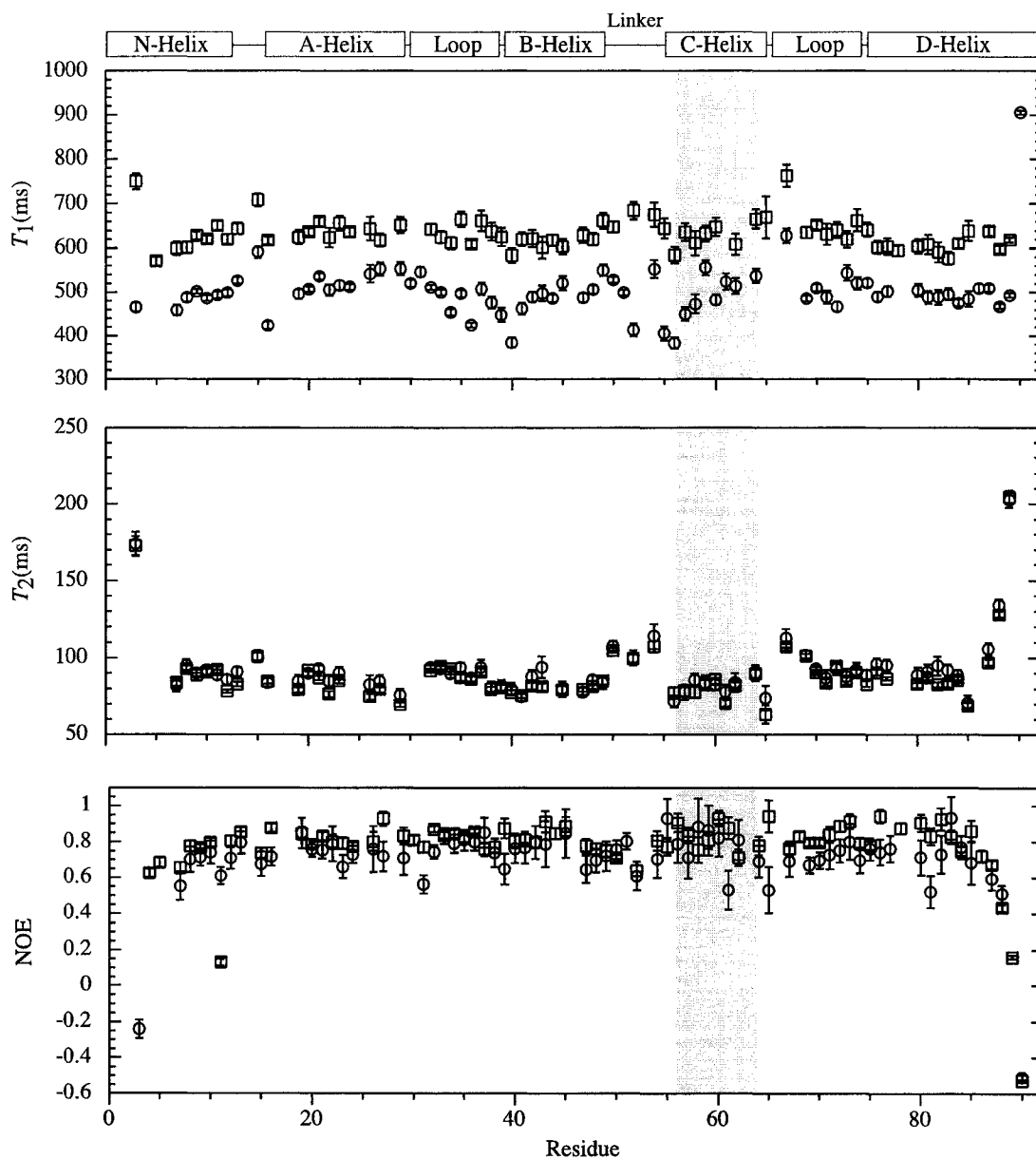


Figure IV-3. Backbone amide  $^{15}\text{N}$  NMR relaxation times and NOEs for  $\text{sNTnC} \cdot 2\text{Ca}^{2+} \cdot \text{TnI}_{115-131} \cdot \text{BR}_{56-63}$  at 320 mM KCl at a magnetic field strength corresponding to a  $^1\text{H}$  Larmor frequency of 500 MHz (circles) and 600 MHz (squares). The gray region corresponds to residues located between the insertion points of the rhodamine label on the C helix of sNTnC.

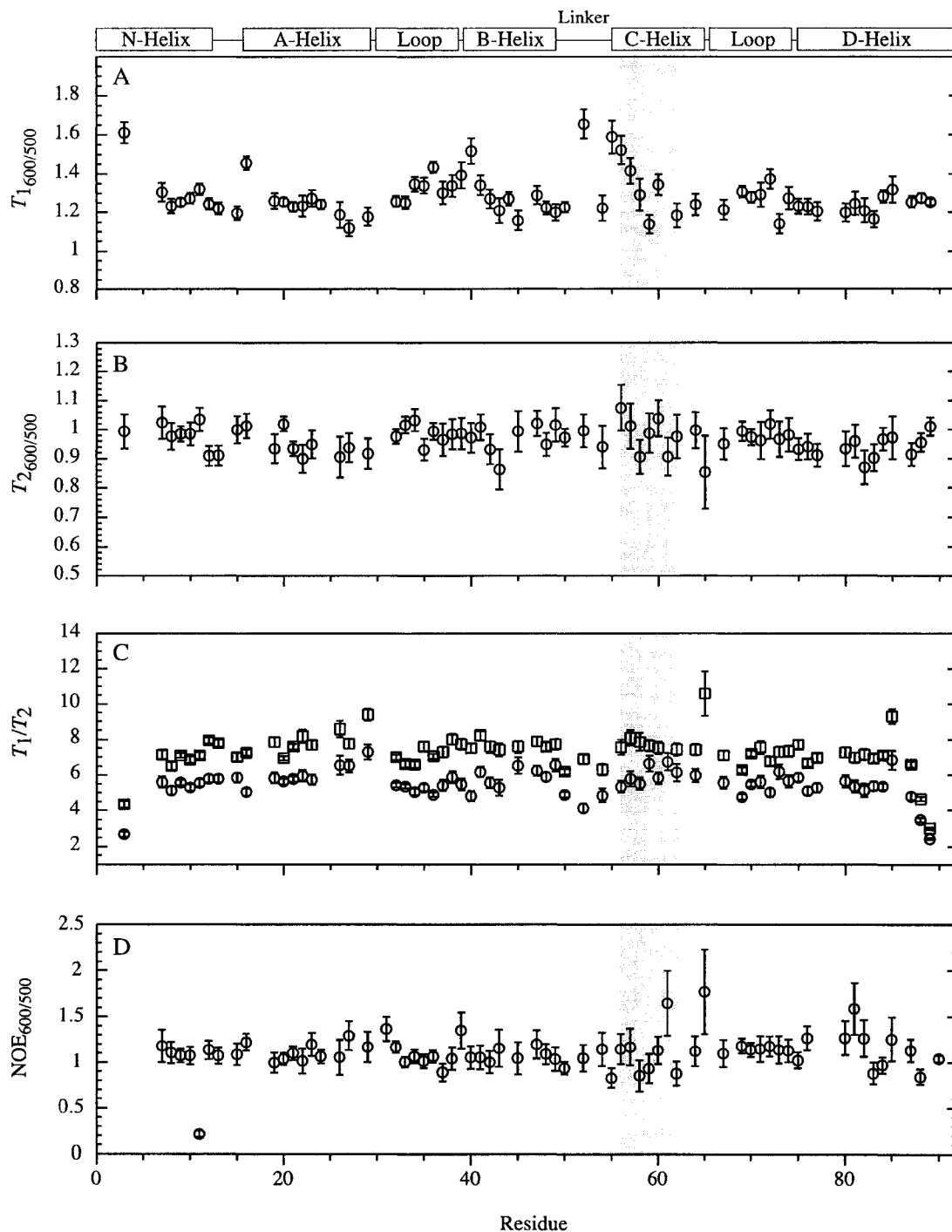


Figure IV-4. Backbone amide  $^{15}\text{N}$  NMR relaxation time and NOE ratios for  $\text{sNTnC}\cdot 2\text{Ca}^{2+}\cdot \text{TnI}_{115-131}\cdot \text{BR}_{56-63}$  at 320 mM KCl and at magnetic field strengths corresponding to  $^1\text{H}$  Larmor frequencies of 500 and 600 MHz. In panel C, the  $T_1/T_2$  ratios are identified by circles at 500 MHz and squares at 600 MHz. The region corresponding to residues located between the insertion points of the rhodamine label on sNTnC is colored in gray.

---

*Spectral Influence of Atropisomerism in the Bifunctional Rhodamine.*

---

The rhodamine used in this study has two linker arms that terminate in iodoacetamide groups, which are the sites of covalent linkage to sNTnC via sulfur atoms of Cys residues (Figure IV-5). The structure also contains a carboxylate group on the pendant phenyl ring. This ring is aligned orthogonally to the plane of the xanthene system, and its attached carboxylate group can have two configurations (atropisomers) that cannot interconvert. The rhodamine molecule itself is symmetric but becomes chiral once attached to NTnC. As a consequence of atropisomerism, two diastereoisomers of the complex exist in solution (38). Here, the two isomers could not be adequately separated during chromatographic purification (FPLC), so the material used for NMR spectroscopy contained two populations in a ratio of ~3:2. In consequence, the  $^{15}\text{N}$ -HSQC spectrum of sNTnC in the  $\text{sNTnC}\cdot 2\text{Ca}^{2+}\cdot \text{TnI}_{115-131}\cdot \text{BR}_{56-63}$  complex (Figure IV-6) showed twin peaks for residues from 56 to 63 (the insertion points of BR on the C helix of sNTnC), as did residue 64. No partner peak could be identified with certainty for residue 57.

Some of the lower intensity twin peaks in the  $^{15}\text{N}$ -HSQC spectrum did not show connective  $d_{\text{NN}}$  NOEs in the 3D  $^{15}\text{N}$ -NOESY-HSQC, but their identity could be verified from the 3D CBCA(CO)NNH and HNCACB experiments. Within each pair of peaks, each had the same  $\text{C}_\alpha$  and  $\text{C}_\beta$  chemical shifts, which suggests that the two diastereoisomers have identical or near-identical secondary structures. The lack of  $d_{\text{NN}}$  connectivity in the 3D  $^{15}\text{N}$ -NOESY-HSQC experiment for some of the peaks belonging to the minor species is likely to arise from its low concentration, rather than from a



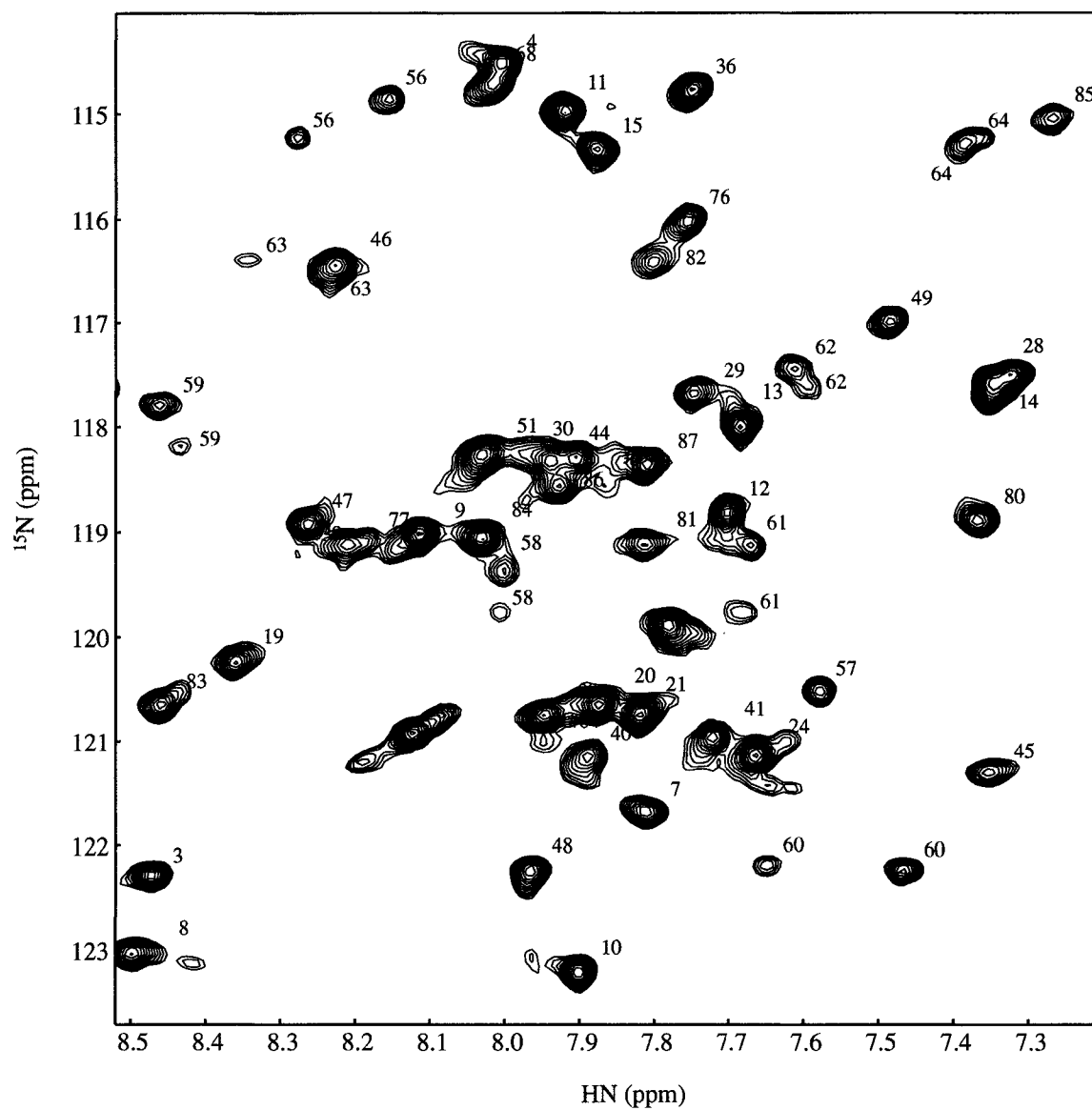


Figure IV-6. Selected region of a 800 MHz  $^{15}\text{N}$ -HSQC spectrum of sNTnC in the sNTnC•2Ca $^{2+}$ •TnI $_{115-131}$ •BR $_{56-63}$  complex. Residues 56-64 (except 57) show twin peaks.

---

*Structure of sNTnC•2Ca<sup>2+</sup>•TnI<sub>115-131</sub>•BR<sub>56-63</sub> Determined by NMR Spectroscopy.*

---

The 20 lowest-energy structures of the sNTnC•2Ca<sup>2+</sup>•TnI<sub>115-131</sub>•BR<sub>56-63</sub> complex, generated with a total of 1191 distance restraints [including 11 Ca<sup>2+</sup>-distance restraints of 2.0 – 2.8 Å based on homologous calcium binding sites (62)] and 70 dihedral restraints (see detailed structural statistics in Table IV-2), are shown superimposed using the backbone heavy atoms in Figure IV-7A. A ribbon representation of the averaged and minimized structure is shown in Figure IV-7B. The conformation and orientation of the BR moiety shown in Figure IV-7B will be discussed below. The NOE distribution (intraresidue, sequential, medium, and long-range) on a per residue basis for both the peptide and the protein is shown as a histogram in Figure IV-8A, and the backbone atom RMSD values relative to the average structure for each residue are shown in Figure 8B. Backbone RMSD values were calculated from the 20 lowest-energy structures after superimposition of the backbone atoms of residues 5-85 of sNTnC in the sNTnC•2Ca<sup>2+</sup>•TnI<sub>115-131</sub>•BR<sub>56-63</sub> complex onto the average structure. The mean ( $\pm$  SD) backbone RMSD to the average structure for residues 5-85 of sNTnC in the complex is  $0.37 \pm 0.10$  using all residues in that region and  $0.32 \pm 0.08$  Å with residues having backbone RMSD < 1.0. The loop between the A and the B helices shows a higher backbone RMSD value than the other helices because of a relatively low number of NOE restraints for the Gly<sup>33</sup>-Gly<sup>34</sup>-Gly<sup>35</sup> segment (see Figure IV-8). No  $\phi$  and  $\psi$  angle restraints were defined for this segment. A total of 80.4% of the residues in well-defined regions were found to be in most favored  $\phi$  and  $\psi$  regions of the Ramachandran map, with another 18.8% in additional allowed regions, as determined with the program Procheck (54). Only three NOE violations in the 0.1 – 0.2 Å range (none above 0.2 Å)

were detected in three different structures of the family of 20 structures, and no structure had more than one distance violation. No dihedral angle violation  $> 1^\circ$  was detected within the final ensemble of structures.

The switch peptide in the  $s\text{NTnC}\cdot 2\text{Ca}^{2+}\cdot \text{TnI}_{115-131}\cdot \text{BR}_{56-63}$  complex is helical from residues 118-124. Although not involved in a well-defined secondary structure, residues 115-117 of the TnI peptide do show interactions with sNTnC, whereas no NOEs between the peptide and the protein were observed for residues 127-131. Moreover, no intramolecular NOEs involving the last four residues of  $\text{TnI}_{115-131}$  could be assigned because of a lack of chemical shift assignments, which explains the large backbone RMSD values for those residues (see Figure IV-8). The helical portion of the switch peptide and the segment making contact with sNTnC are consistent with the observations of Li et al. (12) for the cardiac isoform of the switch peptide in the  $c\text{NTnC}\cdot \text{Ca}^{2+}\cdot c\text{TnI}_{147-163}$  complex. In that study, deuterated forms of the switch peptide were used to make unambiguous assignments of methyl-methyl contacts between A(22,23) and L(157,158). In the present work, the two methyl groups in each of L122, L125, and L126 had distinct proton chemical shifts. However, they were almost identical between the three Leu residues, so it was difficult to define the contacts between these methyl groups and sNTnC. Hence, all NOEs starting on these Leu methyl groups were first assigned without discrimination between the three possibilities. Rounds of refinement eliminated practically all ambiguous assignments of methyl-methyl contacts between sNTnC and L(122,125,126) of the switch peptide.

Table IV-2. Structural statistics for sNTnC in the NTnC•2Ca<sup>2+</sup>•TnI<sub>115-131</sub>•BR<sub>56-63</sub> complex (20 best lowest-energy structures of a family of 100 structures). Error limits are standard deviations.

NOE restraints (sNTnC only)	
Total	1040
Intra-residue	565
Sequential ( i-j  = 1)	221
Medium range (2 ≤  i-j  ≤ 4)	138
Long range ( i-j  ≥ 5)	116
NOE restraints (TnI <sub>115-131</sub> only)	
Total	67
Intra-residue	33
Sequential ( i-j  = 1)	23
Medium range (2 ≤  i-j  ≤ 4)	11
Long range ( i-j  ≥ 5)	0
NOE restraints (between sNTnC and TnI <sub>115-131</sub> )	
Total	59
Non-ambiguous	52
Ambiguous	7
Dihedral Restraints (sNTnC only)	
Total	120
φ	58
ψ	62
χ <sub>1</sub>	0
Dihedral Restraints (TnI <sub>115-131</sub> only)	
Total	12
φ	6
ψ	6
χ <sub>1</sub>	0
Restraint violations	
Distance > 0.1 Å	3
Dihedral > 1°	0
RMSD to averaged minimized structure (Å)	
Well defined regions <sup>a</sup> (N,C <sub>α</sub> ,C)	0.32 ± 0.08
All regions <sup>b</sup> (N,C <sub>α</sub> ,C)	0.37 ± 0.10

Heavy atoms	$0.79 \pm 0.07$
N helix (5-13)	$0.18 \pm 0.05$
A helix (16-29)	$0.18 \pm 0.05$
B helix (39-48)	$0.33 \pm 0.05$
C helix (55-65)	$0.18 \pm 0.05$
D helix (75-85)	$0.21 \pm 0.06$
$\beta$ sheet (32-34,72-74)	$0.17 \pm 0.06$
<hr/>	
Energies <sup>c</sup> (kcal mol <sup>-1</sup> )	
$E_{\text{total}}$	$103 \pm 8$
$E_{\text{NOE}}$	$11.7 \pm 2$
$E_{\text{Dihedral}}$	$0.10 \pm 0.09$
<hr/>	
$\phi, \psi$ in core or allowed regions <sup>d</sup>	
Residues in most favored regions	80.4 %
Residues in additional allowed regions	18.8 %
Residues in generously allowed regions	0.8 %
Residues in disallowed regions	0.1 %

<sup>a</sup> Using residues 5-85 of sNTnC having backbone RMSD smaller than 1.00

<sup>b</sup> Using residues 5-85 of sNTnC

<sup>c</sup> Using all residues of sNTnC in the 20 lowest-energy structures

<sup>d</sup> Using residues 5-85 of sNTnC as determined by the program Procheck (54)

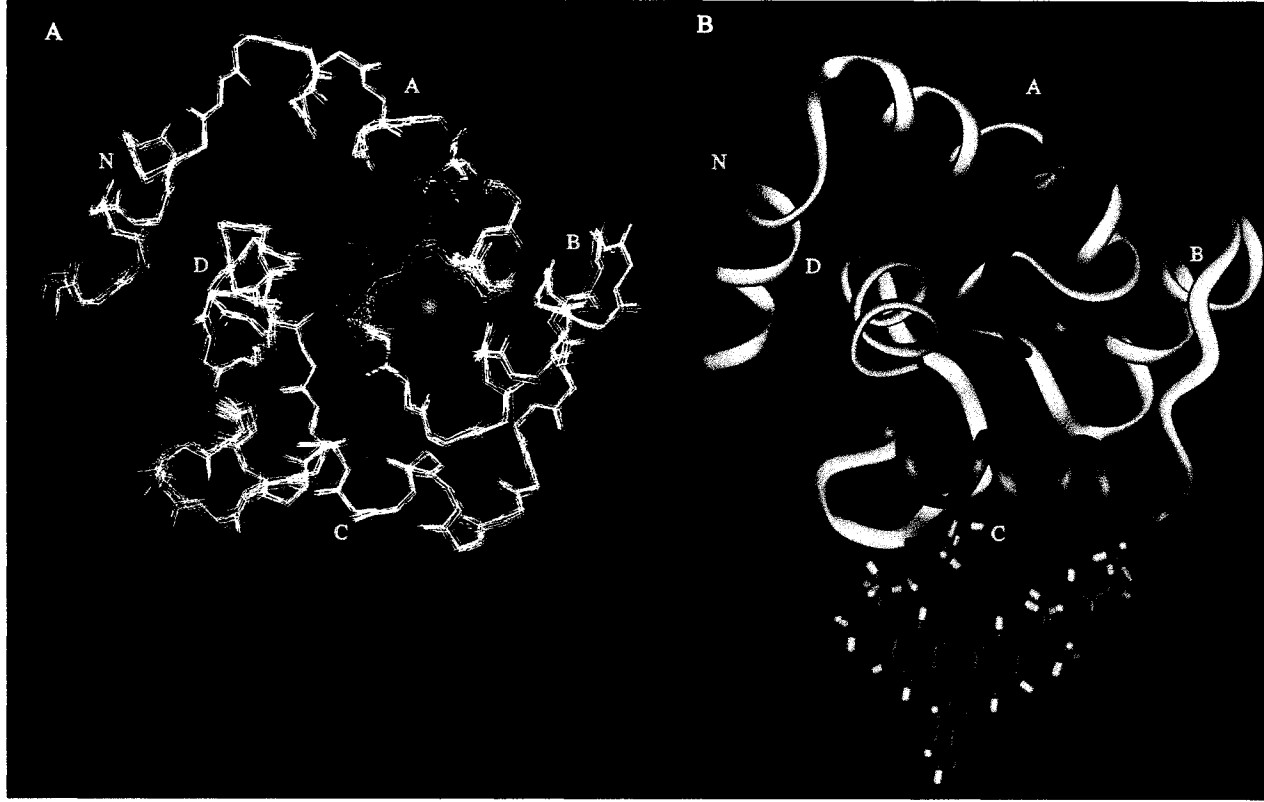


Figure IV-7. (A) Backbone superimposition of the 20 lowest-energy solution structures of the  $sNTnC \cdot 2Ca^{2+} \cdot TnI_{115-131} \cdot BR_{56-63}$  complex (only residues 5-85 of TnC and residues 115-126 of TnI are shown). (B) Ribbon representation of the minimized average solution structure of  $sNTnC \cdot 2Ca^{2+} \cdot TnI_{115-131} \cdot BR_{56-63}$  (TnC 5-85 in white, TnI 115-127 in red). The C helix (residues 55-65) is colored blue. The bifunctional rhodamine label is shown attached to residues 56 and 63 of TnC with a stick representation. The exact relative orientation of the rhodamine label with that of TnC could not be determined in this study (see Results and Discussion).  $Ca^{2+}$  atoms in binding sites I and II are shown as spheres in both panels A and B. In the orientation shown, residue 115 of the switch peptide is at the bottom of the structure.

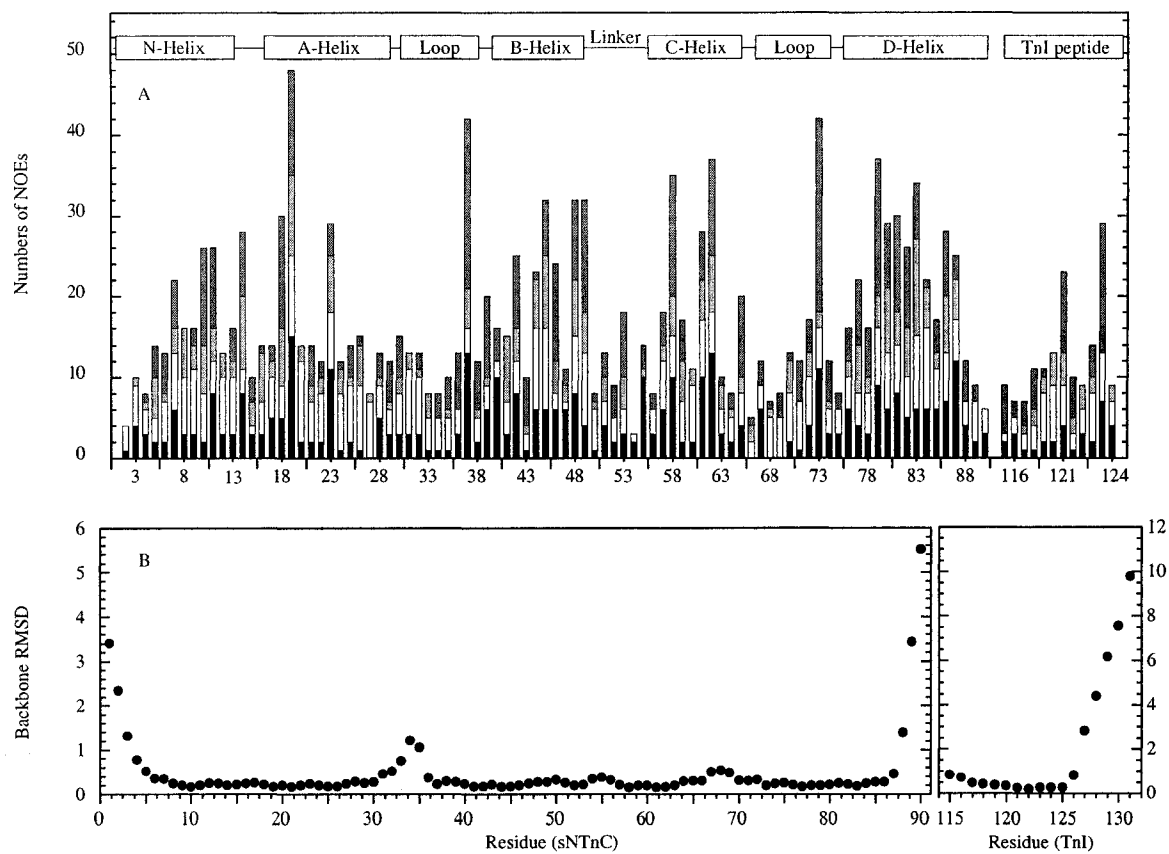


Figure IV-8. (A) Distribution of NOEs as a function of residue number. Intraresidue, sequential, medium, and long-range NOEs are identified by black, white, light gray, and dark gray columns, respectively. (B) Backbone RMSD ( $\text{\AA}$ ) for the ensemble of 20 solution structures with respect to the average coordinates.

TnI<sub>115-131</sub> binds to the hydrophobic cleft of sNTnC and is stabilized by hydrophobic interactions, as is the case with binding of the cardiac peptide to cNTnC (12). The strip plots given in Figure IV-1 identify some of the NOEs between the peptide and the protein. In the 3D <sup>13</sup>C/<sup>15</sup>N-filtered/edited experiment, only NOEs ending on methyl groups of sNTnC could be measured. On the basis of important and numerous contacts of Met21 of the Rp40 peptide with the hydrophobic pocket of sCTnC, it was suggested by Vassylyev et al. (14) that Met121 of TnI<sub>115-131</sub> was the key residue for its interaction with TnC. Here we identified several contacts between NTnC and the H<sub>γ</sub> and H<sub>ε</sub> protons of Met121, which support this hypothesis. The extensive similarity between the type and the location of sNTnC residues involved in TnI<sub>115-131</sub> binding and that of the cardiac complex (12) suggests that both isoforms of the switch peptide bind in a similar manner and that the interaction involves the same key residues.

The incorporation of the rhodamine label and the E(56,63)C mutations had no measurable effect on the secondary and tertiary structures of sNTnC in the present complex when compared with those of sNTnC•TnI<sub>115-131</sub> (R. T. McKay, L. Spyropoulos, P. Mercier, and B. D. Sykes, unpublished results). Thus, the C helix is intact and canonical. The changes in backbone HN, N, C<sub>α</sub>, and C<sub>β</sub> NMR chemical shifts induced by rhodamine labeling are reported in Figure IV-9. Chemical shifts of residues located between rhodamine insertion points 56 and 63 are the most perturbed, but those of residues 65 and 66 are also particularly affected. However, the C<sub>α</sub> chemical shifts, which are the most directly correlated with the protein secondary structure (63), do not show significant changes for the C helix.

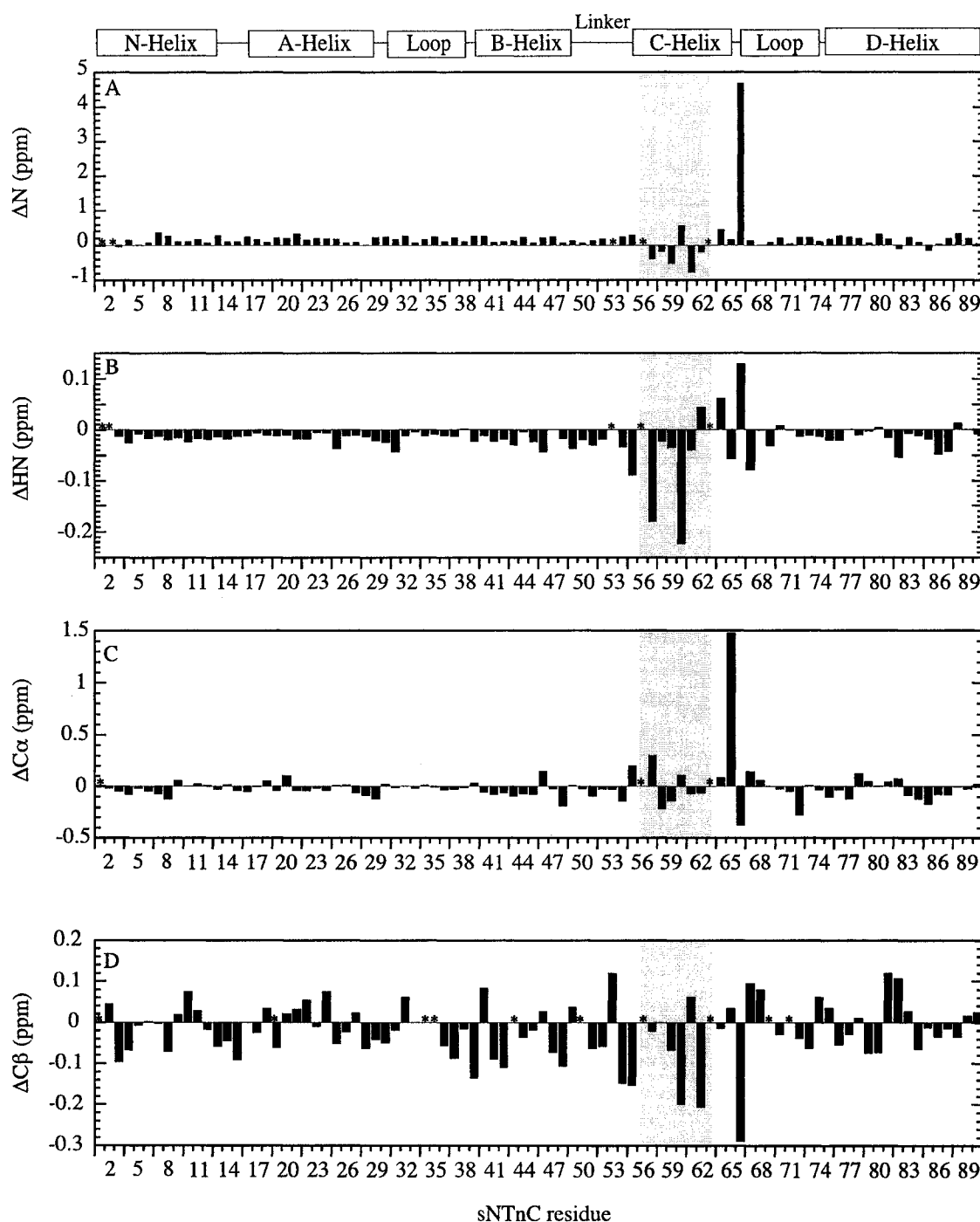


Figure IV-9. Difference in N, HN,  $C_\alpha$ , and  $C_\beta$  chemical shifts induced by BR attached to the C-helix at residues 56 and 63. Chemical shifts for sNTnC in the sNTnC $\cdot$ 2Ca $^{2+}$  $\cdot$ TnI $_{115-131}$  complex were obtained from McKay et al. (R. T. McKay, L. Spyropoulos, P. Mercier, and B. D. Sykes, unpublished results). No differences in chemical shifts were calculated for residues 56 and 63 because of mutations to Cys residues. Asterisks indicate mutagenesis sites and missing or nonexistent chemical shifts (Pro53 in panels A and B, and Gly residues in panel D). The gray region corresponds to residues located between the insertion points of the rhodamine label on the C helix of sNTnC.

The total changes in sNTnC backbone chemical shifts induced by TnI<sub>115-131</sub> binding, mutagenesis and rhodamine labeling are reported in the context of the present structure in Figure IV-10A, using a color gradient on the surface of sNTnC. The chemical shifts used for comparison were those determined by Gagné et al. (9) for sNTnC•2Ca<sup>2+</sup>. McKay et al. (26) used chemical shift mapping in a similar manner to suggest the potential TnI<sub>115-131</sub> binding site on sNTnC, but the structure of the peptide was not determined. The present study shows a close relationship between residues identified from chemical shift mapping as participating in TnI<sub>115-131</sub> binding and the experimentally determined structure and location of the peptide. Large chemical shift changes (strongly colored in red) are observed in this view for Leu49 (middle), Gly50 (middle), Met46 (hidden), and Leu42 (hidden), which is consistent with results reported by McKay et al. (26). Since no backbone chemical shifts were reported by Gagné et al. (9) for Leu49 and Asp66, the extrapolated chemical shifts at 100 mM KCl from McKay et al. (26) were used to calculate chemical shift changes for these two residues. The darker red patch near the lower right-hand corner of the view is the site of the E56C mutation. The E63C mutation is hidden in this view. The chemical shift changes on sNTnC induced by contacts with the terminal Arg115 side chain of TnI<sub>115-131</sub> are particularly well defined. The rear face of sNTnC (see Figure IV-10B) is essentially uncolored, except for small changes at its lower edge induced by the mutations and BR labeling. As with Rp40 bound to sCTnC (20), protein residues of sNTnC undergoing chemical shift changes upon peptide binding are highly correlated with the location of the peptide. Moreover, the structure of TnI<sub>115-131</sub> shows a high level of complementarity with the hydrophobic groove exposed upon calcium binding.

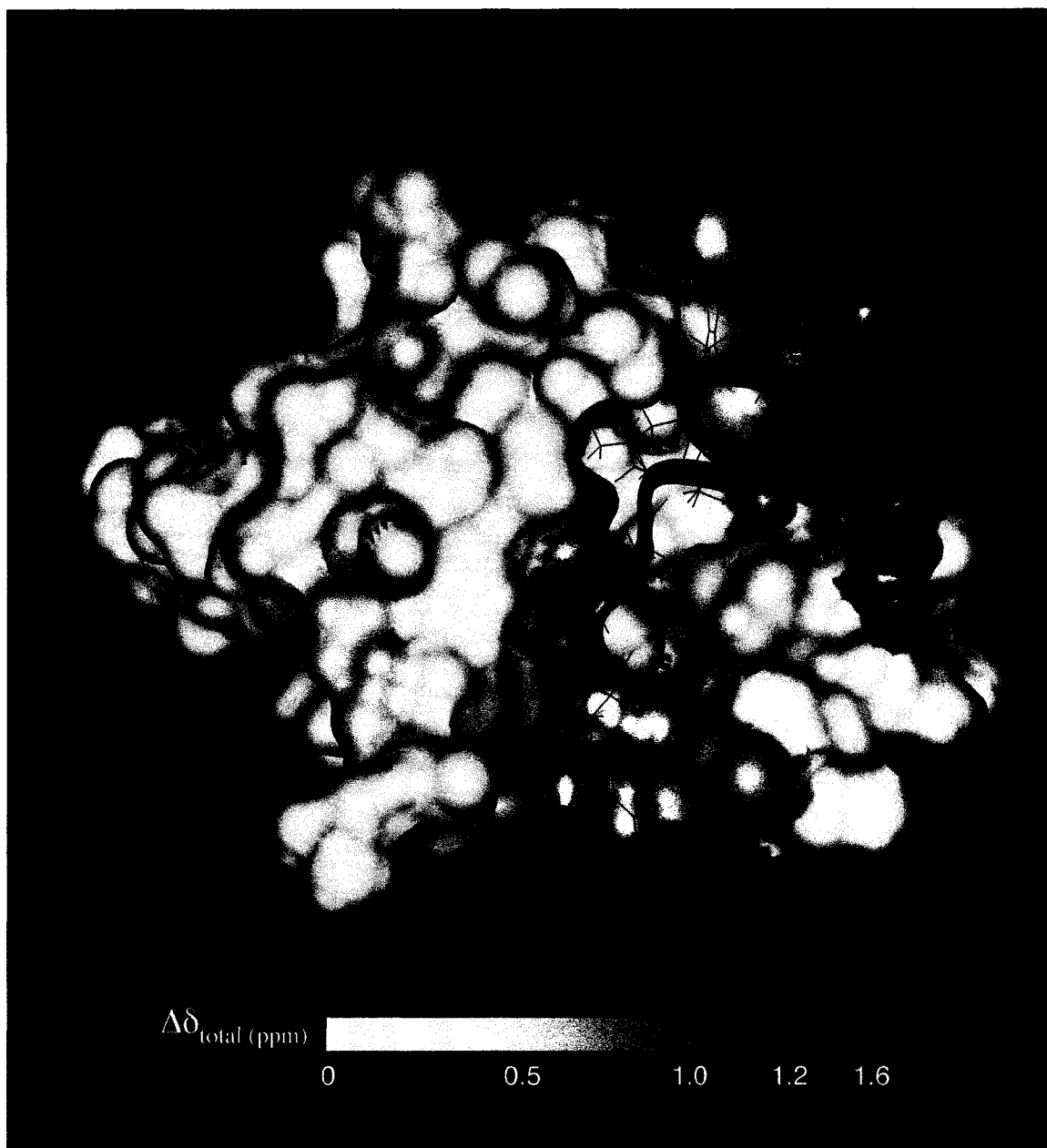


Figure IV-10A. Molecular surface of the sNTnC•2Ca<sup>2+</sup>•TnI<sub>115-131</sub>•BR<sub>56-63</sub> complex. The orientation of the protein backbone is equivalent to that shown in Figure IV-7A. The surface was colored using a color gradient (from white to red – see color bar) to show the difference in the extent of the total chemical shift changes ( $\Delta\delta_{\text{total}}$ ) relative to sNTnC•2Ca<sup>2+</sup> alone (9). Residues undergoing total chemical shift changes larger than 1.6 ppm were colored pure red. Smaller total chemical shift changes were colored on a linear scale. The surface of sNTnC was generated without the rhodamine label coordinates. The TnI peptide is shown in the blue ribbon and side chains in the blue stick form.

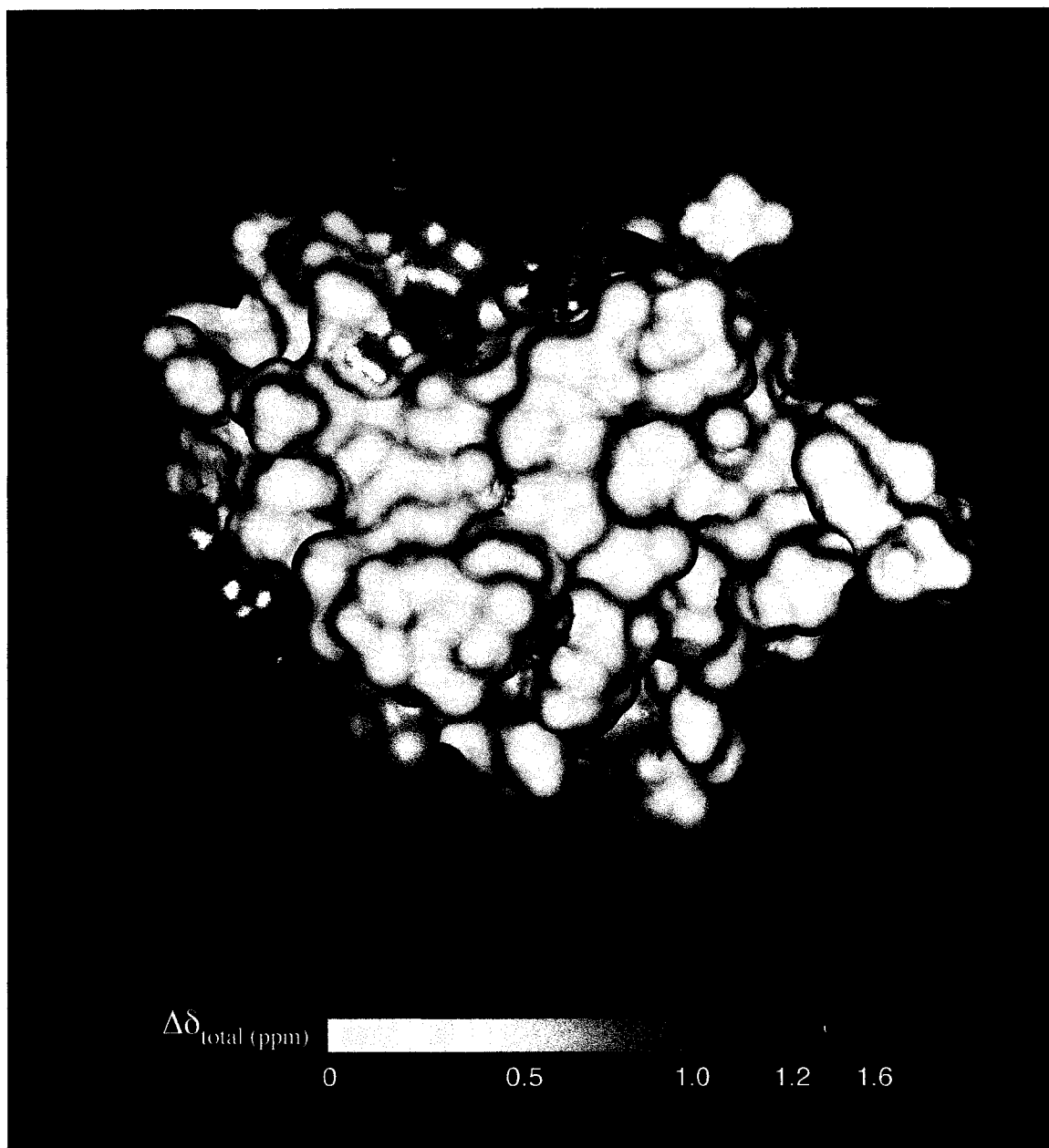


Figure IV-10B. Back view of the molecular surface shown in Figure IV-10A. The same settings apply.

As shown in Figure IV-11A and IV-11B, the structure of the  $s\text{TnC}\cdot 2\text{Ca}^{2+}\cdot \text{TnI}_{115-131}\cdot \text{BR}_{56-63}$  complex is very similar to those of two prior NMR structures of the  $\text{Ca}^{2+}$ -saturated cardiac isoform of TnC ( $c\text{TnC}$ ) in complex with residues 147-163 of cardiac TnI ( $c\text{TnI}_{147-163}$ ) (12, 13). Because of Val28 insertion in the cardiac sequence, it is rather difficult directly to compare skeletal and cardiac structures of the N-domain of TnC. Structures are shown superimposed with a backbone trace using the NAD unit (residues 7-13, 16-29, and 75-85 for  $s\text{TnC}$ ; residues 5-11, 14-27, and 74-84 for  $c\text{TnC}$ ) in Figure IV-11A, and the BCD unit (residues 30-85 for  $s\text{TnC}$ ; 29-84 for  $c\text{TnC}$ ) in Figure IV-11B. All three structures share a common feature in that the N-terminal region of the switch peptide undergoes a kinked turn at the fourth residue from the N-terminus, which brings Met116 of  $\text{TnI}_{115-131}$  near to Met86 of  $s\text{TnC}$ , and Ile148 of  $c\text{TnI}_{147-163}$  into contact with Met85 of  $c\text{TnC}$ .

Calcium binding to  $s\text{TnC}$  and  $c\text{TnC}$  results in an 'opening' of the skeletal TnC domains. The degree of opening can be quantified in terms of interhelical angles (10). Table IV-3 lists the interhelical angle values among the helices of NTnC for different skeletal and cardiac complexes, as well as the interhelical angles with the TnI peptides. These data show that the structure of  $s\text{TnC}$  in the  $s\text{TnC}\cdot 2\text{Ca}^{2+}\cdot \text{TnI}_{115-131}\cdot \text{BR}_{56-63}$  complex is less open than in  $s\text{TnC}\cdot 2\text{Ca}^{2+}$  alone. To verify that the inferred closing upon  $\text{TnI}_{115-131}$  binding did not arise from misassigned NOEs, distance restraints between the B and the C helices for  $s\text{TnC}$  in the  $s\text{TnC}\cdot 2\text{Ca}^{2+}\cdot \text{TnI}_{115-131}\cdot \text{BR}_{56-63}$  complex were carefully compared with those used for  $c\text{TnC}$  in the  $c\text{TnC}\cdot \text{Ca}^{2+}\cdot c\text{TnI}_{147-163}$  complex. No additional or unusual restraints were found in the distance restraint set for the

complex in the current study. Moreover, identical or equivalent restraints were found to be calibrated with the same distance range between the two sets. This result contrasts with the situation in the C-domain, where no significant change occurs in the degree of structural openness or exposure of the hydrophobic patch of CTnC•2Ca<sup>2+</sup> upon binding of Rp40 (11).

Interestingly, even though the cardiac and skeletal isoforms show different Ca<sup>2+</sup> binding properties and Ca<sup>2+</sup>-induced structural changes, the binding of their respective switch peptides makes the two NTnC isoforms more structurally equivalent. The binding to TnI opens cardiac NTnC•Ca<sup>2+</sup> and closes skeletal NTnC•2Ca<sup>2+</sup> (see A/B and C/D interhelical angles in Table IV-3). Thus, despite the differences in Ca<sup>2+</sup> binding stoichiometry and kinetics, the mechanistic pathways involved in muscle contraction for the two NTnC isoforms share common structural states.

As a consequence of the TnI binding and closure of Ca<sup>2+</sup>-bound sNTnC, the accessible surface area of nonpolar residues is reduced by about 200 Å<sup>2</sup>, as determined with the program STC (64) using structures of sNTnC•2Ca<sup>2+</sup> from Gagné et al. (9) as reference. The reduction in hydrophobic surface exposure is caused by the covering effect of the switch peptide in the hydrophobic groove of NTnC. The rhodamine label was not included in the calculations, and the contribution of mutated residues E56C and E63C was also ignored.

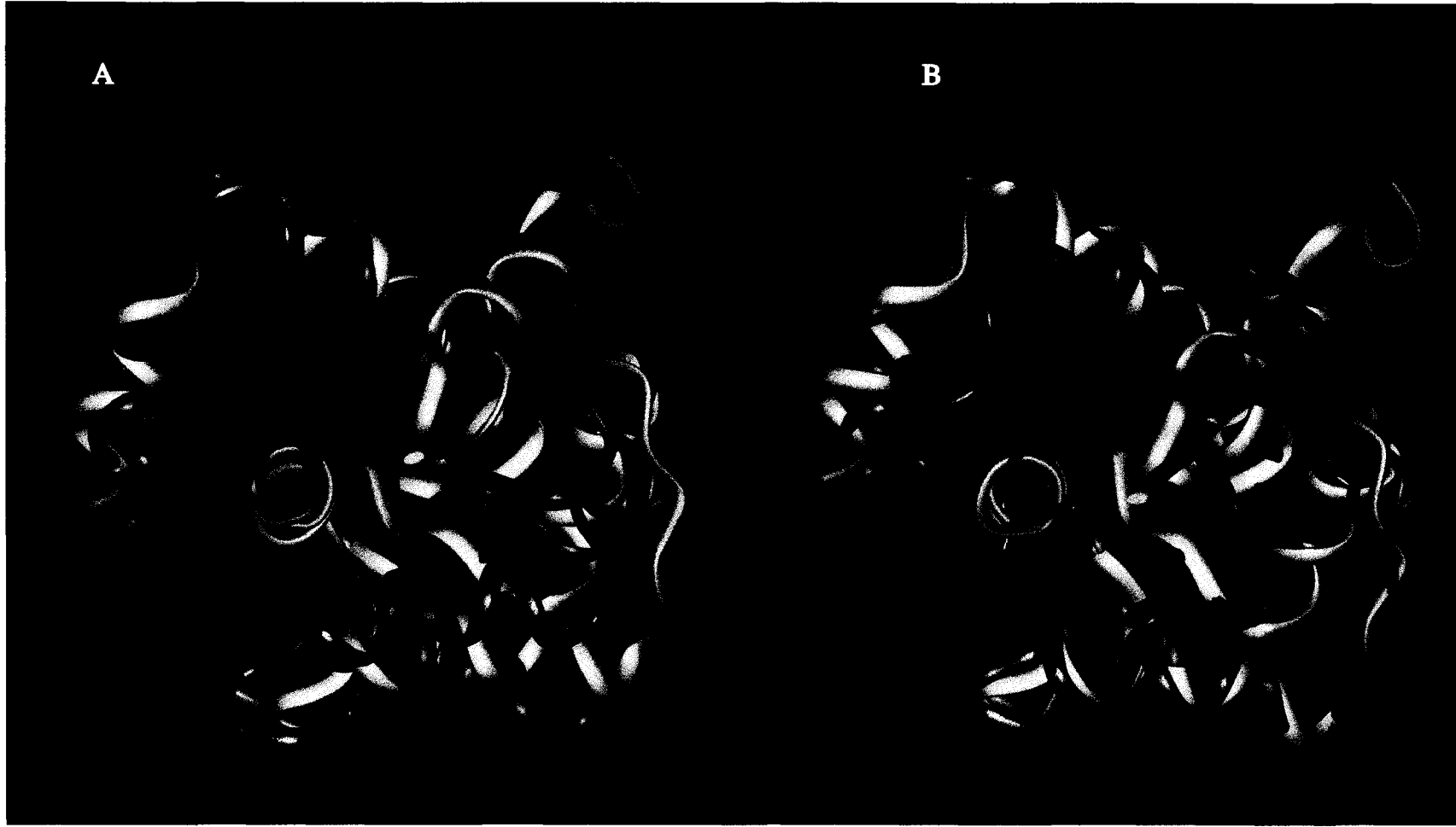


Figure IV-11. Ribbon representation of the backbone superimposition of sNTnC•2Ca<sup>2+</sup>•TnI<sub>115-131</sub>•BR<sub>56-63</sub> (red) with cNTnC•Ca<sup>2+</sup>•cTnI<sub>147-163</sub> (blue) and cNTnC•Ca<sup>2+</sup>•cTnI<sub>147-163</sub>•bepridil (yellow) (residues 5-85 for sNTnC and 3-84 for cNTnC). In panel A, the NAD unit was used for superimposition whereas in panel B, the BCD helices were used. The switch peptide is shown in a brighter tone of the relevant color for each complex.

Table IV-3. Interhelical angles for sNTnC and cNTnC free and bound to TnI peptides. Error limits are standard deviations.

	A/B	B/C	C/D	A/D	A/T <sup>h</sup>	B/T <sup>h</sup>	C/T <sup>h</sup>	D/T <sup>h</sup>
cNTnC•apo <sup>a</sup>	136 ± 3	118 ± 4	129 ± 5	113 ± 3	-	-	-	-
cNTnC•Ca <sup>2+</sup> <sup>b</sup>	132 ± 3	106 ± 4	117 ± 3	116 ± 3	-	-	-	-
cNTnC•Ca <sup>2+</sup> •cTnI <sub>147-163</sub> <sup>c</sup>	103 ± 4	111 ± 7	95 ± 5	113 ± 3	62 ± 6	84 ± 6	120 ± 6	120 ± 5
cNTnC•Ca <sup>2+</sup> •cTnI <sub>147-163</sub> •bepridil <sup>d</sup>	119 ± 3	110 ± 2	90 ± 3	124 ± 3	56 ± 4	93 ± 4	119 ± 5	142 ± 5
sNTnC•apo <sup>e</sup>	130 ± 3	126 ± 5	125 ± 4	111 ± 2	-	-	-	-
sNTnC•2Ca <sup>2+</sup> <sup>f</sup>	90 ± 3	100 ± 6	69 ± 5	109 ± 3	-	-	-	-
sNTnC•2Ca <sup>2+</sup> •TnI <sub>115-131</sub> •BR <sub>56-63</sub> <sup>g</sup>	108 ± 2	124 ± 2	105 ± 3	123 ± 2	64 ± 2	77 ± 3	97 ± 2	146 ± 3

<sup>a</sup>Using residues 14-27 (A helix), 41-48 (B helix), 54-63 (C helix) and 74-83 (D helix), PDB access code 1SPY

<sup>b</sup>PDB access code 1AP4

<sup>c</sup>PDB access code 1MXL

<sup>d</sup>Using residues 14-28 (A helix), 38-48 (B helix), 54-64 (C helix) and 74-83 (D helix), PDB access code 1DTL

<sup>e</sup>PDB access code 1TNP

<sup>f</sup>PDB access code 1TNQ

<sup>g</sup>Using residues 16-29 (A helix), 39-48 (B helix), 55-65 (C helix) and 75-85 (D helix), PDB access code 1NPQ

<sup>h</sup>T is used to designate the TnI peptide.

---

*Consequences of the Structure for Polarized Fluorescence Studies.*

---

The NMR structure of  $s\text{TnC}\cdot 2\text{Ca}^{2+}\cdot \text{TnI}_{115-131}\cdot \text{BR}_{56-63}$  shows directly that the C helix, to which the BR is attached, is intact. Moreover, the overall fold of the N-domain of TnC in this structure is similar to that of previously determined structures (8, 9, 14, 65, 66). The rhodamine molecule did not make any strong interactions with the surface of the protein domain, and in particular, did not bind to the hydrophobic pocket that is created when  $\text{Ca}^{2+}$  binds to the regulatory sites of TnC. This supports our physiological data, in which normal  $\text{Ca}^{2+}$ -regulation of contraction was restored when the full-length  $s\text{TnC}\cdot \text{BR}_{56-63}$  was exchanged into demembrated muscle fibers (40). Both the  $\text{Ca}^{2+}$  concentration required for half-maximal activation and the slope of the force-pCa curve were similar to those obtained with unlabeled sTnC. In the present structure the hydrophobic pocket is occupied by the switch peptide of TnI and this is also likely to be so in the native troponin complex in the presence of  $\text{Ca}^{2+}$ .

The exact orientation of the rhodamine label could not be directly determined from interatomic distances, due to a lack of intermolecular NOEs with the protein. However, in the  $s\text{TnC}\cdot 2\text{Ca}^{2+}\cdot \text{TnI}_{115-131}\cdot \text{BR}_{56-63}$  complex, intramolecular NOEs between the methyl groups of the rhodamine label and the aromatic protons of the xanthene system at positions 2',7' and 1',8' (weaker), and the lack of NOEs to the 4',5' xanthene protons allowed the linker arms to be assigned to the *Z,Z* configuration (see the legend of Figure IV-5 for details of this nomenclature). The stereochemistry (*cis/trans*) of the amide bonds in the rhodamine arms is still unknown, but structures were generated with the *trans* configuration based on what would be expected for a Gly-Gly segment.

Rotation around the  $\text{CH}_2\text{-CH}_2$  and the  $\text{CH}_2\text{-S-CH}_2$  moieties in each arm of the rhodamine-cysteine linkage and at the linkage positions on sNTnC provides the rhodamine with intrinsic flexibility. One possible conformer (*Z,Z* configuration of the linker arms, as in Figure IV-5, and both amide bonds in *trans* configurations) of the rhodamine label is shown in Figure IV-7B. In the calculated NMR structures (see Experimental Procedures), the C helix is coplanar to the mean orientation of the xanthene system, for both configurations of the carboxylate group relative to the xanthene system. The present results do not exclude an interaction of the BR with other regions of the troponin ternary complex or with tropomyosin or actin, but the physiological data summarized above suggest this is unlikely.

The BR dipole has independent motions with respect to the protein backbone, mainly because of bond rotation in the  $N\text{-(CH}_2\text{CH}_2\text{NHCOCH}_2\text{)}$  groups. Polarized fluorescence measurements from sTnC•BR<sub>56-63</sub> in muscle fibers show that the rhodamine dipole exhibits motion on the nanosecond time scale with respect to the protein backbone that is equivalent to wobble in a cone of semi-angle about  $20^\circ$  (40). A similar amplitude of fast wobble was observed with either bifunctional or monofunctional rhodamine probes on the regulatory light chain of myosin in muscle fibers (38, 67, 68). The factors that determine the amplitude and dynamics of probe motions with respect to the protein backbone are still not well understood. More detailed dynamic information should be available in future work from NMR and time-resolved fluorescence anisotropy measurements on sNTnC•2Ca<sup>2+</sup>•TnI<sub>115-131</sub>•BR<sub>56-63</sub> in solution, from time-resolved fluorescence anisotropy in fibers and from molecular dynamic simulations.

A more general implication of the  $s\text{TnC}\cdot 2\text{Ca}^{2+}\cdot \text{TnI}_{115-131}\cdot \text{BR}_{56-63}$  structure relates to the determination of the structure and orientation of protein domains *in situ* using polarized fluorescence intensities from a set of dipole probes. Thus Ferguson et al. (40) used polarized fluorescence intensities from BR probes on the N, A and C helices of TnC to determine the orientation of the N-domain of TnC within  $\text{Ca}^{2+}$ -activated and relaxed skeletal muscle. Intensities from actively contracting muscle fibers were compatible with the published structures for TnC with  $\text{Ca}^{2+}$  bound to the regulatory sites [ $\text{Ca}^{2+}$  state; (8, 9, 66)] and with the  $s\text{TnC}\cdot 2\text{Ca}^{2+}\cdot \text{TnI}_{115-131}\cdot \text{BR}_{56-63}$  structure presented here. However the latter is at present the only structure of skeletal TnC that includes the TnI switch peptide and so was considered likely to mimic most closely the *in situ* conformation of TnC in the  $\text{Ca}^{2+}$  state. Furthermore it was concluded from our structure that the TnI switch peptide is approximately perpendicular to the actin filament axis in actively contracting muscle (40).

Ferguson et al. (40) also noted that the apo TnC structure (9) that was consistent with the fluorescence polarization data from relaxed muscle is the most open of the apo structures, and that the  $s\text{TnC}\cdot 2\text{Ca}^{2+}\cdot \text{TnI}_{115-131}\cdot \text{BR}_{56-63}$  structure used to interpret the fluorescence polarization data from contracting muscle is the most closed of the  $\text{Ca}^{2+}$  structures. The comparison suggests that the opening of the N-domain associated with activation *in situ* may be considerably smaller than in isolated TnC *in vitro*. In the native regulatory complex, the opening of the hydrophobic pocket driven by  $\text{Ca}^{2+}$  binding may be counteracted by closing of the pocket associated with binding of the switch peptide, so

Ca<sup>2+</sup> and switch peptide binding are coupled without a large net change in the degree of opening of the N-domain.

## CONCLUSION

In this paper, we used NMR spectroscopy for the structure determination of a bifunctional rhodamine-labeled N-terminal domain of skeletal TnC in complex with the switch peptide of TnI. Backbone relaxation measurement showed that the complex dimerizes at low salt concentration. Under the conditions at which the structure was calculated (320 mM KCl), 75% of the complex was monomeric. The relatively small portion of dimer in solution did not influence the determined structure. Two diastereoisomers of the complex were present in solution due to atropisomerism caused by restricted rotation of the carboxylate group on the rhodamine label. The structure determined reflects the weighted average of both species. The overall fold of the protein is not affected by the presence of the rhodamine label, and the C helix remains intact. The rhodamine is positioned away from the hydrophobic pocket and the C helix, and no direct NOEs were observed between the two <sup>13</sup>C-labeled methyl groups of the rhodamine and sNTnC. The switch peptide is bound by hydrophobic interactions in the hydrophobic groove of sNTnC, and is helical between residues 118-124. We observed a strong correlation between the location of the peptide and the sNTnC residues perturbed by TnI<sub>115-131</sub> binding as identified from chemical shift mapping. The skeletal and cardiac forms of the complex have very similar structures, in which the switch peptide is bound to the N-terminal hydrophobic pocket of TnC between helices A and B.

These results show that bifunctional rhodamine probes can be attached to protein domains for *in situ* measurements of domain orientation by polarized fluorescence without modifying the backbone structure of the target domain. The structure of the N-domain of skeletal TnC in a complex with  $\text{Ca}^{2+}$  and the switch peptide of TnI determined in the present study has been used in combination with polarized fluorescence measurements from muscle fibers to establish the orientation of this domain, and that of the TnI switch peptide, in actively contracting muscle (40).

**Coordinates.** The coordinates for the structures (without BR) have been deposited in the RCSB Protein Data Bank (PDB accession code 1NPQ).

## REFERENCES

1. Squire, J. M., and Morris, E. P. (1998) *FASEB J.* 12, 761-771.
2. Filatov, V. L., Katrukha, A. G., Bulargina, T. V., and Gusev, N. B. (1999) *Biochemistry (Mosc)* 64, 969-985.
3. Finn, B. E., and Drakenberg, T. (1999) *Adv. Inorg. Chem.* 46, 441-494.
4. Gergely, J. (1998) *Adv. Exp. Med. Biol.* 453, 169-176.
5. Perry, S. V. (1999) *Mol. Cell. Biochem.* 190, 9-32.
6. Gordon, A. M., Homsher, E., and Regnier, M. (2000) *Physiol. Rev.* 80, 853-924.
7. Herzberg, O., and James, M. N. G. (1988) *J. Mol. Biol.* 203, 761-779.
8. Houdusse, A., Love, M. L., Dominguez, R., Grabarek, Z., and Cohen, C. (1997) *Structure* 5, 1695-1711.
9. Gagne, S. M., Tsuda, S., Li, M. X., Smillie, L. B., and Sykes, B. D. (1995) *Nat Struct Biol* 2, 784-789.
10. Gagne, S. M., Li, M. X., McKay, R. T., and Sykes, B. D. (1998) *Biochem Cell Biol* 76, 301-312.
11. Mercier, P., Spyropoulos, L., and Sykes, B. D. (2001) *Biochemistry* 40, 10063-10077.
12. Li, M. X., Spyropoulos, L., and Sykes, B. D. (1999) *Biochemistry* 38, 8289-8298.
13. Wang, X., Li, M. X., and Sykes, B. D. (2002) *J. Biol. Chem.* 277, 31124-31133.
14. Vassilyev, D. G., Takeda, S., Wakatsuki, S., Maeda, K., and Maeda, Y. (1998) *Proc. Natl. Acad. Sci. U.S.A.* 95, 4847-4852.
15. Gasmi-Seabrook, G. M., Howarth, J. W., Finley, N., Abusamhadneh, E., Gaponenko, V., Brito, R. M., Solaro, R. J., and Rosevear, P. R. (1999) *Biochemistry* 38, 8313-8322.
16. Olah, G. A., and Trehwella, J. (1994) *Biochemistry* 33, 12800-12806.
17. Olah, G. A., Rokop, S. E., Wang, C. L., Blechner, S. L., and Trehwella, J. (1994) *Biochemistry* 33, 8233-8239.
18. Stone, D. B., Timmins, P. A., Schneider, D. K., Krylova, I., Ramos, C. H. I., Reinach, F. C., and Mendelson, R. A. (1998) *J. Mol. Biol.* 281, 689-704.
19. Takeda, S., Yamashida, A., Maeda, K., and Maeda, Y. (2002) *Biophys. J.* 82, 170a.
20. Mercier, P., Li, M. X., and Sykes, B. D. (2000) *Biochemistry* 39, 2902-2911.
21. Ngai, S.-M., and Hodges, R. S. (1992) *J. Biol. Chem.* 267, 15715-15720.
22. Abbott, M. B., Dvoretzky, A., Gaponenko, V., and Rosevear, P. R. (2000) *FEBS Lett.* 469, 168-172.
23. Hernández, G., Blumenthal, D. K., Kennedy, M. A., Unkefer, C. J., and Trehwella, J. (1999) *Biochemistry* 38, 6911-6917.
24. Campbell, A. P., Van Eyk, J. E., Hodges, R. S., and Sykes, B. D. (1992) *Biochim. Biophys. Acta* 1160, 35-54.
25. Tripet, B. P., Van Eyk, J. E., and Hodges, R. S. (1997) *J. Mol. Biol.* 271, 728-750.
26. McKay, R. T., Tripet, B. P., Hodges, R. S., and Sykes, B. D. (1997) *J. Biol. Chem.* 272, 28494-28500.

27. Syska, H., Wilkinson, J. M., Grand, R. J., and Perry, S. V. (1976) *Biochem. J.* 153, 375-387.
28. Ngai, S. M., Sonnichsen, F. D., and Hodges, R. S. (1994) *J. Biol. Chem.* 269, 2165-2172.
29. Luo, Y., Leszyk, J., Li, B., Gergely, J., and Tao, T. (2000) *Biochemistry* 39, 15306-15315.
30. Luo, Y., Wu, J. L., Li, B., Langsetmo, K., Gergely, J., and Tao, T. (2000) *J. Mol. Biol.* 296, 899-910.
31. Tung, C. S., Wall, M. E., Gallagher, S. C., and Trewella, J. (2000) *Protein Sci.* 9, 1312-1326.
32. Spyrapoulos, L., Gagné, S. M., Li, M. X., and Sykes, B. D. (1998) *Biochemistry* 37, 18032-18044.
33. Li, M. X., Saude, E. J., Wang, X., Pearlstone, J. R., Smillie, L. B., and Sykes, B. D. (2002) *Eur. Biophys. J.* 31, 245-256.
34. Sia, S. K., Li, M. X., Spyrapoulos, L., Gagné, S. M., Liu, W., Putkey, J. A., and Sykes, B. D. (1997) *J. Biol. Chem.* 272, 18216-18221.
35. Craig, R., and Lehman, W. (2002) *Results. Probl. Cell. Differ.* 36, 149-169.
36. Lehman, W., Vibert, P., Uman, P., and Craig, R. (1995) *J. Mol. Biol.* 251, 191-196.
37. Lehman, W., Rosol, M., Tobacman, L. S., and Craig, R. (2001) *J. Mol. Biol.* 307, 739-744.
38. Corrie, J. E. T., Brandmeier, B. D., Ferguson, R. E., Trentham, D. R., Kendrick-Jones, J., Hopkins, S. C., van der Heide, U. A., Goldman, Y. E., Sabido-David, C., Dale, R. E., Criddle, S., and Irving, M. (1999) *Nature* 400, 425-430.
39. Hopkins, S. C., Sabido-David, C., van der Heide, U. A., Ferguson, R. E., Brandmeier, B. D., Dale, R. E., Kendrick-Jones, J., Corrie, J. E. T., Trentham, D. R., Irving, M., and Goldman, Y. E. (2002) *J. Mol. Biol.* 318, 1275-1291.
40. Ferguson, R. E., Sun, Y. B., Mercier, P., Brack, A. S., Sykes, B. D., Corrie, J. E. T., Trentham, D. R., and Irving, M. (2003) *Mol Cell* 11, in press.
41. Corrie, J. E. T., Craik, J. S., and Munasinghe, V. R. N. (1998) *Bioconjugate Chem.* 9, 160-167.
42. Maniatis, T., Fritsch, E. F., and Sambrook, J. (1982) in *Molecular Cloning: A Laboratory Manual* pp 68-69, Cold Spring Harbor Laboratory Press, Cold Spring Harbor, N.Y.
43. Muhandiram, D. R., and Kay, L. E. (1994) *J. Magn. Reson.* B103, 203-216.
44. Kay, L. E., Keifer, P., and Saarinen, T. (1992) *J. Am. Chem. Soc.* 114, 10663-10665.
45. Kay, L. E., Xu, G. Y., Singer, A. U., Muhandiram, D. R., and Forman-Kay, J. D. (1993) *J. Magn. Reson.* B101, 333-337.
46. Zhang, O., Kay, L. E., Olivier, J. P., and Forman-Kay, J. D. (1994) *J. Biomol. NMR* 4, 845-858.
47. Pascal, S. M., Muhandiram, D. R., Yamazaki, T., Forman-Kay, J. D., and Kay, L. E. (1994) *J. Magn. Reson.* B103, 197-201.
48. Ogura, K., Terasawa, H., and Inagaki, F. (1996) *J. Magn. Reson. B* 112, 63-68.
49. Zwahlen, C., Legault, P., Vincent, S. J. F., Greenblatt, J., Konrat, R., and Kay, L. E. (1997) *J. Am. Chem. Soc.* 119, 6711-6721.

50. Delaglio, F., Grzesiek, S., Vuister, G. W., Zhu, G., Pfeifer, J., and Bax, A. (1995) *J. Biomol. NMR* 6, 277-293.
51. Johnson, B. A., and Blevins, R. A. (1994) *J. Biomol. NMR* 4, 603-614.
52. Brunger, A. T., Adams, P. D., Clore, G. M., DeLano, W. L., Gros, P., Grosse-Kunstleve, R. W., Jiang, J. S., Kuszewski, J., Nilges, M., Pannu, N. S., Read, R. J., Rice, L. M., Simonson, T., and Warren, G. L. (1998) *Acta Crystallogr. D Biol. Crystallogr.* 54, 905-921.
53. Gagné, S. M., Li, M. X., and Sykes, B. D. (1997) *Biochemistry* 36, 4386-4392.
54. Laskowski, R. A., MacArthur, M. W., Moss, D. S., and Thornton, J. M. (1993) *J. Appl. Crystallogr.* 26, 283-291.
55. Gagné, S. M., Tsuda, S., Li, M. X., Chandra, M., Smillie, L. B., and Sykes, B. D. (1994) *Protein Sci.* 3, 1961-1974.
56. Farrow, N. A., Muhandiram, R., Singer, A. U., Pascal, S. M., Kay, C. M., Gish, G., Shoelson, S. E., Pawson, T., Forman-Kay, J. D., and Kay, L. E. (1994) *Biochemistry* 33, 5984-6003.
57. Spyropoulos, L., Gagne, S. M., and Sykes, B. D. (2001) in *Proceedings of the International School of Structural Biology and Magnetic Resonance* (Jardetzky, O., and Lefevre, J. F., Eds.) pp 37-44, Plenum Press, New York.
58. Lipari, G., and Szabo, A. (1982) *J. Am. Chem. Soc.* 104, 4546-4559.
59. Lipari, G., and Szabo, A. (1982) *J. Am. Chem. Soc.* 104, 4559-4570.
60. Gagné, S. M., Tsuda, S., Spyropoulos, L., Kay, L. E., and Sykes, B. D. (1998) *J. Mol. Biol.* 278, 667-686.
61. Schurr, J. M., Babcock, H. P., and Fujimoto, B. S. (1994) *J. Magn. Reson. B* 105, 211-224.
62. Spyropoulos, L., Li, M. X., Sia, S. K., Gagné, S. M., Chandra, M., Solaro, R. J., and Sykes, B. D. (1997) *Biochemistry* 36, 12138-12146.
63. Wishart, D. S., and Sykes, B. D. (1994) *J. Biomol. NMR* 4, 171-180.
64. Lavigne, P., Bagu, J. R., Boyko, R., Willard, L., Holmes, C. F., and Sykes, B. D. (2000) *Protein Sci.* 9, 252-264.
65. Herzberg, O., and James, M. N. G. (1985) *Nature* 313, 653-659.
66. Slupsky, C. M., and Sykes, B. D. (1995) *Biochemistry* 34, 15953-15964.
67. Sabido-David, C., Hopkins, S. C., Saraswat, L. D., Lowey, S., Goldman, Y. E., and Irving, M. (1998) *J. Mol. Biol.* 279, 387-402.
68. Sabido-David, C., Brandmeier, B., Craik, J. S., Corrie, J. E. T., Trentham, D. R., and Irving, M. (1998) *Biophys. J.* 74, 3083-3092.

## Chapter V

### *In situ Orientations of Protein Domains: Troponin C in Skeletal Muscle Fibers*

#### **GENERAL NOTE**

Although our NMR studies on mutant C contributed to the analysis of the results presented here<sup>†</sup>, we did not contribute to the preparation of TnC mutants and muscle fibers, nor did we play any role in the fluorescence measurements. To respect the original figure and table numbering, the experimental section follows Results and Discussion.

#### **SUMMARY**

A recently developed approach for mapping protein-domain orientations in the cellular environment was used to investigate the  $\text{Ca}^{2+}$ -dependent structural changes in the tropomyosin/troponin complex on the actin filament that regulate muscle contraction. Polarized fluorescence from bifunctional rhodamine probes attached along four  $\alpha$ -helices of troponin C (TnC) was measured in permeabilized skeletal muscle fibers. In relaxed muscle the N-terminal lobe of TnC is less closed than in crystal structures of the  $\text{Ca}^{2+}$ -free domain, and its D helix is approximately perpendicular to the actin filament. In contrast to crystal structures of isolated TnC, the D and E helices are not collinear. On muscle activation, the N-lobe orientation becomes more disordered and the average angle

---

<sup>†</sup> The work presented here was published as Ferguson, R. E., Sun, Y. B., Mercier, P., Brack, A. S., Sykes, B. D., Corrie, J. E. T., Trentham, D. R., and Irving, M. (2003) *Mol. Cell*.

between the C helix and the filament changes by  $32 \pm 5^\circ$ . These results illustrate the potential of *in situ* measurements of helix and domain orientations for elucidating structure-function relations in native macromolecular complexes.

## INTRODUCTION

Although X-ray crystallography and NMR can describe the *in vitro* structures of macromolecular components at near-atomic resolution, the cellular function of these molecules often depends on dynamic interactions in macromolecular complexes that cannot be reproduced *in vitro*, particularly in the conditions required for conventional high-resolution structural methods. New techniques are required to elucidate macromolecular structure-function relations *in situ*. One such method, based on polarized fluorescence from bifunctional rhodamine probes cross-linking pairs of cysteines in a target protein domain, was recently developed and used to measure changes in the orientation of myosin domains during force generation in muscle (Corrie et al., 1999; Hopkins et al., 2002). Here we describe further developments of this method and its application to investigate the  $\text{Ca}^{2+}$ -dependent structural changes that regulate muscle contraction.

Regulation of contraction in skeletal and cardiac muscle is mediated by a complex of tropomyosin and troponin bound to the helical actin filament (Figure V-1A; Ebashi et al., 1969). Tropomyosin is a flexible coiled-coil that binds to seven actin monomers in each strand of the filament. Troponin has three components, TnT, TnI and TnC (Greaser and Gergely, 1971), whose arrangement in the ternary complex is unknown. The

schematic representation of troponin in Figure V-1A reflects this lack of structural information, and one aim of the present work is to determine the orientation and conformation of TnC in the complex.

Muscle activation is initiated by binding of  $\text{Ca}^{2+}$  to TnC, which leads to structural changes in the actin/tropomyosin/troponin complex resulting in an azimuthal movement of tropomyosin around the filament that unmask binding sites on actin for myosin (Hazelgrove, 1973; Huxley, 1973; Parry and Squire, 1973). Myosin binding has a positive co-operative effect on regulation (Farah and Reinach, 1995; Gordon et al., 2000), and the complete regulatory mechanism involves dynamic transitions between complexes of eight gene products (actin, tropomyosin, TnT, TnI, TnC, and the three myosin polypeptide chains). Although high-resolution *in vitro* structures are available for most of these components, it is clear that *in situ* structural techniques will be required to describe the mechanism of the functional regulatory complex.

The present work is the first step of such a program and focuses on the first component in the signaling pathway, TnC. Several *in vitro* structures of skeletal muscle TnC (Figure V-1B) and its N- and C-lobes [amino acids 1 to 90 (Gagné et al., 1994) and 88 to 162 (Mercier et al., 2001) respectively] have been described (Gagné et al., 1995; Herzberg and James, 1985; 1988; Houdusse et al., 1997; Mercier et al., 2001; Satyshur et al., 1988; Slupsky and Sykes, 1995; Soman et al., 1999; Strynadka et al., 1997; Sundaralingam et al., 1985; Vassylyev et al., 1998). When crystallized in isolation, TnC

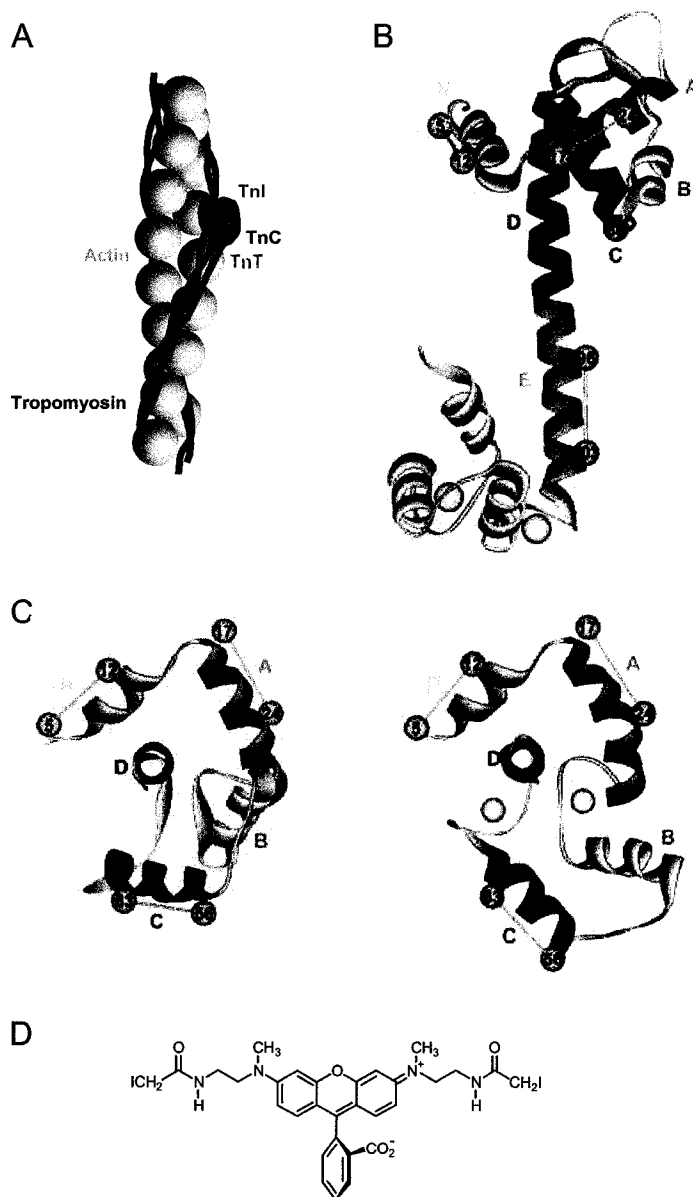


Figure V-1. Bifunctional rhodamine (BR) labeling of TnC. (A) Arrangement of tropomyosin and the troponin components TnT, TnI and TnC on the actin filament, modified from Heeley et al. (1987). (B) Ribbon representation of avian fast skeletal muscle TnC (Herzberg and James, 1988) showing the four pairs of cysteine residues (b-carbons shown as yellow spheres) that were crosslinked in a series of mutant TnCs by the BR probe. Ca<sup>2+</sup> ions are shown as gray spheres. The N-lobe of TnC is in the APO state. Residue 63 on the C helix that was replaced by a cysteine is not visible in this view. (C) Ribbon representation of the N-lobe of avian fast skeletal muscle TnC where the N-lobe is in the apo- (left panel) and Ca<sup>2+</sup>-bound state (right panel) (from Gagné et al., 1995). The view is down the D helix from V83 to E76. Modeled using ViewerPro™ (Accelrys Inc. San Diego, CA). (D) Bis-iodoacetamidorrhodamine (BR-I<sub>2</sub>).

exists as an elongated dumbbell shaped molecule (Figure V-1B; Herzberg and James, 1988; Houdusse et al., 1997). TnC has a bi-lobal but more compact globular shape in solution (Slupsky and Sykes, 1995) and in a crystalline complex with a peptide fragment of troponin I (Vassylyev et al., 1998).

The N-lobe of isolated TnC undergoes a transition over the physiological range of  $[Ca^{2+}]$  from a 'closed'  $Ca^{2+}$ -free to a more 'open'  $Ca^{2+}$ -bound structure in which the B and C helices move away from the 'NAD domain' that contains the N, A and D helices (Figure V-1C). This opening exposes a hydrophobic surface to which the 'switch peptide' of troponin I (residues 115-131 in the skeletal TnI sequence) is thought to bind (Li et al., 1999; McKay et al., 1997; Vassylyev et al., 1998), thereby initiating the tropomyosin movement that allows force generation to occur (Farah et al., 1994; Herzberg and James, 1988; Tripet et al., 1997 and references therein). The C-lobe of TnC also interacts directly with actin filament proteins such as the N-terminal region of troponin I (Mercier et al., 2001; Vassylyev et al., 1998), but its role in the regulation of muscle contraction is unclear (Grabarek et al., 1992).

In the experiments reported below, we measured the orientation and conformation of  $\alpha$ -helices and domains of TnC in isolated muscle fibers by polarized fluorescence. Pairs of cysteine residues in a set of four mutant TnCs were introduced onto the N, A, C or E helices (Figure V-1B), with the cysteines seven residues (i.e. two turns of the helix) apart and their  $\beta$ -carbons at surface-exposed positions. No suitable pair of surface residues was available on the D helix. The introduced cysteines were then cross-linked

by a bifunctional rhodamine (BR) probe (Figure V-1D). Following the replacement of endogenous TnC by the individual labeled BR-TnC mutants in permeabilized skeletal muscle fibers, the orientation and conformation of helices and domains of TnC in the cellular environment were inferred from polarized fluorescence intensities for each rhodamine dipole in the presence and absence of  $\text{Ca}^{2+}$ .

## RESULTS

### *BR probes do not affect TnC function*

---

Each of the labeled TnCs was substituted into single permeabilized rabbit psoas muscle fibers from which the endogenous TnC had been removed. After TnC extraction, the maximum  $\text{Ca}^{2+}$ -activated force was  $33 \pm 9 \%$  (mean  $\pm$  SD; n=44 preparations) of pre-extraction level, indicating 60% extraction of endogenous TnC (Moss et al., 1985). After reconstitution with each BR-TnC, force recovered to  $79 \pm 12 \%$  (n=44) of pre-extraction level. Similar recovery was obtained for unlabeled recombinant TnC ( $83 \pm 8 \%$ , n=5), indicating that neither cysteine mutagenesis nor subsequent labeling with the BR probe significantly altered the functional properties of the TnC. The dependence of force on  $[\text{Ca}^{2+}]$  was fitted with the Hill equation (see Experimental Procedures). For fibers reconstituted with BR-TnC, the  $\text{Ca}^{2+}$  concentration at half-maximum force (expressed as  $\text{pCa}_{50}$ ) and the Hill coefficient ( $n_H$ ) were  $6.18 \pm 0.16$  and  $2.05 \pm 0.49$  (n=8; two for each BR-TnC) respectively.  $\text{pCa}_{50}$  and  $n_H$  for fibers prior to extraction were  $6.38 \pm 0.13$  and  $2.53 \pm 0.47$  (n=8). The exchange caused  $\text{pCa}_{50}$  to decrease by  $0.19 \pm 0.08$ .  $\text{pCa}_{50}$  decreased by a similar amount,  $0.15 \pm 0.09$  (n=4), in fibers reconstituted with

recombinant TnC. These results reflect the properties of a mixed population of native and BR-labeled TnC but similar results, which will be reported elsewhere, were obtained when > 90% of the native TnC was extracted with trifluoperazine and replaced by BR-TnC.

#### *Changes in orientation of TnC helices upon $Ca^{2+}$ activation*

---

The order parameters  $\langle P_{2d} \rangle$ ,  $\langle P_2 \rangle$  and  $\langle P_4 \rangle$  (Dale et al., 1999; Hopkins et al., 2002) were calculated from the polarized fluorescence intensities for each of the BR-labeled TnCs incorporated into fibers (Table V-1). The time-average orientation distribution of the BR dipoles with respect to the actin filament axis is described by the second and fourth-rank order parameters  $\langle P_2 \rangle$  and  $\langle P_4 \rangle$ , respectively. A decrease in  $\langle P_2 \rangle$  shows that  $\theta$ , the average axial angle of a BR dipole relative to the actin filament, has become more perpendicular. Negative  $\langle P_2 \rangle$  shows  $\theta$  is in the range 54.7-90°.  $\langle P_4 \rangle$  provides somewhat higher resolution orientational information. For narrow distributions of  $\theta$ ,  $\langle P_4 \rangle$  is negative for  $\theta = 45^\circ$ , and positive for  $\theta = 0^\circ$  or  $90^\circ$ .

$\langle P_{2d} \rangle$  describes the amplitude of the rapid probe wobble ( $\tau \sim 1$  ns) that is assumed to be a property of the rhodamine probes bound to a specific site on a protein (Dale et al., 1999).  $\langle P_{2d} \rangle = 0$  for unrestricted rapid wobble, and  $\langle P_{2d} \rangle \rightarrow 1$  as the amplitude of the wobble approaches zero. For the N-, A- and C-helix probes, values of  $\langle P_{2d} \rangle$  imply rapid motion equivalent to wobble in a cone of semi-angle 19-23° with no significant change between the different contractile states (Table V-1).  $\langle P_{2d} \rangle$  was somewhat greater for the E-helix probe implying a wobble semi-angle of 17°.

Table V-1. Order parameters for the BR-TnC in various physiological states.

Dipole Location		Relaxed	Ca <sup>2+</sup> -free rigor	Active	Ca <sup>2+</sup> -rigor	Relaxed	Active
		Full-overlap			Non-overlap		
N helix	<P <sub>2d</sub> >	0.906 <i>0.008</i>	0.893 <i>0.006</i>	0.905 <i>0.008</i>	0.907 <i>0.004</i>		
	<P <sub>2</sub> >	-0.004 <i>0.003</i>	-0.010 <i>0.003</i>	-0.017 <i>0.009</i>	0.014 <i>0.004</i>		
	<P <sub>4</sub> >	-0.023 <i>0.008</i>	-0.011 <i>0.005</i>	-0.008 <i>0.008</i>	-0.015 <i>0.004</i>		
A helix	<P <sub>2d</sub> >	0.906 <i>0.012</i>	0.878 <i>0.016</i>	0.907 <i>0.020</i>	0.899 <i>0.020</i>		
	<P <sub>2</sub> >	0.215 <i>0.009</i>	0.145 <i>0.017</i>	0.170 <i>0.019</i>	0.113 <i>0.011</i>		
	<P <sub>4</sub> >	-0.016 <i>0.007</i>	-0.006 <i>0.012</i>	-0.014 <i>0.014</i>	-0.003 <i>0.015</i>		
C helix	<P <sub>2d</sub> >	0.921 <i>0.021</i>	0.881 <i>0.016</i>	0.911 <i>0.031</i>	0.904 <i>0.019</i>	0.869 <i>0.032</i>	0.897 <i>0.017</i>
	<P <sub>2</sub> >	0.369 <i>0.035</i>	0.180 <i>0.030</i>	-0.053 <i>0.027</i>	-0.068 <i>0.044</i>	0.295 <i>0.027</i>	-0.024 <i>0.027</i>
	<P <sub>4</sub> >	0.103 <i>0.038</i>	0.054 <i>0.013</i>	-0.023 <i>0.010</i>	-0.006 <i>0.008</i>	0.098 <i>0.029</i>	-0.024 <i>0.016</i>
E helix	<P <sub>2d</sub> >	0.950 <i>0.004</i>	0.936 <i>0.010</i>	0.948 <i>0.020</i>	0.942 <i>0.006</i>	0.944 <i>0.006</i>	0.944 <i>0.007</i>
	<P <sub>2</sub> >	0.178 <i>0.008</i>	0.046 <i>0.026</i>	-0.008 <i>0.025</i>	-0.080 <i>0.027</i>	0.171 <i>0.008</i>	0.088 <i>0.018</i>
	<P <sub>4</sub> >	-0.109 <i>0.004</i>	-0.058 <i>0.013</i>	-0.052 <i>0.023</i>	-0.016 <i>0.015</i>	-0.101 <i>0.007</i>	-0.093 <i>0.011</i>

Order parameters <P<sub>2d</sub>>, <P<sub>2</sub>> and <P<sub>4</sub>> calculated from polarized intensities from single muscle fibers containing TnC with BR along the N, A, C or E helix in various physiological states. Relaxed, active, Ca<sup>2+</sup>-free rigor and Ca<sup>2+</sup>-rigor values are from BR-TnC (5-10 fibers for each mutant) at 2.4 μm sarcomere length. Relaxed and active values for the C- and E-helix probes were also obtained at 4.0 μm sarcomere length (non-overlap, 5 fibers for each mutant). Temperature 10 °C. Numbers in italics are the standard deviations.

The orientations of individual BR dipoles were estimated by fitting model orientation distributions to the  $\langle P_2 \rangle$  and  $\langle P_4 \rangle$  values in Table V-1. For each BR-TnC the model assumes a single population of dipoles that has a Gaussian angular distribution,  $\exp(-(\theta-\theta_g)^2/2\sigma^2)$ , where  $\theta_g$  is the peak angle and  $\sigma$  represents the orientational disorder of the BR-TnC in the muscle fiber.

Figure V-2 shows  $\theta_g$  and  $\sigma$  values in different physiological states. The most pertinent data from a functional standpoint are the changes in  $\theta_g$  on  $\text{Ca}^{2+}$  activation of relaxed fibers. Activation produced only small changes in  $\theta_g$  for the N- and A-helix probes. In contrast, the C-helix probe showed a large change in  $\theta_g$ , from  $32^\circ$  in relaxation to  $64^\circ$  in active contraction, as might be expected from the opening of the N-lobe on  $\text{Ca}^{2+}$  binding that occurs *in vitro* (Figure V-1C). The E-helix probe changed to a lesser extent, from  $48^\circ$  in relaxation to  $59^\circ$  in active contraction, indicating motion of or within the C-lobe.

$\text{Ca}^{2+}$  activation in fibers stretched to zero filament overlap to minimize actin-myosin interaction increased  $\theta_g$  for the C-helix probe by the same extent as at full overlap (Figure V-2), showing that  $\text{Ca}^{2+}$  binding alone is sufficient to cause the conformational change in the N-lobe. In contrast, the increase in  $\theta_g$  for the E-helix probe was halved, suggesting that the change in the C-lobe is dependent in part on myosin cross-bridge attachment to actin.

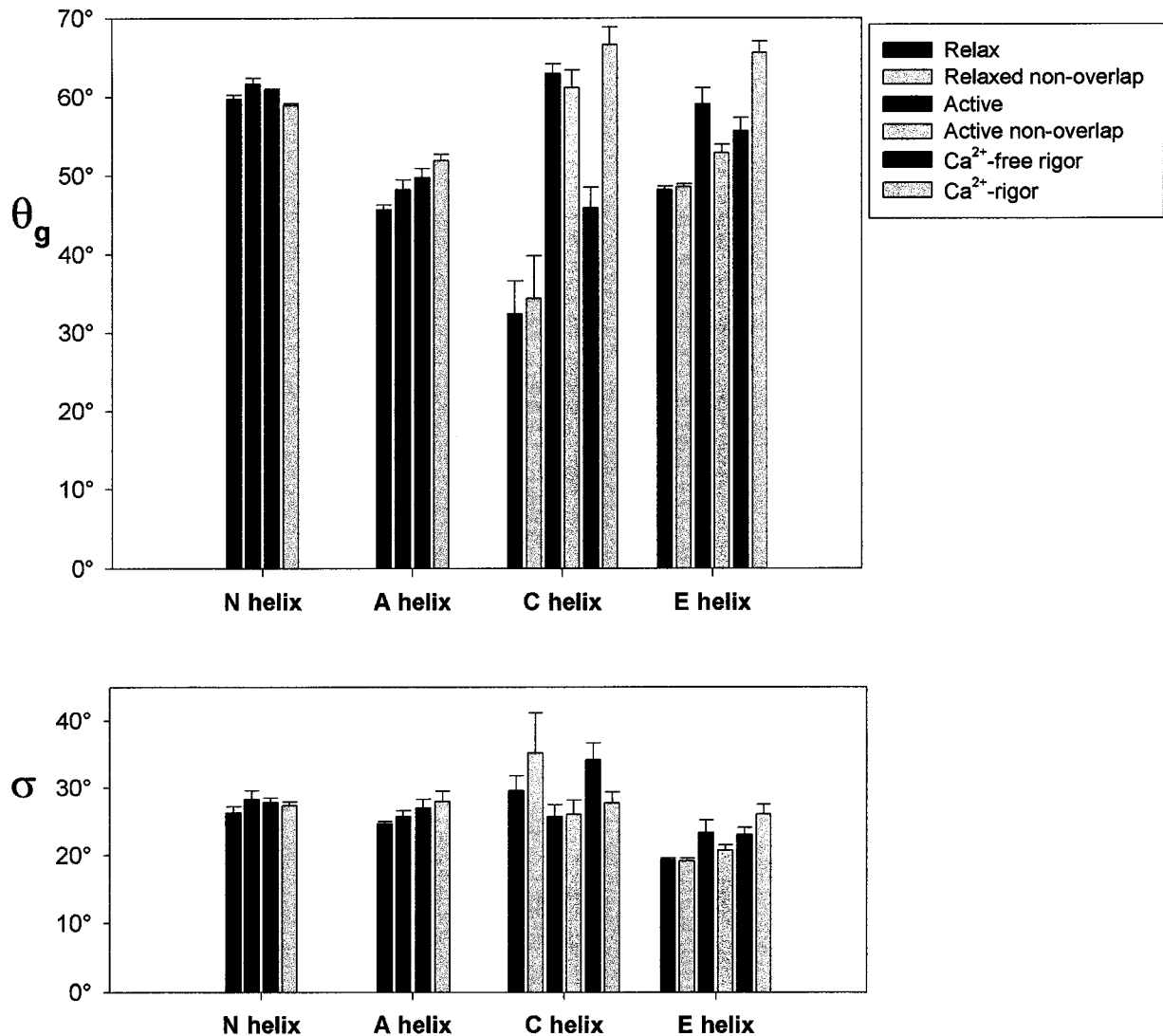


Figure V-2. Fitted Gaussian orientation distribution parameters for each of the BR-labeled TnCs. Relaxed, active, Ca<sup>2+</sup>-free rigor and Ca<sup>2+</sup>-rigor values were measured at 2.4  $\mu\text{m}$  sarcomere length (full overlap).  $\theta_g$  and  $\sigma$  are the peak angle and dispersion of the distribution respectively. Model parameters were fitted to data from individual fibers and then averaged. In the case of the C- and E-helix probes, the relaxed and active values obtained at 2.4  $\mu\text{m}$  sarcomere length are compared with similar data obtained at 4.0  $\mu\text{m}$  sarcomere length (non-overlap). Data (mean  $\pm$  SD) were obtained from 5-10 fibers for each probe.

To investigate further the role of myosin cross-bridge attachment on the structural changes in TnC, fibers were transferred from relaxing to  $\text{Ca}^{2+}$ -free rigor solution.  $\theta_g$  for the C-helix probe increased by  $14^\circ$ , and was  $46^\circ$  at full filament overlap. A similar effect was observed for the E-helix probe, where  $\theta_g$  was  $56^\circ$ , an increase of  $7^\circ$ . Thus cross-bridge attachment induces motions of both lobes in the absence of  $\text{Ca}^{2+}$ . Addition of  $\text{Ca}^{2+}$  to the rigor solution (pCa 4.5) produced a further increase in  $\theta_g$  for the C- and E-helix probes to values beyond those observed during active contraction. Transfer from relaxed to  $\text{Ca}^{2+}$ -rigor solution caused no change in  $\theta_g$  for the N-helix probe and a  $6^\circ$  increase for the A-helix probe.

#### *Orientation of TnC domains*

---

We determined the orientation of the N-terminal lobe of TnC *in situ* by combining polarized fluorescence intensities from the N-, A- and C-helix probes in fibers with *in vitro* data from X-ray crystallographic and NMR studies. As well as using published *in vitro* structures, the NMR structure of the N-lobe of skeletal TnC was determined with bifunctional rhodamine bound to the C helix in a complex with  $\text{Ca}^{2+}$  and the TnI switch peptide (residues 115-131). Details of this structure ( $\text{sNTnC}\cdot 2\text{Ca}^{2+}\cdot \text{TnI}_{115-131}\cdot \text{BR}_{56-63}$ ) will be presented elsewhere (Mercier et al., 2003).

*Structure of the N-lobe of BR-TnC complexed to Ca<sup>2+</sup> and the TnI switch peptide*

The introduction of cysteines at positions 56 and 63 on the C helix of TnC and their cross-linking by BR had little effect on the conformation of the N-lobe of TnC (Figure V-3; Mercier et al., 2003). In particular, the C helix is intact. The fluorescence dipole of BR, parallel to the three coplanar rings of the xanthene, exhibits rapid but restricted wobble with respect to the protein backbone, as discussed above, and the stick model in Figure V-3 shows one possible BR conformer. The average orientation of the BR dipole is expected to be parallel to the C-helix axis.

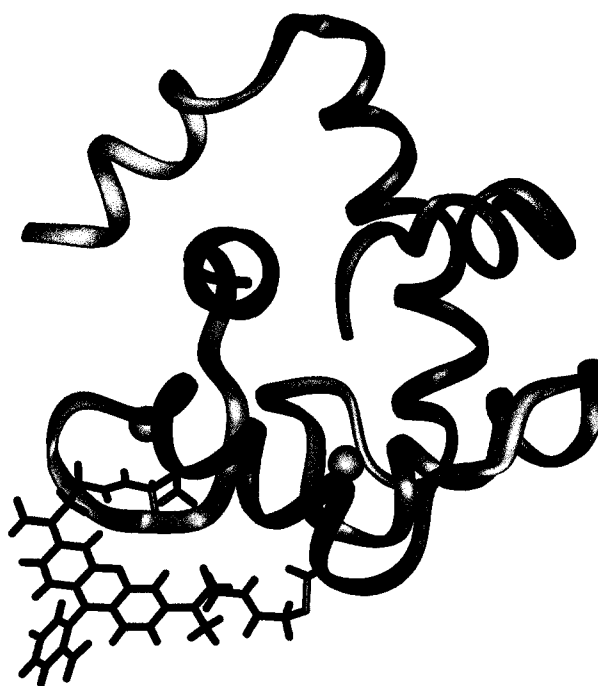


Figure V-3. Ribbon representation of the lowest energy NMR structure of  $s\text{TnC}\cdot 2\text{Ca}^{2+}\cdot \text{TnI}_{115-131}\cdot \text{BR}_{56-63}$  based on Mercier et al. (2003), viewed along the D helix, as in Figure V-1C. The BR is shown in stick representation with the Z,Z configuration of the C-N partial double bonds that join the linker arms to the xanthene ring system, as determined by Mercier et al. (2003). Residues 5-85 of TnC and 115-127 of the TnI peptide are displayed; residue 115 is at the end closer to the D helix. Calcium atoms are shown as gray spheres.

The switch peptide of TnI (magenta) binds to a hydrophobic pocket of TnC in a similar manner to that predicted by McKay et al. (1997) and Vassylyev et al. (1998), and observed in cardiac TnC (Li et al., 1999). However, the orientation of the C helix with respect to the NAD domain in sNTnC•2Ca<sup>2+</sup>•TnI<sub>115-131</sub>•BR<sub>56-63</sub> (Figure V-3) is closer to that in the NMR structure of isolated TnC without Ca<sup>2+</sup> bound to the regulatory sites (Figure V-1C, left; Gagné et al., 1995) than that with Ca<sup>2+</sup> bound to these sites (Figure V-1C right; *ibid.*). Thus, Ca<sup>2+</sup> binding to the regulatory sites opens the N-lobe, but binding of the TnI switch peptide partially recloses it.

#### Determination of *in situ* domain orientations from polarized fluorescence intensities

The analysis is based on the assumption that the fluorescence dipole of the probe is parallel to the  $\beta$ -carbons of the residues cross-linked by the bifunctional rhodamine (Corrie et al., 1999). The orientations of the N-, A-, C- and E-helix probe dipoles in a given *in vitro* TnC structure can then be specified by two angles:  $\phi$ , the angle between the D helix and dipole, and  $\psi$ , the angle between the plane containing the D and A helices and that containing the D helix and dipole (see Experimental Procedures for full definition of  $\phi$  and  $\psi$ ). The values of  $\phi$  and  $\psi$  in seven TnC structures are listed in Table V-2. In the first three structures (APO) the regulatory sites in the N-lobe are Ca<sup>2+</sup> free; in the last four structures (CA) two Ca<sup>2+</sup> ions are bound to these sites.

The orientations of the N- and A-helix dipoles, ( $\phi_N$ ,  $\psi_N$ ) and ( $\phi_A$ ) respectively ( $\psi_A = 0$  by definition), are similar in all the *in vitro* structures; the NAD domain is not much

affected by  $\text{Ca}^{2+}$  binding to the regulatory sites (Figure V-1B and 1C; Gagné et al., 1995; Houdusse et al., 1997). In contrast, the orientation of the C helix changes dramatically on  $\text{Ca}^{2+}$  binding.  $\phi_C$  and  $\psi_C$  decrease, as the N-lobe of TnC adopts a more open conformation (Figure V-1C; Gagné et al., 1995; Houdusse et al., 1997).  $\phi_C$  varies by  $26^\circ$  within the APO group of structures, and by  $47^\circ$  within the CA group. The orientation of the E-helix dipole ( $\phi_E, \psi_E$ ) is even more variable. In crystal structures of isolated TnC the D and E helices form a single continuous helix so  $\phi_E$  is close to zero (Herzberg and James, 1988; Houdusse et al., 1997). However in a crystal complex between TnC and an N-terminal troponin I peptide,  $\phi_E$  is close to  $90^\circ$  (Vassylyev et al., 1998). In solution  $\phi_E$  is highly variable, reflecting considerable mobility between the N- and C-lobes of TnC (Slupsky and Sykes, 1995).

The  $\langle P_2 \rangle$  and  $\langle P_4 \rangle$  values from the N-, A- and C-helix probes (Table V-1) were combined with the  $\phi, \psi$  values from each of the structures (Table V-2) to determine orientations of the N-lobe with respect to the actin filament. We used a maximum entropy analysis that avoids *a priori* assumptions about the shape of the orientational distribution (in contrast to the Gaussian model used in Figure V-2), and yields the broadest distribution that is consistent with  $\langle P_2 \rangle$  and  $\langle P_4 \rangle$  values (Hopkins et al., 2002; van der Heide et al., 2000). Orientations are described by maximum entropy distributions in contour plots of  $\beta$  and  $\gamma$  (Figure V-4), where  $\beta$  is the angle between the D-helix axis and the filament axis, and  $\gamma$  is the angle of rotation of the NAD domain around the D-helix axis (see Experimental Procedures for full definition of  $\beta$  and  $\gamma$ ).

Table V-2. BR dipole orientations for *in vitro* structures of TnC.

		$\phi$ and $\psi$ values for BR-labeled helices of TnC							
State	Structure	N helix		A helix		C helix		E helix	
		$\phi_N$	$\psi_N$	$\phi_A$	$\psi_A$	$\phi_C$	$\psi_C$	$\phi_E$	$\psi_E$
APO	Herzberg and James (1988)-	64	105	121	0	153	-143	3	0
APO	Vassilyev et al. (1998)	53	113	126	0	144	-145	90	147
APO	Gagné et al. (1995) <sup>#</sup>	51	98	115	0	127	-134	*	*
CA/TnI	Mercier et al. (2003) <sup>#</sup>	72	110	123	0	117	-145	*	*
CA	Houdusse et al. (1997)- <sup>†</sup>	54	100	120	0	102	177 <sup>§</sup>	7	-52
CA	Slupsky and Sykes (1995) <sup>#</sup>	79	106	106	0	82	-172	*	*
CA	Gagné et al.(1995) <sup>#</sup>	75	101	106	0	70	-164	*	*

The orientations ( $\phi$  and  $\psi$ ) of the four BR dipoles were calculated for *in vitro* TnC structures (see Experimental Procedures for definition of  $\phi$  and  $\psi$ ). APO denotes structures where the regulatory sites of the N-terminal lobe are Ca<sup>2+</sup>-free; CA indicates structures where these sites are saturated with Ca<sup>2+</sup>. TnI denotes that the TnI switch peptide (residues 115-131) was bound. -Dipole orientations for the APO structure of Satyshur et al. (1988) and the CA structure of Soman et al. (1999) are almost identical to those of Herzberg and James (1998) and the orthorhombic form of Houdusse et al. (1997), respectively. <sup>#</sup>For the NMR structures, dipole orientations were calculated from a representative structure of the family deposited in the Brookhaven database (see Experimental Procedures). \*The orientation of the E-helix dipole ( $\phi_E$  and  $\psi_E$ ) cannot be calculated for the Gagné et al. (1995) and Mercier et al. (2003) models of the N-terminal lobe.  $\phi_E$  and  $\psi_E$  for Slupsky and Sykes (1995) were also not included because of variable orientations between the N- and C-lobes of TnC. <sup>†</sup>Orthorhombic crystal form. <sup>§</sup> $\psi_C$  for the Houdusse model is 11° different that for the Slupsky and Sykes (1995) model; the C-helix dipoles in these models are on the opposite side of 180°.

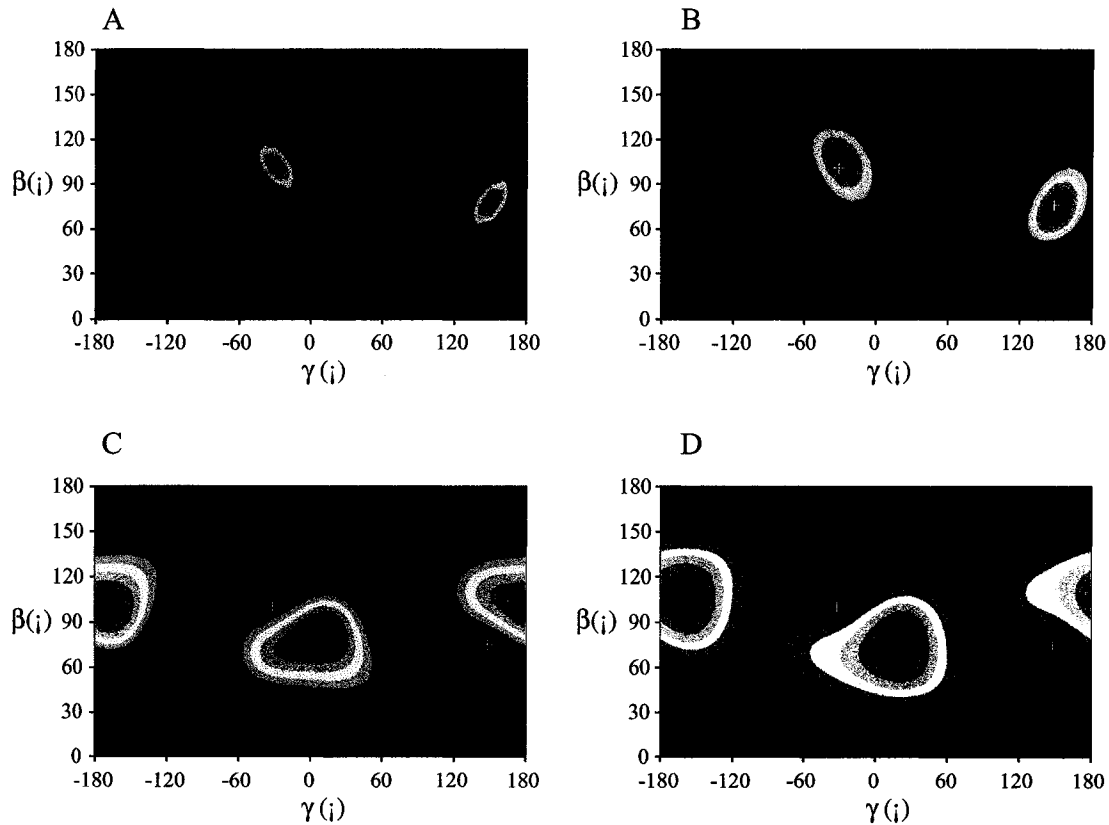


Figure V-4. Maximum entropy distributions for the N-lobe of TnC in various physiological states. Orientation distributions of the N-lobe of TnC with respect to the filament were estimated from measured  $\langle P_2 \rangle$  and  $\langle P_4 \rangle$  values (Table V-1) by maximum entropy and are shown as contour plots.  $\beta$  is the angle between the D helix and the actin filament axis;  $\gamma$  describes rotation of the N-lobe around the D helix. Hotter colors indicate a higher probability of that  $(\beta, \gamma)$  orientation. The orientation distribution for the N-lobe of TnC in (A) relaxed and (B)  $\text{Ca}^{2+}$ -free rigor muscle using the *in vitro* APO structural model of Gagné et al. (1995). The N-lobe distribution in (C) active contraction and (D)  $\text{Ca}^{2+}$ -rigor based on the structure of Mercier et al. (2003) (Figure V-3). The white crosses shown in (B) to (D) indicate peak  $\beta$  and  $\gamma$  values of the maximum entropy distribution observed in relaxed muscle in (A).

---

*In situ orientation of the N-lobe of TnC at low  $[Ca^{2+}]$* 

---

The orientational distribution of the N-lobe of TnC in relaxed muscle fibers based on the NMR-derived solution structure of APO TnC (Gagné et al., 1995) is shown in the contour plot of  $\beta$  and  $\gamma$  in Figure V-4A. There are two equivalent narrow peaks in the distribution, at  $\beta = 102^\circ$ ,  $\gamma = -30^\circ$  and  $\beta = 78^\circ$ ,  $\gamma = 150^\circ$ . These represent the two ends of a dipole (or equivalently the two halves of the muscle sarcomere). Steady-state polarized fluorescence methods cannot distinguish between these alternatives (Corrie et al., 1999), but for consistency we will describe the results in terms of the peak nearer  $\gamma = 0$ . This orientation of the N-lobe of TnC is depicted in Figure V-5A. The D helix is approximately perpendicular to the actin filament axis in relaxed muscle.

Maximum entropy analysis of relaxed fiber data was repeated using the two crystal structures of TnC in the APO state (Table V-2). However, these more closed structures (Herzberg and James, 1988; Vassilyev et al., 1998), with larger  $\phi_C$  values, were inconsistent with the polarized fluorescence data. For these two structural models there is no distribution of  $\beta$  and  $\gamma$  that can reproduce the observed mean  $\langle P_2 \rangle$  and  $\langle P_4 \rangle$  values for the N-, A- and C-helix probes in relaxed muscle, in particular the relatively large values of  $\langle P_2 \rangle$  for the A- and C-helix probes. Varying either of the latter values by up to 3 SDs from the mean did not produce a fit, but reducing  $\phi_C$  from the crystallographic values,  $153^\circ$  (Herzberg and James, 1988) or  $144^\circ$  (Vassilyev et al., 1998) to less than  $130^\circ$  did produce a fit. The APO model of Gagné et al. (1995) has  $\phi_C = 127^\circ$ . We conclude that the N-lobe of TnC in relaxed muscle is more open than in either of the two crystal structures of APO TnC.

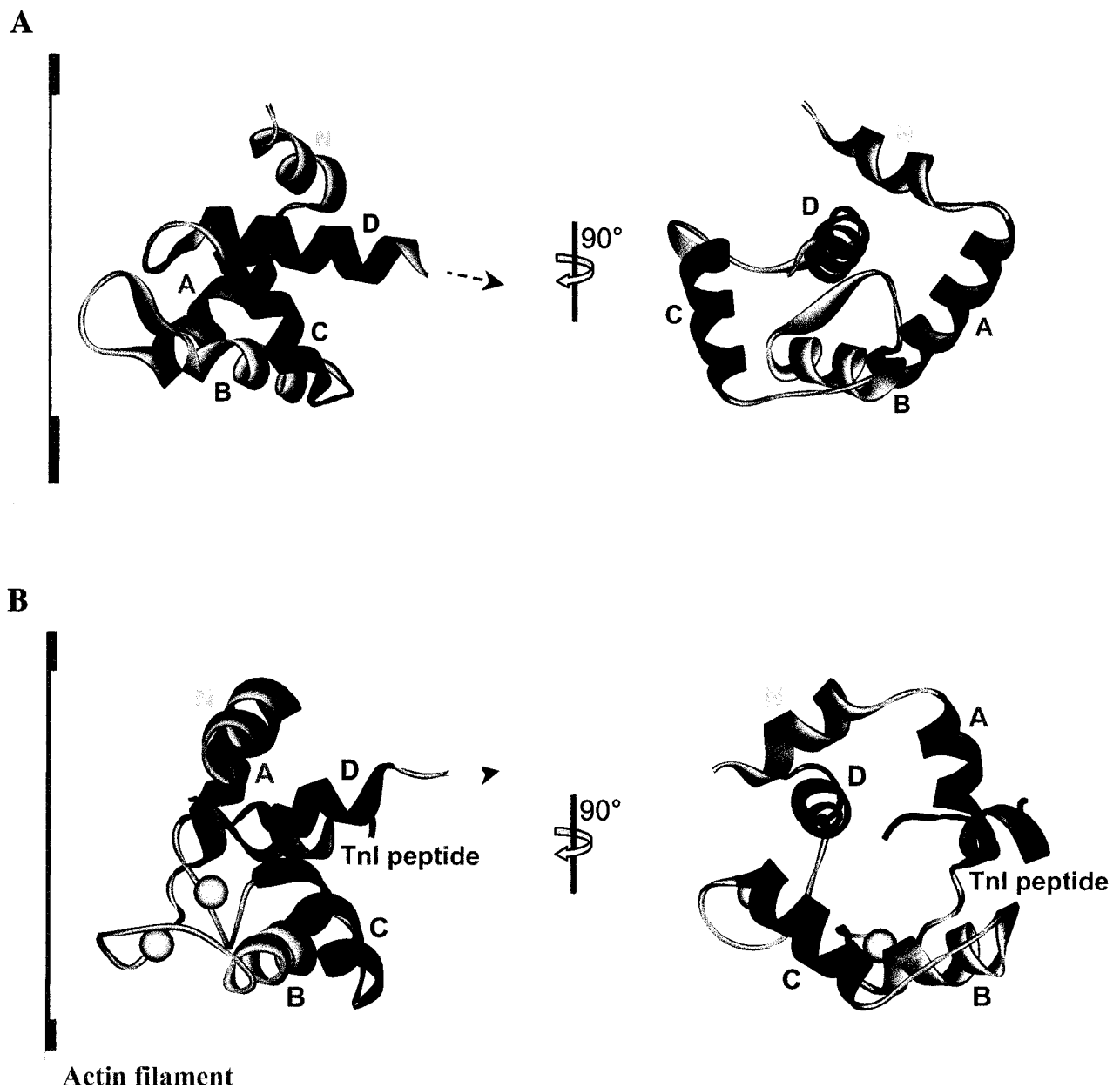


Figure V-5. *In situ* orientation of the N-lobe of TnC on the actin filament. Orientations are derived from peak  $\beta$  and  $\gamma$  values of the maximum entropy distributions shown in Figure V-4. The left panel shows the side-view of TnC orientation with respect to actin; right panel shows the same structure, but rotated  $90^\circ$  azimuthally around the actin filament. (A) Orientation of the N-lobe of TnC in relaxed muscle based on the Gagné et al. (1995) model for the APO state. (B) Orientation of the N-lobe of TnC in active contraction based on the Mercier et al. (2003) model for the CA state.  $\theta_g$  is  $48 \pm 1^\circ$  for the E helix in relaxed muscle (Figure V-2). Since the D helix is roughly perpendicular to the actin filament axis, it follows that the D and E helices are not collinear; there must be a bend of at least  $30^\circ$  between the D and E helices of TnC in relaxed muscle.

When fibers were put into a  $\text{Ca}^{2+}$ -free rigor state (Figure V-4B), the contour plot based on the APO structure of Gagné et al. (1995) was similar to that in relaxing conditions (Figure V-4A) though the distribution is broader in rigor. The white cross in Figure V-4B shows the peak of the contour plot in relaxing conditions. This suggests that binding of myosin heads to actin in  $\text{Ca}^{2+}$ -free rigor induces orientational disorder in the N-lobe without changing its mean orientation.

*In situ orientation of the N-lobe of TnC when  $\text{Ca}^{2+}$  is bound to the regulatory sites*

---

The orientation distribution of the N-lobe of TnC during active contraction, calculated by maximum entropy analysis using the Mercier et al. (2003) structure (Figure V-3), is shown in Figure V-4C. Muscle activation increases the orientational disorder of the N-lobe, and the peak of the orientation distribution moves to  $\beta = 82^\circ$ ,  $\gamma = 10^\circ$ . These values are distinct from those in relaxation (white cross). The conformation of the N-lobe corresponding to the ( $\beta = 82^\circ$ ,  $\gamma = 10^\circ$ ) peak of the contour plot for active contraction is shown in Figure V-5B. The D helix is still quite perpendicular to the actin filament axis but  $\gamma$  increases by  $40^\circ$  on activation, corresponding to a counter-clockwise rotation of the N-lobe around the D helix axis when viewed from the C-lobe, as in the right-hand panels of Figure V-5. The TnI switch peptide is also roughly perpendicular to the actin filament axis during active contraction (Figure V-5B).

The maximum entropy distribution for a rigor fiber in the presence of  $\text{Ca}^{2+}$  (Figure V-4D) was broadly similar to that during active contraction, but the peak values ( $\beta = 75^\circ$ ,  $\gamma = 20^\circ$ ) were somewhat further from those observed during relaxation.

Maximum entropy distributions for the active and Ca-rigor states calculated for the three other CA structural models in Table V-2 also indicated that the ( $\beta$ ,  $\gamma$ ) peak has moved substantially from its relaxed ( $102^\circ$ ,  $-30^\circ$ ) conformation, although this motion is distributed differently between changes in  $\beta$  and  $\gamma$  for the different *in vitro* models. Since the Mercier et al. CA model (Figure V-3) is the only one containing the TnI switch peptide, this model is likely to mimic most closely the *in situ* conformation of the N-lobe with  $\text{Ca}^{2+}$  bound to the regulatory sites.

## DISCUSSION

We used polarized fluorescence from bifunctional rhodamine probes cross-linking pairs of cysteines separated by two turns of an  $\alpha$ -helix to measure the orientation of the helix with respect to a cellular reference axis. The value and accuracy of this approach depend on the mutated and labeled domain having normal structure and function. Here we showed by NMR spectroscopy that mutagenesis and bifunctional rhodamine-labeling of the C helix of TnC did not alter the structure of the labeled domain (Figure V-3; Mercier et al., 2003). At present we cannot exclude the possibility that these modifications may alter *in situ* interactions of TnC with other proteins. The only reported interaction of the residues mutated and labeled in the present work is that of E17 of TnC with R14 of TnI in a binary complex of TnC with the TnI<sub>1-47</sub> peptide (Vassilyev et al., 1998), but this interaction depends on an inter-lobe angle that is not reproduced in the ternary troponin complex (Takeda et al., 2002). Fortunately, the  $\text{Ca}^{2+}$ -sensitivity of active

force production provides an *in situ* measure of possible functional modification of TnC, and all four BR-TnCs used here restored the normal  $\text{Ca}^{2+}$ -sensitivity of active force.

Polarized fluorescence from each of the four BR-TnCs allowed the angle between each labeled helix and the actin filament axis to be measured directly. Thus we showed that the C helix of TnC makes a mean angle of  $32^\circ$  with the actin filament in relaxed muscle (assuming a Gaussian orientational distribution; Figure V-2), and that this changes to  $64^\circ$  during active contraction. These results establish that the C helix undergoes a major reorientation when  $\text{Ca}^{2+}$  binds to the regulatory sites, and provide important constraints on structural models of troponin *in situ* and for the mechanism of muscle regulation.

Analysis of polarized fluorescence data from a set of helices in combination with *in vitro* structural data yields additional information about the orientation and conformation of protein domains *in situ*. The data from the N, A and C helices of TnC in relaxed muscle fibers were inconsistent with the two crystallographic models for APO TnC (Herzberg & James, 1988; Vassylyev et al., 1998). The polarized fluorescence data could however be reproduced by adjusting the orientation of the C helix so that the N-lobe was more open, and the relatively open APO model determined by NMR spectroscopy (Gagné et al., 1995) was consistent with the present results (Figure V-4A). We conclude that the N-lobe of APO TnC is more open *in situ* than in the crystal structures.

The polarized fluorescence data from relaxed muscle, combined with the Gagné et al. (1995) *in vitro* structure, showed that the N-lobe has a narrow range of orientations with respect to the actin filament axis (Figure V-4A), with the D helix approximately perpendicular to the filament (Figure V-5A). This preferred orientation did not change when myosin cross-bridges bound to the actin filament in the absence of  $\text{Ca}^{2+}$  (Figure V-4B). Thus, cross-bridge binding does not change the mean orientation of the N-lobe of TnC, but increases its orientational dispersion.

The polarized fluorescence intensities from probes on the N, A and C helices in active contraction and  $\text{Ca}^{2+}$ -rigor did not allow selection between the four *in vitro* CA models for TnC in Table V-2. Thus our results do not constrain the extent of opening of the N-lobe when  $\text{Ca}^{2+}$  binds to the regulatory sites *in situ*. We presented a detailed analysis of the N-lobe orientation distribution in active contraction (Figure V-4C) and  $\text{Ca}^{2+}$ -rigor (Figure V-4D) based on the structural model of Mercier et al. (2003). Because this model was obtained from the TnC N-lobe with both  $\text{Ca}^{2+}$  and the TnI switch peptide bound, we argued that it is likely to provide the closest approximation to the *in situ* conformation of the N-lobe in the CA state under the conditions of our measurements. The general conclusion that there is a change in the orientation of the N-lobe of TnC on muscle activation (Figure V-5) was independent of the structural model used for the CA state.

Since both the NAD domain (Figure V-5) and the E helix (Figure V-2) change their orientation to the actin filament when  $\text{Ca}^{2+}$  binds, our results, like those of Narita et al.

(2001), do not support models in which either the NAD domain or the C-lobe of TnC acts as a rigid anchor to the actin filament. Rather, they suggest that the whole of the TnC molecule changes conformation when  $\text{Ca}^{2+}$  binds. The change in orientation of the E helix may be indirect and subsequent to that occurring in the C helix, for example if motion of the C-lobe is coupled to that of troponin I and T. Time-resolved fluorescence polarization studies using caged calcium to initiate contraction may help to clarify the sequence of structural changes in the troponin complex following  $\text{Ca}^{2+}$  binding (Bell et al., 2002b).

The bifunctional rhodamine/polarized fluorescence approach has general application for deriving high-resolution *in situ* structures by assembly of component domains with the correct inter-domain angles. Provided that *in vitro* structures are available for the component domains, this approach has three main limitations at present. First, the dipole nature of the probes usually prevents determination of the polarity of the domain orientation with respect to the actin filament or cylindrical symmetry axis; the axial angles  $\beta$  and  $(180^\circ - \beta)$  cannot be distinguished by steady-state measurements. In some cases, this limitation can be overcome by perturbing the structure, for example by applying filament sliding to myosin cross-bridges (Hopkins et al., 2002). Second, changes in the azimuthal orientation of the domain around the symmetry axis cannot be determined. Third, the maximum entropy distribution of domain orientations (Figure V-4) is not unique; it is only the broadest of many possible distributions that are consistent with a given set of observed polarized fluorescence intensities. In this sense the maximum entropy distribution corresponds to a low-resolution view of the actual orientation distribution. These technical limitations make the present technique

complementary in several respects to cryo-electron microscopy, the value of which in describing the structural basis of actin filament regulation in muscle has recently been reviewed (Craig and Lehman, 2002).

Several avenues are open for further development of polarized fluorescence techniques for *in situ* measurements of protein domain orientation and structure. The resolution of orientation measurements can be improved by increasing the number of probe sites (van der Heide et al., 2000) and by the use of pulsed rather than continuous excitation (Bell et al., 2002a; Cone, 1972). These techniques may also allow separate populations of domains with distinct orientations to be resolved, and azimuthal domain motions to be measured. Ambiguities in the interpretation of polarized fluorescence data can also be reduced by applying the approach at the single molecule level (Forkey et al., 2000). The ability to follow structural changes on the millisecond timescale (Corrie et al., 1999; Hopkins et al., 2002) will allow the approach to make an important contribution to mechanistic studies.

We are currently applying these developments to TnC. For example, a set of three or more suitable dipole probes on the NAD domain would allow its orientation to be determined independently of the degree of opening of the N-lobe. The C-helix probe data could then be used to measure the degree of opening *in situ*. Similarly, a set of three or more suitable probes on the C-lobe would allow the TnC inter-lobe angle to be measured during muscle activation.

## EXPERIMENTAL PROCEDURES

### *Mutagenesis of TnC*

---

Double cysteine mutants D5C/A12C, E17C/A24C, E56C/E63C and E96C/R103C of chicken skeletal TnC in the Pet3a expression vector (Pearlstone and Smillie, 1978) were obtained by site-directed mutagenesis using the Stratagene QuikChange™ kit and expressed in *E. coli*. C101 was replaced by alanine. Note that in this recombinant TnC I130 has replaced T130 (Golosinska et al., 1991); this mutation in the C-lobe is unlikely to affect any results in this study. The entire mutant genes were sequenced according to the methods of Sanger et al. (1977).

### *Preparation of TnC*

---

Mutant TnCs were purified from other cellular proteins in 4 L of bacterial lysate by treatment with 5 % TCA, followed by separation on a 100 mL Q-Sepharose fast-flow (Amersham Biosciences) ion exchange column with a 0-400 mM KCl gradient in 6 M urea, 25 mM Tris/HCl, 1 mM MgCl<sub>2</sub> pH 7.5 in a total volume of 1 L, all at 5 °C. TnC typically eluted at 250 mM KCl. Fractions were analyzed by 12 % acrylamide SDS PAGE. Pure fractions were pooled and concentrated by ultrafiltration (PM10 membrane, Amicon) and were dialyzed into 10 mM Tris/HCl, 100 mM NaCl, 1 mM MgCl<sub>2</sub>, pH 7.5 (2 x 5 L each for 2 hr, then 1 x 5 L overnight, all at 4 °C). The dialysis bag was placed on a bed of solid sucrose and TnC concentrated to 10-20 mg/mL. TnC concentration was estimated using calculated extinction coefficients of 2079 M<sup>-1</sup> cm<sup>-1</sup> at 258 nm and 1595

$M^{-1} \text{ cm}^{-1}$  at 263.5 nm, (Gill and von Hippel, 1989); the dual measurement helps correct absorption background anomalies.

### *Bifunctional rhodamine labeling of mutant TnC*

---

Bis-iodoacetamidorhodamine (BR-I<sub>2</sub>) was synthesized as described by Corrie et al. (1998). Approximately 50 mg of mutant TnC was gel filtered (2.5 mL maximum sample volume per PD-10 column, Amersham Biosciences) into labeling buffer containing 25 mM Tris/HCl, 100 mM NaCl, 1 mM MgCl<sub>2</sub>, pH 7.4. The eluted TnC was diluted to ~1 mg/mL (50  $\mu$ M) and incubated with tris(carboxyethyl)phosphine (50  $\mu$ M) for 30 min on ice to reduce disulfides formed during storage. BR-I<sub>2</sub> was added to a final concentration of 100  $\mu$ M from a 15 mM stock solution in dimethylformamide. The solution was incubated in the dark for ~40 min at 20 °C. An aliquot (~6  $\mu$ g of protein) was removed and quenched with sodium 2-mercaptoethanesulfonate (see below) and the time-course of the reaction of BR-I<sub>2</sub> with TnC was monitored by analytical reverse phase HPLC (C18 Hichrom VYDAC column, #218TP54, guard column #218GCC54) with a linear gradient of 60% solvent A (acetonitrile in H<sub>2</sub>O/0.1 % trifluoroacetic acid (TFA)) and 40% solvent B (acetonitrile /0.082 % TFA) to 40% A and 60% B at 1 mL/min over 20 min. Protein elution was monitored by absorbance at 215 nm and rhodamine fluorescence ( $\lambda_{\text{ex}}$  549 nm,  $\lambda_{\text{em}}$  > 580 nm). The elution profiles varied according to mutant and, in general, the desired TnC in which both cysteines had reacted with one BR-I<sub>2</sub> could be resolved from unlabeled TnC and TnC in which the cysteines had reacted with two BR-I<sub>2</sub>. When an optimal level of the 1:1 probe:protein conjugate was obtained, the reaction was quenched by the addition of sodium 2-mercaptoethanesulfonate to a final concentration of 3.3 mM.

2.5 mL aliquots of the quenched reaction were filtered through PD-10 columns in the labeling buffer to remove rhodamine unconjugated to TnC. The eluted protein (typically ~0.4 mg/mL) was purified in 1 mg batches on a preparative reverse phase C4 VYDAC HPLC column (250 x 10 mm). The protein was eluted with a linear 40-60 % acetonitrile gradient (as described above) at 2 mL/min over 1 hr at room temperature. Eluted fractions were immediately transferred to ice and screened by analytical HPLC as above. Fractions containing pure protein from replicate runs (~10 per day) were dialyzed into 10 mM Tris/HCl, 1 mM MgCl<sub>2</sub>, 100 mM NaCl, pH 7.5 (2 x 5 L each for 2 hr, then 1 x 5 L overnight, all at 4 °C). The dialysis bag was placed on a bed of solid sucrose and concentrated to a final concentration of 1-2 mg/mL. Protein concentration was measured using the extinction coefficient of the BR: 52,000 M<sup>-1</sup> cm<sup>-1</sup> at 528 nm (Corrie et al., 1998). Stoichiometry and the specificity of labeling for each mutant TnC were confirmed by a combination of HPLC, tryptic digestion and electrospray mass spectrometry. All the BR-TnCs had the expected molecular weights. As an example, the TnC conjugated with BR along the C helix has a calculated mass of 18,697.3 Da (measured mass 18,696.8 ± 1.2 Da (n=4)).

The 1:1 BR-TnC conjugates were purified to greater than 95 % homogeneity by this procedure, except the N-helix conjugate where purity was > 85 %. The yield of pure protein was typically ~10 %. In general, intramolecular crosslinking of cysteines with BR-I<sub>2</sub> produces diastereoisomers (Corrie et al., 1999), but these were not resolved for any of the BR-TnCs by either analytical or preparative HPLC. In cases where

diastereoisomers were resolved for BR-labeled regulatory light chains, they gave identical polarization ratios in muscle fibers (Corrie et al., 1999).

### *Solutions*

---

Solutions used for fiber measurements were prepared as described previously (Sabido-David et al., 1998a). All experimental solutions contained 1 mM free  $Mg^{2+}$ , 25 mM imidazole, and were adjusted to 150 mM ionic strength and pH 7.1 with KOH and propionic acid except where noted. The relaxing solution also contained 5 mM Mg-ATP, 5 mM  $K_2EGTA$ , 5 mM sodium creatine phosphate (NaCP) and 1 mg/mL creatine phosphokinase (CPK, Sigma). The pre-activating solution in which fibers were incubated for 2 min before activation, contained 5 mM Mg-ATP, 0.2 mM  $K_2EGTA$ , 5 mM NaCP and 1 mg/mL CPK. Activating solution (pCa 4.5) contained 5 mM Mg-ATP, 10 mM CaEGTA, 10 mM NaCP and 1 mg/mL CPK.  $Ca^{2+}$ -free rigor solution contained 5 mM  $K_2EGTA$ , and  $Ca^{2+}$ -rigor solution contained 10 mM CaEGTA.

### *Incorporation of TnC into single muscle fibers*

---

Segments of single fibers were dissected from rabbit glycerinated psoas muscle, and the ends held in aluminium T-clips and fixed by glutaraldehyde (Chase and Kushmerick, 1998). Fibers were extended between two hooks, one of which was fixed and the other attached to a force transducer (AE801; Aksjeselskapet Mikro-elektronikk, Horten, Norway). The microscope stage contained five 40  $\mu$ L glass troughs that could be rotated to change fiber solutions. Fiber diameter and sarcomere length were measured

using a 32 x objective and an ocular graticule. The temperature of the troughs was controlled to  $\pm 0.1$  °C and could be switched between 5 °C and 30 °C within 1 min.

BR-TnC (or recombinant TnC in control experiments) was incorporated into single muscle fibers based on the method of Cox et al. (1981). Native TnC was selectively extracted by bathing the fiber in 10 mM Tris/HCl, 5 mM EDTA, pH 7.85 at 20 °C, at 2.4  $\mu\text{m}$  sarcomere length for 15 min. The fiber was then washed in relaxing solution (2 min) and the sarcomere length re-adjusted to 2.4  $\mu\text{m}$ . The extent of TnC extraction was estimated from the level of residual force at maximal  $\text{Ca}^{2+}$  activation (Moss et al., 1985). Fibers were reconstituted with each BR-TnC by incubation in relaxing solution containing 0.5-1 mg/mL BR-TnC for 35 min at 10 °C. The fiber was given 2 x 2 min washes in relaxing solution and sarcomere length adjusted to 2.4  $\mu\text{m}$ . The TnC content of the fibers was estimated from the force at maximal  $\text{Ca}^{2+}$ -activation.

To determine whether BR-labeling altered TnC's ability to regulate contraction, force-pCa relations were measured and fitted to the Hill equation:

$$\text{Force} = (\text{Maximum } \text{Ca}^{2+} \text{ activated force}) / (1 + 10^{n_H(\text{pCa} - \text{pCa}_{50})})$$

where pCa is the negative  $\log_{10}$  of the  $\text{Ca}^{2+}$  concentration,  $\text{pCa}_{50}$  the negative  $\log_{10}$  of  $[\text{Ca}^{2+}]$  that produces the half-maximum force, and  $n_H$  the Hill coefficient.

---

*Fluorescence polarization, dipole order parameters and orientations*

---

The experimental methods used for measuring steady-state fluorescence polarization have been described previously (Sabido-David et al., 1998a). Steady-state fluorescence polarization was measured with a modified epifluorescence microscope (Ling et al., 1996; Sabido-David et al., 1998a,b). The polarized fluorescence intensities were used to obtain order parameters of the BR dipoles with respect to the muscle fiber axis, using the formalism and assumptions of Dale et al. (1999) and Hopkins et al. (2002). Orientations of BR dipoles with respect to the muscle fiber axis were also calculated as Gaussian distributions (see Figure V-2 legend) from the order parameters (Dale et al., 1999; Hopkins et al., 2002).

---

*BR dipole orientations for in vitro structures of TnC*

---

Assuming that the BR dipole is aligned with the pairs of  $\beta$ -carbons of the labeled residues, the angular coordinates ( $\phi$ ,  $\psi$ ) of the dipoles were calculated for a number of TnC structures.  $\phi$  is the angle between the BR dipole and a D-helix axis that joins the  $\beta$ -carbons of E76 and V83.  $\psi$  is the angle between the plane defined by the D-helix axis and the dipole and that defined by the D-helix axis and an A-helix axis that joins the  $\beta$ -carbons of E17 and A24. An increase in  $\psi$  denotes a counter-clockwise twist of the dipole around the D-helix axis as viewed from V83 to E76.

For the NMR-based solution structures of Gagné et al. (1995) and Slupsky and Sykes (1995), representative structures were selected from the family deposited in the Brookhaven database. For the APO and CA structures of Gagné et al., models 24 and 20 were selected respectively and model 22 was selected from the Slupsky and Sykes structures. In each case the representative structure was chosen on the basis of its  $\phi_C$  and  $\psi_C$  angles being most similar to the average  $\phi_C$  and  $\psi_C$  values in the family of deposited structures.  $\phi_A$ ,  $\phi_C$  and  $\psi_C$  values for the A and C helices of the representative and average structures differed by  $< 1^\circ$  and those for the N helix differed by  $< 8^\circ$ .

#### *Maximum entropy analysis*

---

$\langle P_2 \rangle$  and  $\langle P_4 \rangle$  values recorded from the N-, A- and C-helix probes were combined to describe the angular distribution of the N-lobe of TnC using maximum entropy analysis (van der Heide et al., 2000). The angular distribution of the N-lobe with respect to the filament axis was described in terms of  $\beta$ , the angle between the D-helix axis and the filament axis, and  $\gamma$ , which describes rotation of the NAD domain around the D-helix axis.  $\gamma$  is zero when the plane containing the D- and A-helix axes is parallel to that containing the D helix and the filament axis.  $\beta$  takes values from  $0^\circ$  to  $180^\circ$ , and  $\gamma$  from  $-180^\circ$  to  $+180^\circ$  with an increase in  $\gamma$  denoting a counter-clockwise rotation of the N-lobe around the D-helix axis as viewed from V83 to E76. The contour plots shown in Figure V-4 represent ME number densities, i.e. distribution functions multiplied by  $\sin \beta$  (van der Heide et al., 2000; Hopkins et al., 2002).

---

*Accession Numbers*

---

The atomic coordinates were obtained from the Protein Data Bank with the following ID numbers: 5TNC (Herzberg and James, 1988); 1TN4 (Houdusse et al., 1997); 1TNP (APO structure) and 1TNQ (CA structure) (Gagné et al., 1995); 1TNW (Slupsky and Sykes, 1995); 1TCF (Soman et al., 1999); 1A2X (Vassilyev et al., 1998); 1TOP (Satyshur et al., 1988); xxxx (Mercier et al., 2003).

**REFERENCES**

Bell, M.G., Dale, R.E., van der Heide, U.A., and Goldman, Y.E. (2002a). Polarized fluorescence depletion reports orientation distribution and rotational dynamics of muscle cross-bridges. *Biophys. J.* 83, 1050-1073.

Bell, M.G., Hunter, M., Ellis-Davies, G.C.R., Martyn, D.A., Regnier, M., and Barsotti, R.J. (2002b). Kinetics of cardiac thin-filament activation probed by fluorescence polarization of rhodamine-labeled troponin C. *Biophys. J.* 82, 170a.

Chase, P. B., and Kushmerick, M. J. (1988). Effects of pH on contraction of rabbit fast and slow skeletal muscle fibers. *Biophys. J.* 53, 935-946.

Cone, R.A. (1972). Rotational diffusion of rhodopsin in the visual receptor mechanism. *Nature New Biol.* 236, 39-43.

Corrie, J. E. T., Craik, J. S. & Munasinghe, V. R. N. (1998). A homobifunctional rhodamine for labeling proteins with defined orientations of a fluorophore. *Bioconjug. Chem.* 9, 160-167.

Corrie, J. E. T., Brandmeier, B. D., Ferguson, R. E., Trentham, D. R., Kendrick-Jones, J., Hopkins, S. C., van der Heide, U. A., Goldman, Y. E., Sabido-David, C., Dale, R. E.,

Criddle, S., and Irving, M. (1999). Dynamic measurement of myosin light-chain-domain tilt and twist in muscle contraction. *Nature* 400, 425-430.

Cox, J. A., Comte, M., and Stein, E. A. (1981). Calmodulin-free skeletal-muscle troponin C prepared in the absence of urea. *Biochem. J.* 195, 205-211.

Craig, R., and Lehman, W. (2002). The ultrastructural basis of actin filament regulation. *Results Probl. Cell Differ.* 36, 149-169.

Dale, R. E., Hopkins, S. C., van der Heide, U. A., Marszalek, T., Irving, M., and Goldman, Y. E. (1999). Model-independent analysis of the orientation of fluorescent probes with restricted mobility in muscle fibers. *Biophys. J.* 76, 1606-1618.

Ebashi, S., Endo, M., and Otsuki, I. (1969). Control of muscle contraction. *Q. Rev. Biophys.* 4, 351-384.

Farah, C. S., Miyamoto, C. A., Ramos, C. H., da Silva, A. C., Quaggio, R. B., Fujimori, K., Smillie, L. B., and Reinach, F. C. (1994). Structural and regulatory functions of the NH<sub>2</sub> and COOH-terminal regions of skeletal muscle troponin I. *J. Biol. Chem.* 269, 5230-40.

Farah, C. S., and Reinach, F. C. (1995). The troponin complex and regulation of muscle contraction. *FASEB J.* 9, 755-767.

Forkey, J.N., Quinlan, M.E., and Goldman, Y.E. (2000). Protein structural dynamics by single-molecule fluorescence polarization. *Prog. Biophys. Mol. Biol.* 74, 1-35.

Gagné, S. M., Li, M.X., McKay, R.T., and Sykes, B.D. (1998). The NMR angle on troponin C. *Biochem. Cell Biol.* 76, 302-312.

Gagné, S. M., Tsuda, S., Li, M. X., Chandra, M., Smillie, L.B., and Sykes, B.D. (1994). Quantification of the calcium-induced secondary structural changes in the regulatory domain of troponin-C. *Protein Sci.* *3*, 1961-1974.

Gagné, S. M., Tsuda, S., Li, M. X., Smillie, L. B., and Sykes, B. D. (1995). Structures of the troponin C regulatory domains in the apo and calcium-saturated states. *Nat. Struct. Biol.* *2*, 784-789.

Gill, S. C., and von Hippel, P. H. (1989). Calculation of protein extinction coefficients from amino acid sequence data. *Anal. Biochem.* *182*, 319-326.

Golosinska, K., Pearlstone, J.R., Borgford, T., Oikawa, K., Kay, C.M., Carpenter, M.R., and Smillie, L.B. (1991). Determination of and corrections to sequences of turkey and chicken troponins-C. *J. Biol. Chem.* *266*, 15797-15809.

Gordon A. M., Homsher, E., and Regnier, M. (2000). Regulation of contraction in striated muscle. *Physiol. Rev.* *80*, 853-924.

Grabarek, Z., Tao, T., and Gergely, J. (1992). Molecular mechanism of troponin C function. *J. Muscle Res. Cell Motil.* *13*, 383-393.

Greaser, M. L., and Gergely, J. (1971). Reconstitution of troponin activity from three protein components. *J. Biol. Chem.* *246*, 4226-33.

Hazeltrove, J.C. (1973). X-ray evidence for a conformational change in the actin-containing filaments of vertebrate striated muscle. *Cold Spring Harbor Symp. Quant. Biol.* *37*, 341-352.

Heeley, D.H., Golosinska, K., and Smillie, L.B. (1987). The effects of troponin T fragments T1 and T2 on the binding of nonpolymerizable tropomyosin to F-actin in the presence and absence of troponin I and troponin C. *J. Biol. Chem.* *262*, 9971-9978.

Herzberg, O., and James, M. N. G. (1985). Structure of the calcium regulatory muscle protein troponin-C at 2.8 Å resolution. *Nature* *313*, 653-659.

Herzberg, O., and James, M. N. G. (1988). Refined crystal structure of troponin C from turkey skeletal muscle at 2 Å resolution. *J. Mol. Biol.* 203, 761-779.

Hopkins, S. C., Sabido-David, C., van der Heide, U. A., Ferguson, R. E., Brandmeier, B. D., Dale, R. E., Kendrick-Jones, J., Corrie, J. E. T., Trentham, D. R., Irving, M. and Goldman, Y. E. (2002). Orientation changes of the myosin light chain domain during filament sliding in active and rigor muscle. *J. Mol. Biol.* 318, 1275-1291.

Houdusse A., Love M. L., Dominguez, R., Grabarek, Z., and Cohen C. (1997). Structures of four Ca<sup>2+</sup>-bound troponin C at 2.0 Å resolution: further insights into the Ca<sup>2+</sup>-switch in the calmodulin superfamily. *Structure* 5, 1695-711.

Huxley, H.E. (1973). Structural changes in the actin- and myosin-containing filaments during contraction. *Cold Spring Harbor Symp. Quant. Biol.* 37, 361-376.

Li, M., Spyrapoulos, L. and Sykes, B.D. (1999). Binding of cardiac troponin-I<sub>147-163</sub> induces a structural opening in human cardiac troponin-C. *Biochemistry* 38, 8289-8298.

Ling, N., Shrimpton, C., Sleep, J., Kendrick-Jones, J., and Irving, M. (1996). Fluorescent probes of the orientation of myosin regulatory light chains in relaxed, rigor, and contracting muscle. *Biophys. J.* 70, 1836-1846.

McKay, R.T., Tripet, B.P., Hodges, R.S. and Sykes, B.D. (1997). Interaction of the second binding region of troponin I with the regulatory domain of skeletal muscle troponin C as determined by NMR spectroscopy. *J. Biol. Chem.* 272, 28494-28500.

Mercier, P., Spyrapoulos, L., and Sykes, B.D. (2001). Structure, dynamics, and thermodynamics of the structural domain of troponin C in complex with the regulatory peptide 1-40 of troponin I. *Biochemistry* 40, 10063-10077.

Mercier, P., Ferguson, R.E., Irving, M., Corrie, J.E.T., Trentham, D.R. and Sykes, B.D. (2003). The NMR structure of a bifunctional rhodamine labeled troponin C in complex with the regulatory 'switch' peptide from troponin I; implications for *in situ* fluorescence studies in muscle fibers. *Submitted to Biochemistry*

Moss, R. L., Giulian, G. G., and Greaser, M. L. (1985). The effects of partial extraction of TnC upon the tension-pCa relationship in rabbit skinned skeletal muscle fibers. *J. Gen. Physiol.* 86, 585-600.

Narita, A., Yasunaga, T., Ishikawa, T., Mayanagi, K. and Wakabayashi, T. (2001). Ca<sup>2+</sup>-induced switching of troponin and tropomyosin on actin filaments as revealed by electron cryo-microscopy. *J. Mol. Biol.* 308, 241-261.

Parry, D. A. D., and Squire, J. M. (1973). Structural role of tropomyosin in muscle regulation: analysis of x-ray diffraction patterns from relaxed and contracting muscles. *J. Mol. Biol.* 75, 33-55.

Pearlstone, J. R., and Smillie, L. B. (1978). Troponin T fragments: physical properties and binding to troponin C. *Can. J. Biochem.* 56, 521-527.

Sabido-David, C., Brandmeier, B., Craik, J. S., Corrie, J. E. T., Trentham, D. R., and Irving, M. (1998a). Steady-state fluorescence polarization studies of the orientation of myosin regulatory light chains in single skeletal muscle fibers using pure isomers of iodoacetamidotetramethylrhodamine. *Biophys. J.* 74, 3083-3092.

Sabido-David, C., Hopkins, S. C., Saraswat, L. D., Lowey, S., Goldman, Y. E., and Irving, M. (1998b). Orientation changes of fluorescent probes at five sites on the myosin regulatory light chain during contraction of single skeletal muscle fibers. *J. Mol. Biol.* 279, 387-402.

Sanger, F., Nicklens, S., and Coulsen, A. R. (1977). DNA sequencing with chain terminating inhibitors. *Proc. Natl. Acad. Sci. USA* 74, 5463-5467.

Satyshur, K. A., Rao, S. T., Pyzalska, D., Drendel, W., Greaser, M., and Sundaralingam, M. (1988). Refined structure of chicken skeletal muscle troponin C in the two-calcium state at 2-Å resolution. *J. Biol. Chem.* 263, 1628-1647.

Slupsky, C. M., and Sykes, B. D. (1995). NMR solution structure of calcium-saturated skeletal muscle troponin C. *Biochemistry* 34, 15953-15964.

Soman, J., Tao, T., and Phillips, G. N. (1999). Conformational variation of calcium-bound troponin C. *Proteins* 37, 510-511.

Strynadka, N. C. J., Cherney, M., Sielecki, A. R., Li, M. X., Smillie, L. B., and James M. N. G. (1997). Structural details of a calcium-induced molecular switch: X-ray crystallographic analysis of the calcium-saturated N-terminal domain of troponin C at 1.75 Å resolution. *J. Mol. Biol.* 273, 238-255.

Sundaralingam, M., Bergstrom, R., Strasburg, G., Rao, S. T., Roychowdhury, P., Greaser, M., and Wang, B. C. (1985). Molecular structure of troponin C from chicken skeletal muscle at 3 Å resolution. *Science* 227, 945-948.

Takeda, S., Yamashita, A., Maeda, K. and Maeda, Y. (2002). Crystal structure of the troponin ternary complex. *Biophys. J.* 82, 170a.

Tripet, B., van Eyk, J. E., and Hodges, R. S. (1997). Mapping of a second actin-tropomyosin and a second troponin C binding site within the C terminus of troponin I, and their importance in the Ca<sup>2+</sup>-dependent regulation of muscle contraction. *J. Mol. Biol.* 271, 728-750.

van der Heide, U. A., Hopkins, S. C., and Goldman, Y. E. (2000). A maximum entropy analysis of protein orientations using fluorescence polarization data from multiple probes. *Biophys. J.* 78, 2138-2150.

Vassilyev, D. G., Takeda, S., Wakatsuki, S., Maeda, K., and Maeda Y. (1998). Crystal structure of troponin C in complex with troponin I fragment at 2.3-Å resolution. *Proc. Natl.*

## CHAPTER VI

### *NMR Investigation of the C-domain of Troponin C in the Magnesium State*

#### **GENERAL NOTE**

This chapter reports the first NMR investigation of the structure of the C-terminal domain of skeletal TnC in the magnesium state. The results presented here have not been submitted for publication. The project was originally started in 1999, but was not completed at that time because of the “non-classical” behavior of the C-domain in the Mg<sup>2+</sup> state relative to the well-known Ca<sup>2+</sup> state. Difficulties arose from the presence of multiple species or conformations of sCTnC•Mg<sup>2+</sup>, even at relatively high Mg<sup>2+</sup> concentration. Recently I returned to look at this data, and have calculated the structure of the sCTnC•Mg<sup>2+</sup> complex using an in-house script that I wrote for the automatic assignment of NOEs. This approach had proven to be successful with calbrain (1), a calcium binding protein located in the brain, and was repeated here. Any final conclusions regarding the Mg<sup>2+</sup> state will require more research, so the results presented here should be regarded as preliminary only.

#### **INTRODUCTION**

Magnesium plays an important role in the biochemistry of living creatures. It is involved in several catalytic functions and as a part of different structures. Yet, in a world dominated by a 100-10,000-fold excess of magnesium, Ca<sup>2+</sup>-binding proteins are able to respond to increases in cytosolic concentration from less than 0.1 μM in resting cells to

1-10  $\mu\text{M}$  in activated cells (2), while the  $\text{Mg}^{2+}$  concentration remains between 0.5 and 5.0 mM (3). Taking into account the large excess of  $\text{Mg}^{2+}$  in the cytosol, some or several  $\text{Ca}^{2+}$ -binding sites will inevitably be occupied by  $\text{Mg}^{2+}$ .

Biochemical functional studies on different  $\text{Ca}^{2+}$ -binding proteins have reported a decrease in their apparent affinity for  $\text{Ca}^{2+}$  when studied at physiological  $\text{Mg}^{2+}$  levels (4, 5). For instance, fluorescent studies have demonstrated a decrease in  $\text{Ca}^{2+}$  sensitivity for the N-domain of TnC upon addition of  $\text{Mg}^{2+}$ , for the isolated form (6, 7), the isolated troponin complex (6, 8) and in reconstituted muscle fibers (9, 10). Understanding the behavior of  $\text{Ca}^{2+}$ -binding proteins in their inactivated form and how they accomplish discrimination against  $\text{Mg}^{2+}$  is thus an issue of great importance.

To this day, only a very small number of X-ray structures of  $\text{Ca}^{2+}$ -binding proteins in their  $\text{Mg}^{2+}$ -loaded form have been reported. These include pike parvalbumin (11), myosin regulatory light chain (12) and calbindin  $\text{D}_{9\text{k}}$  (13). Troponin-C and calmodulin (CaM) have not been crystallized in the  $\text{Mg}^{2+}$  form, which explains the absence of any structural information from x-ray crystallography for the muscle regulatory protein and the ubiquitous regulatory  $\text{Ca}^{2+}$ -binding protein in eukaryotic cells.

The mechanisms surrounding  $\text{Mg}^{2+}$  binding to EF-hand motifs are not fully understood. It has been proposed from the analysis of currently available  $\text{Mg}^{2+}$ -loaded structures that the larger ionic radius of  $\text{Ca}^{2+}$  (1.06 Å vs. 0.76 Å) may be one of the major factors contributing to discrimination against  $\text{Mg}^{2+}$ .  $\text{Mg}^{2+}$  binding to

EF-hands imposes more rigorous structural constraints than does  $\text{Ca}^{2+}$ , as  $\text{Mg}^{2+}$  has an inflexible demand for 6-fold coordination in an octahedral symmetry (14, 15). In all cases previously reported, the coordination of  $\text{Mg}^{2+}$  is achieved using the same ligands as  $\text{Ca}^{2+}$ , with the exception that the residues in the 12<sup>th</sup> positions acts as monodentate ligands, rather than bidentate. However, in the x-ray structure of calbindin  $\text{D}_{9k}$  (13), a water molecule ligates  $\text{Mg}^{2+}$  instead of the glutamic acid in the 12<sup>th</sup> position.

A number of NMR investigations of the effects of magnesium binding to CaM have been reported in the literature (16, 17). Similar to TnC, CaM is comprised of two structural domains linked by a flexible tether, each containing 2  $\text{Ca}^{2+}$ -binding loops. As with TnC, the binding of  $\text{Ca}^{2+}$  promotes the “opening” of the structure, resulting in the exposure of a hydrophobic patch that acts as anchoring dock for target protein (18). NMR studies of CaM have revealed only small structural arrangements upon  $\text{Mg}^{2+}$  binding and negligible activation of CAM target proteins (19).

Metal binding to TnC has extensively been inspected by biophysical and biochemical methods (20-24). The affinity of CTnC for  $\text{Ca}^{2+}$  ( $K_{\text{Ca}}=2.1 \times 10^7 \text{ M}^{-1}$ ) is ~100 fold larger than that of NTnC ( $K_{\text{Ca}}=3.2 \times 10^5 \text{ M}^{-1}$ ) (25, 26), and the calcium exchange rate is ~100 fold less for CTnC compared to that of NTnC (23, 27). For these reasons, a study of the effect of  $\text{Mg}^{2+}$  on the N-terminal domain may appear more biologically relevant than with the C-terminal domain. On the other hand, different studies have promoted the notion that the occupancy of the EF-hands by  $\text{Ca}^{2+}$  or  $\text{Mg}^{2+}$  depends on the concentration of both cations and the history of the time course and amplitude of previous  $[\text{Ca}^{2+}]$

transients. There are no experimental data at this time to suggest that  $Mg^{2+}$  cannot exchange with  $Ca^{2+}$  within the C-domain of TnC during the course of the contraction process, so a structural investigation of the CTnC in the  $Mg^{2+}$  state seems biologically justified.

Rosevear et al. recently published an NMR study on the  $Mg^{2+}/Ca^{2+}$  exchange in the cardiac isoform of CTnC (28). Some conclusions in that study were severely criticized by a follow-up letter (29). However, the work of Rosevear et al. showed that metal-binding sites in the C-domain of cardiac TnC exhibited different  $Mg^{2+}$  binding properties, with site III showing a greater affinity for  $Mg^{2+}$  than site IV. In presence of the cTnI<sub>33-80</sub> peptide, the  $Mg^{2+}$  exchange was reduced and the affinity of site IV for  $Mg^{2+}$  was increased. Binding competition assays showed that  $Ca^{2+}$  totally displaces pre-bound  $Mg^{2+}$  in both binding loops. Unfortunately, no quantitative results (dissociation constants, line-shape analysis, etc) from the titration with  $Mg^{2+}$  were reported.

Whether  $Mg^{2+}/Ca^{2+}$  exchange occurs during muscle contraction within the C-domain of TnC is still unknown, as is the biological relevance and consequences of such a process. This chapter presents an NMR investigation of magnesium binding to sCTnC, along with preliminary structures. The object of this research was to get an indication of the possible existence of sCTnC• $Mg^{2+}$  as an active biological complex, measure the  $Mg^{2+}$  affinity and binding kinetics, get an overall behavior of sCTnC in the  $Mg^{2+}$ -loaded form at different temperatures, judge of the stability of the complex, and identify structural changes upon  $Mg^{2+}$  binding.

Important innovations are presently under way in many laboratories worldwide to speed up different processes associated with protein studies by NMR. The ultimate goal is to come up with an automated approach that would allow for the processing of sets of NMR spectra directly into structures in the shortest amount of time and with limited human intervention, while retaining structure quality and precision. Progress has been made at different levels, from ultra-fast data acquisition (30-32) and data processing (33-37), to automatic chemical shift (38-42) and peak assignments (42-44), to structure software (44-46). There is no integrated software suite yet available to do all of this in one single step. Unfortunately, there is a lack of homogeneity in data format as each different piece of software that is available uses a different standard. In this study, chemical shift assignment was done “the old-fashioned way”, i.e. using standard sequential assignment procedures implemented by hand. However, we have used an improved version of an in-house NMRView script for the automatic assignments of NOE peaks from the  $^{15}\text{N}$ -NOESY and  $^{13}\text{C}$ -NOESY experiments. An earlier version of the script had proven to be successful in the generation of structures for calbrain, a calcium-binding protein found in the brain (1). Our script has the advantage to be integrated in the NMRView analysis package software so that no data conversion is required. We tested the performance of the script against the Aria (45, 46) software suite, which also automatically assigns NOEs based on chemical shifts.

## EXPERIMENTAL PROCEDURES

### *Expression and purification of sCTnC.*

---

The expression of sCTnC (88-162) was carried out in *E. coli* using the expression vector pET3a, as described previously for sNTnC (1-90) (47). The expression system differed only in the use of two different oligonucleotides that are complimentary to the sequence and restriction enzyme sites. The expression and purification of [<sup>15</sup>N]sCTnC and [<sup>13</sup>C/<sup>15</sup>N]CTnC in minimal media follows the procedure described for [<sup>15</sup>N]sNTnC (47, 48). Amino acid analysis has shown that the N-terminal methionine, corresponding to the initiation codon, was not cleaved off.

Preparation of both [<sup>15</sup>N]sCTnC and [<sup>13</sup>C/<sup>15</sup>N]sCTnC in the apo state was as described for [<sup>15</sup>N]sNTnC (48). Because of the higher affinity of sCTnC for Ca<sup>2+</sup> than sNTnC, the pH of the 25 mM (NH<sub>4</sub>)HCO<sub>3</sub> buffer for the G25 column was adjusted to 8.6 to increase the efficiency of EDTA.

### *Mg<sup>2+</sup> titration of [<sup>15</sup>N]sCTnC.*

---

Using a Hamilton syringe, aliquots of 0.5 μL or 1 μL of stock 1M ultra pure MgCl<sub>2</sub> solution were added to a 2.7 mM [<sup>15</sup>N]sCTnC sample (as determined by amino acid analysis in triplicate) containing 100 mM KCl, 10 mM imidazole and 15 mM DTT in 90% H<sub>2</sub>O/10% D<sub>2</sub>O at pH 6.8 (uncorrected for <sup>2</sup>H isotope effects). Changes in pH due to additions of MgCl<sub>2</sub> were negligible. Both 1D <sup>1</sup>H and 2D-<sup>1</sup>H, <sup>15</sup>N}-HSQC NMR spectra were acquired at 30 °C at every titration point. All plastic ware used, including

the NMR tube, were washed with 6M HCl to remove potential traces of calcium and any other metal contaminants, and washed with deionized water.

*NMR sample preparation for chemical shift assignment and structure determination*

---

$[^{15}\text{N}]s\text{CTnC}$  and  $[^{13}\text{C}, ^{15}\text{N}]s\text{CTnC}$  were dissolved in 600  $\mu\text{L}$  NMR buffer (treated with Chelex 100 to remove metal contaminants) containing 100 mM KCl, 10 mM imidazole and 15 mM DTT in 90%  $\text{H}_2\text{O}/10\%$   $\text{D}_2\text{O}$ . The pH of the final sample was adjusted to 6.8 if necessary (uncorrected for  $^2\text{H}$  isotope effects). The solution was then filtered, and 480  $\mu\text{L}$  were transferred into an NMR tube, to which 10  $\mu\text{L}$  of 1M DSS and 10  $\mu\text{L}$  of 1.3%  $\text{NaN}_3$  were added. Based on the anticipated protein water and salt content as estimated from amino acid analysis results using similar protein samples in previous studies, the protein concentration was estimated to be  $\approx 2$  mM for both the single and double labeled samples. The content of  $\text{Mg}^{2+}$  was adjusted to the desired concentration by adding 1M  $\text{MgCl}_2$  aliquots from a stock solution. All NMR experiments for chemical shift assignment were run at a  $\text{Mg}^{2+}$  concentration of 50 mM. The unlabeled Rp40 peptide, acetyl-GDEEKRNRAITARRQHLKSVMLQIAATELEK-EEGRREA EK-amide (see (49) for details on synthesis and purification) was later added in progressive amounts to investigate the possible effect of the presence of this peptide on the structure of sCTnC in the magnesium state.

---

*NMR experiments for structure determination.*

---

The assignment of  $^1\text{H}$ ,  $^{13}\text{C}$ , and  $^{15}\text{N}$  resonances, and the subsequent structural determination, were carried out using NMR experiments listed in Table VI-1. The aromatic protons of Phe residues are unassigned. All NMR spectra were acquired at 30 °C on Varian INOVA 500 or Unity 600 spectrometers equipped with 5 mm triple resonance probes and z-axis pulsed field gradients. Processing of the NMR FIDs was performed using the program NMRpipe (50). Generally, linear prediction up to half the number of experimental points was used in indirect dimensions. Data were then zero-filled to twice the number of acquired plus predicted points, and typically multiplied by a sine-bell apodization function shifted by 60° to 90° before Fourier transformation. The program NMRView (51) was used for the analysis and spectral assignment.

---

*Distance and torsion angle restraints.*

---

A novel method based on automatic NOE assignments using an in-house NMRView scripts (see Appendix 2) that I have developed was employed to extract proton-proton distance restraints from the 3D  $^{15}\text{N}$ -NOESY-HSQC and  $^{13}\text{C}$ ,  $^{15}\text{N}$ -NOESY experiments. The NMRView scripts for automatic resonance assignments proceed as follows. First, based on chemical shift information (see Appendix 3 for a list of chemical shifts for sCTnC in the sCTnC•Mg<sup>2+</sup> complex), the assignment possibilities for each cross peaks in both spectra are inspected. Next, the assignment possibilities are automatically eliminated when the corresponding proton interatomic distance in (a) model structure(s) is larger than a threshold distance.

Table VI-1. NMR experiments conducted for the purpose of chemical shift assignment for sCTnC•Mg<sup>2+</sup> and obtaining NOE-based distance restraints at 30 °C.

Exp. Name	Nuclei <sup>a</sup>	<sup>1</sup> H	nt <sup>b</sup>	x-pts <sup>c</sup>	y-pts	z-pts	x-sw	y-sw	z-sw	Ref.
<sup>15</sup> N-HSQC	<sup>1</sup> H, <sup>15</sup> N	600	16	960	256	-	7500	1800	-	(52, 53)
DISPI-HSQC	<sup>1</sup> H, <sup>1</sup> H, <sup>15</sup> N	600	12	960	120	32	7500	6587	1542	(54)
HCCH-TOCSY	<sup>1</sup> H, <sup>1</sup> H, <sup>13</sup> C	600	8	960	128	32	7500	4000	3164	(55)
CBCA(CO)NNH	<sup>1</sup> H, <sup>13</sup> C, <sup>15</sup> N	600	16	960	50	32	7500	9174	1641	(52)
HNCACB	<sup>1</sup> H, <sup>13</sup> C, <sup>15</sup> N	600	32	960	40	32	7500	9174	1641	(52)
<sup>15</sup> N-NOESY-HSQC <sup>d</sup>	<sup>1</sup> H, <sup>1</sup> H, <sup>15</sup> N	600	12	960	128	32	7500	6587	1542	(54)
<sup>13</sup> C, <sup>15</sup> N-NOESY <sup>e</sup>	<sup>1</sup> H, <sup>1</sup> H, <sup>13</sup> C/ <sup>15</sup> N	600	16	832	128	32	7500	7031	3164	(56)
HNHA	<sup>1</sup> H, <sup>1</sup> H, <sup>15</sup> N	500	8	896	64	48	6200	4000	1500	(57)

<sup>a</sup> the nucleus acquired in each dimension (*e.g.* <sup>1</sup>H, <sup>15</sup>N indicates proton x, nitrogen y).

<sup>b</sup> the number of transients acquired for each FID.

<sup>c</sup> 'x,y,z'-pts and 'sw' is the number of complex points and sweep width in each respective dimension (x is the directly detected dimension).

<sup>d</sup> recorded with a NOE mixing time of 125 ms.

<sup>e</sup> recorded with a NOE mixing time of 75 ms.

In the current case, the minimized averaged structure of sCTnC•2Ca<sup>2+</sup>•Rp40 was chosen as the starting model structure, and the cutoff distance for NOE filtering was set to 12 Å.

Because there is chemical shift folding occurring in the carbon dimension of the <sup>13</sup>C,<sup>15</sup>N-NOESY experiment, NOE peaks might have negative or positive intensities in the spectra. The script uses this feature as an additional assignment filter, by comparing the sign of the intensity of a given peak to the expected intensity (negative or positive) of the

current assignment possibility, based on the sweep width of the carbon dimension and the chemical shift of the carbon atom. The program only keeps the assignment for future analysis (see below) if there is a match between the expected and current intensities.

After applying the distance and intensity filtering procedures, each remaining assignment possibility is subjected to a third filtering step, which involves the search for a symmetric peak. For example, for an NOE peak in the  $^{15}\text{N}$ -NOESY-HSQC that could potentially be assigned to (12.HG, 10.HN, 10.N), the computer automatically checks for the presence of a peak in the  $^{13}\text{C}$ ,  $^{15}\text{N}$ -NOESY at a position corresponding to the chemical shift of (10.HN, 12.HG, 12.CG), provided there is chemical shift assignment for 12.CG. If there is no chemical shift assignment for the “parent atom” (the CG carbon of residue 12 in this example), the user can allow or prohibit the assignment from being made. For the current study, because the database of chemical shifts for the protein was incomplete, such cases were not discarded. The computer automatically detects which peak list to look in for symmetric peaks. As such, both peak lists for the  $^{15}\text{N}$ -NOESY-HSQC and  $^{13}\text{C}$ ,  $^{15}\text{N}$ -NOESY are employed simultaneously.

The procedure is repeated for all peaks in both experiments. The unambiguous NOE peaks from the  $^{15}\text{N}$ -NOESY-HSQC and  $^{13}\text{C}$ ,  $^{15}\text{N}$ -NOESY were calibrated separately using the bin method from the built-in NMRView script, which categorized the NOE peaks as weak (1.8-5 Å), medium (1.8-3.4 Å) or strong NOEs (1.8-2.8 Å). The resulting restraints are then merged into one single file and an in-house modification to the NOE calibration script is used to eliminate repetitive NOEs, keeping the largest distance

calibration in case of discordance. The ambiguous peaks from the two peak lists are combined and left uncalibrated (1.8-5Å). This whole procedure was repeated 10 times, with the generation of 100 structures per run. After each run, NOEs that were violated in the majority of the best 30 lowest energy structures were manually inspected and the corresponding NOE peaks were deleted from the peak list if the same violations would reappear in subsequent runs. With the only exception of the use of the model structure of sCTnC•2Ca<sup>2+</sup>•Rp40 for the first round, all subsequent runs were generated using the best 30 lowest energy structures the previous run as input models for the auto-assignment script. The cutoff distance was also reduced from 12 Å for the first round to 6 Å for the second round, to 5.5 Å in the forth round and to 5 Å from the 6<sup>th</sup> round. A total number of 518 unambiguous and 128 ambiguous NOEs were used for the final round of structures.

Backbone  $\phi$  and  $\psi$  restraints were obtained from  $C_{\alpha}$ ,  $C_{\beta}$  and  $H_{\alpha}$  chemical shift information with the software Talos. The Talos output file was automatically calibrated into dihedral angle restraints by Aria (45, 46), using a minimum error of 20 ° on both types of angles.

#### *Backbone amide <sup>15</sup>N relaxation measurements.*

---

All relaxation data (<sup>15</sup>N- $T_1$ , <sup>15</sup>N- $T_2$ , and {<sup>1</sup>H}-<sup>15</sup>N NOE) were acquired with a sample containing 2.7 mM sCTnC in the presence of 20.2 mM Mg<sup>2+</sup> at 30 °C using sensitivity-enhanced pulse sequences developed by Farrow et al. (58) on a Varian INOVA 500 MHz spectrometer.

All  $^{15}\text{N}$ - $T_1$ ,  $^{15}\text{N}$ - $T_2$ , and  $\{^1\text{H}\}$ - $^{15}\text{N}$  NOE experiments were collected with  $768 (t_1) \times 96 (t_2)$  complex points. The  $T_1$  relaxation delays were 11.1, 55.5, 122.1, 199.8, 277.5, 388.5, 499.5, 666, 888 and 1254.3 ms with a 1.2 s delay between repetitions of the pulse sequence. The  $T_2$  experiments were performed with a 3 s delay between repetitions of the pulse sequence to avoid heating effects and the relaxation delays were set to  $16.608 \times n$  ms (where  $n = 1, 2, \dots, 10$ ).  $\{^1\text{H}\}$ - $^{15}\text{N}$  NOEs were measured in the absence (incorporating a relaxation delay of 5 s between repetitions of the pulse sequence) and presence of proton saturation (incorporating 3 s of  $^1\text{H}$  saturation, and a delay between repetitions of the pulse sequence of 2 s). All relaxation data were processed using the NMRpipe program (50) and analyzed using NMRView (51). The data were processed as described above.

**RESULTS***Titration of [<sup>15</sup>N]sCTnC with Mg<sup>2+</sup>.*

Mg<sup>2+</sup> binding to [<sup>15</sup>N]sCTnC was followed by 2D-<sup>1</sup>H, <sup>15</sup>N}-HSQC NMR spectroscopy. The 2D-<sup>1</sup>H, <sup>15</sup>N}-HSQC NMR spectra of a 2.7 mM sample of [<sup>15</sup>N]sCTnC at the beginning of the titration (sCTnC•apo) and the end of the titration (sCTnC•Mg<sup>2+</sup>, 1:8, 20.2 mM Mg<sup>2+</sup>) are shown in Figure VI-1. In Figure VI-1A, the backbone amide peaks fall within regions of <sup>1</sup>H chemical shift characterized as random coil (59, 60), with weak dispersion in the <sup>1</sup>H dimension. Coupled with the lack of downfield backbone Gly peaks in the 10 ppm region in the proton dimension (which is the characteristic signature of G111 and G147 involved in metal binding), this observation is consistent with the lack of secondary structure for sCTnC in the apo state. As the  $[Mg^{2+}]_{total}:[sCTnC]_{total}$  ratio is increased, resonances increase in intensity throughout the entire titration until the spectrum shown in Figure VI-1B is obtained. Concomitantly, the resonances corresponding to CTnC•apo become less intense and completely disappear. However, the number of peaks in the final HSQC spectrum presented in Figure VI-1B is higher than what is predicted from the amino acid sequence. Because of the known difference in Mg<sup>2+</sup>-binding affinity for the two metal binding sites, up to three species can coexist in solution: sCTnC•Mg<sup>2+</sup><sub>siteIII</sub>, sCTnC•Mg<sup>2+</sup><sub>siteIV</sub> and sCTnC•2Mg<sup>2+</sup>. Due to lower Mg<sup>2+</sup>-binding affinity for site IV, sCTnC•Mg<sup>2+</sup><sub>siteIV</sub> is the less populated of the three. For simplicity, and because the relative proportion of each species were not determined in this study, we refer simply to sCTnC•Mg<sup>2+</sup> in the text.

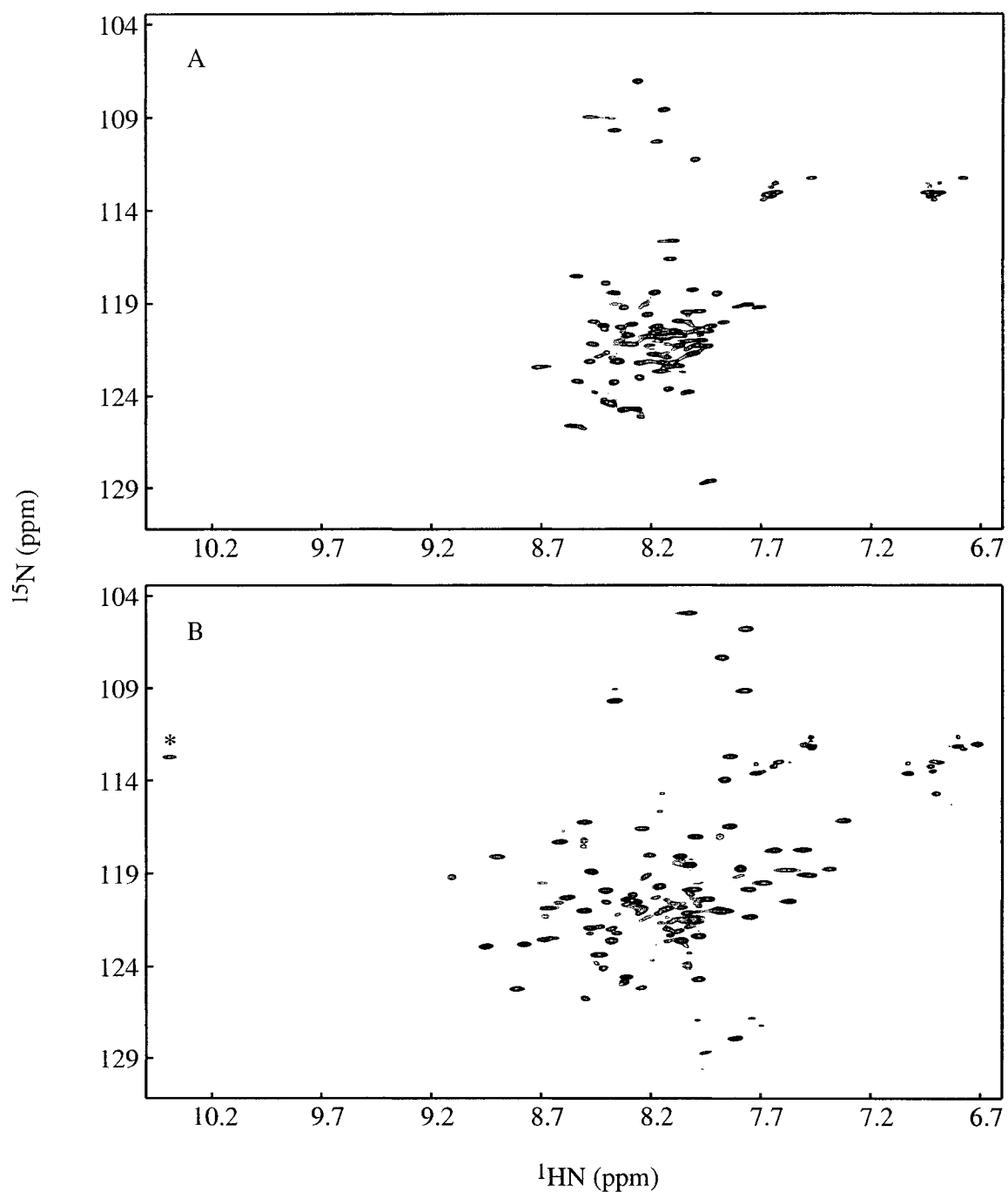


Figure VI-1. 500 MHz 2D- $\{^1\text{H}, ^{15}\text{N}\}$ -HSQC NMR spectrum of (A) 2.7 mM apo sCTnC and (B) sCTnC• $\text{Mg}^{2+}$  (20.2 mM  $\text{Mg}^{2+}$ ) at 30 °C. In B), the asterisk shows the position of the only observed downfield peak.

The increased chemical shift dispersion upon  $\text{Mg}^{2+}$  addition suggests à priori that sCTnC is undergoing  $\text{Mg}^{2+}$ -induced structural folding. Similar to the  $\text{Ca}^{2+}$  titration presented in Chapter II, the spectral changes are consistent with slow exchange kinetics on the NMR time scale. This observation is somewhat different than the titration results previously reported for CaM, where  $\text{Mg}^{2+}$  binding was observed to occur on the fast to intermediate NMR chemical shift timescale, but agrees with previous observations of  $\text{Mg}^{2+}$  binding to TnC (28, 61). Because the spectral changes in the current case occur on slow exchange, the  $\text{Mg}^{2+}$  titration was analyzed from the changes in peak intensity.

The sCTnC response to  $\text{Mg}^{2+}$  is very different to that of  $\text{Ca}^{2+}$ , as judged from the series of 2D- $\{^1\text{H}, ^{15}\text{N}\}$ -HSQC NMR spectra. Figure VI-2 shows the normalized intensity changes for a set of selected resonances as a function of the  $[\text{Mg}^{2+}]_{\text{total}}:[\text{sCTnC}]_{\text{total}}$  ratio. These particular resonances were chosen for their lack of overlap with other peaks and the absence of peaks at their respective frequencies in the apo state. The intensity of some resonances plateau after a threshold concentration of  $\text{Mg}^{2+}$ , whereas others keep increasing through the entire course of the titration. Consequently, an overall  $\text{Mg}^{2+}$  binding curve cannot be obtained from the average of normalized intensity changes measured for different residues, as previously done for the  $\text{Ca}^{2+}$  titration presented in chapter II. As a first approximation, each individual curve was fit according to chemical equilibrium  $\text{P} + \text{Mg} \leftrightarrow \text{P} \cdot \text{Mg}$ , with the assumption of equal and independent  $\text{Mg}^{2+}$  binding sites. The initial protein concentration was doubled to reflect the number of binding sites ( $\text{P}_0 = 2 \cdot [\text{sCTnC}]$ ). The extracted dissociation constant for each selected residue is summarized in Table VI-2. Curve fitting using two different  $\text{Mg}^{2+}$  binding sites (two different dissociation constants) did not statistically improve the quality of the fits.

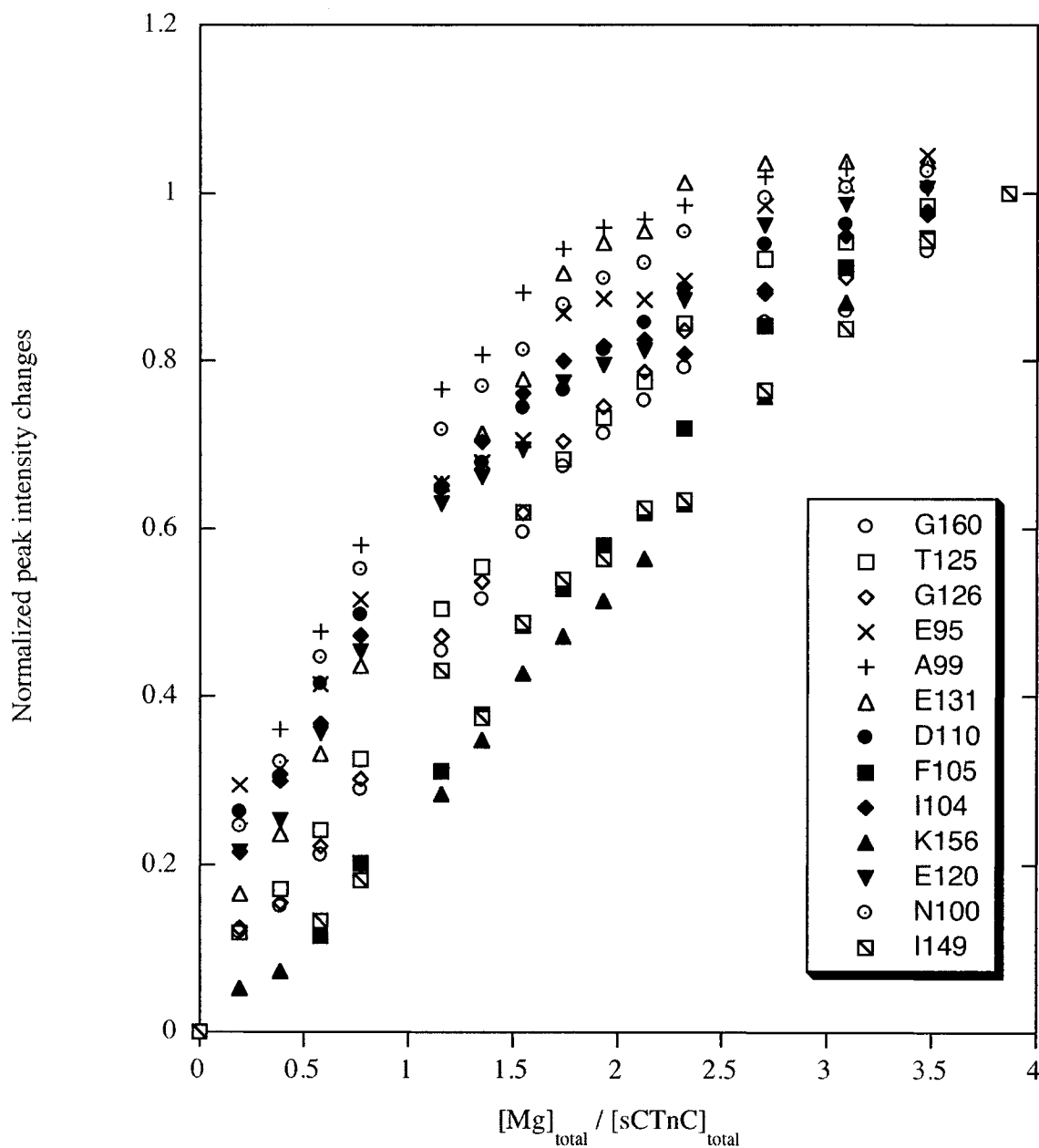


Figure VI-2. Binding curves obtained from the averaged normalized peak intensity changes of different residues (see figure legend) in the 2D- $\{^1H, ^{15}N\}$ -HSQC NMR spectrum of sCTnC during titration with Mg<sup>2+</sup>.

The extracted dissociation constants are not consistent for all residues. The inhomogeneity in the intensity changes could be due to line width changes upon  $Mg^{2+}$  binding. It could also be suggestive of localized and non-cooperative structural changes on the protein upon  $Mg^{2+}$  binding, i.e. certain regions of the protein might get structured before others. This could be the consequence of different affinities of the two binding loops for  $Mg^{2+}$ , and stepwise binding of the  $Mg^{2+}$  ions.

The binding curves in Figure VI-2 show the same profiles as reported by Tsuda et al. in their study of  $Mg^{2+}$  binding to full length rabbit TnC by  $^1H$  NMR (61). Their  $Mg^{2+}$  binding curves for both the N-terminal and C-terminal domains exhibited different dissociation constants for selected residues, and no explanation for the wide dispersion of the data points was put forward. The binding constants were estimated to be in the order of  $10^2$ - $10^5$   $M^{-1}$  for both binding sites of the N and C domains. From our results, the dissociation constant can safely be estimated to be between 1 and 10 mM.

Table VI-2. Dissociation constant and maximum shift extracted from changes in peak intensity of selected residues during sCTnC titration with  $Mg^{2+}$ .

Residue	$K_d$ (mM)	Maximum shift
G160	$12.7 \pm 2.4$	$1.74 \pm 0.16$
T125	$11.1 \pm 1.7$	$1.72 \pm 0.12$
G126	$11.5 \pm 2.3$	$1.72 \pm 0.16$
E95	$2.7 \pm 0.7$	$1.21 \pm 0.07$
A99	$1.0 \pm 0.2$	$1.11 \pm 0.03$
E131	$3.22 \pm 0.8$	$1.13 \pm 0.09$
D110	$2.65 \pm 0.05$	$1.17 \pm 0.06$
F105	$111 \pm 74$	$7.08 \pm 4.00$
I104	$2.4 \pm 0.4$	$1.12 \pm 0.04$
K156	(linear curve)	-
E120	$4.03 \pm 0.61$	$1.28 \pm 0.06$
N100	$1.57 \pm 0.23$	$1.13 \pm 0.03$
I149	$73 \pm 33$	$4.89 \pm 1.78$

*Effect of temperature on sCTnC•Mg<sup>2+</sup>*

---

The spectrum reported in Figure VI-1B shows the unusual characteristic of having only one downfield Gly peak (see position labeled with an asterisk), as two (G111 and G147) would normally be expected. Different causes can explain the presence of a single peak: it may be that the two downfield Gly peaks overlap, that only one of the Mg<sup>2+</sup> site is occupied, or that Mg<sup>2+</sup> binding to one of the site is weak so that metal exchange is faster and the resonance peak is broadened beyond detection. A series of 2D-<sup>1</sup>H, <sup>15</sup>N}-HSQC NMR spectra were recorded at different temperatures (5, 10, 15, 20, 30, 35, 40 and 45 °C) in order to identify the source of this observation. The series of HSQCs showing the selected region of the downfield Gly peaks in Figure VI-3 clearly demonstrate that the Gly peak observed at 30 °C on Figure VI-1B is the result of an overlap between G111 and G147, as the two peaks resolve when the temperature is lowered. The separation of the downfield Gly peaks at 500 MHz starts being visible at 30 °C.

As shown in Figure VI-3, the G111 and G147 backbone amide peaks undergo a downfield shift as the temperature is lowered, moving from (10.31, 112.53) ppm at 45 °C to (10.46, 112.92) ppm and (10.52, 113.59) ppm at 5 °C. No chemical shift assignments were made for the two Gly peaks at 5 °C. The magnitude of the amide proton downfield shift has been shown to correlate with the increased hydrogen bond strength (62). Rosevear et al. also reported the downfield backbone amide shifts of some loop residues and further interpreted the changes in terms of tighter hydrogen bond formation between the corresponding amide protons and the adjacent carboxylate groups. In view of this

rationale, the observed shifts in the current study suggest that a decrease in temperature slows down the  $Mg^{2+}$  exchange and favors  $Mg^{2+}$  binding to sCTnC.

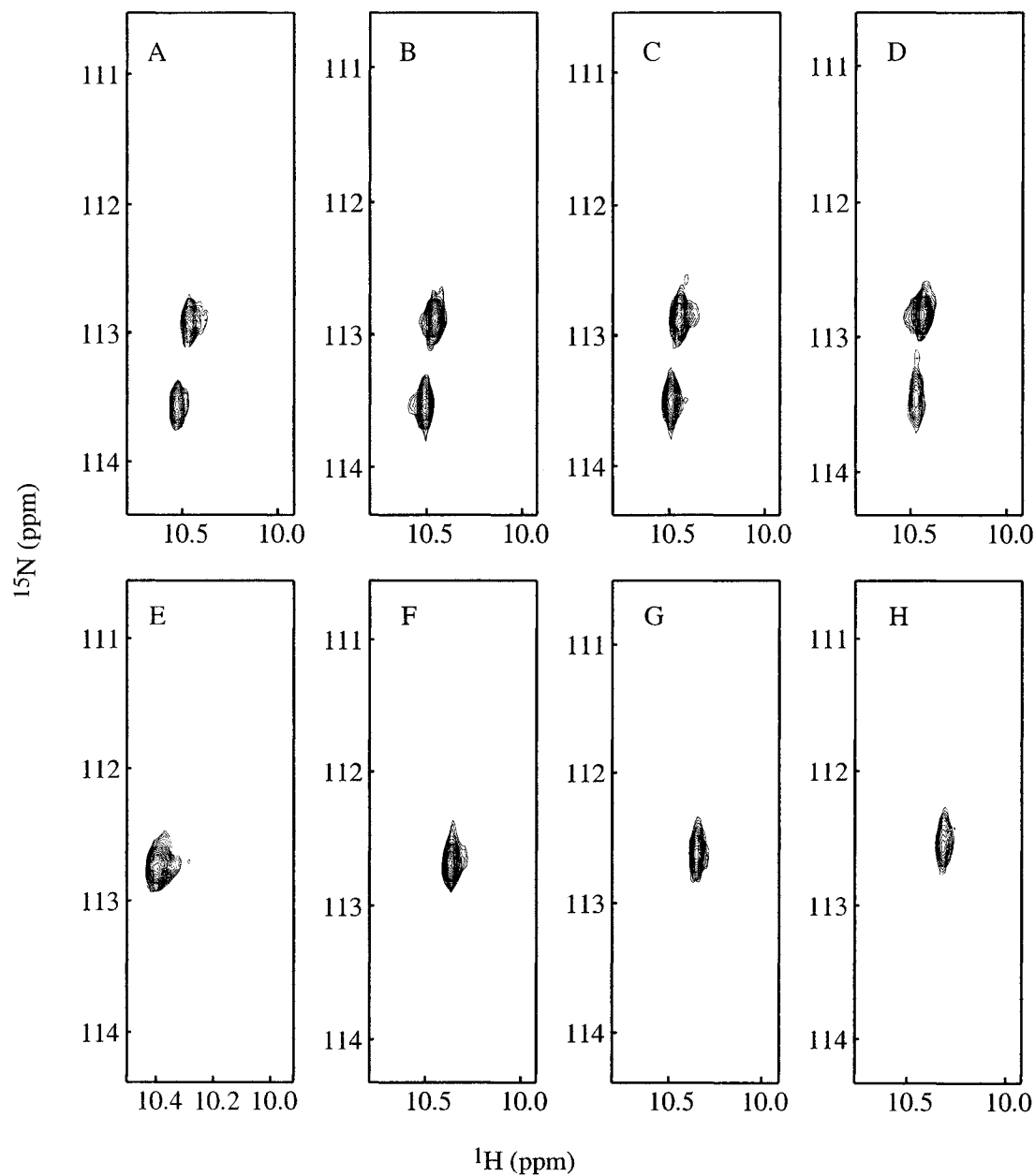


Figure VI-3. Series of 500 MHz 2D- $\{^1H, ^{15}N\}$ -HSQC NMR spectra of sCTnC• $Mg^{2+}$  recorded at (A) 5°C, (B) 10 °C, (C) 15 °C, (D) 20 °C, (E) 30 °C, (F) 35°C, (G) 40 °C and (H) 45 °C. The  $Mg^{2+}$  concentration is 20.2 mM for a  $\sim 8 Mg^{2+}:1$  sCTnC ratio. All spectra are plotted at the same vertical scale.

Figure VI-4 shows the other region of the 2D- $\{^1\text{H}, ^{15}\text{N}\}$ -HSQC NMR spectrum of sNTnC•Mg<sup>2+</sup> recorded at 5 and 45 °C. The larger number of peaks observed on the HSQC spectrum at 5 °C (147 peaks vs. 100 peaks at 45 °C) indicate that multiple conformations (in slow exchange on the NMR timescale) or populations coexist in solution and that the exchange rate is fast enough to broaden the line width beyond detection for some of the peaks at 45 °C. Backbone NH exchange can also contribute to the disappearance of some peaks, for regions of the protein that are exposed to the solvent.

---

*Backbone amide  $^{15}\text{N}$  relaxation measurements on sCTnC•Mg<sup>2+</sup>*

---

The experimental  $^{15}\text{N}$  relaxation values for sCTnC•Mg<sup>2+</sup> are shown in Figure VI-5. Backbone amide  $^{15}\text{N}$  NMR relaxation data were analyzed for only 46 of the 76 residues (60% of the residues). Peak overlap and missing backbone chemical shift information are responsible for the relatively small number of residues for which all three relaxation parameters could be measured ( $T_1$ ,  $T_2$  and NOE).

The dynamic behavior of sCTnC•Mg<sup>2+</sup> shares some features with that of sCTnC•2Ca<sup>2+</sup> as judged for the  $T_1$ ,  $T_2$  and NOE patterns, with a slightly higher flexibility in the linker region (between helices F and G) and prominent flexibility at both termini (63). On the other hand, the relatively high  $T_1$  and  $T_2$  values in site IV are not observed for the Ca<sup>2+</sup>-saturated state, and are indicative here of large backbone motion amplitudes. Unfortunately, relaxation parameters for the majority of the residues near the  $\beta$ -sheets

regions in the binding loops, which are among the most interesting parts of the protein in the current study, could not be measured due to missing backbone chemical shift information and/or peak overlap. However, it is clear from Figure VI-5 that site IV shows a significantly increased flexibility compared to that of site III. This is consistent with previous studies, where site III was reported to have a higher  $Mg^{2+}$  binding affinity than site IV, and where the  $Mg^{2+}$  exchange rate was more pronounced in site IV than site III (28, 64). Although a small portion of relaxation data is missing for residues involved in site III, the current available data suggests that the backbone dynamic occurring in site III is of the same order as observed for the E and F helices. The average backbone NOE (0.63, calculated excluding residues having an NOE < 0.5) is significantly lower than the observed value for residues located in regions of well-defined secondary structures for  $sCTnC \cdot 2Ca^{2+}$  ( $\sim 0.85$ ). Therefore,  $Mg^{2+}$  binding to  $sCTnC$  at 30 °C in presence of 20 mM  $Mg^{2+}$  is not sufficient for the formation of a rigid complex. This could be because of a high  $Mg^{2+}$  exchange at this temperature, or incomplete saturation of the protein with  $Mg^{2+}$ . Using the procedure described in chapter 3, an overall rotational correlation time of  $\sim 5.1$  ns was extracted from the relaxation data, which is in agreement with the value of 5 ns expected for a  $\sim 10$  kDa protein undergoing isotropic tumbling. Therefore, the  $sCTnC \cdot Mg^{2+}$  complex exists as a monomer in solution.

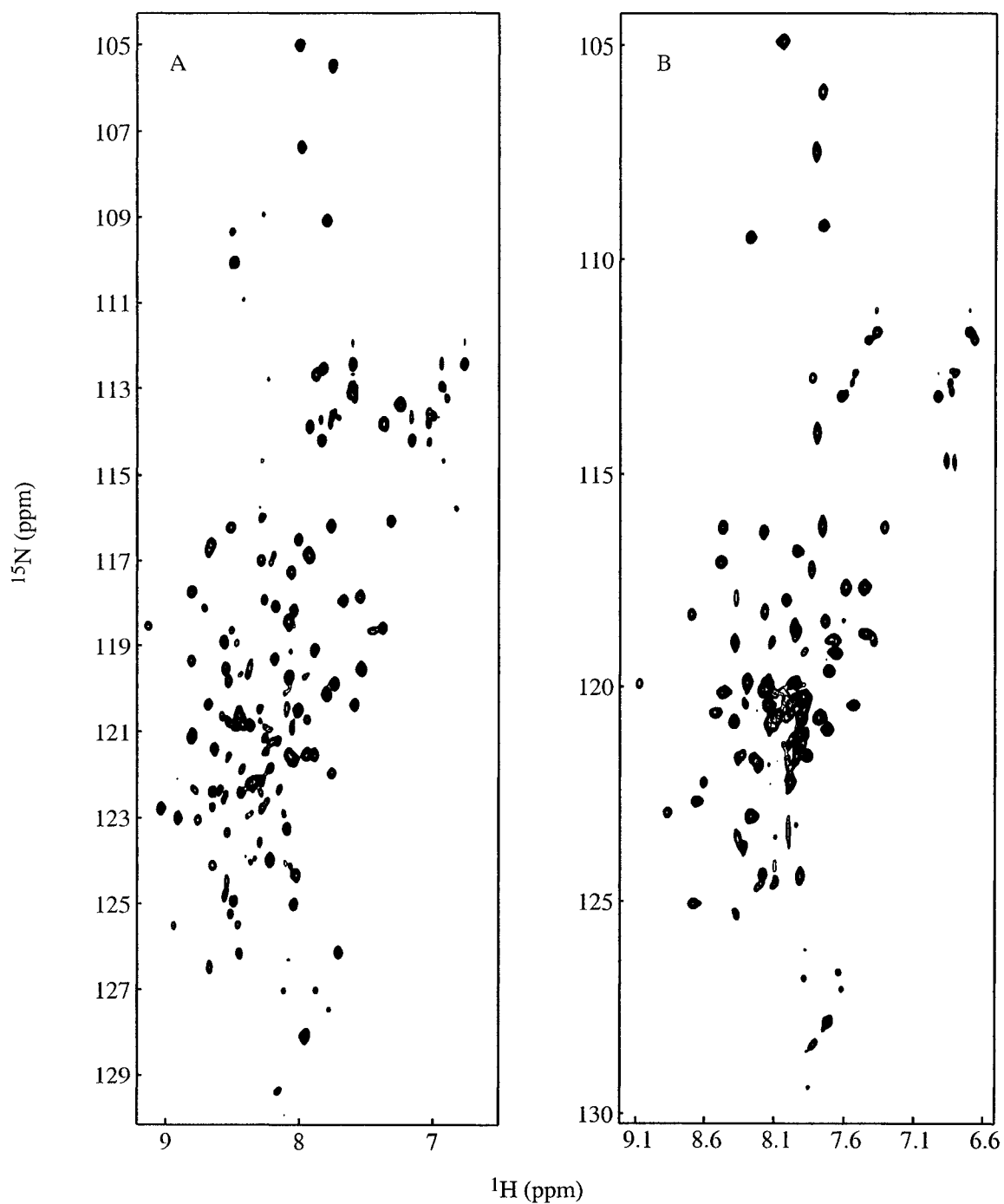


Figure VI-4. Comparison of the 500 MHz 2D- $\{^1\text{H}, ^{15}\text{N}\}$ -HSQC NMR spectrum of  $\text{sCTnC}\cdot\text{Mg}^{2+}$  (20.2 mM  $\text{Mg}^{2+}$ , 7.73  $\text{Mg}^{2+}$ :1  $\text{sCTnC}$  ratio) at (A) 5 °C and (B) 45 °C. For the region corresponding to the downfield Gly peaks, see Figure VI-3. No resonance assignment was done at both of these temperatures.

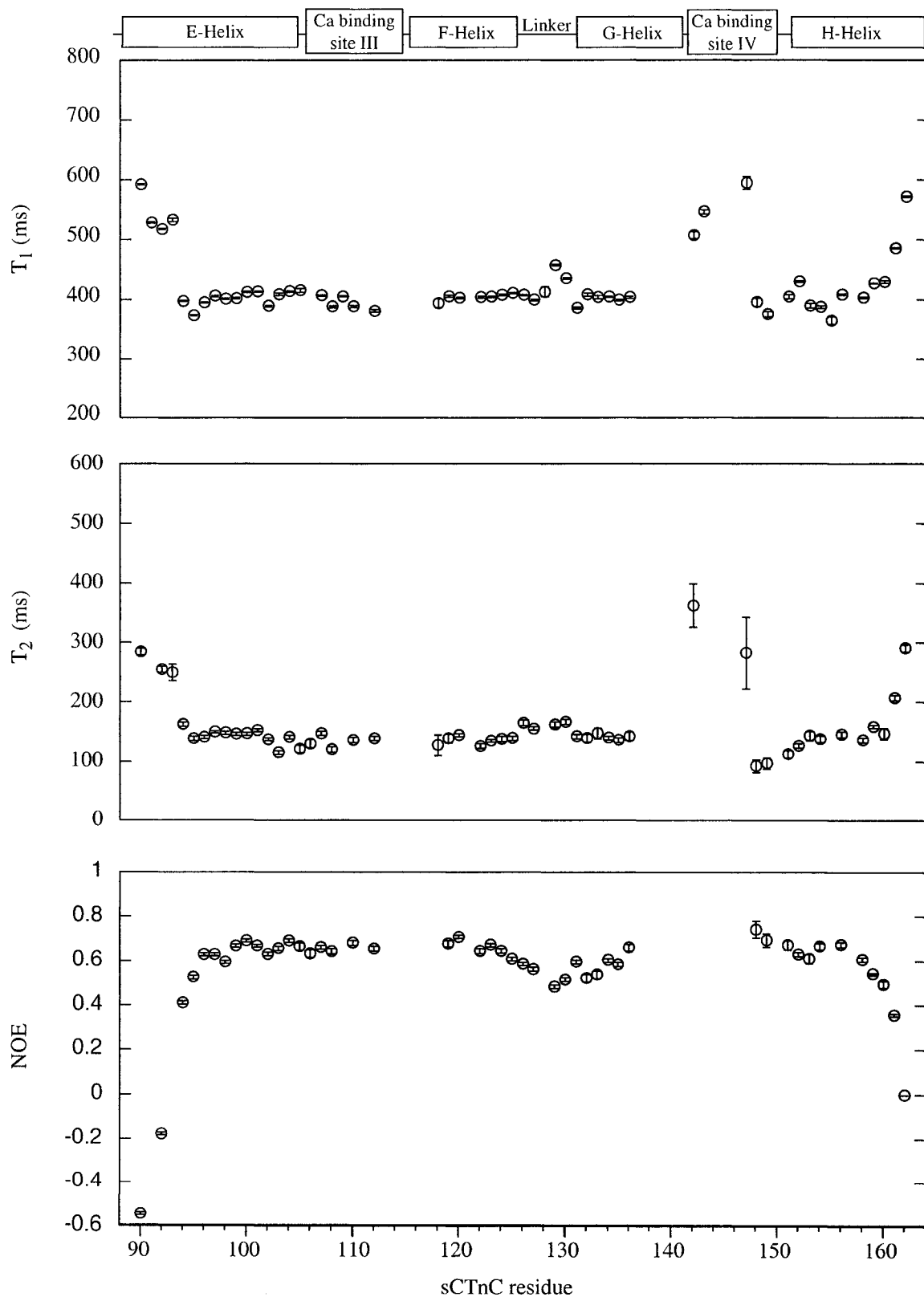


Figure VI-5.  $^{15}\text{N}$  backbone relaxation times for  $\text{sCTnC}\cdot\text{Mg}^{2+}$  (20.2 mM  $\text{Mg}^{2+}$ ) at a magnetic field strength corresponding to a  $^1\text{H}$  Larmor frequency of 500 MHz.

---

*Effect of the addition of Rp40 on sCTnC•Mg<sup>2+</sup>*

---

For cCTnC, the addition of cardiac TnI<sub>33-80</sub> (which is equivalent to the Rp40 region of skeletal TnI) enhanced the binding affinity of site IV for Mg<sup>2+</sup> (28). In order to determine if Rp40 would have the same effect on sCTnC•Mg<sup>2+</sup>, 2D-<sup>1</sup>H, <sup>15</sup>N}-HSQC NMR spectra of sNTnC•Mg<sup>2+</sup> were acquired at increasing concentrations of Rp40. Figure VI-6 presents the last spectrum acquired at a high Rp40 concentration. In these spectra an extra set of peaks becomes visible at lower contour levels around the neighborhood of the downfield shifted G111 and G147 peaks, at the exact position of G111 and G147 in the 2D <sup>1</sup>H, <sup>15</sup>N}-HSQC NMR spectrum of sCTnC•2Ca<sup>2+</sup>•Rp40. We believe that these peaks are due to metal contamination, more specifically Ca<sup>2+</sup>, from the Rp40 peptide. Addition of EGTA did not suppress these peaks. As discussed in Chapter 3, Rp40 forms a tight complex with sCTnC•2Ca<sup>2+</sup> as its binding is thermodynamically highly favorable. Further, the affinity of sCTnC for Ca<sup>2+</sup> is greater than that of EGTA at pH ~ 6.5.

One of the most important characteristics of the spectrum in Figure VI-6 is the appearance of a second downfield Gly peak. The new peak could be the result of a modification in the Mg<sup>2+</sup> binding affinity of site IV, and/or a variation in Mg<sup>2+</sup> exchange kinetics in that site. Structural modifications occurring in site III are not excluded, so that it is formally ambiguous whether the new Gly downfield peak corresponds to G147 or G111. Some peaks in Figure VI-6 (marked by asterisks) share common chemical shifts with those observed for sCTnC•2Ca<sup>2+</sup>•Rp40. These include backbone amide resonances of residues E95, I104, F105, A124, E132, I134, K156, G159, G160 and V161, most of

which have been identified to be involved in the binding of Rp40. These peaks are at a higher concentration than the minor peaks arising from  $\text{Ca}^{2+}$  contamination discussed above. Taking this into consideration, it suggests that these resonances are from  $\text{sCTnC}\cdot\text{Mg}^{2+}\cdot\text{Rp40}$ . The large similarity of these peaks compared to those of  $\text{sCTnC}\cdot 2\text{Ca}^{2+}\cdot\text{Rp40}$  further indicates that the two complexes are structurally very similar. The difference observed in the G111 and G147 backbone chemical shifts in the  $\text{sCTnC}\cdot\text{Mg}^{2+}\cdot\text{Rp40}$  and  $\text{sCTnC}\cdot 2\text{Ca}^{2+}\cdot\text{Rp40}$  complexes are suggestive of slight different geometric arrangements of the binding loops. The fact that the spectrum is not completely converted to a single species implies that the affinity of Rp40 for  $\text{sCTnC}\cdot\text{Mg}^{2+}$  is less than for  $\text{sCTnC}\cdot 2\text{Ca}^{2+}$ .

It was originally proposed that  $\text{TnI}_{96-115}$  would be in competition with Rp40 for binding to sCTnC (65), but recent studies strongly support the conclusion that Rp40 binds to CTnC at all times, i.e. during the relaxed and contractile states of muscle contraction (66-68). In particular, photocrosslinking studies by Luo et al. conducted with different complex constructs of TnC, TnI, TnT, tropomyosin and actin in the presence and absence of  $\text{Ca}^{2+}$  showed no  $\text{Ca}^{2+}$ -dependant distance changes between the Cys-mutated residue 6 of TnI and residue 89 of CTnC, which argues against Tripets's model (67, 68).

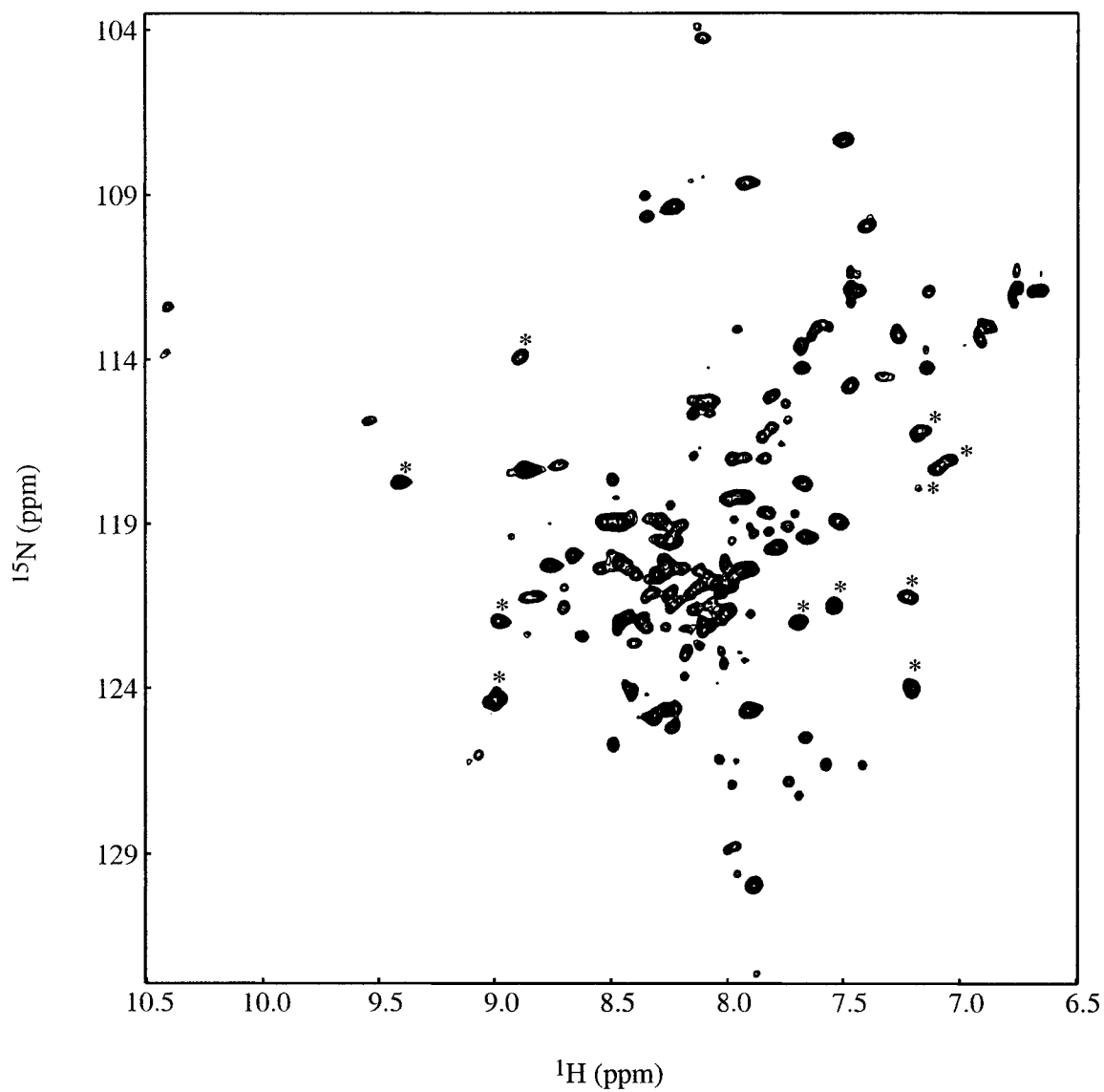


Figure VI-6. 500 MHz 2D  $\{^1\text{H}, ^{15}\text{N}\}$ -HSQC NMR spectrum of sNTnC•Mg<sup>2+</sup>•Rp40 (20.2 mM Mg<sup>2+</sup>) at 30 °C. Backbone resonance peaks that share common chemical shifts with that of sCTnC•2Ca<sup>2+</sup>•Rp40 are indicated with asterisks.

---

*Effect of higher magnesium concentration on sTnC•Mg<sup>2+</sup>*

---

Because all 2D-<sup>1</sup>H, <sup>15</sup>N}-HSQC NMR spectra of sNTnC•Mg<sup>2+</sup> at 20 mM Mg<sup>2+</sup> contain a higher number of peaks than what is predicted from the amino acid sequence, and because some peak intensities had not reached a plateau during Mg<sup>2+</sup> titration presented in the last section, the concentration of Mg<sup>2+</sup> was increased to 50 mM for subsequent studies, to ensure complete saturation of the protein. A second temperature study was performed to assess the influence of higher Mg<sup>2+</sup> concentration. Figure VI-7 depicts the 2D-<sup>1</sup>H, <sup>15</sup>N}-HSQC NMR spectra of sNTnC•Mg<sup>2+</sup> recorded at 5 and 50 °C in presence of 50 mM Mg<sup>2+</sup>. The spectrum in Figure VI-7A is very similar to that of the one shown on Figure VI-4A, with the exception of fewer peaks, especially in the upper part of the spectrum where most of the Gly peaks appear (the effect is more visible at lower contour levels than Figure VI-7A was drawn at). The backbone resonance peaks for residues G111 and G147 did not undergo any chemical shift changes upon increasing the Mg<sup>2+</sup> concentration to 50 mM, suggestive of no additional structural changes in the binding loops. In order to carry on a investigation which would be biologically relevant, it was decided to perform the structural study at 30 °C rather than 5 °C. The 2D-<sup>1</sup>H, <sup>15</sup>N}-HSQC NMR spectra of sNTnC•Mg<sup>2+</sup> at 30 °C is shown in Figure VI-7B. About 98 peaks are present in the spectrum, which is still slightly higher than the expected number from the amino acid sequence. However, the spectrum shows a nice dispersion of chemical shifts in both the <sup>15</sup>N and <sup>1</sup>H dimensions, allowing for a structural determination to be performed. Further addition of Mg<sup>2+</sup> to 100 mM had no consequence on the number of peaks or on their position in 2D-<sup>1</sup>H, <sup>15</sup>N}-HSQC spectrum (data not shown).

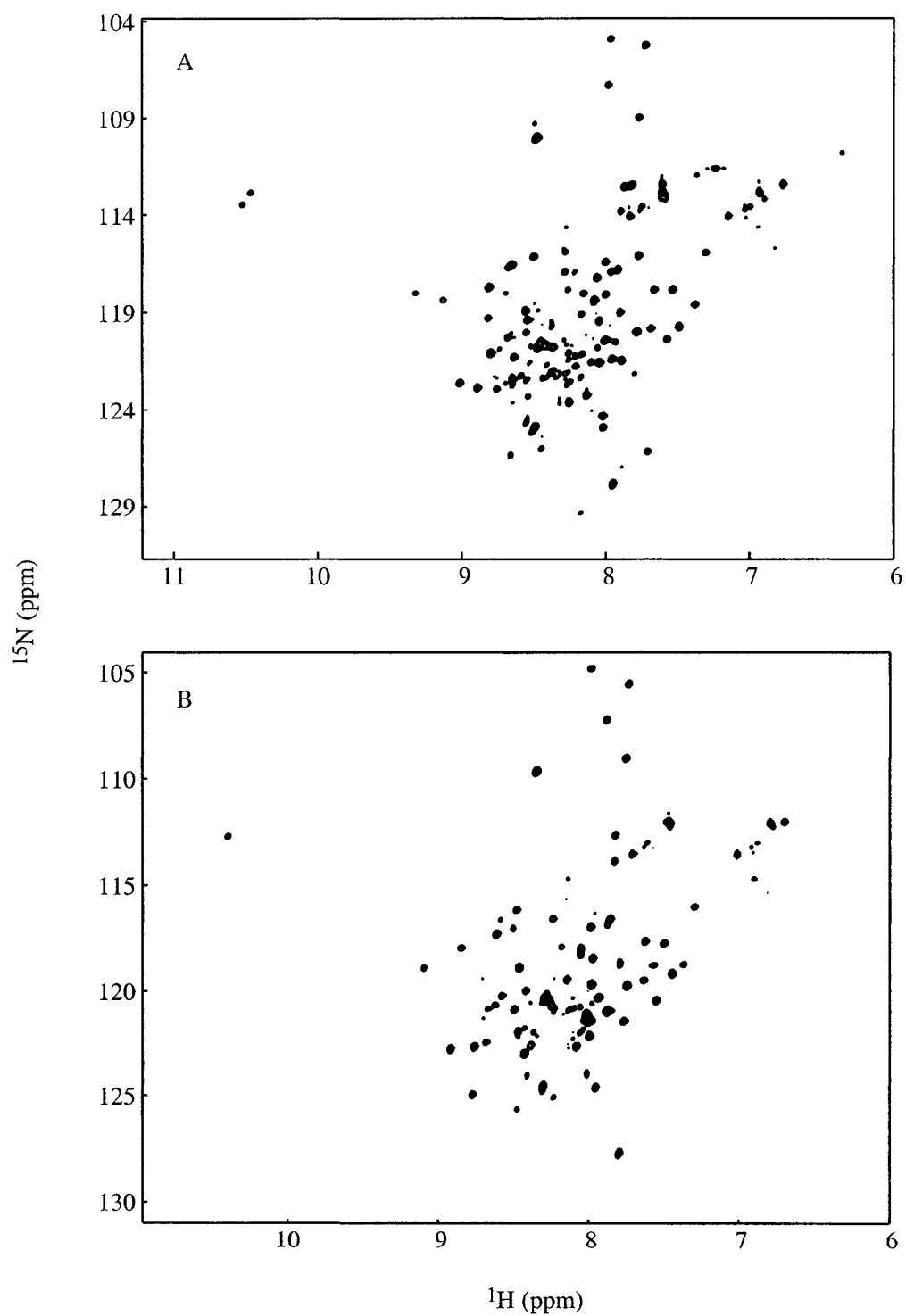


Figure VI-7. Comparison of the 600 MHz 2D- $\{^1\text{H}, ^{15}\text{N}\}$ -HSQC NMR spectrum of sCTnC•Mg $^{2+}$  (50 mM Mg $^{2+}$ ) at (A) 5 °C and (B) 30 °C.

*Mg<sup>2+</sup>-Induced structural changes on sCTnC*

---

Several factors control cation affinity in EF-hand motifs. Several studies have established a correlation between the Ca<sup>2+</sup> affinity of binding loops with the number and location of acid amino acid residues in chelating positions X, Y, Z, -Y, -X and -Z(69-71). In addition to the number of acidic pairs, the hydrophobicity of the  $\alpha$ -helices (72) and the nature of non-coordinating residues have been shown to have a drastic effect on Ca<sup>2+</sup> affinity(64, 73-75). By monitoring tyrosine fluorescence of different CAM/TnC chimeras, Wang et al. demonstrated that the first EF-hand of sCTnC is primary responsible for the higher Ca<sup>2+</sup> and Mg<sup>2+</sup> affinity of the C-domain of TnC relative to that of CaM and that the first EF-hand of sCTnC was largely responsible for Mg<sup>2+</sup> binding (64).

The effects of the Mg<sup>2+</sup>-induced structural changes on sCTnC have never been probed at high atomic resolution. Previous NMR studies have monitored only the changes in chemical shifts of specific residues (61), while fluorescence results have revealed only changes at probed residues. The outcome of Mg<sup>2+</sup>-binding on the tertiary structure of sCTnC and its potential biological relevance are still unknown.

Since chemical shifts are influenced by the secondary structure, the network of hydrogen bonding and chemical environment in general, chemical shift analysis provides a simple yet powerful method for probing changes at specific sites. Contrary to sNTnC (76), since apo sCTnC is largely unstructured, there exists no reference chemical shift data for sCTnC in the apo form. Hence, the analysis is limited to comparisons relative to

chemical shifts obtained in the  $\text{Ca}^{2+}$  state. Figure VI-8 pictures the difference in backbone chemical shifts between the sCTnC  $\text{Ca}^{2+}$ - and  $\text{Mg}^{2+}$ -states. Clearly, the major differences are located in the  $\text{Ca}^{2+}$ -binding sites III and IV. Residues I113, D114 in the first binding loop, and I149 and D150 are particularly affected by  $\text{Mg}^{2+}$  binding relative to  $\text{Ca}^{2+}$  binding. These particular residues are involved in the formation of short 3 residue long anti-parallel  $\beta$ -sheet. The minor perturbations observed for the backbone amide proton chemical shift suggest that the  $\beta$ -sheets are intact in the presence of  $\text{Mg}^{2+}$ . However, the negative difference of the amide backbone proton chemical shift for these residues relative to the  $\text{Ca}^{2+}$  state is might indicate a weaker hydrogen bounding network across the strands due to an increase in distance between the strands and loop condensation around the smaller cation. Similar results were obtained by Finley et al. for cCTnC (28). A  $D_{\text{NN}}$  NOE peak is observed between I113 and I149 in the 3D  $^{15}\text{N}$ -NOESY-HSQC spectrum, which indicates that the  $\beta$ -strands are still in close proximity. Using  $C_{\alpha}$ ,  $C_{\beta}$  and  $H_{\alpha}$  chemical shift information, the program Talos (77) detected the formation of  $\beta$ -sheet for residues F112-I113-D114 and R148-I149-D150. Other regions of sCTnC are fairly unperturbed by  $\text{Mg}^{2+}$  binding relative to the  $\text{Ca}^{2+}$  state, as judged from the backbone chemical shift differences in Figure VI-8.

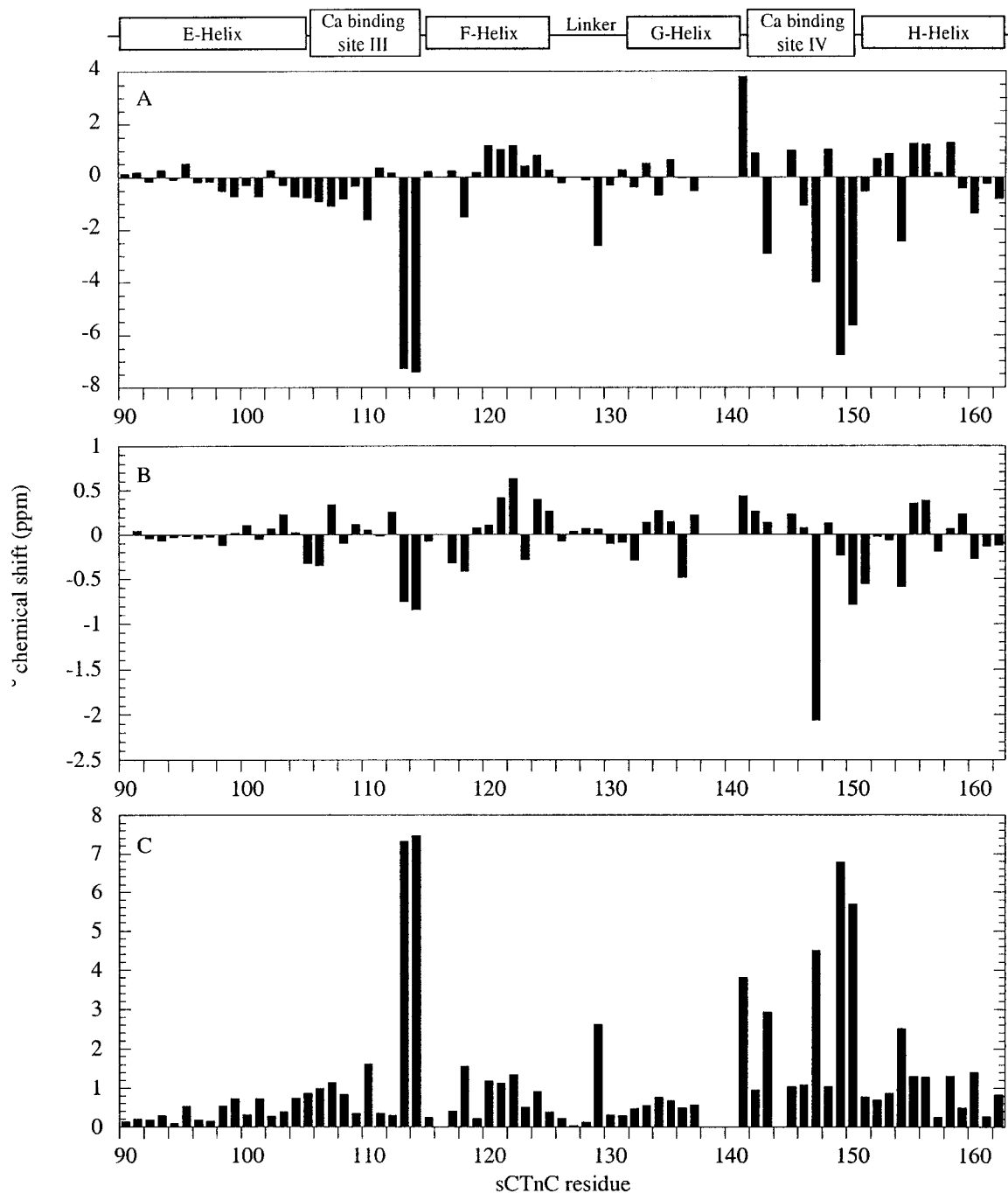


Figure VI-8. Backbone amide chemical shift difference between the  $\text{Mg}^{2+}$ - and  $\text{Ca}^{2+}$ -saturated state of sCTnC. A)  $\Delta N = N_{\text{Mg}} - N_{\text{Ca}}$ , (B)  $\Delta \text{HN} = \text{HN}_{\text{Mg}} - \text{HN}_{\text{Ca}}$ , (C)  $\Delta_{\text{total}} = \sqrt{(\Delta \text{HN})^2 + (\Delta N)^2}$ . The backbone chemical shifts for sCTnC• $2\text{Ca}^{2+}$  were obtained from Mercier et al. (63, 66, 78).

These  $^1\text{H}$  and  $^{15}\text{N}$  chemical shift comparisons suggest that the integrity of the secondary structure of sCTnC is kept in the  $\text{Mg}^{2+}$  state relative to that of  $\text{sCTnC}\cdot 2\text{Ca}^{2+}$ . More evidence are brought by the analysis of the  $\text{C}_\alpha$  and  $\text{C}_\beta$  chemical shifts (60, 79) relative to the  $\text{Ca}^{2+}$  state (see Figure VI-9). Except for the large differences in  $\text{C}_\alpha$  and  $\text{C}_\beta$  chemical shifts observed for C101, which could be a consequence of a different degree of oxidation of the SH group, the modifications to the  $\text{C}_\alpha$  and  $\text{C}_\beta$  chemical shifts relative to the  $\text{Ca}^{2+}$  state are minimal. Here, the chemical shifts used as reference were those of  $\text{TnC}\cdot 4\text{Ca}^{2+}$  measured in 15% TFE (80). The presence of the N-domain and the N/C domain central linker are probably the major cause of the observed changes at the beginning of the E-helix. Interestingly, the most important modifications for the rest of the proteins involve the  $\text{C}_\alpha$  shift of F105, D140, S141 and K142, as well as the  $\text{C}_\beta$  shifts of F112, I113, L122 and D140. All these residues are involved in the binding loop regions or in their close vicinity. The reason for the relatively large  $\text{C}_\beta$  chemical shift change for L122 is unknown.

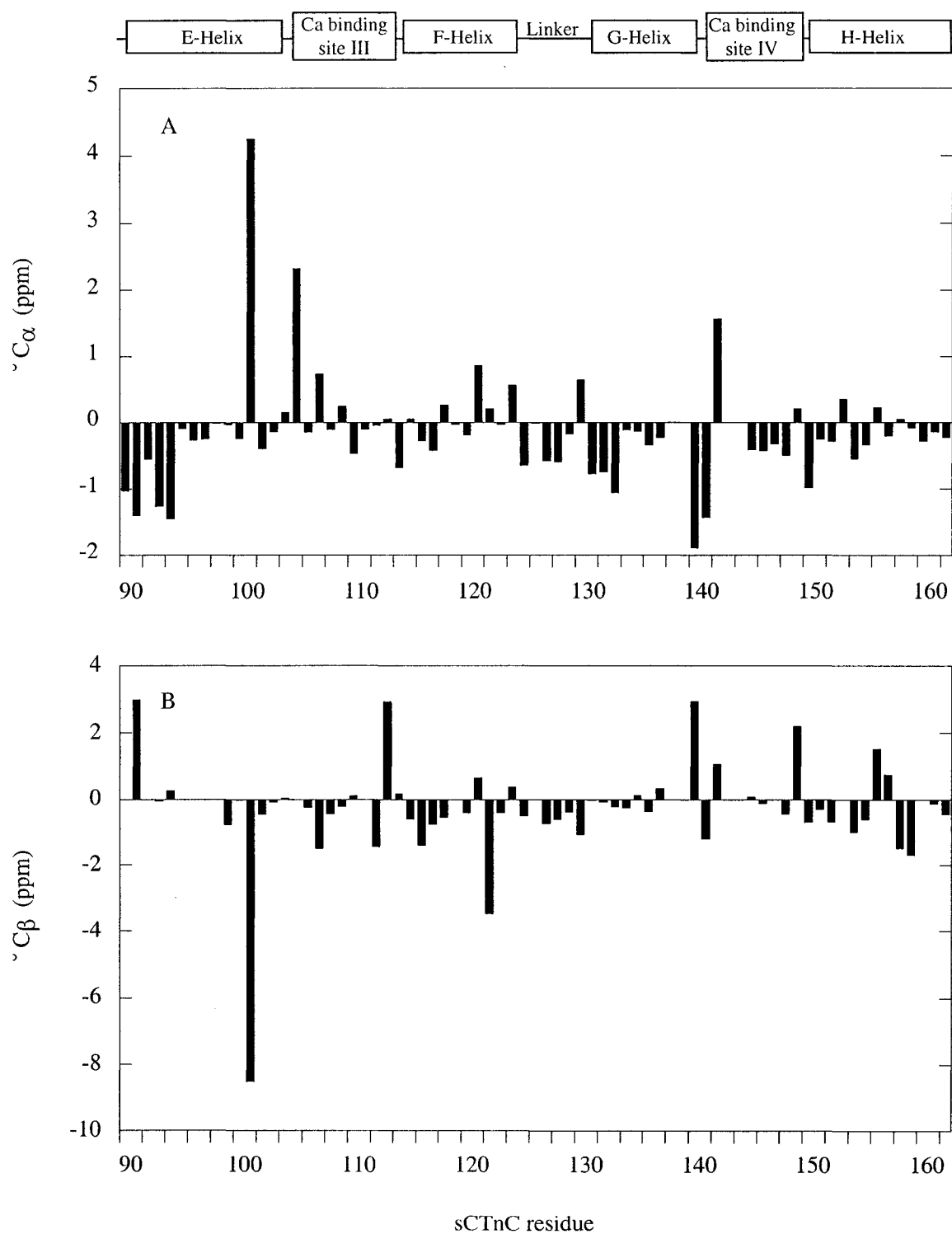


Figure VI-9. Mg<sup>2+</sup>-induced C<sub>α</sub> (A) and C<sub>β</sub> (B) chemical shifts differences in sCTnC•Mg<sup>2+</sup> compared to that of TnC•4Ca<sup>2+</sup> (8I).

---

*Structure of sCTnC•Mg<sup>2+</sup> determined by NMR spectroscopy*

---

Since Mg<sup>2+</sup> did not seem to induce large changes in the secondary structure of sCTnC based on all the observations reported in the previous section, we proceeded to the structural determination of sCTnC•Mg<sup>2+</sup>. For this purpose, we opted for an automated procedure for the assignment of NOEs using an in-house NMRView script that I have developed for that purpose (see Appendix 2). An earlier version of the script has previously been used for the derivation of distance restraints and the successful production of 3-dimensional structures of the calcium regulatory protein calbrain (1) (see Figure VI-10A).

In the current case, 3-dimensional structures of sCTnC•Mg<sup>2+</sup> were generated using the structure of sCTnC•2Ca<sup>2+</sup>•Rp40 as a starting point (see Experimental section for important details). The 50 lowest-energy structures of the sCTnC•Mg<sup>2+</sup>, generated with a total of 646 distance and 88 dihedral restraints, are shown in Figure VI-10B. A comparison between the lowest backbone RMSD structure (using residues 95-160) of sCTnC•Mg<sup>2+</sup> to that of sCTnC•2Ca<sup>2+</sup>•Rp40 is presented in the form of ribbon diagram in Figure VI-10C (see discussion below). The Ramachandran distribution of the individual residues as reported by the Procheck (82) is shown in Figure VI-11 and detailed structural statistics are given in Table VI-3.

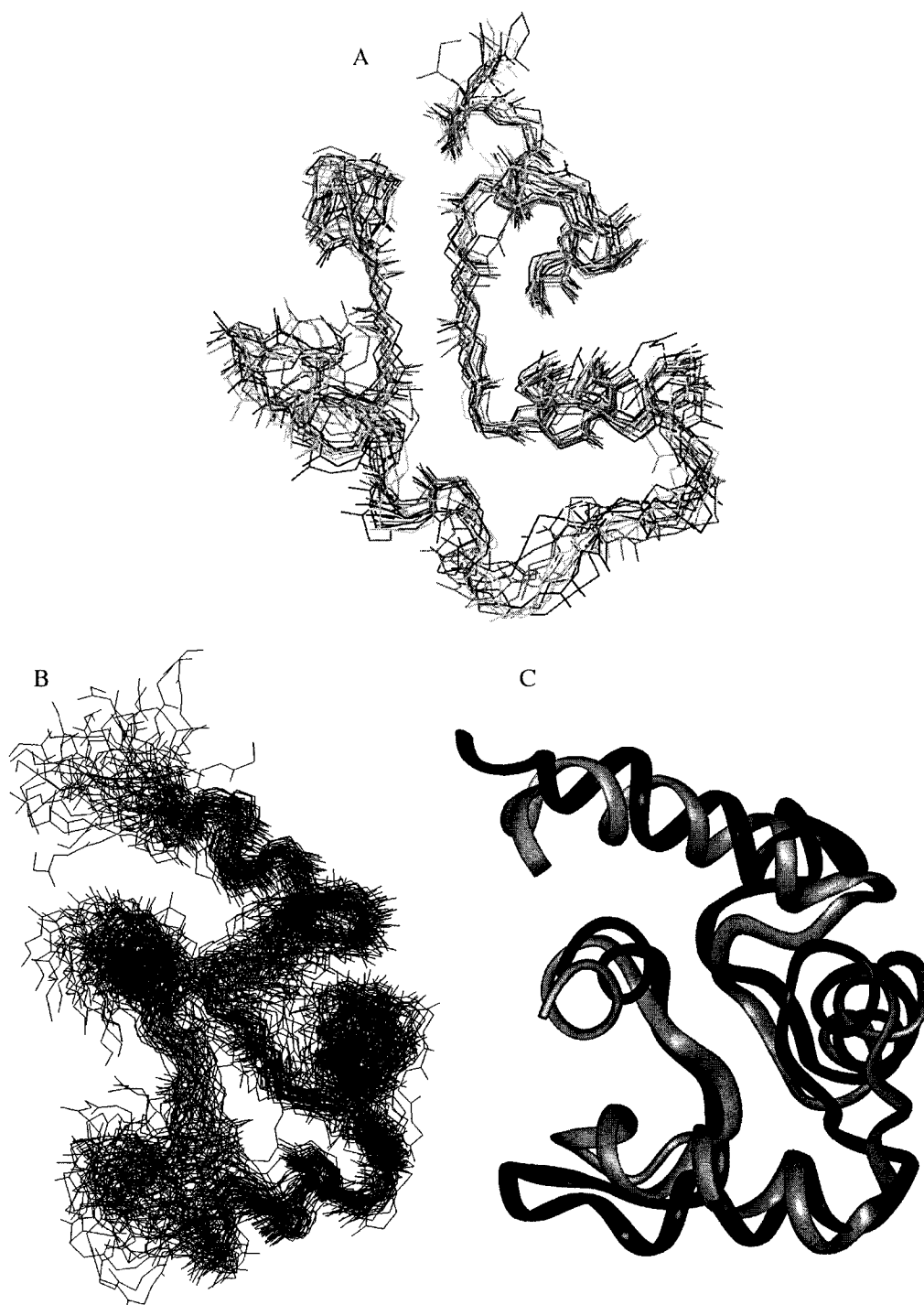


Figure VI-10. Backbone superimposition of A), 16 lowest-energy solution structures of calbrain, (1) B) the 50 lowest-energy solution structures of sNTnC•Mg<sup>2+</sup> (only residues 95-160 are shown). The superimposition was performed using the backbone heavy atoms of residues 95-104, 118-124, 133-140 and 152-157). C) Ribbon diagrams of sCTnC•Mg<sup>2+</sup> (black) and sCTnC in the sCTnC•2Ca<sup>2+</sup>•Rp40 complex (gray) (63).

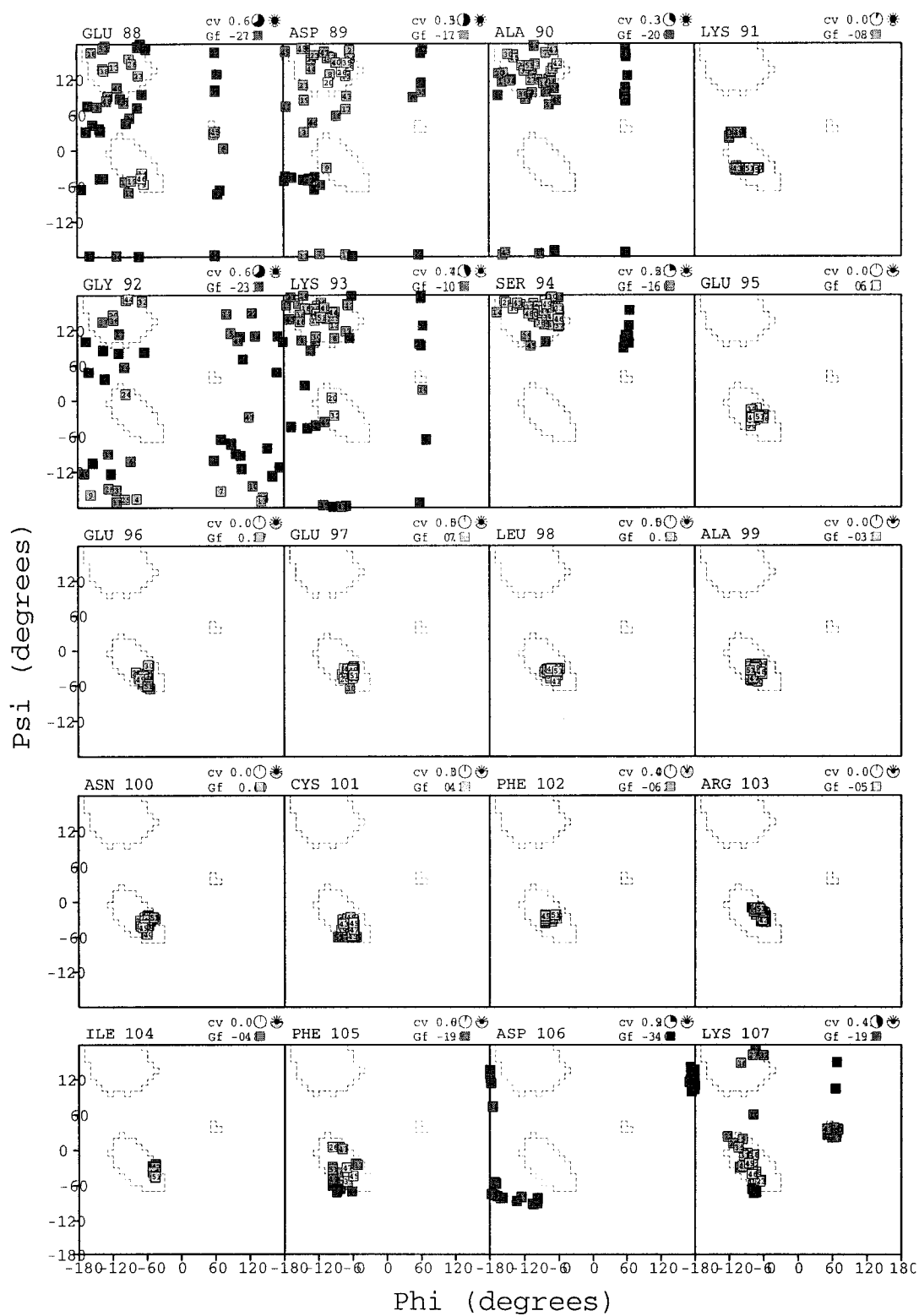


Figure VI-11. Ramachandran plots of sCTnC•Mg<sup>2+</sup> on a per residue basis as determined by the program Procheck (82). (Continued)

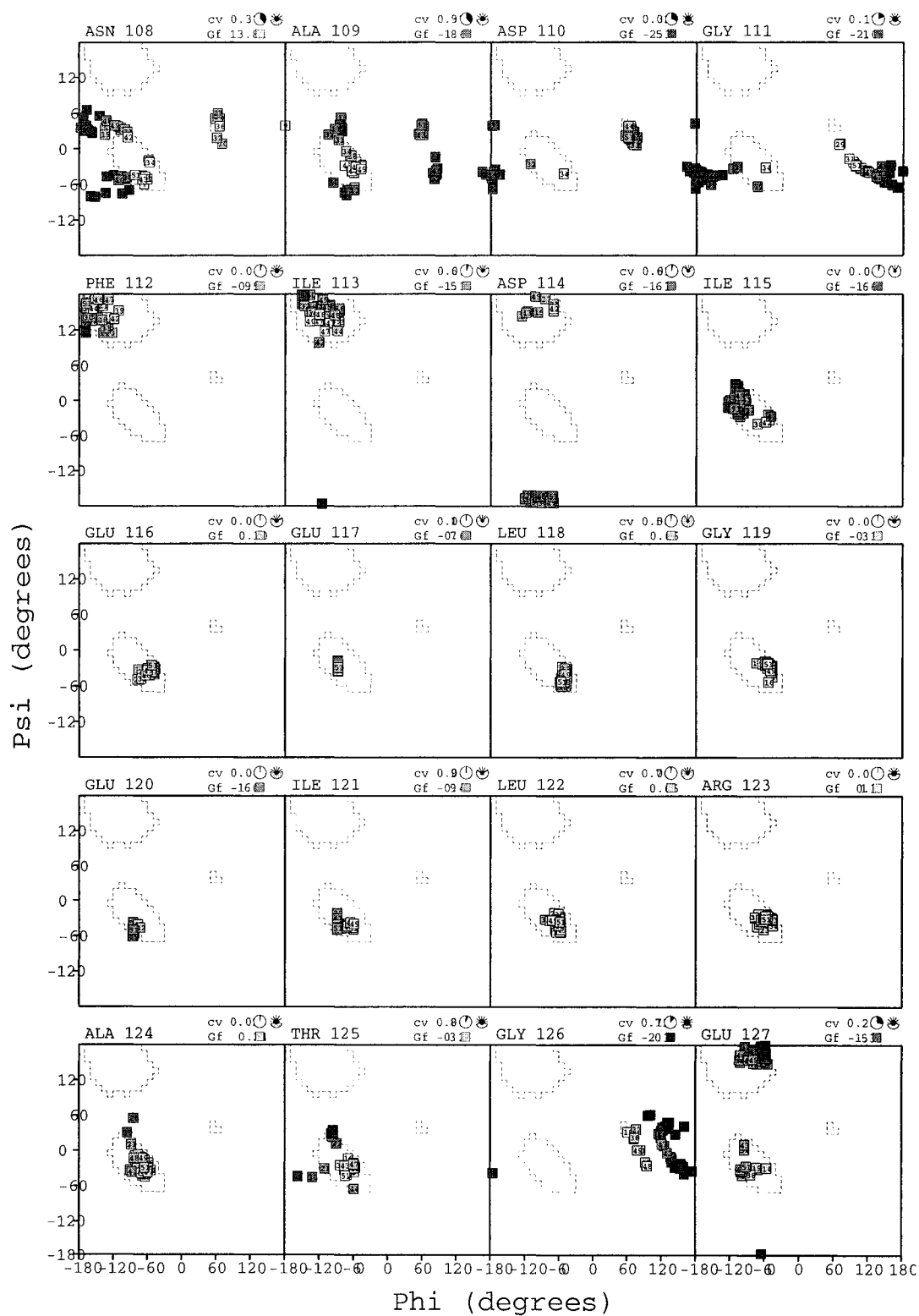


Figure VI-11. Ramachandran plots of sCTnC•Mg<sup>2+</sup> on a per residue basis as determined by the program Procheck (82). (Continued)

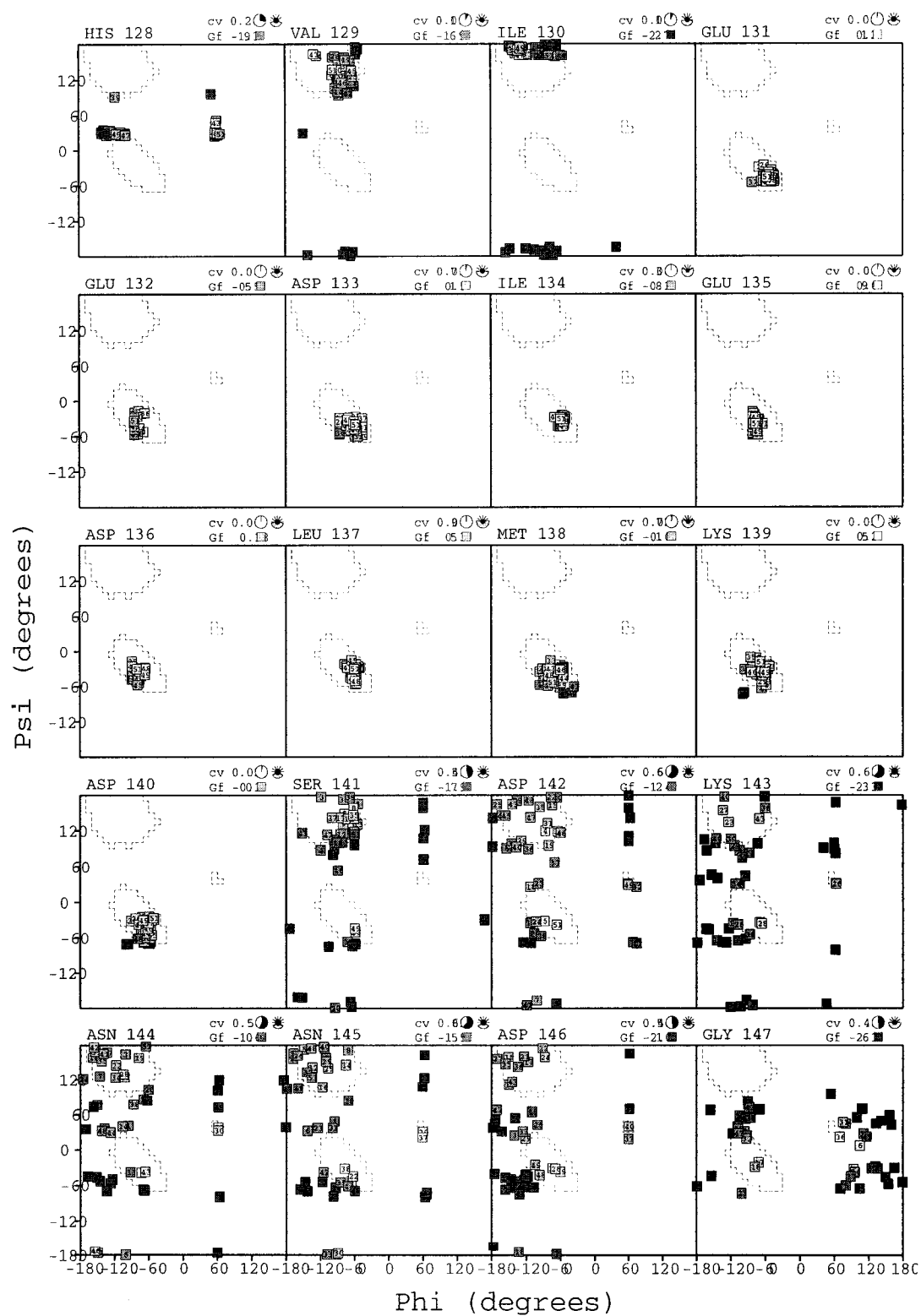


Figure VI-11. Ramachandran plots of sCTnC•Mg<sup>2+</sup> on a per residue basis as determined by the program Procheck (82). (Continued)

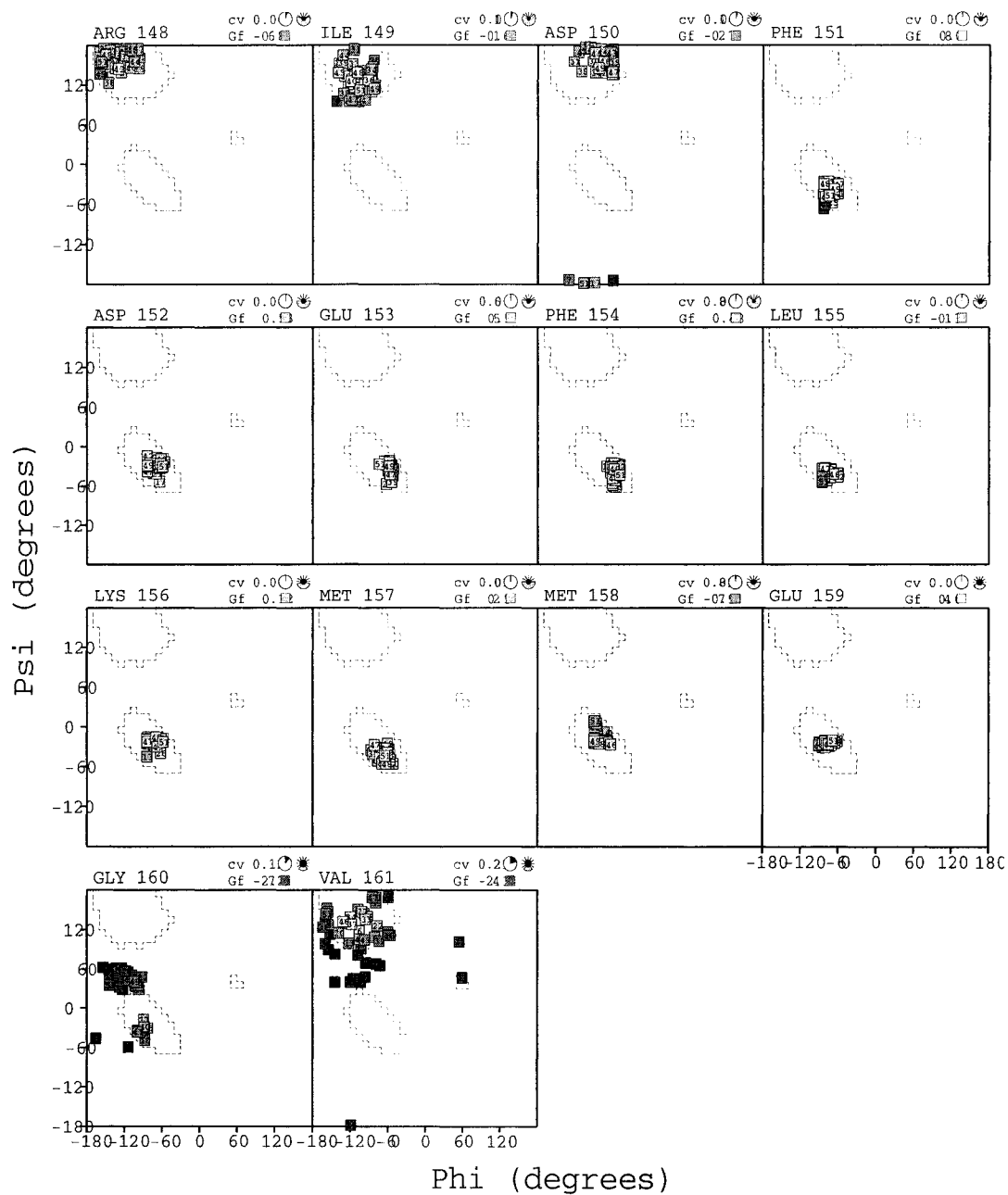


Figure VI-11. Ramachandran plots of sCTnC•Mg<sup>2+</sup> on a per residue basis as determined by the program Procheck (82).

Table VI-3. Structural statistics for sCTnC•Mg<sup>2+</sup> (50 best lowest-energy structures of a family of 200 structures). Error limits are standard deviations.

NOE restraints	
Total (unambiguous)	646
Intra-residue	280
Sequential ( i-j  = 1)	110
Medium range (2 ≤  i-j  ≤ 4)	87
Long range ( i-j  ≥ 5)	41
Ambiguous	128
Dihedral Restraints	
Total	88
ϕ	44
ψ	44
χ <sub>1</sub>	0
Restraint violations	
Distance < 0.2 Å > 0.1 Å	8
Dihedral > 1°	0
RMSD to averaged minimized structure (Å)	
Well defined regions <sup>a</sup> (N,Cα,C)	1.37 ± 0.42
A helix (16-29)	0.44 ± 0.13
B helix (39-48)	0.20 ± 0.10
C helix (55-65)	0.47 ± 0.23
D helix (75-85)	0.22 ± 0.07
Energies <sup>b</sup> (kcal mol <sup>-1</sup> )	
E <sub>total</sub>	103 ± 8
E <sub>NOE</sub>	11.7 ± 2
E <sub>Dihedral</sub>	0.10 ± 0.09
ϕ,ψ in core or allowed regions <sup>c</sup>	
Residues in most favored regions	80.7 %
Residues in additional allowed regions	16.0 %
Residues in generously allowed regions	2.4 %
Residues in disallowed regions	0.9 %

<sup>a</sup> Using residues 95-104, 118-124, 133-140 and 152-157.

<sup>b</sup> Using all residues of sNTnC in the 50 first lowest-energy structures

<sup>c</sup> Using residues 96-160 of sNTnC as determined by the program Procheck (82)

The distribution of NOEs (intraresidue, sequential, medium, and long-range) on a per residue basis is shown as a histogram in Figure VI-12A. RMSD values for the backbone and side chain atoms were calculated from the 50 lowest-energy structures after superimposition of the backbone atoms of residues 95-104, 118-124, 113-140 and 152-157 onto the average minimized structure. The results are plotted in Figure VI-12B. The lack of NOEs observed for residues in the second binding loop is most likely responsible for the larger observed RMSD values in this region. Moreover, backbone relaxation data (Figure VI-5) indicated increased backbone dynamics in the second binding loop, so increased motional freedom will intrinsically contribute as well to larger RMSD values.

The overall average backbone RMD ( $1.37 \pm 0.42$ ) Å is relatively large. However, considering the dynamic nature of sCTnC in the  $\text{Mg}^{2+}$ -state and the incomplete chemical shift database used for assignment purposes, this is not surprising. Still, superimposition using individual helices leads to backbone RMSD  $< 0.5$  Å (see Table VI-3), which is more than satisfactory considering the circumstances of structure generation in the current study. These observations suggest that lack of NOEs in binding site IV is largely responsible for the overall large backbone RMSD value, and that it prevents the four helices to be positioned with high precision relative to one another. This is indeed reflected by the slightly larger variations in interhelical angle values for sCTnC• $\text{Mg}^{2+}$  compared to that of other structures of sCTnC, as reported in Table VI-4. The structure of sCTnC• $\text{Mg}^{2+}$  shows the same degree of “openness” as of sCTnC in the sTnC• $2\text{Ca}^{2+}$  complex (X-ray), but is slightly more closed than sTnC• $4\text{Ca}^{2+}$  (NMR), as judged from the interhelical angle between the helices E and F.

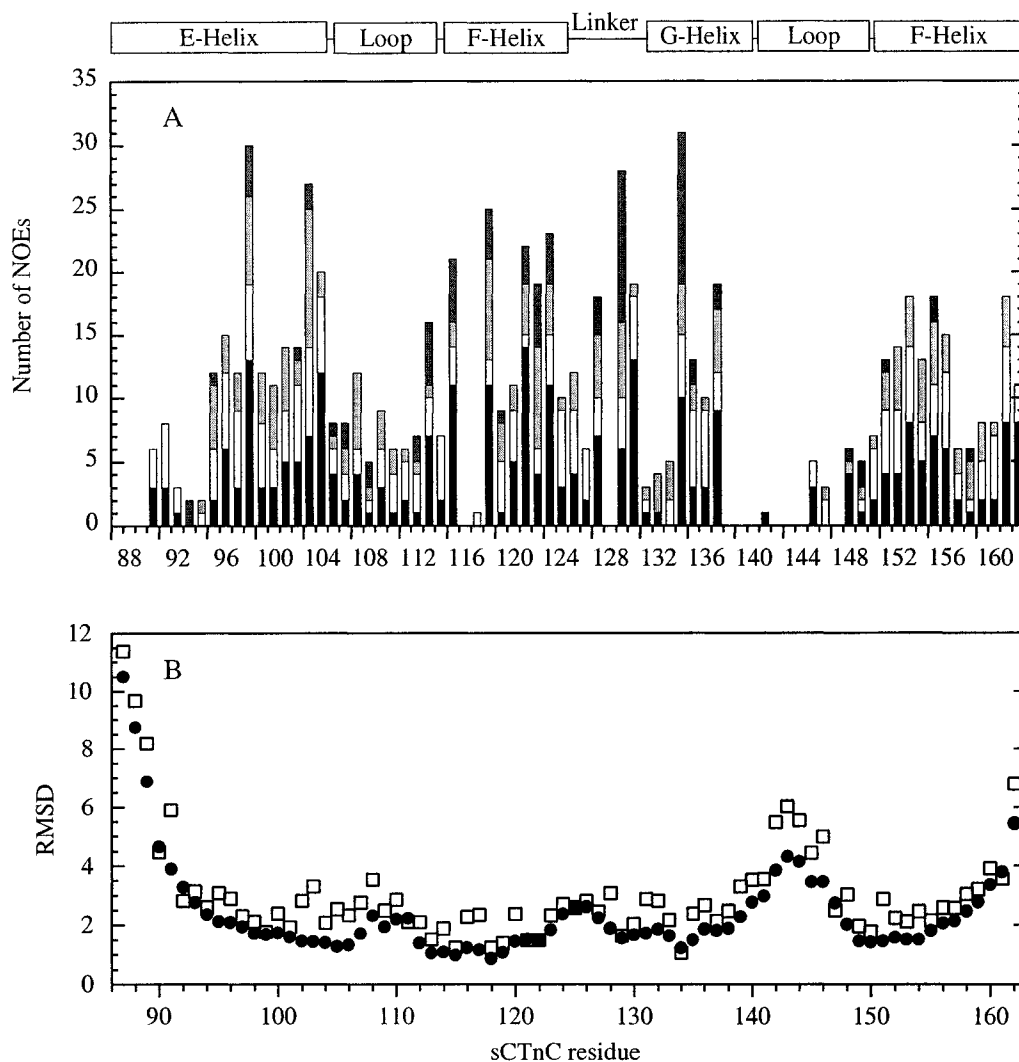


Figure VI-12. A) Distribution of NOEs as a function of residue number. Intraresidue, sequential, medium, and long-range NOEs are identified by black, white, light gray, and dark gray columns, respectively. B) Backbone (black circles) and side chain (white squares) RMSD for the ensemble of 50 solution structures with respect to the average coordinates.

Table VI-4. Interhelical angles for sNTnC and cNTnC free and bound to TnI peptides. Error limits are standard deviations.

Helix pair	sCTnC•Mg <sup>2+</sup> <sup>a</sup>	sTnC•2Ca <sup>2+</sup> <sup>b</sup>	sTnC•4Ca <sup>2+</sup> <sup>c</sup>	sCTnC•2Ca <sup>2+</sup> •Rp40 <sup>d</sup>
E/F	112 ± 13	108	89 ± 6	93 ± 7
E/G	127 ± 14	124	137 ± 6	132 ± 7
E/H	116 ± 9	122	110 ± 5	112 ± 6
F/G	98 ± 7	126	133 ± 6	127 ± 5
F/H	27 ± 12	33	36 ± 6	41 ± 6
G/H	78 ± 15	111	107 ± 7	115 ± 3

<sup>a</sup> Using residues 95-104, 117-124, 131-140 and 151-160 for helices E, F, G and H, respectively.

<sup>b</sup> Using residues 89-105, 115-125, 131-142 and 151-159 for helices E, F, G and H, respectively. (pdb entry 5TNC) (83)

<sup>c</sup> Using residues 96-105, 115-124, 131-141 and 151-157 for helices E, F, G and H, respectively. (pdb entry 1TNW) (81)

<sup>d</sup> Using residues 95-105, 115-124, 131-141 and 151-158 for helices E, F, G and H, respectively. (pdb entry 1JC2) (66)

*Influence of the starting model structure for automatic assignment and structures of sNTnC•Mg<sup>2+</sup>*

---

The use of a model structure within the automated NOE assignment procedure constitutes a potential source of criticism of the methodology presented here. How much influence the starting model structure has on the outcome of the final structures must be investigated. The distance cutoff is also an important parameter to consider. These questions represent ongoing research in our laboratory.

As previously mentioned, NOEs were automatically assigned starting from the structure of sCTnC•2Ca<sup>2+</sup>•Rp40, using an arbitrary chosen 12 Å cutoff distance. Other available structures of the C-domain were considered as starting model. The NMR structure of sTnC•4Ca<sup>2+</sup> could not be used as starting structure because of missing atom coordinates for residues at the beginning of the E helix and at the end of the H helix. The X-ray structure of sTnC•2Ca<sup>2+</sup> was judged too similar to that of sCTnC•2Ca<sup>2+</sup>•Rp40 (backbone RMSD ~ 1.1 Å) to make a difference in the final structures of sCTnC•Mg<sup>2+</sup>, considering the large distance cutoff value used in the automatic assignment script. Considering that NOEs between protons are usually not observable over an inter-atomic distance of 5 Å, the chosen cutoff distance (12 Å) represents a fairly safe range.

The most noticeable change between the structure of sCTnC•Mg<sup>2+</sup> to that of sCTnC•2Ca<sup>2+</sup>•Rp40 is the position of the F-helix relative to the G-helix (see Figure VI-10C). This is reflected by the difference in the F/G interhelical angle between the two species (see Table VI-4). It is somewhat unclear at this time whether the position of the

G-helix is real or simply a consequence of the lack of a sufficient number of NOEs in the loop region starting at the end of the G-helix, and/or the low number of long range NOEs for residues of the G-helix to fix its position relative to other structural elements of the protein. However, even when superimposing the set of structures using all residues located in well-defined secondary structural regions, the G-helix shows very little variation in its position (see Figure VI-10B).

In order to test the performance of the auto-assignment script, several tests were conducted using the program Aria 1.2 (45, 46). The software repeatedly generated 9 rounds of 20 structures with CNS 1.1, during which NOEs were automatically back-calculated using a relaxation matrix and recalibrated if needed, reassigned or simply rejected if continuously violated. However, contrary to the NMRView script, it does not check for the presence of symmetry when assigning peaks. The three different tests performed: one starting from an extended structure, one starting from the structure of sCTnC•2Ca<sup>2+</sup>•Rp40, and the third one like the latter but including the list of the final 518 unambiguous distance restraints obtained using my script. Using the same chemical shift error range in protons dimensions (0.03 ppm) and <sup>13</sup>C or <sup>15</sup>N dimension (0.5 ppm) as with the NMRView script, all Aria tests failed to fold the protein in a shape that could resemble sCTnC. For the third test, the computer started with 210 unambiguous and 1995 ambiguous distance restraints, and finished with 955 unambiguous and 212 ambiguous restraints, which represents close to twice the number of restraints obtained with the NMRView script. The lack of symmetry check is probably responsible for the higher number of restraints obtained by Aria. It is highly likely that most of these additional

restraints are caused by artifacts (noise, or misattribution of peaks). Contrary to the approach used here, Aria is a fully automated process. In the present methodology, human intervention was necessary between runs of structures to eliminate redundant NOE violations. Most importantly, long range NOEs that were driving the three-dimensional folding of the protein in a distorted way were manually inspected and eliminated if necessary. As such, the NMRView script does not therefore constitute a fully integrated automated process per se.

Long ranges NOEs are the most structurally important group of NOEs in folding the protein and positioning parts of the protein relative to one another. Because all the NOEs are energetically weighed equally, misassigned long range NOEs can sometime be easily satisfied through non-native folding, especially if the total number of long range distance restraints is relatively low. These misassigned NOEs will often generate violations for other NOEs that would otherwise be correct. Since Aria ultimately eliminates NOEs to decrease the total energy, it is sometimes faulty in the NOEs it keeps and rejects. The lack of full complete assignment of chemical shifts for sCTnC•Mg<sup>2+</sup> is potentially largely responsible for the failure of Aria in the current study. Nevertheless, improvements could be made in the algorithms of the software by allowing for different weighing of long range NOEs and the use of a cross-validation process, by which NOEs are randomly temporary eliminated from the structure generated process and post-verified using the structures accordingly generated.

## CONCLUSIONS

The weaker affinity of the C-domain of skeletal TnC for  $Mg^{2+}$  compared to that of  $Ca^{2+}$  gives  $sCTnC \cdot Mg^{2+}$  a different behavior in solution compared to that of  $sCTnC \cdot 2Ca^{2+}$ . The current study shows that  $Mg^{2+}$  binding occurs in a non-cooperative fashion to the two EF-hands, and the results are consistent with lower affinity of site IV than site III, although no dissociation constants were independently measured for the sites. Backbone relaxation measurements indicate that both binding loops are undergoing fast time scale dynamics compared to that of  $sCTnC \cdot 2Ca^{2+}$ , which is consistent with a lower Mg affinity. The rotational correlation time calculated from the NMR relaxation data is indicative of the formation of a monomeric complex in solution.

Structural studies conducted at 50 mM  $Mg^{2+}$  and using an automated approach for the derivation of distance restraints derived from NOE data resulted in a structure that shares several similarities with that of  $sCTnC \cdot 2Ca^{2+}$ , although binding site IV is poorly defined due to the lack of chemical shift assignment in this region. Completion of the chemical shift assignment for all residues in the protein will be necessary to obtain more reliable structures. The process is complicated due to the existence of up to three different species in solution due to different  $Mg^{2+}$ -binding affinity for site III and IV.

At high concentrations of Rp40, the protein was not completely saturated by the peptide, indicative of a reduced binding affinity of Rp40 for  $sCTnC$  in the  $Mg^{2+}$  state. However, the residues most affected by Rp40 binding in the  $Ca^{2+}$ -saturated state (see

Chapter 2) showed identical backbone chemical shifts in the  $Mg^{2+}$  state, suggestive of structural similarities between  $sCTnC \cdot Mg^{2+} \cdot Rp40$  and  $sCTnC \cdot 2Ca^{2+} \cdot Rp40$ .

A reduced affinity of Rp40 for sTnC in the  $Mg^{2+}$  state versus the  $Ca^{2+}$  state would have important implications for the models of interactions of TnC with various regions of TnI at various times during the contraction cycle. It has been proposed that the inhibitory peptide displaces the Rp40 regions during  $Ca^{2+}$  activation (65), but the relative affinities of Rp40 and the inhibitory peptide for  $sCTnC \cdot 2Ca^{2+}$  do not support this proposal (63, 66). However, a reduced affinity of Rp40 for  $sCTnC \cdot Mg^{2+}$  would make this mechanism more plausible. It rests at the question whether  $Ca^{2+}$  or  $Mg^{2+}$  occupies CTnC in the resting phase of the contraction cycle. Clearly this is an area that requires more investigation.

**REFERENCES**

1. McKay, R. T., Vladimir, L., M., T., and Vogel, H. J. (2002) in *XXth International Conference on Magnetic Resonance in Biological Systems (ICMRBS)* pp 256, Toronto.
2. Evenas, J., Malmendal, A., and Forsen, S. (1998) *Curr Opin Chem Biol* 2, 293-302.
3. Brinley, F. J., Jr., Scarpa, A., and Tiffert, T. (1977) *J Physiol* 266, 545-565.
4. Drabikowski, W., Brzeska, H., and Venyaminov, S. (1982) *J. Biol. Chem.* 257, 11584-11590.
5. Tsai, M. D., Drakenberg, T., Thulin, E., and Forsen, S. (1987) *Biochemistry* 26, 3635-3643.
6. Potter, J. D., Robertson, S. P., and Johnson, J. D. (1981) *Fed Proc* 40, 2653-2656.
7. Francois, J. M., Gerday, C., Prendergast, F. G., and Potter, J. D. (1993) *J Muscle Res Cell Motil* 14, 585-593.
8. Zot, H. G., and Potter, J. D. (1987) *J Muscle Res Cell Motil* 8, 428-436.
9. Zot, A. S., and Potter, J. D. (1987) *J. Biol. Chem.* 262, 1966-1969.
10. Allen, T. S., Yates, L. D., and Gordon, A. M. (1992) *Biophys. J.* 61, 399-409.
11. Declercq, J. P., Tinant, B., Parello, J., and Rambaud, J. (1991) *J. Mol. Biol.* 220, 1017-1039.
12. Houdusse, A., Silver, M., and Cohen, C. (1996) *Structure* 4, 1475-1490.
13. Andersson, M., Malmendal, A., Linse, S., Ivarsson, I., Forsen, S., and Svensson, L. A. (1997) *Protein Sci.* 6, 1139-1147.
14. Falke, J. J., Drake, S. K., Hazard, A. L., and Peersen, O. B. (1994) *Q Rev Biophys* 27, 219-290.
15. Linse, S., and Forsen, S. (1995) *Adv Second Messenger Phosphoprotein Res* 30, 89-151.
16. Malmendal, A., Evenas, J., Thulin, E., Gippert, G. P., Drakenberg, T., and Forsen, S. (1998) *J. Biol. Chem.* 273, 28994-29001.
17. Malmendal, A., Linse, S., Evenas, J., Forsen, S., and Drakenberg, T. (1999) *Biochemistry* 38, 11844-11850.
18. Nelson, M. R., and Chazin, W. J. (1998) *Protein Sci.* 7, 270-282.
19. Ohki, S., Ikura, M., and Zhang, M. (1997) *Biochemistry* 36, 4309-4316.
20. Potter, J. D., and Gergely, J. (1975) *J. Biol. Chem.* 250, 4628-4633.
21. Johnson, J. D., and Potter, J. D. (1978) *J. Biol. Chem.* 253, 3775-3777.
22. Johnson, J. D., Collins, J. H., and Potter, J. D. (1978) *J. Biol. Chem.* 253, 6451-6458.
23. Johnson, J. D., Charlton, S. C., and Potter, J. D. (1979) *J. Biol. Chem.* 254, 3497-3502.
24. Ogawa, Y. (1985) *J. Biochem. (Tokyo)* 97, 1011-1023.
25. Holroyde, M. J., Robertson, S. P., Johnson, J. D., Solaro, R. J., and Potter, J. D. (1980) *J. Biol. Chem.* 255, 11688-11693.
26. Vogel, H. J., Drakenberg, T., and Forsen, S. (1983) *NMR of NEWLY ACCESSIBLE NUCLEI* 1, 157.

27. Johnson, J. D., Nakkula, R. J., Vasulka, C., and Smillie, L. B. (1994) *J. Biol. Chem.* 269, 8919-8923.
28. Finley, N., Dvoretzky, A., and Rosevear, P. R. (2000) *J. Mol. Cell. Cardiol.* 32, 1439-1446.
29. Harada, K., Arana, C., and Potter, J. D. (2001) *J. Mol. Cell. Cardiol.* 33, 593-596.
30. Krishnamurthy, K. (2001) *J. Magn. Reson.* 153, 144-150.
31. Kim, S., and Szyperski. (2003) *J. Am. Chem. Soc.*
32. Szyperski, T., Yeh, D. C., Sukumaran, D. K., Moseley, H. N., and Montelione, G. T. (2002) *Proc. Natl. Acad. Sci. U.S.A.* 99, 8009-8014.
33. Korzhneva, D. M., Ibraghimov, I. V., Billeter, M., and Orekhov, V. Y. (2001) *J. Biomol. NMR* 21, 263-268.
34. Orekhov, V. Y., Ibraghimov, I. V., and Billeter, M. (2001) *J. Biomol. NMR* 20, 49-60.
35. Chen, J., Mandelshtam, V. A., and Shaka, A. J. (2000) *J. Magn. Reson.* 146, 363-368.
36. Hu, H., De Angelis, A. A., Mandelshtam, V. A., and Shaka, A. J. (2000) *J. Magn. Reson.* 144, 357-366.
37. Mandelshtam, V. A. (2000) *J. Magn. Reson.* 144, 343-356.
38. Hitchens, K. T., Lukin, J. A., Zhan, Y., McCallum, S. A., and Rule, G. S. (2003) *J. Biomol. NMR* 25, 1-9.
39. Bailey-Kellogg, C., Widge, A., Kelley, J. J., Berardi, M. J., Bushweller, J. H., and Donald, B. R. (2000) *J Comput Biol* 7, 537-558.
40. Guntert, P., Salzmann, M., Braun, D., and Wuthrich, K. (2000) *J. Biomol. NMR* 18, 129-137.
41. Moseley, H. N., Monleon, D., and Montelione, G. T. (2001) *Methods Enzymol.* 339, 91-108.
42. Monleón, D., Colson, K., Moseley, H. N. B., Anklin, C., Oswald, R., Szyperski, T., and Montelione, G. T. (2002) *J. Struct. Funct. Genomics* 2, 93-101.
43. Herrmann, T., Guntert, P., and Wuthrich, K. (2002) *J. Mol. Biol.* 319, 209-27.
44. Herrmann, T., Guntert, P., and Wuthrich, K. (2002) *J. Biomol. NMR* 24, 171-89.
45. Linge, J. P., O'Donoghue, S. I., and Nilges, M. (2001) *Methods Enzymol.* 339, 71-90.
46. Linge, J. P., Habeck, M., Rieping, W., and Nilges, M. (2003) *Bioinformatics* 19, 315-316.
47. Gagné, S. M., Tsuda, S., Li, M. X., Chandra, M., Smillie, L. B., and Sykes, B. D. (1994) *Protein Sci.* 3, 1961-1974.
48. Li, M. X., Gagné, S. M., Tsuda, S., Kay, C. M., Smillie, L. B., and Sykes, B. D. (1995) *Biochemistry* 34, 8330-8340.
49. Ngai, S.-M., and Hodges, R. S. (1992) *J. Biol. Chem.* 267, 15715-15720.
50. Delaglio, F., Grzesiek, S., Vuister, G. W., Zhu, G., Pfeifer, J., and Bax, A. (1995) *J. Biomol. NMR* 6, 277-293.
51. Johnson, B. A., and Blevins, R. A. (1994) *J. Biomol. NMR* 4, 603-614.
52. Muhandiram, D. R., and Kay, L. E. (1994) *J. Magn. Reson.* B103, 203-216.
53. Kay, L. E., Keifer, P., and Saarinen, T. (1992) *J. Am. Chem. Soc.* 114, 10663-10665.

54. Zhang, O., Kay, L. E., Olivier, J. P., and Forman-Kay, J. D. (1994) *J. Biomol. NMR* 4, 845-858.
55. Kay, L. E., Xu, G. Y., Singer, A. U., Muhandiram, D. R., and Forman-Kay, J. D. (1993) *J. Magn. Reson. B101*, 333-337.
56. Pascal, S. M., Muhandiram, D. R., Yamazaki, T., Forman-Kay, J. D., and Kay, L. E. (1994) *J. Magn. Reson. B103*, 197-201.
57. Kuboniwa, H., Grzesiek, S., Delaglio, F., and Bax, A. (1994) *J. Biomol. NMR* 4, 871-878.
58. Farrow, N. A., Muhandiram, R., Singer, A. U., Pascal, S. M., Kay, C. M., Gish, G., Shoelson, S. E., Pawson, T., Forman-Kay, J. D., and Kay, L. E. (1994) *Biochemistry* 33, 5984-6003.
59. Wüthrich, K. (1986) *NMR of proteins and nucleic acids.*, John Wiley & Sons, New York.
60. Wishart, D. S., Sykes, B. D., and Richards, F. M. (1991) *J. Mol. Biol.* 222, 311-333.
61. Tsuda, S., Ogura, K., Hasegawa, Y., Yagi, K., and Hikichi, K. (1990) *Biochemistry* 29, 4951-4958.
62. Pardi, A., Wagner, G., and Wuthrich, K. (1983) *Eur J Biochem* 137, 445-454.
63. Mercier, P., Spyrapoulos, L., and Sykes, B. D. (2001) *Biochemistry* 40, 10063-10077.
64. Wang, S., George, S. E., Davis, J. P., and Johnson, J. D. (1998) *Biochemistry* 37, 14539-14544.
65. Tripet, B. P., Van Eyk, J. E., and Hodges, R. S. (1997) *J. Mol. Biol.* 271, 728-750.
66. Mercier, P., Li, M. X., and Sykes, B. D. (2000) *Biochemistry* 39, 2902-2911.
67. Luo, Y., Leszyk, J., Li, B., Gergely, J., and Tao, T. (2000) *Biochemistry* 39, 15306-15315.
68. Luo, Y., Wu, J. L., Li, B., Langsetmo, K., Gergely, J., and Tao, T. (2000) *J. Mol. Biol.* 296, 899-910.
69. Reid, R. E. (1987) *Biochemistry* 26, 6070-6073.
70. Reid, R. E., and Hodges, R. S. (1980) *J Theor Biol* 84, 401-444.
71. Marsden, B. J., Hodges, R. S., and Sykes, B. D. (1988) *Biochemistry* 27, 4198-4206.
72. Sekharudu, Y. C., and Sundaralingam, M. (1988) *Protein Eng* 2, 139-146.
73. Gagné, S. M., Li, M. X., and Sykes, B. D. (1997) *Biochemistry* 36, 4386-4392.
74. Davis, J. P., Rall, J. A., Reiser, P. J., Smillie, L. B., and Tikunova, S. B. (2002) *J. Biol. Chem.* 277, 49716-49726.
75. Wang, X., Li, M. X., and Sykes, B. D. (2002) *J. Biol. Chem.* 277, 31124-31133.
76. Gagné, S. M., Tsuda, S., Li, M. X., Smillie, L. B., and Sykes, B. D. (1995) *Nat. Struct. Biol.* 2, 784-789.
77. Cornilescu, G., Delaglio, F., and Bax, A. (1999) *J. Biomol. NMR* 13, 289-302.
78. Vassylyev, D. G., Takeda, S., Wakatsuki, S., Maeda, K., and Maeda, Y. (1998) *Proc. Natl. Acad. Sci. U.S.A.* 95, 4847-4852.
79. Wishart, D. S., and Sykes, B. D. (1994) *Methods Enzymol.* 239, 363-392.
80. Slupsky, C. M., Reinach, F. C., Smillie, L. B., and Sykes, B. D. (1995) *Protein Sci.* 4, 1279-1290.
81. Slupsky, C. M., and Sykes, B. D. (1995) *Biochemistry* 34, 15953-15964.

- 
82. Laskowski, R. A., MacArthur, M. W., Moss, D. S., and Thornton, J. M. (1993) *J. Appl. Crystallogr.* 26, 283-291.
  83. Herzberg, O., and James, M. N. G. (1988) *J. Mol. Biol.* 203, 761-779.

## CHAPTER VII

### *Conclusion*

The aim of this thesis was to expand the current knowledge about the interactions between the calcium-binding protein TnC and the inhibitory protein TnI, two proteins involved in the regulation of muscle contraction. Using predominantly NMR as biophysical tool, the properties of three different binary complexes of skeletal TnC with functional regions of TnI (residues 1-40 [Rp40], 96-115 [inhibitory region] and 115-131 [“switch peptide”]) were investigated. The results concerning each complex studied were summarized at the end of the relevant chapter and will not be repeated here. In this section I will attempt to integrate the results from my published and unpublished research with new results that have emerged from other laboratories since some of the early chapters were published. In particular, the implications of my work in relation to recent functional and structural models of TnC•TnI (1-4) will be discussed.

### Model of TnC•TnI interactions in muscle regulation

The competitive binding results reported in Chapter 2 clearly established the stronger affinity of the TnI peptide Rp40 for the Ca<sup>2+</sup>-saturated C-domain of TnC compared to that of the inhibitory peptide TnI<sub>96-115</sub>. The sources of the Rp40 interactions with CTnC were highlighted by the thermodynamic results presented in Chapter 3. In the context of various mechanisms proposed for the calcium regulation wherein the inhibitory and Rp40 peptides compete with one another in a temporal fashion for binding

to sCTnC, these results strongly suggest constant occupancy of Rp40 on CTnC•Ca<sup>2+</sup>. This implies in turn that the C-domain of TnC performs a structural role rather than regulatory functions, although this would clearly be an over simplification. These results are in agreement with photocrosslinking studies of Luo et al. (3, 4) and support their functional model of TnC•TnI, which is shown in Figure VII-1.

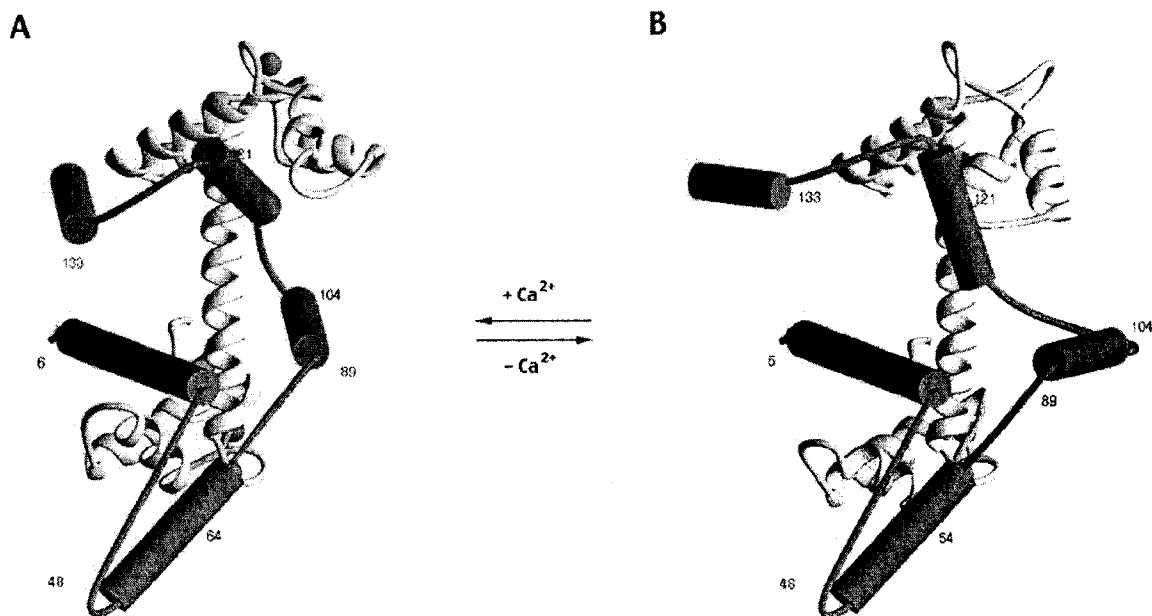


Figure VII-1. A model for the structures of TnC and TnI in the ternary TnC•TnI•TnT complex, in the presence (a) and absence (b) of Ca<sup>2+</sup>. The C-terminal residues 151-181 of TnI are not included. The segments drawn as barrels indicate  $\alpha$ -helices predicted by sequence analysis. The numbers indicate TnI residues that were mutated to cysteine for photocrosslinker attachment. Figure and legend adapted from (4).

According to this model, in the presence of  $\text{Ca}^{2+}$ , residues 1-33 of TnI interact with the hydrophobic groove of CTnC, 48-89 with TnT, 90-113 with the central helix of TnC, 114-125 with NTnC and 130-150 with the A-helix of TnC. In the absence of  $\text{Ca}^{2+}$ , residues 114-125 of TnI move away from NTnC and trigger the translocation of residues 89-113 and 130-150 away from TnC towards interaction sites on actin.

The model presented in Figure VII-1 is in agreement with the majority of current experimental data, and hence illustrates well the temporal changes in TnC•TnI interactions during muscle contraction. A central feature of the model mainly is the binding of Rp40 to CTnC in both the relaxed and contraction states. The results presented in Chapters 2 are in agreement with that hypothesis, although the binding affinity of Rp40 to CTnC is reduced in the  $\text{Mg}^{2+}$  state compared with that of the  $\text{Ca}^{2+}$  state and this could have important ramifications. However, the study was carried on an isolated domain, and other proteins of the thin filament may well influence the affinities of all components. Nevertheless, the role of the  $\text{Mg}^{2+}$  occupancy on sCTnC has never been clearly established, and the lack of high-resolution structure in that state is in part responsible. Clearly, the role of  $\text{Mg}^{2+}$  binding and its consequence on the overall structure of TnC and its affinity for its target proteins need to be investigated in more details. It would greatly enhance, or even change, the current notions surrounding the mechanism of the action of TnC and its associated proteins.

---

Three-dimensional models of interaction between TnC and TnI

---

One of the major unknowns regarding TnI is the location the inhibitory region on TnC during the contraction phase of muscle activity. We did not experimentally determine the structure of the inhibitory TnI peptide bound to TnC in the work presented in Chapter 2. However, our chemical shift mapping results strongly suggested that the inhibitory peptide did not bind in hydrophobic patch of CTnC, contrary to what had previously been suggested (5). In light of the ionic character of the peptide and the nature of the perturbed TnC residues upon TnI<sub>96-115</sub> binding, we proposed that the TnI inhibitory peptide would bind through electrostatic forces and that the peptide would pass over the hydrophobic pocket on TnC, allowing for the simultaneous presence of both the Rp40 and inhibitory TnI peptides (6, 7). Chemical shift mapping is commonly used in NMR as an indirect method to approximate the location of peptide sites on proteins (6, 8-11). There is no known direct correlation between the extent of protein chemical shifts changes upon peptide binding and peptide binding affinities. However, a high degree of correlation was observed between the changes in TnC backbone chemical shifts upon peptide binding of Rp40 (1, 6) (Chapter 2) and the TnI switch peptide (Chapter 5) with their experimentally determined locations.

Very recently, Lindhout et al. solved the structure of the human cardiac cCTnC•2Ca<sup>2+</sup>•cTnI<sub>128-147</sub> using NMR (10), where cTnI<sub>128-147</sub> is the cardiac equivalent of skeletal TnI<sub>96-115</sub>. The molecular surface representation of cCTnC as obtained from backbone chemical shift mapping is very similar to that of sCTnC presented in Figure II-6 (comparison not shown), which suggests common binding sites for both isoforms of the

inhibitory peptide on CTnC. This is expected from the high similarity of the amino acid sequence of the two peptides and the high sequence conservation of the TnI inhibitory region among species. The reported dissociation constant for cTnI<sub>128-147</sub> ( $31 \pm 11 \mu\text{M}$ ) is similar to that of skeletal TnI<sub>96-115</sub> ( $47 \pm 7 \mu\text{M}$ ) (7). As we had predicted from our study with the skeletal system, the inhibitory peptide in the cCTnC•2Ca<sup>2+</sup>•cTnI<sub>128-147</sub> complex does not interact with the hydrophobic pocket of cCTnC. Instead, the binary complex is stabilized via electrostatic interactions. The region of the peptide between residues 134 and 139 in cCTnC•2Ca<sup>2+</sup>•cTnI<sub>128-147</sub> shows a certain degree of helical propensity, but it does not have enough of a helical character to be recognized as a  $\alpha$ -helix by the program Procheck (12). <sup>1</sup>H <sub>$\alpha$</sub> , <sup>13</sup>C <sub>$\alpha$</sub> , <sup>13</sup>C <sub>$\beta$</sub>  chemical shifts and <sup>3</sup>J<sub>H $\alpha$ HN</sub> coupling constant values for residues of TnI<sub>128-147</sub> were shown to deviate from expected values of a well-defined  $\alpha$ -helix. These observations are in agreement with the recent work of Brown et al., which showed from solvent accessibility parameters derived from electron paramagnetic resonance (ERP) that the cardiac inhibitory peptide was unstructured when complex with TnC (13). However, it was demonstrated that the addition of TnT into the cTnC•cTnI binary complex induces a helical structure on the TnI inhibitory peptide.

The absence of TnT, and/or NTnC in the study by Lindhout et al. might account for the lack of well-defined structure in the C-terminal portion of the inhibitory peptide and the lack of interactions with the protein in this region. However, backbone relaxation measurements revealed stiffening of the F/G linker and the H helix of cTnC upon TnI<sub>128-147</sub> binding, which suggests interaction of the TnI inhibitory peptide with these

regions of TnC. All of the binding and structural studies indicate that Rp40 and the inhibitory peptide share common epitopes on CTnC and must overlap in some way.

The Maeda and Trehwella research groups have both presented two different three-dimensional models of TnI•TnC (1, 2). The Maeda et al. model is restricted to two separated segments of TnI (Rp40 and TnI<sub>96-131</sub>), whereas the Trehwella et al. model contains all residues of TnI. Both models were presented in Chapter 1. In addition to different interdomain orientation of TnC, the central difference between the two models for the purpose of this thesis is the position and structure of the inhibitory TnI peptide. The TnI<sub>128-147</sub> peptide in the cCTnC•2Ca<sup>2+</sup>•cTnI<sub>128-147</sub> structure from Lindhout does not form a  $\beta$ -hairpin structure as suggested from Trehwella et al. (2) (see Figure I-11), but interacts with the central D/E linker, as suggested from several previous studies (see (14) and reference therein). In that regard, the Maeda model is in better agreement with the experimentally determined secondary structure adopted by the inhibitory peptide. However, although the TnI<sub>128-147</sub> peptide seems to exhibit some helical character, it does not form a fully extended  $\alpha$ -helix as modeled by Maeda et al. Therefore, both models need to be reconsidered and revised.

In an attempt to propose a correction to the Trehwella and Maeda models, chimera structures of sTnC•Rp40•cTnI<sub>128-147</sub>•sTnI<sub>115-131</sub>•4Ca<sup>2+</sup> were generated using distance and dihedral experimental restraints derived from different partial TnC•TnI complexes. Distance restraints from Lindhout et al. were used for the inhibitory peptide. Those used for sCTnC•Rp40•2Ca<sup>2+</sup> (Chapter 2) and sNTnC•sTnI<sub>115-131</sub>•2Ca<sup>2+</sup> (Chapter 4)

were combined for in a single set for sTnC. Because the structure of Rp40 was not determined by NMR and no NOE distance restraints were available to recreate its structure and position relative to sCTnC, artificial distance restraints were created for Rp40 from interatomic distances extracted from the X-ray coordinates of TnC•TnI<sub>1-47</sub>•2Ca<sup>2+</sup> (1). A total number of 2871 NOE restraints and 219 dihedral restraints were employed for structure generation. A set of 100 structures were generated with the software CNS in two stages: with torsion angle dynamics for the hot phase and the first cooling phase, and including Ca<sup>2+</sup> restraints for the second cooling using cartesian dynamics (see the experimental section in Chapter 4)

A superimposition of the backbone trace of the best 15 lowest-energy structures of sTnC•cTnI<sub>128-147</sub>•sTnI<sub>115-131</sub>•4Ca<sup>2+</sup> (using only cCTnC for superimposition) is shown in Figure VII-2. Because of the lack of NOEs between the TnI peptides and the N-terminal portion of cCTnC and the C-terminal region of sNTnC in the separate studies, the contacts between TnI and the D/E linker of TnC are undefined. Additionally, the position of both domains of CTnC relative to one another could not be determined. This situation is similar to that of the earlier NMR investigation of sTnC•4Ca<sup>2+</sup> where the orientation of both domains could not be unambiguously determined due to flexibility and lack of secondary structure in the D/E linker (15). Dvoretzky et al. have used rigid body minimization on isolated structures of cCTnC•cTnI<sub>147-163</sub> (16) and cTnC•cCTnI<sub>33-80</sub> (17, 18), and experimental residual dipolar couplings information on cCTnC•cCTnI to determine the relative orientation of cCTnC and cNTnC in the cCTnC•cCTnI complex (19). However, no experimental information was presented in the paper or deposited

with the structure that could be used to directly generate structures in which both domains of TnC would adopt the proposed orientation.



Figure VII-2. Backbone trace superimposition of the 15 lowest energy structures of  $sTnC \cdot cTnI_{128-147} \cdot sTnI_{115-131} \cdot 4Ca^{2+}$  using  $sCTnC$  (residues 95 to 160) for superimposition calculations.

The lowest energy structure is shown in ribbon form in Figure VII-3. Although the relative orientation of the two domains of TnC differs from the results reported by Dvoretzky et al., this particular structure was chosen from the set because of the ease with which the different domains of TnI can be seen interacting with TnC. The TnI inhibitory

peptide is passing over the Rp40 peptide, which occupies the hydrophobic groove of sCTnC. In the shown representation, the peptide lies somewhat parallel to the inter domain central helix. This feature was observed for all the generated structures. However, none of 15 lowest energy structures have a C/N-TnC interdomain orientation similar to that of the one proposed by Dvoretzky et al (19).

It is important not to overanalyze or over interpret the model given in Figure VII-3, for several reasons. First, the structural information used is incomplete. The addition of long range distance restraints derived from fluorescence, neutron scattering studies or NMR residual dipolar coupling would definitely improve our model. Moreover, as previously mentioned, the region of TnI interacting with the central helix linking the two domains of TnC is poorly defined due to the absence of distance restraints in this region. Finally, TnT is absent from our model, as with the previous ones. The TnI<sub>40-96</sub> region of TnI, which is absent from our model, is believed to have contacts with TnT in the form of coil-coil interactions (20). Clearly, this sets a new starting point for future work. The elucidation of the whole TnC•TnI•TnT complex will eventually solve a lot of issues. A preliminary structure of this ternary complex has been presented (20) by the Maeda research group. Work is also currently underway in our laboratory to elucidate the structure and dynamics of the complex by NMR.



Figure VII-3. A) Ribbon diagram of a chimera structure of  $sTnC \cdot cTnI_{128-147} \cdot sTnI_{115-131} \cdot 4Ca^{2+}$ . TnC is shown in silver from residues 3 to 159, TnI is shown in red from residues 96-127 (numbering relative to the skeletal isoform), Rp40 is shown in green from residues 3 to 35 and the calcium ions are represented as yellow spheres.

**REFERENCES**

1. Vassilyev, D. G., Takeda, S., Wakatsuki, S., Maeda, K., and Maeda, Y. (1998) *Proc. Natl. Acad. Sci. U.S.A.* 95, 4847-4852.
2. Tung, C. S., Wall, M. E., Gallagher, S. C., and Trehwella, J. (2000) *Protein Sci.* 9, 1312-1326.
3. Luo, Y., Leszyk, J., Li, B., Gergely, J., and Tao, T. (2000) *Biochemistry* 39, 15306-15315.
4. Luo, Y., Wu, J. L., Li, B., Langsetmo, K., Gergely, J., and Tao, T. (2000) *J. Mol. Biol.* 296, 899-910.
5. Ngai, S. M., Sonnichsen, F. D., and Hodges, R. S. (1994) *J. Biol. Chem.* 269, 2165-2172.
6. Mercier, P., Li, M. X., and Sykes, B. D. (2000) *Biochemistry* 39, 2902-2911.
7. Mercier, P., Spyrapoulos, L., and Sykes, B. D. (2001) *Biochemistry* 40, 10063-10077.
8. Blumenschein, T. M., Tripet, B. P., Hodges, R. S., and Sykes, B. D. (2001) *J. Biol. Chem.* 276, 36606-36612.
9. Wang, X., Li, M. X., and Sykes, B. D. (2002) *J. Biol. Chem.* 277, 31124-31133.
10. Lindhout, D. A., and Sykes, B. D. (2003) *J. Mol. Biol.*
11. McKay, R. T., Tripet, B. P., Hodges, R. S., and Sykes, B. D. (1997) *J. Biol. Chem.* 272, 28494-28500.
12. Laskowski, R. A., MacArthur, M. W., Moss, D. S., and Thornton, J. M. (1993) *J. Appl. Crystallogr.* 26, 283-291.
13. Brown, L. J., Sale, K. L., Hills, R., Rouviere, C., Song, L., Zhang, X., and Fajer, P. G. (2002) *Proc. Natl. Acad. Sci. U.S.A.* 99, 12765-12770.
14. Tripet, B. P., Van Eyk, J. E., and Hodges, R. S. (1997) *J. Mol. Biol.* 271, 728-750.
15. Slupsky, C. M. (1995) in *Thesis: Biochemistry* pp 352, University of Alberta, Edmonton.
16. Li, M. X., Spyrapoulos, L., and Sykes, B. D. (1999) *Biochemistry* 38, 8289-8298.
17. Gasmi-Seabrook, G. M., Howarth, J. W., Finley, N., Abusamhadneh, E., Gaponenko, V., Brito, R. M., Solaro, R. J., and Rosevear, P. R. (1999) *Biochemistry* 38, 8313-8322.
18. Gasmi-Seabrook, G. M., Howarth, J. W., Finley, N., Abusamhadneh, E., Gaponenko, V. V., Brito, R. M., Solaro, R. J., and Rosevear, P. R. (1999) *Biochemistry* 38, 14432.
19. Dvoretzky, A., Abusamhadneh, E. M., Howarth, J. W., and Rosevear, P. R. (2002) *J. Biol. Chem.* 277, 38565-38570.
20. Takeda, S., Yamashida, A., Maeda, K., and Maeda, Y. (2002) *Biophys. J.* 82, 170a.

## Appendix I

### *Bifunctional rhodamine force field and topology file*

#### **CREATION OF TOPOLOGY AND PARAMETER FILES FOR RHODAMINE**

In order to generate structures with coordinates of the bifunctional rhodamine (BR), a topology and parameter file (the forcefield) had to be created for the software CNS (version 1.1) (1). First, the structure of rhodamine was build and covalently attached to a right-handed  $\alpha$ -helix constituted of residues 55-65 from the C-helix of sCTnC using InsightII (2). The hybrid complex was minimized within InsightII with the cvv forcefield. The resulting structure was saved in pdb format, and BR coordinates were manually extracted and exported into a second independent pdb file for submission to the Gerard Kleywegt's XPLO2D server (<http://alpha2.bmc.uu.se/hicup/xdict.html>) (version 3.0.2), which automatically produces energy and parameter files from pdb input files. By default, the server returns a different atom type for each atom in the molecule. However, since the BR molecule is symmetric, there is no such requirement. Therefore, both files returned by the server were manually modified to merge equivalent atoms into a single atom type (see Figure AI-1). This greatly shortened and eased subsequent manipulations of the files, which were carefully inspected and later modified to properly reflect the desired stereospecificity of different moieties and to allow for flexibility around single bonds in arms of BR (see content of the files is provided below). Finally, the BR molecule was covalently attached to a pre-folded structure of sCTnC•2Ca<sup>2+</sup>•TnI<sub>115-131</sub> with the program CNS using a custom patch command. The CNS script used for the linkage is provided below. The sulfur groups of Cys56 and Cys63 were changed to the atom type

SM, based on the situation in Met residues where the S atom is bonded to two carbon atoms, instead of one carbon and one hydrogen. All BR atoms are uncharged in the topology file. The application of valid partial charges will necessitate *ab initio* calculations.

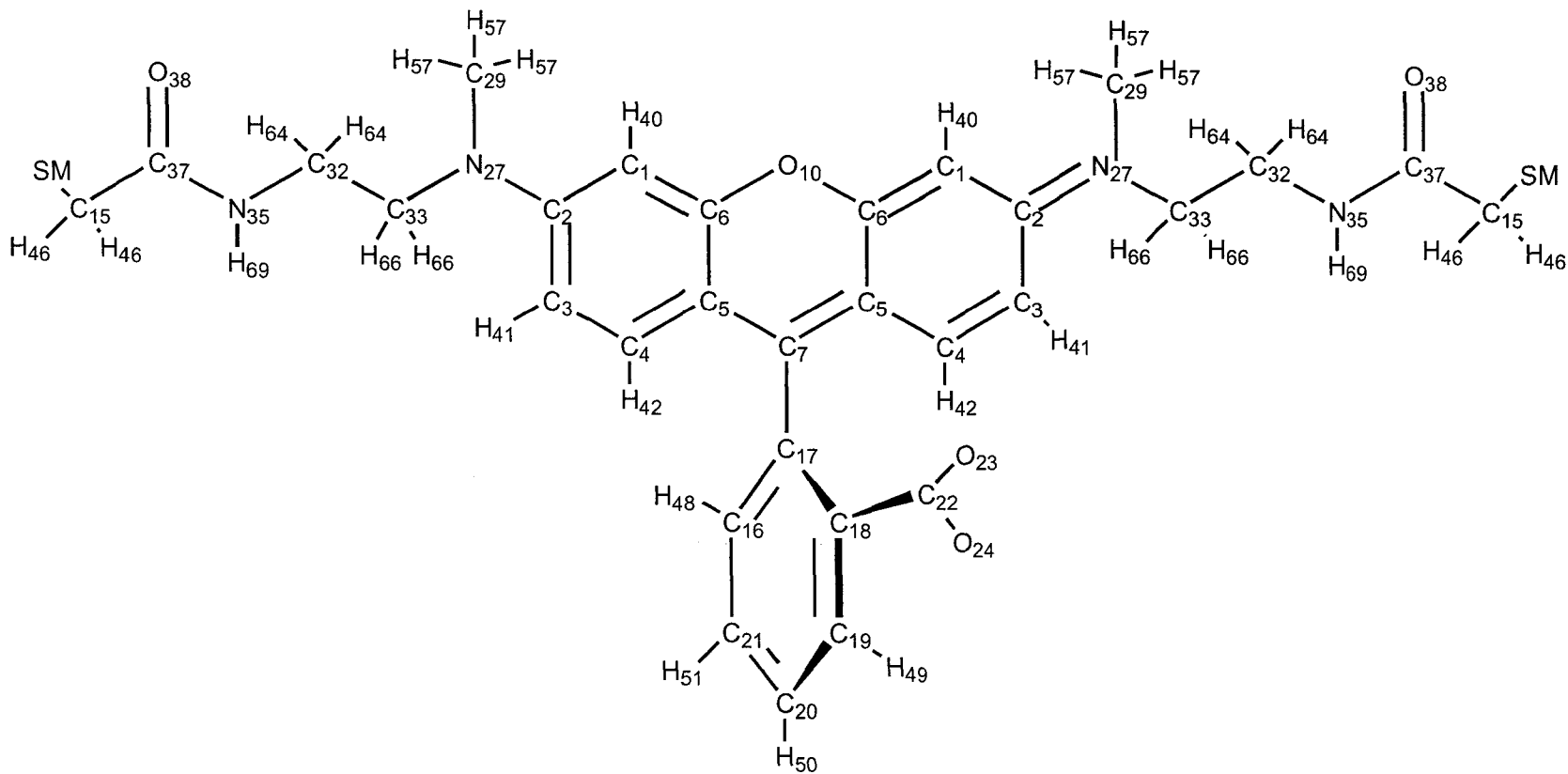


Figure AI-1. Chemical structure of BR showing each atom type in the molecular topology file. Note that for economy of labeling space, the X letter was dropped for each atom type ( $C_6$  is CX6 in the molecular topology file given below).

*BR Molecular topology file in mtf format (CNS)*

---

data\_cns\_mtf

\_cns\_mtf.title

```
; FILENAME="rhodamine_generated.mtf"
  file toppar/protein.link
```

this is a macro to define standard protein peptide bonds  
and termini to generate a protein sequence.

DATE:24-Sep-02 12:56:58 created by user: pmercier

VERSION:1.1

;

loop\_

\_cns\_mtf\_atom.id

\_cns\_mtf\_atom.segment\_id

\_cns\_mtf\_atom.residue\_id

\_cns\_mtf\_atom.residue\_name

\_cns\_mtf\_atom.atom\_name

\_cns\_mtf\_atom.chemical\_type

\_cns\_mtf\_atom.charge

\_cns\_mtf\_atom.atom\_mass

1	'RHOD'	'134'	'RHO'	'C1'	'CX1'	0.00000	12.0110
2	'RHOD'	'134'	'RHO'	'C2'	'CX2'	0.00000	12.0110
3	'RHOD'	'134'	'RHO'	'C3'	'CX3'	0.00000	12.0110
4	'RHOD'	'134'	'RHO'	'C4'	'CX4'	0.00000	12.0110
5	'RHOD'	'134'	'RHO'	'C5'	'CX5'	0.00000	12.0110
6	'RHOD'	'134'	'RHO'	'C6'	'CX6'	0.00000	12.0110
7	'RHOD'	'134'	'RHO'	'C7'	'CX7'	0.00000	12.0110
8	'RHOD'	'134'	'RHO'	'C8'	'CX5'	0.00000	12.0110
9	'RHOD'	'134'	'RHO'	'C9'	'CX6'	0.00000	12.0110
10	'RHOD'	'134'	'RHO'	'O1'	'OX10'	0.00000	15.9990
11	'RHOD'	'134'	'RHO'	'C10'	'CX4'	0.00000	12.0110
12	'RHOD'	'134'	'RHO'	'C11'	'CX3'	0.00000	12.0110
13	'RHOD'	'134'	'RHO'	'C12'	'CX2'	0.00000	12.0110
14	'RHOD'	'134'	'RHO'	'C13'	'CX1'	0.00000	12.0110
15	'RHOD'	'134'	'RHO'	'C14'	'CX15'	0.00000	13.0190
16	'RHOD'	'134'	'RHO'	'C15'	'CX16'	0.00000	12.0110
17	'RHOD'	'134'	'RHO'	'C16'	'CX17'	0.00000	12.0110
18	'RHOD'	'134'	'RHO'	'C17'	'CX18'	0.00000	12.0110
19	'RHOD'	'134'	'RHO'	'C18'	'CX19'	0.00000	12.0110
20	'RHOD'	'134'	'RHO'	'C19'	'CX20'	0.00000	12.0110
21	'RHOD'	'134'	'RHO'	'C20'	'CX21'	0.00000	12.0110
22	'RHOD'	'134'	'RHO'	'C21'	'CX22'	0.00000	12.0110
23	'RHOD'	'134'	'RHO'	'O2'	'OX23'	0.00000	15.9990
24	'RHOD'	'134'	'RHO'	'O3'	'OX24'	0.00000	15.9990

25	'RHOD'	'134'	'RHO'	'N1'	'NX27'	0.00000	14.0070
26	'RHOD'	'134'	'RHO'	'C22'	'CX15'	0.00000	13.0190
27	'RHOD'	'134'	'RHO'	'N2'	'NX27'	0.00000	14.0070
28	'RHOD'	'134'	'RHO'	'C23'	'CX29'	0.00000	12.0110
29	'RHOD'	'134'	'RHO'	'C24'	'CX29'	0.00000	12.0110
30	'RHOD'	'134'	'RHO'	'C25'	'CX32'	0.00000	12.0110
31	'RHOD'	'134'	'RHO'	'C26'	'CX33'	0.00000	12.0110
32	'RHOD'	'134'	'RHO'	'C27'	'CX32'	0.00000	12.0110
33	'RHOD'	'134'	'RHO'	'C28'	'CX33'	0.00000	12.0110
34	'RHOD'	'134'	'RHO'	'N3'	'NX35'	0.00000	14.0070
35	'RHOD'	'134'	'RHO'	'N4'	'NX35'	0.00000	14.0070
36	'RHOD'	'134'	'RHO'	'C29'	'CX37'	0.00000	12.0110
37	'RHOD'	'134'	'RHO'	'C30'	'CX37'	0.00000	12.0110
38	'RHOD'	'134'	'RHO'	'04'	'OX38'	0.00000	15.9990
39	'RHOD'	'134'	'RHO'	'05'	'OX38'	0.00000	15.9990
40	'RHOD'	'134'	'RHO'	'H1'	'HX40'	0.00000	1.00800
41	'RHOD'	'134'	'RHO'	'H2'	'HX41'	0.00000	1.00800
42	'RHOD'	'134'	'RHO'	'H3'	'HX42'	0.00000	1.00800
43	'RHOD'	'134'	'RHO'	'H4'	'HX42'	0.00000	1.00800
44	'RHOD'	'134'	'RHO'	'H5'	'HX41'	0.00000	1.00800
45	'RHOD'	'134'	'RHO'	'H6'	'HX40'	0.00000	1.00800
46	'RHOD'	'134'	'RHO'	'H7'	'HX46'	0.00000	1.00800
47	'RHOD'	'134'	'RHO'	'H8'	'HX46'	0.00000	1.00800
48	'RHOD'	'134'	'RHO'	'H9'	'HX48'	0.00000	1.00800
49	'RHOD'	'134'	'RHO'	'H10'	'HX49'	0.00000	1.00800
50	'RHOD'	'134'	'RHO'	'H11'	'HX50'	0.00000	1.00800
51	'RHOD'	'134'	'RHO'	'H12'	'HX51'	0.00000	1.00800
52	'RHOD'	'134'	'RHO'	'H13'	'HX46'	0.00000	1.00800
53	'RHOD'	'134'	'RHO'	'H14'	'HX46'	0.00000	1.00800
54	'RHOD'	'134'	'RHO'	'H15'	'HX57'	0.00000	1.00800
55	'RHOD'	'134'	'RHO'	'H16'	'HX57'	0.00000	1.00800
56	'RHOD'	'134'	'RHO'	'H17'	'HX57'	0.00000	1.00800
57	'RHOD'	'134'	'RHO'	'H18'	'HX57'	0.00000	1.00800
58	'RHOD'	'134'	'RHO'	'H19'	'HX57'	0.00000	1.00800
59	'RHOD'	'134'	'RHO'	'H20'	'HX57'	0.00000	1.00800
60	'RHOD'	'134'	'RHO'	'H21'	'HX64'	0.00000	1.00800
61	'RHOD'	'134'	'RHO'	'H22'	'HX64'	0.00000	1.00800
62	'RHOD'	'134'	'RHO'	'H23'	'HX66'	0.00000	1.00800
63	'RHOD'	'134'	'RHO'	'H24'	'HX66'	0.00000	1.00800
64	'RHOD'	'134'	'RHO'	'H25'	'HX64'	0.00000	1.00800
65	'RHOD'	'134'	'RHO'	'H26'	'HX64'	0.00000	1.00800
66	'RHOD'	'134'	'RHO'	'H27'	'HX66'	0.00000	1.00800
67	'RHOD'	'134'	'RHO'	'H28'	'HX66'	0.00000	1.00800
68	'RHOD'	'134'	'RHO'	'H29'	'HX69'	0.00000	1.00800
69	'RHOD'	'134'	'RHO'	'H30'	'HX69'	0.00000	1.00800
-1	'	'	'	'	'	-1.00000	-1.00000

loop\_

```
_cns_mtf_bond.id[1]
_cns_mtf_bond.id[2]
1 2
1 6
1 40
2 3
2 27
3 4
3 41
4 5
4 42
5 6
5 7
6 10
7 8
7 17
8 9
8 11
9 10
9 14
11 12
11 43
12 13
12 44
13 14
13 25
14 45
15 37
15 46
15 47
16 17
16 21
16 48
17 18
18 19
18 22
19 20
19 49
20 21
20 50
21 51
22 23
22 24
25 28
25 31
26 36
26 52
26 53
```

27 29  
27 33  
28 54  
28 55  
28 56  
29 57  
29 58  
29 59  
30 31  
30 34  
30 60  
30 61  
31 62  
31 63  
32 33  
32 35  
32 64  
32 65  
33 66  
33 67  
34 36  
34 68  
35 37  
35 69  
36 39  
37 38  
-1 -1

loop\_  
\_cns\_mtf\_angle.id[1]  
\_cns\_mtf\_angle.id[2]  
\_cns\_mtf\_angle.id[3]  
2 1 6  
2 1 40  
1 2 3  
1 2 27  
6 1 40  
1 6 5  
1 6 10  
3 2 27  
2 3 4  
2 3 41  
2 27 29  
2 27 33  
4 3 41  
3 4 5  
3 4 42  
5 4 42

4 5 6  
4 5 7  
6 5 7  
5 6 10  
5 7 8  
5 7 17  
6 10 9  
8 7 17  
7 8 9  
7 8 11  
7 17 16  
7 17 18  
9 8 11  
8 9 10  
8 9 14  
8 11 12  
8 11 43  
10 9 14  
9 14 13  
9 14 45  
12 11 43  
11 12 13  
11 12 44  
13 12 44  
12 13 14  
12 13 25  
14 13 25  
13 14 45  
13 25 28  
13 25 31  
37 15 46  
37 15 47  
15 37 35  
15 37 38  
46 15 47  
17 16 21  
17 16 48  
16 17 18  
21 16 48  
16 21 20  
16 21 51  
17 18 19  
17 18 22  
19 18 22  
18 19 20  
18 19 49  
18 22 23  
18 22 24

20 19 49  
19 20 21  
19 20 50  
21 20 50  
20 21 51  
23 22 24  
28 25 31  
25 28 54  
25 28 55  
25 28 56  
25 31 30  
25 31 62  
25 31 63  
36 26 52  
36 26 53  
26 36 34  
26 36 39  
52 26 53  
29 27 33  
27 29 57  
27 29 58  
27 29 59  
27 33 32  
27 33 66  
27 33 67  
54 28 55  
54 28 56  
55 28 56  
57 29 58  
57 29 59  
58 29 59  
31 30 34  
31 30 60  
31 30 61  
30 31 62  
30 31 63  
34 30 60  
34 30 61  
30 34 36  
30 34 68  
60 30 61  
62 31 63  
33 32 35  
33 32 64  
33 32 65  
32 33 66  
32 33 67  
35 32 64

35 32 65  
32 35 37  
32 35 69  
64 32 65  
66 33 67  
36 34 68  
34 36 39  
37 35 69  
35 37 38  
-1 -1 -1

loop\_  
\_cns\_mtf\_dihedral.id[1]  
\_cns\_mtf\_dihedral.id[2]  
\_cns\_mtf\_dihedral.id[3]  
\_cns\_mtf\_dihedral.id[4]  
6 1 2 3  
6 1 2 27  
40 1 2 3  
40 1 2 27  
2 1 6 5  
2 1 6 10  
40 1 6 5  
40 1 6 10  
1 2 3 4  
1 2 3 41  
27 2 3 4  
27 2 3 41  
1 2 27 29  
2 3 4 5  
2 3 4 42  
41 3 4 5  
41 3 4 42  
3 4 5 6  
3 4 5 7  
42 4 5 6  
42 4 5 7  
4 5 6 1  
4 5 6 10  
7 5 6 1  
7 5 6 10  
4 5 7 8  
4 5 7 17  
6 5 7 8  
6 5 7 17  
1 6 10 9  
5 6 10 9  
5 7 8 9

5 7 8 11  
17 7 8 9  
17 7 8 11  
7 8 9 10  
7 8 9 14  
11 8 9 10  
11 8 9 14  
7 8 11 12  
7 8 11 43  
9 8 11 12  
9 8 11 43  
8 9 10 6  
14 9 10 6  
8 9 14 13  
8 9 14 45  
10 9 14 13  
10 9 14 45  
8 11 12 13  
8 11 12 44  
43 11 12 13  
43 11 12 44  
11 12 13 14  
11 12 13 25  
44 12 13 14  
44 12 13 25  
12 13 14 9  
12 13 14 45  
25 13 14 9  
25 13 14 45  
21 16 17 7  
21 16 17 18  
48 16 17 7  
48 16 17 18  
17 16 21 20  
17 16 21 51  
48 16 21 20  
48 16 21 51  
7 17 18 19  
7 17 18 22  
16 17 18 19  
16 17 18 22  
17 18 19 20  
17 18 19 49  
22 18 19 20  
22 18 19 49  
17 18 22 23  
17 18 22 24  
19 18 22 23

19 18 22 24  
18 19 20 21  
18 19 20 50  
49 19 20 21  
49 19 20 50  
19 20 21 16  
19 20 21 51  
50 20 21 16  
50 20 21 51  
68 34 36 39  
69 35 37 38  
12 13 25 28  
-1 -1 -1 -1

loop\_  
\_cns\_mtf\_improper.id[1]  
\_cns\_mtf\_improper.id[2]  
\_cns\_mtf\_improper.id[3]  
\_cns\_mtf\_improper.id[4]  
1 2 6 40  
2 1 3 27  
3 2 4 41  
4 3 5 42  
5 4 6 7  
6 1 5 10  
7 5 8 17  
8 7 9 11  
9 8 10 14  
11 8 12 43  
12 11 13 44  
13 12 14 25  
14 9 13 45  
15 37 46 47  
16 17 21 48  
17 7 16 18  
18 17 19 22  
19 18 20 49  
20 19 21 50  
21 16 20 51  
22 18 23 24  
25 13 28 31  
26 36 52 53  
27 2 29 33  
28 25 54 55  
29 27 57 58  
30 31 34 60  
31 25 30 62  
32 33 35 64





*BR parameter file (CNS)*

---

Remarks /var/tmp/xdict\_12439.par  
Remarks Created by XPL02D V. 020227/2.9.7 at Fri Mar 15 21:34:05 2002  
for A. Nonymous  
Remarks Auto-generated by XPL02D from file /var/tmp/xdict\_12439.pdb  
Remarks Parameters for residue type RHO

set echo=false end

{ edit if necessary }

BOND	CX1	CX2	1000.0	1.400	!	Nobs	=	1
BOND	CX1	CX6	1000.0	1.389	!	Nobs	=	1
BOND	CX1	HX40	1000.0	1.078	!	Nobs	=	1
BOND	CX2	CX3	1000.0	1.402	!	Nobs	=	1
BOND	CX2	NX27	1000.0	1.497	!	Nobs	=	1
BOND	CX3	CX4	1000.0	1.389	!	Nobs	=	1
BOND	CX3	HX41	1000.0	1.076	!	Nobs	=	1
BOND	CX4	CX5	1000.0	1.413	!	Nobs	=	1
BOND	CX4	HX42	1000.0	1.080	!	Nobs	=	1
BOND	CX5	CX6	1000.0	1.418	!	Nobs	=	1
BOND	CX5	CX7	1000.0	1.427	!	Nobs	=	1
BOND	CX6	OX10	1000.0	1.402	!	Nobs	=	1
BOND	CX7	CX17	1000.0	1.398	!	Nobs	=	1
BOND	CX15	CX37	1000.0	1.518	!	Nobs	=	1
BOND	CX15	HX46	1000.0	1.103	!	Nobs	=	1
BOND	CX16	CX17	1000.0	1.407	!	Nobs	=	1
BOND	CX16	CX21	1000.0	1.386	!	Nobs	=	1
BOND	CX16	HX48	1000.0	1.082	!	Nobs	=	1
BOND	CX17	CX18	1000.0	1.431	!	Nobs	=	1
BOND	CX18	CX19	1000.0	1.408	!	Nobs	=	1
BOND	CX18	CX22	1000.0	1.531	!	Nobs	=	1
BOND	CX19	CX20	1000.0	1.388	!	Nobs	=	1
BOND	CX19	HX49	1000.0	1.081	!	Nobs	=	1
BOND	CX20	CX21	1000.0	1.385	!	Nobs	=	1
BOND	CX20	HX50	1000.0	1.080	!	Nobs	=	1
BOND	CX21	HX51	1000.0	1.080	!	Nobs	=	1
BOND	CX22	OX23	1000.0	1.255	!	Nobs	=	1
BOND	CX22	OX24	1000.0	1.252	!	Nobs	=	1
BOND	NX27	CX29	1000.0	1.487	!	Nobs	=	1
BOND	NX27	CX33	1000.0	1.497	!	Nobs	=	1
BOND	CX29	HX57	1000.0	1.108	!	Nobs	=	1
BOND	CX32	CX33	1000.0	1.550	!	Nobs	=	1
BOND	CX32	NX35	1000.0	1.485	!	Nobs	=	1
BOND	CX32	HX64	1000.0	1.107	!	Nobs	=	1
BOND	CX33	HX66	1000.0	1.106	!	Nobs	=	1
BOND	NX35	CX37	1000.0	1.333	!	Nobs	=	1

```
BOND NX35 HX69 1000.0 1.025 ! Nobs = 1
BOND CX37 OX38 1000.0 1.228 ! Nobs = 1

{ edit if necessary }
ANGLe CX2 CX1 CX6 500.0 121.34 ! Nobs = 1
ANGLe CX2 CX1 HX40 500.0 120.86 ! Nobs = 1
ANGLe CX6 CX1 HX40 500.0 117.74 ! Nobs = 1
ANGLe CX1 CX2 CX3 500.0 117.92 ! Nobs = 1
ANGLe CX1 CX2 NX27 500.0 120.51 ! Nobs = 1
ANGLe CX3 CX2 NX27 500.0 121.55 ! Nobs = 1
ANGLe CX2 CX3 CX4 500.0 121.26 ! Nobs = 1
ANGLe CX2 CX3 HX41 500.0 121.91 ! Nobs = 1
ANGLe CX4 CX3 HX41 500.0 116.83 ! Nobs = 1
ANGLe CX3 CX4 CX5 500.0 121.26 ! Nobs = 1
ANGLe CX3 CX4 HX42 500.0 117.73 ! Nobs = 1
ANGLe CX5 CX4 HX42 500.0 121.01 ! Nobs = 1
ANGLe CX4 CX5 CX6 500.0 117.02 ! Nobs = 1
ANGLe CX4 CX5 CX7 500.0 124.60 ! Nobs = 1
ANGLe CX6 CX5 CX7 500.0 118.36 ! Nobs = 1
ANGLe CX1 CX6 CX5 500.0 121.13 ! Nobs = 1
ANGLe CX1 CX6 OX10 500.0 117.43 ! Nobs = 1
ANGLe CX5 CX6 OX10 500.0 121.37 ! Nobs = 1
ANGLe CX5 CX7 CX5 500.0 120.86 ! Nobs = 1
ANGLe CX5 CX7 CX17 500.0 119.54 ! Nobs = 1
ANGLe CX6 OX10 CX6 500.0 119.64 ! Nobs = 1
ANGLe CX37 CX15 HX46 500.0 109.89 ! Nobs = 1
ANGLe HX46 CX15 HX46 500.0 106.04 ! Nobs = 1
ANGLe CX17 CX16 CX21 500.0 120.66 ! Nobs = 1
ANGLe CX17 CX16 HX48 500.0 120.78 ! Nobs = 1
ANGLe CX21 CX16 HX48 500.0 118.56 ! Nobs = 1
ANGLe CX7 CX17 CX16 500.0 117.50 ! Nobs = 1
ANGLe CX7 CX17 CX18 500.0 122.92 ! Nobs = 1
ANGLe CX16 CX17 CX18 500.0 119.56 ! Nobs = 1
ANGLe CX17 CX18 CX19 500.0 117.78 ! Nobs = 1
ANGLe CX17 CX18 CX22 500.0 126.41 ! Nobs = 1
ANGLe CX19 CX18 CX22 500.0 115.81 ! Nobs = 1
ANGLe CX18 CX19 CX20 500.0 121.54 ! Nobs = 1
ANGLe CX18 CX19 HX49 500.0 120.00 ! Nobs = 1
ANGLe CX20 CX19 HX49 500.0 118.47 ! Nobs = 1
ANGLe CX19 CX20 CX21 500.0 120.17 ! Nobs = 1
ANGLe CX19 CX20 HX50 500.0 119.62 ! Nobs = 1
ANGLe CX21 CX20 HX50 500.0 120.21 ! Nobs = 1
ANGLe CX16 CX21 CX20 500.0 120.29 ! Nobs = 1
ANGLe CX16 CX21 HX51 500.0 119.93 ! Nobs = 1
ANGLe CX20 CX21 HX51 500.0 119.79 ! Nobs = 1
ANGLe CX18 CX22 OX23 500.0 120.70 ! Nobs = 1
ANGLe CX18 CX22 OX24 500.0 120.00 ! Nobs = 1
ANGLe OX23 CX22 OX24 500.0 119.30 ! Nobs = 1
```

ANGL	e	CX2	NX27	CX29	500.0	119.49	!	Nobs =	1
ANGL	e	CX2	NX27	CX33	500.0	122.70	!	Nobs =	1
ANGL	e	CX29	NX27	CX33	500.0	117.73	!	Nobs =	1
ANGL	e	NX27	CX29	HX57	500.0	110.83	!	Nobs =	1
ANGL	e	HX57	CX29	HX57	500.0	106.89	!	Nobs =	1
ANGL	e	CX33	CX32	NX35	500.0	114.23	!	Nobs =	1
ANGL	e	CX33	CX32	HX64	500.0	108.49	!	Nobs =	1
ANGL	e	NX35	CX32	HX64	500.0	108.92	!	Nobs =	1
ANGL	e	HX64	CX32	HX64	500.0	102.92	!	Nobs =	1
ANGL	e	NX27	CX33	CX32	500.0	112.73	!	Nobs =	1
ANGL	e	NX27	CX33	HX66	500.0	110.07	!	Nobs =	1
ANGL	e	CX32	CX33	HX66	500.0	110.03	!	Nobs =	1
ANGL	e	HX66	CX33	HX66	500.0	104.49	!	Nobs =	1
ANGL	e	CX32	NX35	CX37	500.0	124.48	!	Nobs =	1
ANGL	e	CX32	NX35	HX69	500.0	124.14	!	Nobs =	1
ANGL	e	CX37	NX35	HX69	500.0	110.99	!	Nobs =	1
ANGL	e	CX15	CX37	NX35	500.0	123.94	!	Nobs =	1
ANGL	e	CX15	CX37	OX38	500.0	119.46	!	Nobs =	1
ANGL	e	NX35	CX37	OX38	500.0	116.58	!	Nobs =	1
{ edit if necessary }									
DIHEC	X6	CX1	CX2	CX3	500.0	0	0.00	!	Nobs=1...Value=-1.97
DIHEC	X6	CX1	CX2	NX27	500.0	0	180.00	!	Nobs=1...Value= 176.59
DIHEH	X40	CX1	CX2	CX3	500.0	0	180.00	!	Nobs=1...Value=-178.91
DIHEH	X40	CX1	CX2	NX27	500.0	0	0.00	!	Nobs=1...Value=-0.36
DIHEC	X2	CX1	CX6	CX5	500.0	0	0.00	!	Nobs=1...Value= 0.13
DIHEC	X2	CX1	CX6	OX10	500.0	0	180.00	!	Nobs=1...Value=-176.89
DIHEH	X40	CX1	CX6	CX5	500.0	0	180.00	!	Nobs=1...Value= 177.17
DIHEH	X40	CX1	CX6	OX10	500.0	0	0.00	!	Nobs=1...Value= 0.15
DIHEC	X1	CX2	CX3	CX4	500.0	0	0.00	!	Nobs=1...Value= 1.36
DIHEC	X1	CX2	CX3	HX41	500.0	0	180.00	!	Nobs=1...Value=-178.44
DIHEN	X27	CX2	CX3	CX4	500.0	0	180.00	!	Nobs=1...Value=-177.18
DIHEN	X27	CX2	CX3	HX41	500.0	0	0.00	!	Nobs=1...Value= 3.02
DIHEC	X1	CX2	NX27	CX29	500.0	0	180.00	!	Nobs=1...Value= 7.96
!!DIHEC	X3	CX2	NX27	CX29	500.0	1	180.00	!	Nobs=1...Value= 173.53
DIHEC	X2	CX3	CX4	CX5	500.0	0	0.00	!	Nobs=1...Value= 1.11
DIHEC	X2	CX3	CX4	HX42	500.0	0	180.00	!	Nobs=1...Value=-179.21
DIHEH	X41	CX3	CX4	HX42	500.0	0	0.00	!	Nobs=1...Value= 0.60
DIHEC	X3	CX4	CX5	CX6	500.0	0	0.00	!	Nobs=1...Value=-2.88
DIHEH	X42	CX4	CX5	CX6	500.0	0	180.00	!	Nobs=1...Value= 177.44
DIHEC	X4	CX5	CX6	CX1	500.0	0	0.00	!	Nobs=1...Value= 2.27
DIHEC	X4	CX5	CX6	OX10	500.0	0	180.00	!	Nobs=1...Value= 179.17
DIHEC	X7	CX5	CX6	CX1	500.0	0	180.00	!	Nobs=1...Value=-176.03
DIHEC	X4	CX5	CX7	CX5	500.0	0	180.00	!	Nobs=1...Value=-176.77
DIHEC	X4	CX5	CX7	CX17	500.0	0	0.00	!	Nobs=1...Value= 4.62
DIHEC	X6	CX5	CX7	CX17	500.0	0	180.00	!	Nobs=1...Value=-177.21
DIHEC	X1	CX6	OX10	CX6	500.0	0	180.00	!	Nobs=1...Value= 175.83
DIHEC	X5	CX6	OX10	CX6	500.0	0	0.00	!	Nobs=1...Value=-1.18

```

DIHECX5  CX7  CX5  CX6      500.0 0      0.00 ! Nobs=1...Value=-3.25

!controls orientation of C02 group (set to front here)
!the second line is to set the C02 group facing back
  DIHECX5  CX7  CX17 CX16    500.0 0     90.00 ! Nobs=1...Value= -90.66
!!DIHECX5  CX7  CX17 CX18    500.0 0    -90.00 ! Nobs=1...Value=  87.84

DIHECX7  CX5  CX6  OX10    500.0 0      0.00 ! Nobs=1...Value=  2.97
DIHECX7  CX5  CX4  CX3    500.0 0    180.00 ! Nobs=1...Value=-179.91
DIHECX7  CX5  CX4  HX42    500.0 0      0.00 ! Nobs=1...Value=  1.19
DIHECX5  CX4  CX3  HX41    500.0 0    180.00 ! Nobs=1...Value=-179.34
!!DIHEHX46 CX15 CX37 NX35    500.0 0     60.00 ! Nobs=1...Value=  61.22
!!DIHEHX46 CX15 CX37 NX35    500.0 0    -60.00 ! Nobs=1...Value= -54.58
DIHECX21 CX16 CX17 CX7    500.0 0    180.00 ! Nobs=1...Value=  177.94
DIHECX21 CX16 CX17 CX18    500.0 0      0.00 ! Nobs=1...Value=-0.62
DIHEHX48 CX16 CX17 CX7    500.0 0      0.00 ! Nobs=1...Value=-2.08
DIHEHX48 CX16 CX17 CX18    500.0 0    180.00 ! Nobs=1...Value=  179.37
DIHECX17 CX16 CX21 CX20    500.0 0      0.00 ! Nobs=1...Value=-0.05
DIHECX17 CX16 CX21 HX51    500.0 0    180.00 ! Nobs=1...Value=-179.95
DIHEHX48 CX16 CX21 CX20    500.0 0    180.00 ! Nobs=1...Value=  179.96
DIHEHX48 CX16 CX21 HX51    500.0 0      0.00 ! Nobs=1...Value=  0.06
DIHECX7  CX17 CX18 CX19    500.0 0    180.00 ! Nobs=1...Value=-177.50
DIHECX7  CX17 CX18 CX22    500.0 0      0.00 ! Nobs=1...Value=  2.92
DIHECX16 CX17 CX18 CX19    500.0 0      0.00 ! Nobs=1...Value=  0.98
DIHECX16 CX17 CX18 CX22    500.0 0    180.00 ! Nobs=1...Value=-178.61
DIHECX17 CX18 CX19 CX20    500.0 0      0.00 ! Nobs=1...Value=-0.71
DIHECX17 CX18 CX19 HX49    500.0 0    180.00 ! Nobs=1...Value=  179.82
DIHECX22 CX18 CX19 CX20    500.0 0    180.00 ! Nobs=1...Value=  178.92
DIHECX22 CX18 CX19 HX49    500.0 0      0.00 ! Nobs=1...Value=-0.54
DIHECX17 CX18 CX22 OX23    500.0 0    180.00 ! Nobs=1...Value=-176.38
DIHECX17 CX18 CX22 OX24    500.0 0      0.00 ! Nobs=1...Value=  3.87
DIHECX19 CX18 CX22 OX23    500.0 0      0.00 ! Nobs=1...Value=  4.03
DIHECX19 CX18 CX22 OX24    500.0 0    180.00 ! Nobs=1...Value=-175.72
DIHECX18 CX19 CX20 CX21    500.0 0      0.00 ! Nobs=1...Value=  0.06
DIHECX18 CX19 CX20 HX50    500.0 0    180.00 ! Nobs=1...Value=-179.66
DIHEHX49 CX19 CX20 CX21    500.0 0    180.00 ! Nobs=1...Value=  179.53
DIHEHX49 CX19 CX20 HX50    500.0 0      0.00 ! Nobs=1...Value=-0.18
DIHECX19 CX20 CX21 CX16    500.0 0      0.00 ! Nobs=1...Value=  0.34
DIHECX19 CX20 CX21 HX51    500.0 0    180.00 ! Nobs=1...Value=-179.76
DIHEHX50 CX20 CX21 CX16    500.0 0    180.00 ! Nobs=1...Value=-179.95
DIHEHX50 CX20 CX21 HX51    500.0 0      0.00 ! Nobs=1...Value=-0.05
!!DIHECX2  NX27 CX33 CX32    500.0 0    -60.00 ! Nobs=1...Value=-52.35
!!DIHECX2  NX27 CX33 HX66    500.0 0    180.00 ! Nobs=1...Value=-174.34
!!DIHECX29 NX27 CX33 HX66    500.0 0      0.00 ! Nobs=1...Value=8.92
!!DIHEHX46 CX15 CX37 NX35    500.0 0    180.00 ! Nobs=1...Value=-173.82
!!DIHEHX46 CX15 CX37 OX38    500.0 0      0.00 ! Nobs=1...Value=4.37
!!DIHEHX46 CX15 CX37 NX35    500.0 0    -60.00 ! Nobs=1...Value=-60.36

```

```

!!DIHECX2  NX27 CX29 HX57    500.0 0   180.00 ! Nobs=1...Value=
171.93
!!DIHECX2  NX27 CX29 HX57    500.0 0   -60.00 ! Nobs=1...Value=-67.64
!!DIHECX2  NX27 CX29 HX57    500.0 0    60.00 ! Nobs=1...Value=
51.79
!!DIHECX2  NX27 CX33 CX32    500.0 0    90.00 ! Nobs=1...Value=
95.30
!!DIHECX29 NX27 CX33 CX32    500.0 0   -90.00 ! Nobs=1...Value=-81.02
!!DIHEHX64 CX32 CX33 NX27    500.0 0    90.00 ! Nobs=1...Value= 81.21
!!DIHEHX64 CX32 CX33 HX66    500.0 0    90.00 ! Nobs=1...Value=
91.91
!!DIHECX33 CX32 NX35 CX37    500.0 0    90.00 ! Nobs=1...Value=
93.45
!!DIHECX33 CX32 NX35 HX69    500.0 0   -90.00 ! Nobs=1...Value=-94.38
!!DIHENX35 CX32 CX33 NX27    500.0 0   -60.00 ! Nobs=1...Value=-64.29
!!DIHENX35 CX32 CX33 HX66    500.0 0   180.00 ! Nobs=1...Value=
173.32
!!DIHENX35 CX32 CX33 HX66    500.0 0    60.00 ! Nobs=1...Value=
62.82
!!DIHEHX64 CX32 CX33 NX27    500.0 0   180.00 ! Nobs=1...Value=
171.82
!!DIHEHX64 CX32 CX33 HX66    500.0 0   -60.00 ! Nobs=1...Value=-61.07
!!DIHEHX64 CX32 CX33 NX27    500.0 0    60.00 ! Nobs=1...Value=
58.04
!!DIHEHX64 CX32 CX33 HX66    500.0 0   -60.00 ! Nobs=1...Value=-64.36
!!DIHEHX64 CX32 CX33 HX66    500.0 0   180.00 ! Nobs=1...Value=-174.85
!!DIHEHX64 CX32 NX35 CX37    500.0 0    90.00 ! Nobs=1...Value=
83.78
!!DIHEHX64 CX32 NX35 HX69    500.0 0   -90.00 ! Nobs=1...Value=-90.24
!!DIHECX32 NX35 CX37 CX15    500.0 0    0.00 ! Nobs=1...Value=6.08
!!DIHECX32 NX35 CX37 OX38    500.0 1   180.00 ! Nobs=1...Value=
175.68
!!DIHEHX69 NX35 CX37 CX15    500.0 1   180.00 ! Nobs=1...Value=-179.15
!!DIHEHX69 NX35 CX37 OX38    500.0 0   180.00 ! Nobs=1...Value=2.62
!!DIHECX32 NX35 CX37 CX15    500.0 0   180.00 ! Nobs=1...Value=-176.18
!!DIHECX32 NX35 CX37 OX38    500.0 1    0.00 ! Nobs=1...Value=4.78
!!DIHEHX69 NX35 CX37 CX15    500.0 1    0.00 ! Nobs=1...Value=1.79
  DIHEHX69 NX35 CX37 OX38    500.0 0   180.00 ! Nobs=1...Value=
179.17
  DIHECX3 CX2 NX27 CX29    500.0 0    0.00 ! Nobs=1...Value=-173.53
!! DIHECX1 CX2 NX27 CX29    500.0 1   180.00 ! Nobs=1...Value= 8.06

{ edit if necessary }
IMPRoper CX1 CX2 CX6 HX40    750.0 0    0.000 !
Nobs=1...Value=1.608
IMPRoper CX2 CX1 CX3 NX27    750.0 0    0.000 !
Nobs=1...Value=0.838

```

```

IMPRoper CX3 CX2 CX4 HX41 750.0 0 0.000 !
Nobs=1...Value=0.105
IMPRoper CX4 CX3 CX5 HX42 750.0 0 0.000 !
Nobs=1...Value=0.168
IMPRoper CX5 CX4 CX6 CX7 750.0 0 0.000 !
Nobs=1...Value=0.984
IMPRoper CX6 CX1 CX5 OX10 750.0 0 0.000 !
Nobs=1...Value=1.774
IMPRoper CX7 CX5 CX5 CX17 750.0 0 0.000 !
Nobs=1...Value=0.807
IMPRoper CX5 CX7 CX6 CX4 750.0 0 0.000 ! Nobs=1...Value=0.123
IMPRoper CX6 CX5 OX10 CX1 750.0 0 0.000 ! Nobs=1...Value=-
0.466
IMPRoper CX4 CX5 CX3 HX42 750.0 0 0.000 ! Nobs=1...Value=0.577
IMPRoper CX3 CX4 CX2 HX41 750.0 0 0.000 ! Nobs=1...Value=1.341
IMPRoper CX2 CX3 CX1 NX27 750.0 0 0.000 ! Nobs=1...Value=-1.505
IMPRoper CX1 CX6 CX2 HX40 750.0 0 0.000 ! Nobs=1...Value=1.283
IMPRoper CX16 CX17 CX21 HX48 750.0 0 0.000 !
Nobs=1...Value=0.008
IMPRoper CX17 CX7 CX16 CX18 750.0 0 0.000 !
Nobs=1...Value=0.833
IMPRoper CX18 CX17 CX19 CX22 750.0 0 0.000 !
Nobs=1...Value=0.224
IMPRoper CX19 CX18 CX20 HX49 750.0 0 0.000 !
Nobs=1...Value=0.284
IMPRoper CX20 CX19 CX21 HX50 750.0 0 0.000 !
Nobs=1...Value=0.151
IMPRoper CX21 CX16 CX20 HX51 750.0 0 0.000 !
Nobs=1...Value=0.053
IMPRoper CX22 CX18 OX23 OX24 750.0 0 0.000 !
Nobs=1...Value=0.139
IMPRoper NX27 CX2 CX29 CX33 750.0 0 0.000 ! Nobs=1...Value=1.862
IMPRoper CX15 CX37 HX46 HX46 0.0 0 -35.000 ! Nobs=1...Value=-
37.143
IMPRoper CX29 NX27 HX57 HX57 0.0 0 -35.000 ! Nobs=1...Value=-
33.769
IMPRoper CX32 CX33 NX35 HX64 0.0 0 35.000 ! Nobs=1...Value=31.159
! >>> NOTE - unusual value for following improper :-29.62 reset to -
35.0
IMPRoper CX33 NX27 CX32 HX66 0.0 0 -35.000 ! Nobs=1...Value=-
29.621
IMPRoper NX35 CX32 CX37 HX69 750.0 0 0.000 !
Nobs=1...Value=3.979
IMPRoper CX37 CX15 NX35 OX38 750.0 0 0.000 !
Nobs=1...Value=1.020

{ edit if necessary }
NONBonded CX1 0.1200 3.7418 0.1000 3.3854 ! assuming Carbon

```

NONBonded	CX2	0.1200	3.7418	0.1000	3.3854	!	assuming	Carbon
NONBonded	CX3	0.1200	3.7418	0.1000	3.3854	!	assuming	Carbon
NONBonded	CX4	0.1200	3.7418	0.1000	3.3854	!	assuming	Carbon
NONBonded	CX5	0.1200	3.7418	0.1000	3.3854	!	assuming	Carbon
NONBonded	CX6	0.1200	3.7418	0.1000	3.3854	!	assuming	Carbon
NONBonded	CX7	0.1200	3.7418	0.1000	3.3854	!	assuming	Carbon
NONBonded	OX10	0.1591	2.8509	0.1591	2.8509	!	assuming	Oxygen
NONBonded	CX15	0.1200	3.7418	0.1000	3.3854	!	assuming	Carbon
NONBonded	CX16	0.1200	3.7418	0.1000	3.3854	!	assuming	Carbon
NONBonded	CX17	0.1200	3.7418	0.1000	3.3854	!	assuming	Carbon
NONBonded	CX18	0.1200	3.7418	0.1000	3.3854	!	assuming	Carbon
NONBonded	CX19	0.1200	3.7418	0.1000	3.3854	!	assuming	Carbon
NONBonded	CX20	0.1200	3.7418	0.1000	3.3854	!	assuming	Carbon
NONBonded	CX21	0.1200	3.7418	0.1000	3.3854	!	assuming	Carbon
NONBonded	CX22	0.1200	3.7418	0.1000	3.3854	!	assuming	Carbon
NONBonded	OX23	0.1591	2.8509	0.1591	2.8509	!	assuming	Oxygen
NONBonded	OX24	0.1591	2.8509	0.1591	2.8509	!	assuming	Oxygen
NONBonded	NX27	0.2384	2.8509	0.2384	2.8509	!	assuming	Nitrogen
NONBonded	CX29	0.1200	3.7418	0.1000	3.3854	!	assuming	Carbon
NONBonded	CX32	0.1200	3.7418	0.1000	3.3854	!	assuming	Carbon
NONBonded	CX33	0.1200	3.7418	0.1000	3.3854	!	assuming	Carbon
NONBonded	NX35	0.2384	2.8509	0.2384	2.8509	!	assuming	Nitrogen
NONBonded	CX37	0.1200	3.7418	0.1000	3.3854	!	assuming	Carbon
NONBonded	OX38	0.1591	2.8509	0.1591	2.8509	!	assuming	Oxygen
NONBonded	HX40	0.0498	1.4254	0.0498	1.4254	!	assuming	Hydrogen
NONBonded	HX41	0.0498	1.4254	0.0498	1.4254	!	assuming	Hydrogen
NONBonded	HX42	0.0498	1.4254	0.0498	1.4254	!	assuming	Hydrogen
NONBonded	HX46	0.0498	1.4254	0.0498	1.4254	!	assuming	Hydrogen
NONBonded	HX48	0.0498	1.4254	0.0498	1.4254	!	assuming	Hydrogen
NONBonded	HX49	0.0498	1.4254	0.0498	1.4254	!	assuming	Hydrogen
NONBonded	HX50	0.0498	1.4254	0.0498	1.4254	!	assuming	Hydrogen
NONBonded	HX51	0.0498	1.4254	0.0498	1.4254	!	assuming	Hydrogen
NONBonded	HX57	0.0498	1.4254	0.0498	1.4254	!	assuming	Hydrogen
NONBonded	HX64	0.0498	1.4254	0.0498	1.4254	!	assuming	Hydrogen
NONBonded	HX66	0.0498	1.4254	0.0498	1.4254	!	assuming	Hydrogen
NONBonded	HX69	0.0498	1.4254	0.0498	1.4254	!	assuming	Hydrogen

set echo=true end

*CNS script for BR linkage to sCTnC*

```

set message=normal echo=on end

parameter
@CNS_TOPPAR:protein-allhdg.param
!@CNS_TOPPAR:ion.param
@prep_of_Rhodamine/rhodamine.par

BOND  SM CX15          1000.000 {sd=    0.001}    1.803
ANGLE CH2E SM  CX15     500.000 {sd=    1.394}    100.90
ANGLE SM CX15  CX37     500.000 {sd=    1.394}    112.6822
ANGLE SM CX15  HX46     500.000 {sd=    1.394}    108.6768
ANGLE CH1E CH2E SM     500.00 {sd=    0.031}    114.3558

IMPRoper HX46 HX46 CX37 SM      500.0                0 -72.4655
IMPRoper HA  HA  CH1E SM      500.0 {sd=    0.031}    0 -72.4655

DIHE NH1  CH1E CH2E SM  0.00 {sd=    0.031}    3 0.0000
DIHE CH1E CH2E SM  CX15 0.00 {sd=    0.031}    3 0.0000

end

structure
@tni-tnc.mtf
!@calcium.mtf
end

coord @tnc-tni.pdb

structure
@prep_of_Rhodamine/rhodamine_generated.mtf
end

coord @prep_of_Rhodamine/rhodamine_custom.pdb

topology
@/usr/local/packages/cns_solve_1.1_pgf_optimized/libraries/toppar/prote
in-allhdg.top
@prep_of_Rhodamine/rhodamine.top
end

topology
presidue rhodamineSS

```

```
delete atom 1HG END
delete atom 3HG END

modify atom 1SG    type=SM      END
modify atom 3SG    type=SM      END

add bond 1SG 2C14
add bond 3SG 2C22

add angle 1CB 1SG 2C14
add angle 1SG 2C14 2C30
add angle 1SG 2C14 2H7
add angle 1SG 2C14 2H8

add angle 3CB 3SG 2C22
add angle 3SG 2C22 2C29
add angle 3SG 2C22 2H13
add angle 3SG 2C22 2H14

add improper 2H13 2H14 2C29 3SG
add improper 2H7 2H8 2C30 1SG

add improper 1HB1 1HB2 1CA 1SG
add improper 3HB1 3HB2 3CA 3SG

add dihedral 1N 1CA 1CB 1SG
add dihedral 3N 3CA 3CB 3SG

add dihedral 1CA 1CB 1SG 2C14
add dihedral 3CA 3CB 3SG 2C22

end

end

patch rhodomineSS
reference=1=(resid 63)
reference=2=(resid 134)
reference=3=(resid 56)
end
```

```
show sum(1) ( (resid 63 and name SG) and bondedto (resid 134 and name
C14) )
  if ( $result = 1 ) then
    buffer message
    display bond added between 63 and 134
  end
end if

show sum(1) ( (resid 56 and name SG) and bondedto (resid 134 and name
C22) )
  if ( $result = 1 ) then
    buffer message
    display bond added between 56 and 134
  end
end if

write structure output=fullthing.mtf end
write coordinates output=fullthing.pdb end
write parameter output=fullthing.param end

stop
```

**REFERENCES**

1. Brunger, A. T., Adams, P. D., Clore, G. M., DeLano, W. L., Gros, P., Grosse-Kunstleve, R. W., Jiang, J. S., Kuszewski, J., Nilges, M., Pannu, N. S., Read, R. J., Rice, L. M., Simonson, T., and Warren, G. L. (1998) *Acta Crystallogr. D Biol. Crystallogr.* 54, 905-921.
2. Inc., M. S. (1995), San Diego.

## Appendix II

### *Automatic NOE assignments with NMRView*

Scripting is a hobby. Good scripting is an art. Here I report one of the most helpful NMRView scripts of my library. It is surely not a piece of art as there is plenty of room for improvement and the addition of new features. Originally designed to help in the assignment of unassigned peaks, it became the primary tool in the structure determination of sNTnC in the Mg<sup>2+</sup> state. Starting from blank <sup>13</sup>C-NOESY and <sup>15</sup>N-NOESY peak lists, this script generated the distance restraints needed for the calculation of structures presented in Chapter 5. The script does in a few seconds what would take weeks for a graduate student and has the advantage of being written in Tcl so that it integrates directly as an external module within NMRView. The script does not offer any graphical interface for now.

#### *How to use the script:*

---

In order to use this NMRView script, you first must have the following items ready:

1. A <sup>13</sup>C-NOESY dataset opened (does not need to be drawn), along with its corresponding peak list
2. A <sup>15</sup>N-NOESY dataset opened (does not need to be drawn), along with its corresponding peak list
3. A sequence file (.seq) loaded

4. Chemical shifts assignments for your protein
5. A single or series of structures (in pdb format) loaded as starting model (optional)
6. The relation, the id tolerance and peak template set (in the peak analysis panel)  
For example, if the peak labeling for the  $^{13}\text{C}$ -NOESY is H1 H2 13C, where the proton in the first dimension is attached to the carbon atom in the third dimension, the above parameters would be the following:

```
id tolerance: 0.03 0.03 0.5
pattern: i.H* j.H* i.C*
relation: {D3} {} {}
template: H 0.02 H2 0.02 13C 0.5
```

With the above settings, a chemical shift error of 0.03 ppm in both proton dimensions and 0.5 ppm in the carbon dimension are allowed when building a list of possible assignments for each peak according to chemical shifts. An error range of 0.02 ppm in both proton dimensions and 0.2 ppm in the carbon are allowed during the search for symmetric peaks.

The script is called from the NMRView console with the `IassignUwatch` command, followed by 4 arguments. The first one specifies which peaklist the script will operate on, the second one specifies the distance cut-off (in Å) for assignment, the third one indicates the minimum required (in %) of structures having the two protons involved in the assignment within 5 Å, and the final argument designates the name of the partner peak list (see below for more details about the nature and significance of the partner peak list). For example, typing

```
IassignUwatch mothernoesy 4.5 30 n15noesy
```

would automatically assign the peak list “mothernoesy”, keeping only assignment possibilities for which the maximum distance between the two involved protons in the loaded model structures is smaller or equal to 4.5 Å, and for which at least 30% of the structures have the two involved protons within 5 Å. The use of a starting model structure is not mandatory. In a case where no model structure are available, the user can simply specify a very high number as the second argument, and 0 for the third argument.

A partner list is always necessary, as NOE contacts to HN backbone atoms have no corresponding symmetric peaks in a  $^{13}\text{C}$ -NOESY spectrum. The presence of symmetry in such cases must be verified in a  $^{15}\text{N}$ -edited experiment, such as a  $^{15}\text{N}$ -NOESY. The same logic holds true for a  $^{15}\text{N}$ -NOESY experiment, where the presence of symmetric peaks to protons other than backbone HN must be verified in a  $^{13}\text{C}$ -NOESY spectrum. For example, a  $^{13}\text{C}$ -NOESY peak that could potentially be assigned to (12.HA 15.CB 15.CB) will require the presence of a symmetric peak at (15.HB 12.HA 12.HA) in the same peak list, but symmetry to a NOE at (12.HN 15.CB 15.CB) will need to be verified at coordinates (15.HB 12.HN 12.N) in a  $^{15}\text{N}$ -NOESY spectrum.

### *Source code*

---

```
proc IassignUwatch {curr_list cutoff percentagestruc partnerlist } {  
  
global Nv_Natoms  
  
#retrieve information about current datasets
```

```
set labels      [nv_peak label $curr_list]
set patterns    [nv_peak pattern $curr_list]
set relations   [nv_peak relation $curr_list]
set tolerances [nv_peak idtol $curr_list]
set ndim        [llength $labels]
set activedataset [nv_peak dataset $curr_list]

set sf [nv_dataset sf $activedataset 3]
set sw [nv_dataset sw $activedataset 3]
set size [nv_dataset size $activedataset 3]
set folded [expr $sw/$sf]

set namefirstdim [lindex $labels 0]
set namesecnddim [lindex $labels 1]
set namethirddim [lindex $labels 2]

set datasetcenter [nv_dataset ref $activedataset 3]
set datasetinf [expr $datasetcenter-($sw*0.5/$sf)]
set datasetsup [expr $datasetcenter+($sw*0.5/$sf)]

set labels_part [nv_peak label $partnerlist]
set partnerdataset [nv_peak dataset $partnerlist]
set sf_part      [nv_dataset sf $partnerdataset 3]
set sw_part      [nv_dataset sw $partnerdataset 3]
set size_part    [nv_dataset size $partnerdataset 3]
set folded_part  [expr $sw_part/$sf_part]
set datasetcenter_part [nv_dataset ref $partnerdataset 3]
set datasetinf_part [expr $datasetcenter_part-($sw_part*0.5/$sf_part)]
set datasetsup_part [expr $datasetcenter_part+($sw_part*0.5/$sf_part)]

#loop through each peak

foreachpeak currentpeak $curr_list {

    set assigndim1 ""
    set assigndim2 ""
    set assigndim3 ""

    #build a block of possible assignment possibilities
    #this part is simply code borrowed from some internal NMRViewprocedure, but it
automatically checks
    #for folded chemical shifts

    set search ""
    set ppms ""
```

```

set useDims 0
set foundit false

set searchfolded1 ""
set searchfolded2 ""

#check if the peak is not assigned or not marked for deletion

if {[nv_peak elem $namefirstdim.L $curr_list.$currentpeak]== "?" && [nv_peak
status $curr_list.$currentpeak]==0} {

    if {[length [nv_peak lab $curr_list]]==3} {
        set ppm1 [nv_peak elem [lindex $labels 2] $curr_list.$currentpeak]
        set ppm2 [expr $ppm1 + $folded]
        set ppm3 [expr $ppm1 - $folded]
    }

    # this block builds a search string
    for {set i 0} {$i<$ndim} {incr i} {
        set tolerance [string trim [lindex $tolerances $i]]
        if {[expr {$tolerance > 30.0}]} {continue}
        incr useDims
        set label [lindex $labels $i]
        set ppm [nv_peak elem $label.P $curr_list.$currentpeak]
        lappend ppms $ppm
        set pattern [string trim [lindex $patterns $i]]
        if {$pattern==""} {set pattern *}
        if {$pattern=="."} {set pattern *}
        set relation [string trim [lindex $relations $i]]

        if {([string length $relation]>0) && ($relation != ".")} {
            append search "$pattern\($relation\)@${ppm}~$tolerance"
        } else {
            lappend search "$pattern@${ppm}~$tolerance"
        }
    }

    set search "$search "
}

set ndim $useDims
set dataset [nv_peak dataset $curr_list]

if {$scutoff == ""} {
    set cutoff 100000.0
}

```

```
if {$folded!=""} {
    set a [lindex $search 2]
    set b [string first @ $a]
    set c [string first ~ $a]
    set newsearch [string range $a 0 $b]
    set tolerance [string range $a $c end]
    set searchfolded1 [concat [lindex $search 0] [lindex $search 1]
$newsearch$ppm2$tolerance]
    set searchfolded2 [concat [lindex $search 0] [lindex $search 1]
$newsearch$ppm3$tolerance]

    set idResult [concat [eval nv_idpeak -thresh $cutoff $search] [eval
nv_idpeak -thresh $cutoff $searchfolded1] [eval nv_idpeak -thresh $cutoff
$searchfolded2]]
    } else {
        set idResult [eval nv_idpeak -thresh $cutoff $search]
    }
}

set peakintensity [nv_peak elem int $curr_list.$currentpeak]

#inspect each solution for that peak
foreach solution $idResult {

    #check if the percentage of structures that have the restraint >5A is larger
than the minimum specified
    set percentagecurrent [lindex $solution 6]
    if {$percentagecurrent<$percentagestruc} {continue}

    set atom1 [lindex $solution 0]
    set atom2 [lindex $solution 1]
    set atom3 [lindex $solution 2]

    set ppmatom3 [nv_atom elem ppm $atom3]
    #check if atom3 has the expected sign for its intensity
#if it's a positive peak, then the chemical shift is within $datasetup
and $datasetinf

    if {$peakintensity>0} {set currentint "pos"} else {set currentint
"neg"}
```

```

        if {$ppmatom3 <=$datasetsup && $ppmatom3 >= $datasetinf}
{set expectedint "pos"} else {set expectedint "neg"}

        #check if it has the right intensity
        #if not, skip this assignment
        if {$currentint!=$expectedint} {
            puts "rejected $solution for peak $currentpeak because its
intensity doesn't match expected one for $atom3"
            continue
        }

set ppmatom1 [nv_atom elem ppm $atom1]
set ppmatom2 [nv_atom elem ppm $atom2]

#find the parent of atom1
set parentnum [nv_atom elem parent $atom1]
set parentcarbon [nv_atom elem aname $parentnum]

set ppmparent [nv_atom elem ppm $parentnum]

if {[string range $parentcarbon 0 0]=="C" && $ppmparent>0} {
    #the parent atom is a carbon and there is chemical shift
assignment for it
    #now have to check for the chemical shift assignment of the parent
atom
    #fold the chemical shift if it's not within the limit of the spectrum

    if {$ppmparent > $datasetsup} {set ppmparent [expr $datasetinf-
$datasetsup + $ppmparent]}
    if {$ppmparent < $datasetinf} {set ppmparent [expr $datasetsup-$datasetinf +
$ppmparent]}

    #now check for the presence of a symmetric peak
    set checkforsym [nv_peak find $curr_list $ppmatom2 $ppmatom1
$ppmparent]

    set numpossiblesympeaks [llength $checkforsym]

    if {$numpossiblesympeaks>0} {

        #consider the assignment

        set assigndim1 [concat $assigndim1 $atom1]

```

```

        set assigndim2 [concat $assigndim2 $atom2]
        set assigndim3 [concat $assigndim3 $atom3]
    }
}

if {[string range $parentcarbon 0 0]=="N" && $ppmparent>0} {
assignment for it
    #the parent atom is a Nitrogen and there is chemical shift
    #now have to check for the chemical shift assignment of the parent
    #fold the chemical shift if it's not within the limit of the 'partner'
    atom
    spectrum

    if {$ppmparent > $datasetsup_part} {set ppmparent [expr
    $datasetinf_part-$datasetsup_part + $ppmparent]}
    if {$ppmparent < $datasetinf_part} {set ppmparent [expr
    $datasetsup_part-$datasetinf_part + $ppmparent]}

    #now check for the presence of a symmetric peak
    set checkforsym [nv_peak find $partnerlist $ppmatom1
    $ppmatom2 $ppmparent]

    set numpossiblesympeaks [llength $checkforsym]

    if {$numpossiblesympeaks>0} {

        #consider the assignment

        set assigndim1 [concat $assigndim1 $atom1]
        set assigndim2 [concat $assigndim2 $atom2]
        set assigndim3 [concat $assigndim3 $atom3]

    }
}

if {$ppmparent<0} {
    #there is no chemical shift assignment for the parent carbon
    # assign it for now
    set assigndim1 [concat $assigndim1 $atom1]
    set assigndim2 [concat $assigndim2 $atom2]
    set assigndim3 [concat $assigndim3 $atom3]
}
}

```

```

    }

    #assign the peak to what was found
    if {[length $assigndim1]>0} {
        nv_peak elem $namefirstdim.L $curr_list.$currentpeak $assigndim1
        nv_peak elem $nameseccondim.L $curr_list.$currentpeak $assigndim2
        nv_peak elem $namethirddim.L $curr_list.$currentpeak $assigndim3
    }
}

#end looping through each peak
}

#this part verifies that the automatically assigned peaks make sense
#in terms of intensity sign (all peaks of a given carbon should all be of the same intensity)

puts "doing verification of the assignments"

#initialize an array of intensity signs for each carbon
for {set i 1} {$i<=$Nv_Natoms} {incr i} {
    set listofsigns{$i} ""
}

foreachpeak currentpeak $curr_list {
    #check if the peak is assigned
    set assignments [nv_peak elem $namethirddim.L $curr_list.$currentpeak]

    if {$assignments!="?"} {
        set peakint [nv_peak elem int $curr_list.$currentpeak]

        foreach assignment $assignments {

            if {$peakint==[expr abs($peakint)]} {
                set intensity pos.$currentpeak
            } else {
                set intensity neg.$currentpeak
            }

            set atomnum [nv_atom num $assignment]
        }
    }
}

```

```

                                set listofsigns{$atomnum} [concat [set
listofsigns{$atomnum}] $intensity]
                                }
                                }
                                }

#now verify if the peaks assigned for a given carbon all have the same sign

for {set i 1} {$i<=$Nv_Natoms} {incr i} {
    set attributions [set listofsigns{$i}]
    if {$attributions!=""} {
        if {[string match "*pos*" $attributions]==1 && [string match "*neg*"
$attributions]==1} {
            puts "problems with [nv_atom elem seq $i].[nv_atom elem aname
$i]: $attributions"
        }
    }
}

#end of procedure
}
```

## Appendix III

### *Chemical shift assignment of sCTnC in complex with magnesium*

The chemical shift database for sCTnC in the sCTnC•Mg<sup>2+</sup> complex is provided below in NMRView format. Assignments are missing for residues in Ca<sup>2+</sup>-binding site IV. The three output decimal digits are from the standard output of NMRView and do not reflect the precision of the chemical shifts.

Table AIII-1. Chemical shift assignment of sCTnC in the sCTnC•Mg<sup>2+</sup> complex.

ASP	89.CA	54.297	LYS	93.HG2	1.440	GLU	97.CA	59.398
ASP	89.CB	41.228	LYS	93.CD	29.580	GLU	97.HA	4.227
ALA	90.N	124.650	LYS	93.HD2	1.680	GLU	97.CB	29.997
ALA	90.HN	8.301	LYS	93.HE2	3.010	GLU	97.HB2	2.290
ALA	90.CA	52.756	SER	94.N	117.280	GLU	97.HB1	2.120
ALA	90.HA	4.310	SER	94.HN	8.612	GLU	97.CG	37.090
ALA	90.CB	19.389	SER	94.CA	58.250	GLU	97.HG2	2.410
ALA	90.HB1	1.410	SER	94.HA	4.500	GLU	97.HG1	2.360
LYS	91.N	120.350	SER	94.CB	64.580	LEU	98.N	120.879
LYS	91.HN	8.293	SER	94.HB2	4.260	LEU	98.HN	8.495
LYS	91.CA	56.660	SER	94.HB1	4.060	LEU	98.CA	58.341
LYS	91.HA	4.314	GLU	95.N	122.813	LEU	98.HA	4.296
LYS	91.CB	32.990	GLU	95.HN	8.923	LEU	98.CB	41.633
LYS	91.HB2	1.870	GLU	95.CA	60.350	LEU	98.HB2	2.230
LYS	91.HB1	1.820	GLU	95.HA	4.006	LEU	98.HB1	1.670
LYS	91.CG	25.300	GLU	95.CB	29.380	LEU	98.CG	27.260
LYS	91.HG2	1.440	GLU	95.HB2	2.460	LEU	98.HG	1.930
LYS	91.CD	29.560	GLU	95.HB1	2.350	LEU	98.CD1	23.650
LYS	91.HD2	1.710	GLU	95.CG	37.060	LEU	98.HD11	0.970
LYS	91.HE2	3.020	GLU	95.HG2	2.180	LEU	98.CD2	26.270
GLY	92.N	109.668	GLU	95.HG1	2.120	LEU	98.HD21	0.800
GLY	92.HN	8.349	GLU	96.N	119.000	ALA	99.N	122.702
GLY	92.CA	45.396	GLU	96.HN	8.463	ALA	99.HN	8.761
GLY	92.HA2	3.991	GLU	96.CA	59.380	ALA	99.CA	55.506
LYS	93.N	120.878	GLU	96.HA	4.122	ALA	99.HA	3.932
LYS	93.HN	8.123	GLU	96.CB	29.512	ALA	99.CB	17.872
LYS	93.CA	56.024	GLU	96.HB2	2.110	ALA	99.HB1	1.319
LYS	93.HA	4.400	GLU	96.HB1	2.017	ASN	100.N	116.945
LYS	93.CB	33.465	GLU	96.CG	36.660	ASN	100.HN	7.985
LYS	93.HB2	1.860	GLU	96.HG2	2.320	ASN	100.CA	56.264
LYS	93.HB1	1.780	GLU	97.N	120.305	ASN	100.HA	4.453
LYS	93.CG	25.290	GLU	97.HN	7.933	ASN	100.CB	38.347

ASN	100.HB2	2.981	ASP	106.HB1	1.920	ILE	113.CG1	25.000
ASN	100.HB1	2.916	LYS	107.N	124.630	ILE	113.HG12	1.385
CYS	101.N	117.978	LYS	107.HN	7.960	ILE	113.HG11	0.990
CYS	101.HN	8.053	LYS	107.CA	59.370	ILE	113.CD1	15.770
CYS	101.CA	63.270	LYS	107.HA	4.110	ILE	113.HD11	0.070
CYS	101.HA	4.204	LYS	107.CB	31.940	ILE	113.CG2	24.900
CYS	101.CB	27.064	LYS	107.HB2	1.910	ILE	113.HG21	0.470
CYS	101.HB2	3.313	LYS	107.CG	25.290	ASP	114.N	121.260
CYS	101.HB1	3.030	LYS	107.HG2	1.540	ASP	114.HN	8.034
PHE	102.N	120.229	LYS	107.HG1	1.610	ASP	114.CA	51.600
PHE	102.HN	8.576	LYS	107.CD	29.220	ASP	114.HA	5.240
PHE	102.CA	62.096	LYS	107.HD2	1.750	ASP	114.CB	42.440
PHE	102.HA	3.686	LYS	107.HD1	1.719	ASP	114.HB2	3.260
PHE	102.CB	40.074	LYS	107.CE	42.310	ASP	114.HB1	2.680
PHE	102.HB2	3.261	LYS	107.HE2	3.122	ILE	115.N	117.027
PHE	102.HB1	2.902	ASN	108.N	112.647	ILE	115.HN	8.500
ARG	103.N	113.875	ASN	108.HN	7.823	ILE	115.CA	64.804
ARG	103.HN	7.831	ASN	108.CA	51.690	ILE	115.HA	4.034
ARG	103.CA	59.009	ASN	108.HA	4.695	ILE	115.CB	38.220
ARG	103.HA	4.113	ASN	108.CB	36.690	ILE	115.HB	1.923
ARG	103.CB	30.401	ASN	108.HB2	3.306	ILE	115.CG1	30.210
ARG	103.HB2	1.960	ASN	108.HB1	2.820	ILE	115.HG12	1.464
ARG	103.HG2	1.850	ALA	109.N	121.370	ILE	115.HG11	1.338
ARG	103.HG1	1.705	ALA	109.HN	8.004	ILE	115.CD1	14.800
ARG	103.CD	43.600	ALA	109.CA	53.465	ILE	115.HD11	0.916
ARG	103.HD2	3.223	ALA	109.HA	4.040	ILE	115.CG2	17.100
ARG	103.HD1	3.014	ALA	109.CB	17.100	ILE	115.HG21	0.989
ILE	104.N	117.630	ALA	109.HB1	1.382	GLU	116.CA	59.216
ILE	104.HN	7.621	ASP	110.N	116.137	GLU	116.CB	29.056
ILE	104.CA	64.270	ASP	110.HN	8.479	GLU	117.N	122.636
ILE	104.HA	3.566	ASP	110.CA	52.847	GLU	117.HN	8.382
ILE	104.CB	37.940	ASP	110.HA	4.783	GLU	117.CA	58.730
ILE	104.HB	1.720	ASP	110.CB	41.495	GLU	117.CB	29.330
ILE	104.CG1	29.220	ASP	110.HB2	3.206	LEU	118.N	119.397
ILE	104.HG12	1.560	ASP	110.HB1	2.576	LEU	118.HN	8.698
ILE	104.HG11	1.046	GLY	111.N	112.707	LEU	118.CA	58.116
ILE	104.CD1	13.830	GLY	111.HN	10.398	LEU	118.HA	3.958
ILE	104.HD11	0.740	GLY	111.CA	45.063	LEU	118.CB	41.253
ILE	104.CG2	16.770	GLY	111.HA2	4.145	LEU	118.HB2	2.080
ILE	104.HG21	0.188	GLY	111.HA1	3.559	LEU	118.HB1	1.400
PHE	105.N	116.021	PHE	112.N	116.557	LEU	118.CG	27.910
PHE	105.HN	7.298	PHE	112.HN	8.237	LEU	118.HG	1.530
PHE	105.CA	60.480	PHE	112.CA	55.951	LEU	118.CD1	23.800
PHE	105.HA	4.281	PHE	112.HA	5.741	LEU	118.HD11	1.068
PHE	105.CB	39.340	PHE	112.CB	43.010	LEU	118.CD2	26.940
PHE	105.HB2	3.071	PHE	112.HB2	2.956	LEU	118.HD21	0.970
PHE	105.HB1	2.410	PHE	112.HB1	2.765	GLY	119.N	104.824
ASP	106.N	118.728	ILE	113.N	118.561	GLY	119.HN	7.985
ASP	106.HN	7.370	ILE	113.HN	9.284	GLY	119.CA	47.850
ASP	106.CA	52.254	ILE	113.CA	59.820	GLY	119.HA2	3.954
ASP	106.HA	4.846	ILE	113.HA	5.162	GLY	119.HA1	3.592
ASP	106.CB	38.897	ILE	113.CB	42.124	GLU	120.N	120.445
ASP	106.HB2	2.741	ILE	113.HB	2.023	GLU	120.HN	7.545

GLU	120.CA	59.493	THR	125.CB	70.220	GLU	132.N	117.930
GLU	120.HA	3.836	THR	125.HB	4.430	GLU	132.HN	8.838
GLU	120.CB	29.547	THR	125.CG2	22.340	GLU	132.CA	59.293
GLU	120.CG	36.760	THR	125.HG21	1.401	GLU	132.HA	4.111
GLU	120.HG2	2.450	GLY	126.N	109.066	GLU	132.CB	29.590
GLU	120.HG1	2.180	GLY	126.HN	7.752	ASP	133.N	118.759
ILE	121.N	121.280	GLY	126.CA	45.630	ASP	133.HN	7.580
ILE	121.HN	8.024	GLY	126.HA2	4.173	ASP	133.CA	55.887
ILE	121.CA	65.463	GLY	126.HA1	3.831	ASP	133.HA	4.633
ILE	121.HA	3.120	GLU	127.N	119.804	ASP	133.CB	40.763
ILE	121.CB	38.390	GLU	127.HN	7.983	ASP	133.HB2	2.841
ILE	121.HB	1.760	GLU	127.CA	55.550	ASP	133.HB1	2.746
ILE	121.CG1	30.540	GLU	127.HA	4.332	ILE	134.N	121.442
ILE	121.HG12	1.410	GLU	127.CB	30.124	ILE	134.HN	7.763
ILE	121.HG11	0.640	GLU	127.HB2	1.951	ILE	134.CA	64.916
ILE	121.CD1	15.790	GLU	127.HB1	1.702	ILE	134.HA	3.661
ILE	121.HD11	0.480	GLU	127.CG	35.590	ILE	134.CB	37.650
ILE	121.CG2	18.080	GLU	127.HG2	2.164	ILE	134.HB	1.982
ILE	121.HG21	0.890	HIS	128.N	121.290	ILE	134.HG12	1.600
LEU	122.N	119.950	HIS	128.HN	8.681	ILE	134.HG11	29.220
LEU	122.HN	8.411	HIS	128.CA	55.580	ILE	134.CD1	14.150
LEU	122.CA	58.091	HIS	128.HA	4.680	ILE	134.HD11	0.845
LEU	122.HA	3.971	HIS	128.CB	29.420	ILE	134.CG2	18.080
LEU	122.CB	40.966	HIS	128.HB2	3.167	ILE	134.HG21	0.921
LEU	122.HB2	1.880	HIS	128.HB1	3.080	GLU	135.N	119.494
LEU	122.HB1	1.330	VAL	129.N	122.320	GLU	135.HN	8.140
LEU	122.HG	1.290	VAL	129.HN	7.980	GLU	135.CA	60.031
LEU	122.CD1	23.001	VAL	129.CA	61.586	GLU	135.HA	3.914
LEU	122.HD11	0.848	VAL	129.HA	4.263	GLU	135.CB	29.700
LEU	122.CD2	26.600	VAL	129.CB	33.610	GLU	135.HB2	2.360
LEU	122.HD21	0.810	VAL	129.HB	1.970	GLU	135.HB1	2.080
ARG	123.N	118.460	VAL	129.CG2	22.340	GLU	135.CG	36.580
ARG	123.HN	7.974	VAL	129.HG21	0.880	GLU	135.HG2	2.220
ARG	123.CA	59.370	VAL	129.CG1	21.360	ASP	136.N	119.466
ARG	123.HA	4.159	VAL	129.HG11	0.840	ASP	136.HN	7.631
ARG	123.CB	30.230	ILE	130.N	123.038	ASP	136.CA	57.403
ARG	123.HB2	1.863	ILE	130.HN	8.416	ASP	136.HA	4.429
ARG	123.CG	28.750	ILE	130.CA	60.994	ASP	136.CB	40.600
ARG	123.HG2	1.578	ILE	130.HA	4.340	ASP	136.HB2	2.780
ARG	123.HG1	1.851	ILE	130.CB	39.080	ASP	136.HB1	2.730
ARG	123.CD	43.310	ILE	130.HB	2.090	LEU	137.N	120.880
ARG	123.HD2	3.280	ILE	130.CG1	27.590	LEU	137.HN	7.879
ARG	123.HD1	3.160	ILE	130.HG12	1.397	LEU	137.CA	57.800
ALA	124.N	122.662	ILE	130.HG11	1.292	LEU	137.HA	4.123
ALA	124.HN	8.077	ILE	130.CD1	13.800	LEU	137.CB	42.195
ALA	124.CA	54.880	ILE	130.HD11	0.907	LEU	137.HB2	1.870
ALA	124.HA	4.288	ILE	130.CG2	18.100	LEU	137.HB1	1.664
ALA	124.CB	19.032	ILE	130.HG21	0.986	LEU	137.CG	27.260
ALA	124.HB1	1.646	GLU	131.N	124.978	LEU	137.HG	1.774
THR	125.N	107.257	GLU	131.HN	8.773	LEU	137.CD1	25.620
THR	125.HN	7.881	GLU	131.CA	60.293	LEU	137.HD11	0.856
THR	125.CA	62.380	GLU	131.HA	3.902	ASP	140.CA	54.870
THR	125.HA	4.422	GLU	131.CB	29.646	ASP	140.CB	41.280

SER	141.N	115.608	ASP	150.N	122.644	LYS	156.CA	58.714
SER	141.HN	8.147	ASP	150.HN	8.390	LYS	156.HA	3.940
SER	141.CA	58.950	ASP	150.CA	51.510	LYS	156.CB	31.992
SER	141.HA	4.397	ASP	150.HA	5.480	LYS	156.HB2	1.862
SER	141.CB	63.811	ASP	150.CB	42.050	LYS	156.CG	25.290
SER	141.HB2	3.950	ASP	150.HB2	2.970	LYS	156.HG2	1.520
SER	141.HB1	3.880	ASP	150.HB1	2.600	LYS	156.HG1	1.420
ASP	142.N	122.166	PHE	151.N	117.885	LYS	156.CD	29.220
ASP	142.HN	8.343	PHE	151.HN	8.180	LYS	156.HD2	1.660
ASP	142.CA	54.707	PHE	151.CA	61.750	LYS	156.CE	42.010
ASP	142.HA	4.630	PHE	151.HA	3.512	LYS	156.HE2	2.963
ASP	142.CB	41.171	PHE	151.CB	38.862	MET	157.N	120.965
ASP	142.HB2	2.760	PHE	151.HB2	2.519	MET	157.HN	7.877
LYS	143.N	122.000	PHE	151.HB1	2.116	MET	157.CA	58.445
LYS	143.HN	8.056	ASP	152.N	118.694	MET	157.HA	3.930
LYS	143.CB	33.014	ASP	152.HN	7.785	MET	157.CB	33.128
ASN	145.N	116.296	ASP	152.CA	57.843	MET	157.HB2	2.290
ASN	145.HN	7.960	ASP	152.HA	4.058	MET	158.N	116.558
ASN	145.CA	54.706	ASP	152.CB	40.695	MET	158.HN	7.854
ASN	145.HA	4.430	ASP	152.HB2	2.727	MET	158.CA	55.379
ASN	145.CB	38.012	ASP	152.HB1	2.572	MET	158.HA	4.291
ASN	145.HB2	3.050	GLU	153.N	120.858	MET	158.CB	30.785
ASN	145.HB1	2.654	GLU	153.HN	8.670	MET	158.HB2	1.740
ASP	146.N	116.600	GLU	153.CA	59.309	MET	158.HB1	1.720
ASP	146.HN	8.588	GLU	153.HA	3.904	GLU	159.N	119.831
ASP	146.CA	52.650	GLU	153.CB	29.860	GLU	159.HN	7.739
ASP	146.HA	4.770	GLU	153.HB2	2.513	GLU	159.CA	58.343
ASP	146.CB	41.230	GLU	153.HB1	1.910	GLU	159.HA	4.066
ASP	146.HB2	2.955	GLU	153.CG	37.740	GLU	159.CB	29.750
ASP	146.HB1	2.392	GLU	153.HG2	2.820	GLU	159.HB2	2.057
GLY	147.N	109.050	GLU	153.HG1	2.507	GLU	159.CG	30.210
GLY	147.HN	8.350	PHE	154.N	122.470	GLU	159.HG2	2.420
GLY	147.CA	45.696	PHE	154.HN	8.683	GLU	159.HG1	2.220
GLY	147.HA2	3.935	PHE	154.CA	60.959	GLY	160.N	105.660
ARG	148.N	116.890	PHE	154.HA	4.236	GLY	160.HN	7.730
ARG	148.HN	7.877	PHE	154.CB	39.200	GLY	160.CA	45.460
ARG	148.CA	53.580	PHE	154.HB2	3.363	GLY	160.HA2	4.146
ARG	148.HA	5.489	PHE	154.HB1	3.220	GLY	160.HA1	3.858
ARG	148.CB	34.130	LEU	155.N	120.596	VAL	161.N	119.144
ARG	148.HB2	1.620	LEU	155.HN	8.620	VAL	161.HN	7.440
ARG	148.CG	26.260	LEU	155.CA	58.105	VAL	161.CA	62.619
ARG	148.HG2	1.350	LEU	155.HA	3.324	VAL	161.HA	4.136
ARG	148.CD	43.311	LEU	155.CB	41.200	VAL	161.CB	32.686
ARG	148.HD2	2.893	LEU	155.HB2	1.320	VAL	161.HB	2.142
ARG	148.HD1	2.590	LEU	155.HB1	1.270	VAL	161.CG2	21.360
ILE	149.N	119.000	LEU	155.CG	26.270	VAL	161.HG21	0.942
ILE	149.HN	9.096	LEU	155.HG	1.044	VAL	161.CG1	21.690
ILE	149.CA	60.202	LEU	155.CD1	24.310	VAL	161.HG11	0.897
ILE	149.HA	5.321	LEU	155.HD11	0.670	GLN	162.N	127.715
ILE	149.CB	42.230	LEU	155.CD2	25.620	GLN	162.HN	7.793
ILE	149.HB	2.440	LEU	155.HD21	0.637	GLN	162.CA	57.440
ILE	149.CG2	17.750	LYS	156.N	117.734	GLN	162.HA	4.158
ILE	149.HG21	0.990	LYS	156.HN	7.499	GLN	162.CB	30.468

---

GLN	162.HB2	2.100	GLN	162.CG	34.470
GLN	162.HB1	1.941	GLN	162.HG2	2.325